Plasma Physics Reports, Vol. 31, No. 10, 2005, pp. 803–808. Translated from Fizika Plazmy, Vol. 31, No. 10, 2005, pp. 867–872.

TOKAMAKS

Electron Density Modulation in Magnetic Islands in the TUMAN-3M Tokamak

V. A. Kornev, L. G. Askinazi, M. I. Vil'dzhyunas, V. E. Golant, N. A. Zhubr, S. V. Krikunov, S. V. Lebedev, V. V. Rozhdestvenskiĭ, and A. S. Tukachinskiĭ

Ioffe Physicotechnical Institute, Russian Academy of Sciences, Politekhnicheskaya ul. 26, St. Petersburg, 194021 Russia

Received March 19, 2004; in final form, December 27, 2004

Abstract—MHD oscillations with m/n = 4/1 and 3/1 that arise at the periphery of the TUMAN-3M tokamak in the initial stage of a discharge are investigated. It is found that these oscillations lead to a significant modulation of the electron density n_e, which is attributable to the accumulation of plasma within a magnetic island. Numerical simulations of the modulation structure made it possible to determine the radius of the resonant surface and the radial width of the island and to evaluate the characteristic density gradient in the island. The gradient was found to be ten times larger than that of the unperturbed profile of $n_e(r)$ near the resonant surface. This points to reduced plasma transport within the magnetic island. © *2005 Pleiades Publishing, Inc.*

1. INTRODUCTION

Oscillations of the poloidal magnetic field (hereafter, MHD oscillations), which are detected by pick-up coils placed outside the plasma, have been observed in different stages of a tokamak discharge [1, 2]. Such oscillations are generally caused by the onset of tearing instability, which gives rise to magnetic islands near the resonant magnetic surfaces. Magnetic islands have a helical structure with the poloidal and toroidal numbers m and n, respectively, and are separated from the main plasma by a separatrix. As a matter of fact, a magnetic island is a closed helical tube with nested magnetic surfaces within it. Since the island is, in a sense, separated from the main plasma, the plasma parameters within it have specific spatial distributions. For this reason, the island structure can be observed, e.g., with the help of multichannel soft X-ray diagnostics [3].

If the plasma transport characteristics in an island differ substantially from those in the surrounding plasma, then the temperature and density can be significantly modulated. For example, studies of the magnetic structures by means of a microwave reflectometer in the TEXTOR-94 tokamak showed that the density modulation between the X-point of an island and its magnetic axis was 20–30% [4].

This paper presents the results from studies of density modulation in the magnetic islands of the TUMAN-3M tokamak with the help of a multichannel microwave interferometer. Experiments and numerical simulations show that the electron density is modulated by more than 50% in the direction from the X-point to the magnetic axis of an island. Within a magnetic island, the density gradient exceeds that in the unperturbed surrounding plasma by one order of magnitude.

2. DESCRIPTION OF THE EXPERIMENT

The experiments were conducted in ohmic discharges of the TUMAN-3M tokamak at the following plasma parameters: the major radius R_0 = 0.53 m, the minor radius a_l = 0.22 m, the toroidal magnetic field $B_t \simeq 0.9$ T, the plasma current $I_p \simeq 150$ kA, the average electron density $n_e = (1.5–2.0) \times 10^{19}$ m^{-3}, the central electron temperature $T_e(0)$ = 0.4–0.6 keV, and the central ion temperature $T_i(0)$ = 0.15–0.2 keV. The working gas was deuterium. The tokamak was equipped with a data acquisition system, which recorded the main plasma parameters: the loop voltage U_p, the plasma current I_p, the intensity of soft X-ray (SXR) emission, signals from Mirnov probes (≈1-cm-diameter multiturn coils measuring the poloidal component of the magnetic field), microwave-interferometer signals averaged along several chords, etc. The radial density profile was reconstructed by the integral inversion of the microwave-interferometer signals measured along ten vertical chords (λ = 2.2 mm). Two sets of magnetic probes installed outside of the vacuum vessel were used to study MHD oscillations. Each set consisted of 24 probes placed equidistantly in the poloidal direction and separated from one another by 60° in the toroidal direction. This allowed us to determine both the poloidal and toroidal numbers of oscillations. To perform Fourier analysis, the probe signals were recorded with the use of three 16-channel analog-to-digit converters.

The time evolution of the main plasma parameters in a typical discharge is presented in Fig. 1. In the early stage of the discharge, rapidly oscillating MHD signals are clearly seen. The poloidal wavenumbers vary from m = 6 to m = 3 or 2, the toroidal wavenumber being

1063-780X/05/3110-0803$26.00 © 2005 Pleiades Publishing, Inc.

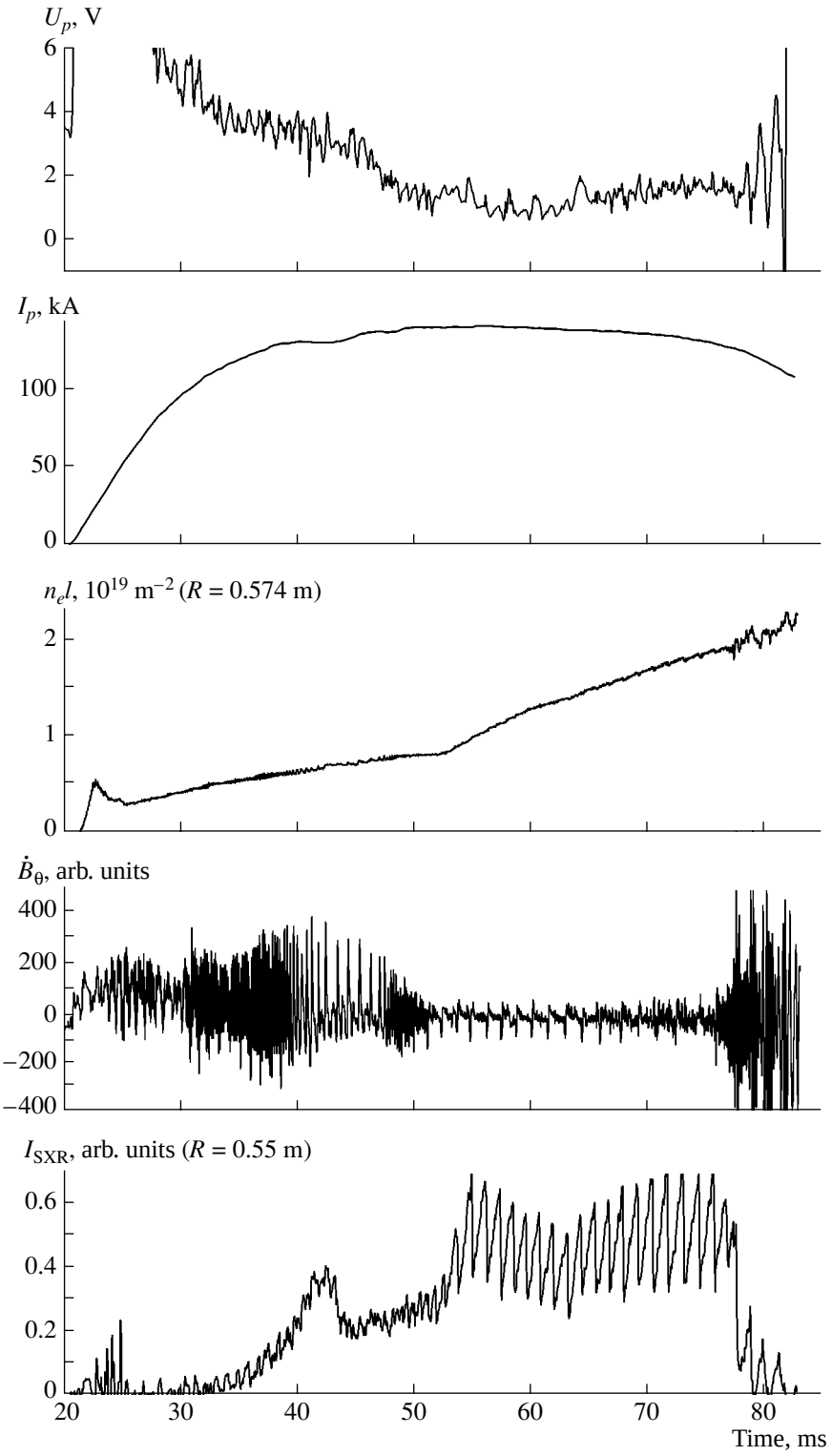

Fig. 1. Time evolution of the main plasma parameters in a discharge with MHD oscillations at the end of the plasma current ramp-up phase.

$n = 1$. As time elapses, nearly steady-state oscillations with a frequency of about 8 kHz are established. In the case presented in Fig. 1, the $m/n = 4/1$ mode is predominant within a time interval from 35 to 52 ms.

3. EXPERIMENTAL RESULTS

MHD oscillations with $m/n = 4/1$ were observed not only in the probe signals but also in the signals from the microwave interferometer measuring the integrated

density along vertical chords. Typical interferometric signals for the central and the innermost chords are shown in Fig. 2. It was found that the amplitude of MHD oscillations detected by the Mirnov probes depends on the plasma density. Figure 3 shows the amplitude of MHD oscillations (Mirnov probe signal divided by the oscillation frequency) as a function of the plasma density. It should be noted that an increase in the oscillation amplitude during a discharge is accompanied by a decrease in the rotation frequency (see Fig. 1) and, in some cases, by a full stop of rotation, i.e., by the onset of a locked mode [5]. In most cases, however, slowed down rotation is followed by the acceleration phase and subsequent damping of oscillations. The onset and damping of the modes during the relaxation of the current profile is in qualitative agreement with calculations of the plasma stability against MHD oscillations with $m/n = 4/1$ and 3/1.

The dependences of the normalized beta, β_N, and the averaged amplitude of MHD oscillations, $\dot{B}_\theta/\omega$, on the plasma density are presented in Fig. 4. Here, β_N is the ratio of the toroidal beta, $\beta_t = \dfrac{\langle nT \rangle}{B^2/8\pi}$, to the Troyon parameter [6],

$$\beta_N = \frac{\beta_t}{I_p/aB_t}, \qquad (1)$$

where the current is in A, the minor plasma radius is in m, and the magnetic field is in T. It can be seen that, at densities higher than 1.3×10^{19} m^{-3} (which corresponds to $n_e l > 0.6 \times 10^{19}$ m^{-2}), a decrease in the normalized beta correlates with an increase in $\dot{B}_\theta/\omega$. Such a correlation indicates that MHD oscillations affect the maximum attainable value of β_N. It should be noted that the β_N values achieved in this experiment are substantially lower than those in the absence of MHD oscillations [7].

A distinguishing feature of the perturbations under study is the deep modulation of the chord-averaged electron density at the frequency of MHD oscillations (see Fig. 2 and [8]). The modulation is clearly seen in signals from all the channels of the microwave interferometer. The modulation depth of the averaged density as a function of the major radius R is shown in Fig. 5. It should be noted that the modulation depth at the plasma periphery is as high as 20%.

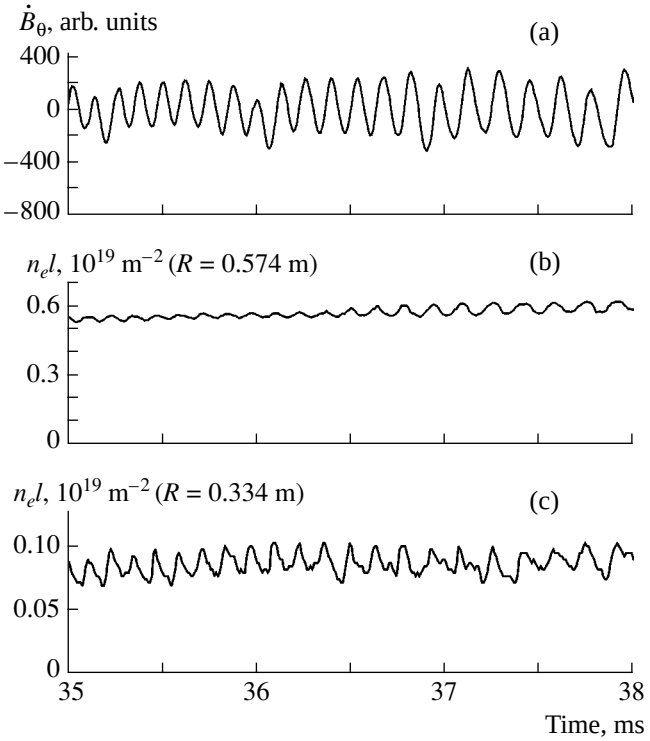

Fig. 2. (a) Mirnov-probe signal and microwave-interferometer signals taken from the (b) central and (c) innermost chords.

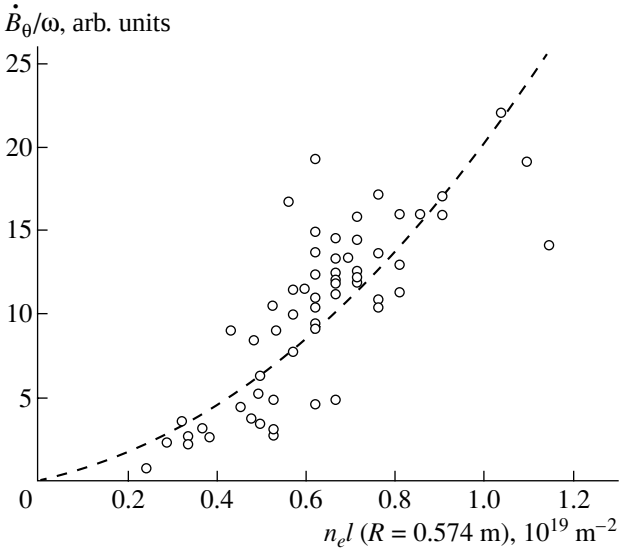

Fig. 3. Measured amplitude of MHD oscillations vs. chord-integrated density (symbols) and its approximation (dashed line) for $B_t = 0.83$ T and $I_p = 125$ kA.

4. NUMERICAL SIMULATIONS OF THE DENSITY MODULATION IN A MAGNETIC ISLAND

Generally, the local density cannot be reconstructed unambiguously from measurements along a finite number of chords N (in our case $N = 9$) viewing in one direction [9]. Nevertheless, adopting some a priori assumptions about the modulation structure characterized by a few (M) parameters, the problem may be solved if $M < N$.

The following parameters were chosen to describe density modulation: the poloidal number m of an MHD

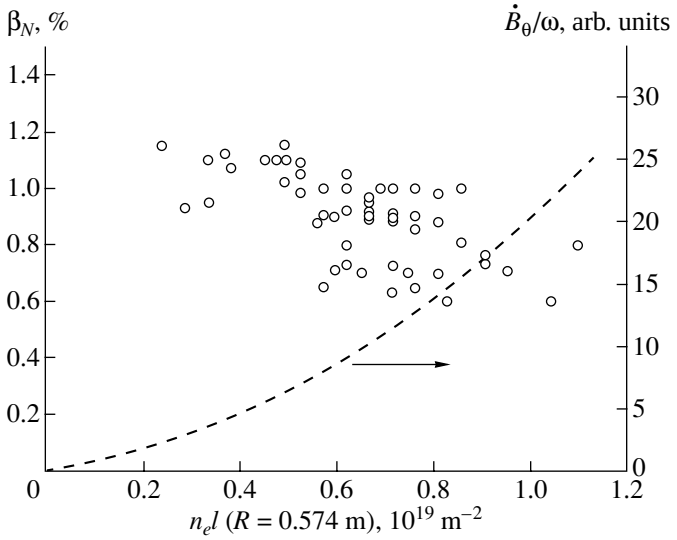

Fig. 4. Measured value of β_N (symbols) and the amplitude of MHD oscillations $\dot{B}_\theta/\omega$ from Fig. 3 (dashed line) vs. chord-integrated density for B_t = 0.83 T and I_p = 125 kA.

mode, the radial position r_s of the modulation (the radius of the resonant surface), the radial size w of the modulation (the width of the magnetic island), and the amplitude n_{island} of the modulation (the difference in the electron densities at the O-point and at the separatrix of the magnetic island).

The shape of the density modulation within the island was described by the formula

$$\delta n(r) = n_{\text{island}} e^{-\left(\frac{r-r_s}{w}\right)^2} f(\varphi_0), \qquad (2)$$

where

$$f(\varphi_0) = 1 + \cos[m(\varphi_0 - \varepsilon \sin\varphi_0)] \qquad (3)$$

describes the poloidal inhomogeneity of the modulation [10]. Note that the poloidal inhomogeneity of the modulation should account for a toroidicity correction related to the concentration of the magnetic field lines on the high field side of the magnetic surface. In Eq. (3), this effect is taken into account by introducing the term $\varepsilon \sin\varphi_0$, where φ_0 is the poloidal angle. The value of ε, which was constant during a run of the code, was defined as

$$\varepsilon = \frac{a}{R_0}\left(\beta + \frac{l_i}{2} + 1\right), \qquad (4)$$

where the value of $\beta + l_i/2$ was determined from magnetic measurements.

The results of integration of Eq. (2) along each of the nine viewing chords of the microwave interferometer were compared to the oscillating component of the measured signals. The values of w, r_s, and n_{island} were

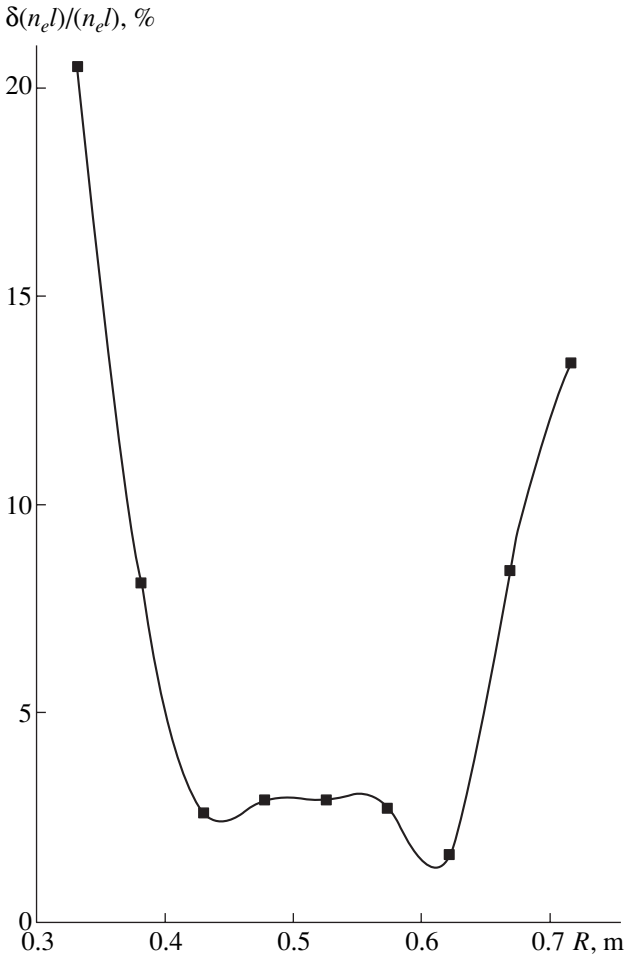

Fig. 5. Modulation depth of the chord-integrated density vs. major radius.

determined by the least-squares method. The poloidal structure used to simulate the electron density modulation is shown in Fig. 6. Figure 7 compares the calculated and measured amplitudes of the density modulation for several vertical chords with different positions along the major axis R. It can be seen that the model adequately describes the experiment. In this case, the poloidal number is m = 4, the width of the magnetic island is w = 0.016 m, the radius of the resonant surface is r_s = 0.19 m, and the difference in the densities at the O-point and at the separatrix of the magnetic island is $n_{\text{island}} = 0.45 \times 10^{19}$ m^{-3}.

The thus obtained density modulation within a magnetic island turned out to be rather deep. The value of n_e changes twofold between the X- and O-points. Knowing the modulation parameters, we can evaluate the radial density gradient within the island. The value of ∇n_e in different calculations varied from 4×10^{20} to 7×10^{20} m^{-4}, which was larger by one order of magnitude than the unperturbed plasma density gradient near the resonant surface. Since there were no additional plasma sources within the magnetic island, we may conclude

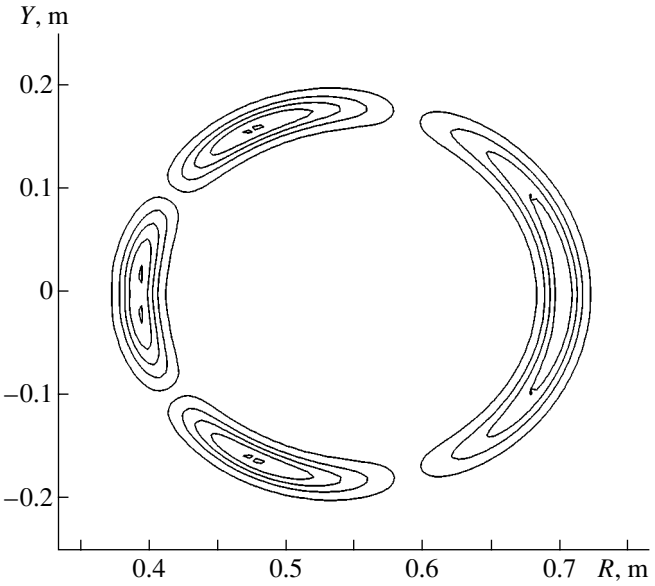

Fig. 6. Structure of electron density perturbation obtained from numerical simulations of the chord-integrated density modulation.

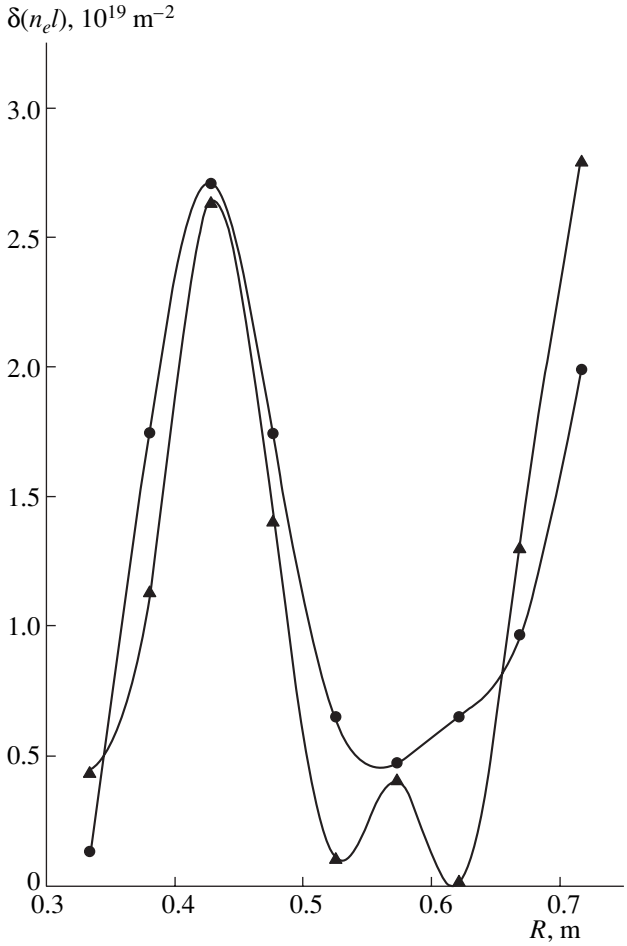

Fig. 7. Measured (triangles) and calculated (circles) amplitude of the chord-integrated density modulation vs. major radius.

that the effective coefficient of diffusion within the island was nearly ten times lower than that in the surrounding plasma. It should be noted that a similar (but somewhat shallower) density modulation in a magnetic island (20–30%) was observed in the TEXTOR-94 tokamak [4]. Note that the mode structures of oscillations in our experiments and in [4] were different: in TEXTOR-94, the m/n = 2/1 mode was analyzed, whereas, in our case, the plasma was accumulated in the more stable m/n = 4/1 mode. Density modulations were also observed in experiments with pellet injection [11], in which the pellet ablated within an island. In [11], such perturbations were called "snakes." The density modulations observed in our experiments (as well as in [4]) differ from snakes in that, in our case, the plasma is accumulated within an island in the absence of an additional particle source. This indicates that, in TEXTOR-94 and TUMAN-3M, cross-field transport is reduced within an island.

5. SIMULATION OF MHD STABILITY

MHD stability of the current profiles was simulated in a cylindrical model by means of Δ' analysis without allowance for the pressure effects. The equation for the flux function ψ,

$$(r\psi')' = \left(\frac{m^2}{r} + \frac{4\pi R}{cB_t}\frac{j'}{\mu - n/m}\right)\psi, \qquad (5)$$

was used to determine the stability parameter Δ',

$$\Delta'(W) = \frac{\psi'(r_s + W/2) - \psi'(r_s - W/2)}{\psi(r_s)}, \quad W \longrightarrow 0. \qquad (6)$$

If Δ' < 0, then the current profile is stable, and vice versa. The current density profile $j(r)$ was described by the model function $j(r) = j_0(1 - (r/a)^2)^\nu$. At large values of ν, the $j(r)$ profile is peaked, and it flattens as ν decreases. It was assumed that ψ = 0 either at the plasma boundary ($r = a$) or beyond it ($r = 1.1a$). The radius of the resonant surface r_s was determined from calculations of the density modulation in a magnetic island (see Section 4). It was found that, in the cases under analysis, a fairly flat current profile at which modes with low values of m/n were stable was necessary for the excitation the m/n =4/1 mode. Our simulations show that the experimentally observed MHD oscillations may indicate a flat current profile, which is typical of the initial stage of a discharge. After the $j(r)$ profile relaxes to a steady-state distribution, all the modes become stable and the MHD oscillations vanish. Hence, the observed time evolution of MHD oscillations is in qualitative agreement with the Δ' analysis of MHD stability.

6. CONCLUSIONS

MHD oscillations in the initial stage of an ohmic discharge in the TUMAN-3M tokamak have been investigated. It is found that the amplitude of these oscillations increases with electron density. At the maximum amplitude of the MHD oscillations, the value of β_N saturates at a level of about unity. This value is significantly lower than the maximum value of β_N that was achieved in the TUMAN-3M tokamak in the absence of MHD activity.

MHD oscillations with $m/n = 4/1$ are accompanied by a substantial modulation of the electron density. Between the X- and O-points, the density changes twofold. The gradient of the electron density within an island is found to be ten times larger than that in the unperturbed surrounding plasma. This points to reduced plasma transport within the magnetic island. The results of calculations of the MHD stability agree qualitatively with the observed evolution of the MHD oscillations.

ACKNOWLEDGMENTS

We are grateful to A.N. Chudnovskiĭ for his help in performing Δ' analysis. This work was supported by the Russian Foundation for Basic Research (project nos. 01-02-17922 and 02-02-17597), the "RF Presidential Program for Support of Leading Scientific Schools" (grant no. NSh-2216.2003.2), and the US Civilian Research and Development Foundation for the Independent States of the Former Soviet Union (CRDF) (grant no. RP1-2408-ST-02).

REFERENCES

1. S. V. Mirnov and I. B. Semenov, At. Énerg. **30**, 20 (1971).
2. J. A. Wesson, Nucl. Fusion **18**, 87 (1978).
3. N. Sauthoff, S. von Goeler, and W. Stodiek, Nucl. Fusion **18**, 1445 (1978).
4. P. C. de Vries, A. J. H. Donne, S. H. Heijnen, *et al.*, Nucl. Fusion **37**, 1641 (1997).
5. A. N. Arbuzov and M. P. Gryaznevich, Preprint No. 1431 (Ioffe Physicotechnical Institute, Leningrad, 1990).
6. F. Troyon, R. Gruber, H. Saurenmann, *et al.*, Plasma Phys. Controlled Fusion **26**, 209 (1984).
7. S. V. Lebedev, L. G. Askinazi, V. E. Golant, *et al.*, Plasma Phys. Controlled Fusion **40**, 741 (1998).
8. L. G. Askinazi, M. I. Vild'junas, V. E. Golant, *et al.*, in *Proceedings of the 28th EPS Conference on Fusion and Plasma Physics, Funchal, 2001*; ECA **25A**, 101 (2001).
9. Yu. N. Dnestrovskij, E. S. Lyadina, and P. V. Savrukhin, in *Proceedings of the 20th Conference on Phenomena in Ionized Gases, Piza, 1991*, p. 802.
10. M. Kikuchi, Nucl. Fusion **26**, 101 (1986).
11. A. Weller, A. D. Cheetham, A. W. Edwards, *et al.*, Phys. Rev. Lett. **59**, 2303 (1987).

Translated by V.I. Bugarya

Plasma Physics Reports, Vol. 31, No. 10, 2005, pp. 809–817. From Fizika Plazmy, Vol. 31, No. 10, 2005, pp. 873–882.

MAGNETIC CONFINEMENT SYSTEMS

Plasma and Ion Beam Injection into an FRC*

M. Anderson[1], M. Binderbauer[2], V. Bystritskii[1], E. Garate[1], N. Rostoker[1], Y. Song[1], A. Van Drie[1], and I. Isakov[3]

[1] *Department of Physics and Astronomy, University of California at Irvine, CA, 92697, USA*
[2] *Tri Alpha Energy Inc., Foothill Ranch, CA, 92610, USA*
[3] *Institute of High Voltage Technology, Tomsk, 634050 Russia*

Received November 9, 2004

Abstract—Experiments on the transverse injection of intense (5–20 A/cm^2), wide cross-section (10-cm), neutralized, ~100-eV H^+ plasma and 100-keV H^+ ion beams into a preformed B-field reversed configuration (FRC) are described. The FRC background plasma temperature was ~5 eV with densities of ~10^{13} cm^{-3}. In contrast to earlier experiments, the background plasma was generated by separate plasma gun arrays. For the startup of the FRC, a betatron-type "slow" coaxial source was used. Injection of the plasma beam into the preformed FRC resulted in a 30–40% increase of the FRC lifetime and the amplitude of the reversed magnetic field. As for the ion beam injection experiment into the preformed FRC, there was evidence of beam capture within the configuration. © *2005 Pleiades Publishing, Inc.*

1. INTRODUCTION

The field reversed configuration (FRC) has attracted a variety of research for its potential as an alternative approach for magnetic fusion [1]. Among the various scenarios for the production of an FRC, a "slow coaxial source" promises a long lifetime configuration [2]. The use of the slow coaxial source for the FRC startup has resulted in FRC durations in the 50- to 100-μs range [2]. Numerous studies have shown that the loss of plasma particles from the FRC via anomalous drift of the thermal ions across the magnetic field and plasma cooling via collisions and charge exchange with impurities set the critical limits for attainable temperature and lifetimes of FRCs. A variety of approaches were considered and some of them tested to provide additional energy input into the FRC, such as a rotating magnetic field, neutral beam injection, radio-frequency heating, etc. [3–6]. Theoretical and some experimental studies on plasma ion dynamics in the FRC indicate that only large-orbit (i.e., nonadiabatic) ions are free from anomalous drift, which may be beneficial for the extension of FRC lifetimes [7, 8].

In this paper, we present the first results on the transverse injection of intense H^+ plasma (PB) and low-energy H^+ ion beams (IB) into a preformed FRC, which was generated by a coaxial slow source. In Section 2 of the paper, a short description is given of the experimental setup. Section 3 is dedicated to diagnostics and Section 4 to subsystems. A brief review of previous experiments on PB/IB propagation across the magnetic field in vacuum and magnetized plasma that are pertinent to the study of the beam injection into an FRC is given in Section 5. Section 6 is dedicated to characterizing the FRC formed in background plasma without beam injection. Experiments on FRC formation by PB injection in vacuum and in background plasma are described in Sections 7 and 8. Section 9 describes the results on IB injection into preformed FRC with background plasma. Gross characteristics of the FRC (the lifetime and the amplitude of the reversed magnetic field) with and without PB injection are compared in Section 10. Analysis and discussion of the obtained results are given in Section 11, followed by the Conclusions and Acknowledgments.

2. EXPERIMENTAL SETUP

The general layout of the experiment is shown in Fig. 1a. The setup consists of a 3-m-long main coaxial vacuum vessel with outer and inner diameters of 80 and 22.5 cm, respectively; two external coaxial solenoids (outer solenoid (OS) and inner solenoid (IS)), which provided a controlled magnetic field configuration inside the vessel, inductive acceleration and heating of the plasma, and formation and confinement of the FRC; two circular plasma gun arrays located symmetrically with respect to the middle of the vessel that could be placed at variable distances from each other; a plasma beam (PB) or ion beam (IB) accelerator, delivering neutralized ion flows to the vessel midplane with energies of 100 eV and 100 keV, respectively; pulsed power supplies for the OS/IS, accelerators, plasma gun arrays, puff valves, and various diagnostics; a data acquisition system that included multiple Tektronix oscilloscopes; and a computer controlled triggering system.

* The text was submitted by the authors in English.

1063-780X/05/3110-0809$26.00 © 2005 Pleiades Publishing, Inc.

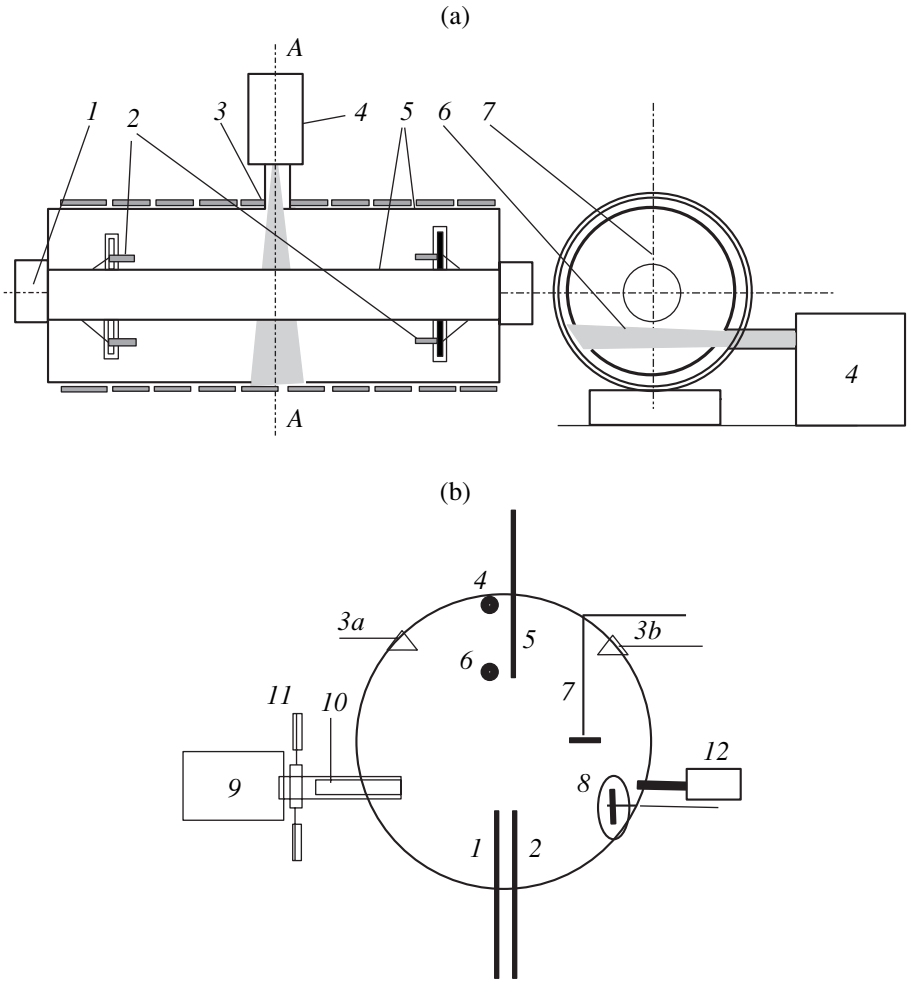

Fig. 1. (a) Schematic of the experimental setup: (*1*) plasma gun arrays power supplies, (*2*) plasma gun arrays, (*3*) transport solenoid, (*4*) plasma/ion accelerator, (*5*) outer and inner coaxial coils, (*6*) plasma/ion beam, (*7*) background plasma column, and (*A*) median plane. (b) Diagnostics and their locations: (*1*) double Langmuir probe, (*2*, *5*) linear vertical CFC arrays, (*3a*, *3b*) microwave source and receiver, (*4*, *6*) two B_z-dot arrays along axis of vessel, (*7*) 90°-turn CFC array, (*8*) circular rotatable "showerhead" CFC array, (*9*) PB/IB accelerator, (*10*) transport solenoid, (*11*) cable guns, and *(12*) H_α detector.

3. DIAGNOSTICS

The measurements of the magnetic field dynamics, ambient plasma, and beam parameters were carried out using a variety of diagnostics (see Fig. 1b). A large area Rogowski coil (encompassing the lower part of the longitudinal cross section of the vessel) measured the net azimuthal plasma current. The spatial distribution of the magnetic field and its temporal dynamics were measured by axial B_z-dot and radial B_z-dot probe arrays. Three arrays of collimated Faraday cups (CFCs) measured the PB/IB current densities. The two vertical linear CFC arrays were located near the middle of the vessel. The lower linear CFC array was positioned to intercept the beams as they entered the vessel, while the upper array was positioned to register a 180° turn of the beams. The "showerhead" CFC array was located 32 cm from the beam entrance port and in line with the beam injection axis. The plasma temperature was measured by double Langmuir probes. A 40-GHz microwave antenna/detector system that cuts off at $(3–4) \times 10^{13}$ cm^{-3} was used to determine the background plasma column density at a radius of 25 cm, which corresponds to the radius of the plasma gun arrays. Photomultiplier tubes (PMTs) with H_α and H_β filters provided data on hydrogen plasma radiation dynamics. The currents in the OS and IS were measured by standard Pearson probes and *B*-dot probes.

4. SUBSYSTEMS (DESIGN AND OPERATION)

Two plasma gun arrays were placed coaxial with respect to the vessel and symmetrically about its middle plane. These sources could be positioned at variable distances ranging from 40 to 65 cm from the mid-plane and provided a ≈25-cm-radius background plasma column which propagated along the applied axial magnetic field. The plasma guns themselves were a coaxial

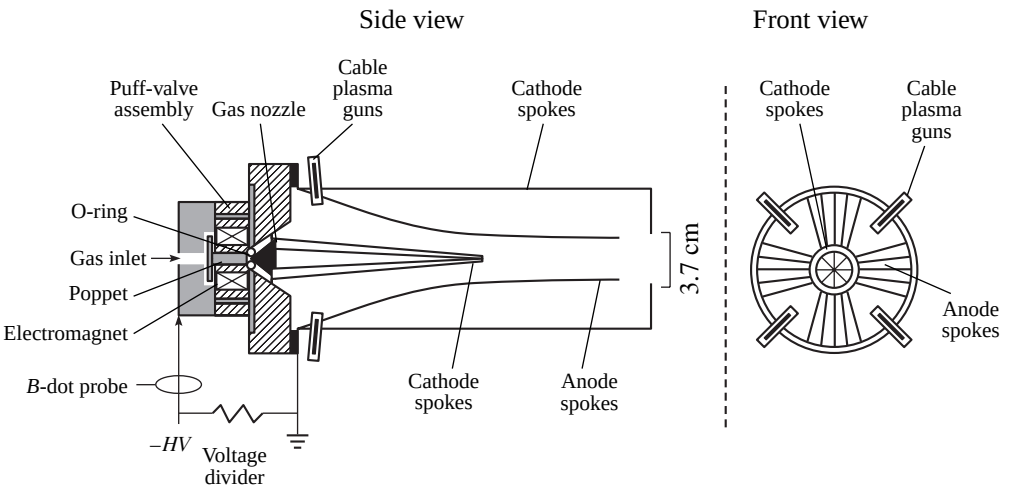

Fig. 2. Plasma accelerator.

$I \times B$ type with TiH electrodes, 16 in each array. The guns were driven in groups of four in parallel with inductive decoupling and a 20-μF capacitor in each group. Each of the capacitors was switched by a commercial ignitron in a circuit containing a second ignitron connected in opposite polarity to prevent ringing of the capacitor. With charging voltages of 7–13 kV, the current amplitude through each group of guns was 80–150 kA with a 25-μs FWHM duration pulse. Both the central and outer titanium electrodes were hydrogenated to a level of 1 : 1 following the procedure outlined in [9].

In several experimental runs, the background plasma was generated by an inductive discharge in H_2 gas driven by an external 40-cm-diameter one-turn loop and was organized in the middle section of the vessel from several of the OS turns connected in parallel. The loop, playing the role of gas preionizer, was energized by a fast capacitor bank (0.32 μF, 25 nH, 15–20 kV, and t_f = 1.0 μs). The hydrogen gas, in this approach, was injected at the midplane of the vessel in a radial direction outward from the surface of the IS.

The OS generated magnetic fields up to 2.0 kG with a rise time of ~230 μs. The IS generated magnetic fields up to 2.5 T with a rise time of ~190 μs. Variable combination of series/parallel connections of the OS turns provided the possibility to experiment with passive magnetic-field end mirrors with ratios of up to 3 : 1. By properly adjusting current amplitudes in the OS and IS, the residual vacuum magnetic field in the vessel during the first 100-μs could be made as low as a few percent of the maximum magnetic field value from the OS alone. This independent OS and IS operation then enabled us to maintain a magnetic field pressure balance during the initial stage of FRC formation.

The PB/IB accelerator was placed in the midplane of the vessel that injected plasma/ion beams transversely to the applied axial magnetic field and tangential to the plasma column (25 cm off the equatorial plane of the vessel).

The design of the plasma accelerator (PA) followed the recommendations of [10] to increase the plasma flow pulse duration. In most of the experiments, we used squirrel-cage-type coaxial conical electrodes, with and without additional radial plasma cable guns placed at the breach of the accelerating channel. A simplified schematic of the PA is given in Fig. 2.

The PA was driven by a 4- to 9-kV pulse 150-μF capacitor bank that was switched by a commercial ignitron. At charging voltages of 9 kV, the PA delivered a current amplitude of 140 kA with a 15-μs rise time. The hydrogen was delivered to the breach of the PA by a fast electromagnetic puff-valve with an opening time of ~80 μs and was driven by a current pulse of 5–7 kA with a plenum pressure in the range of 100–400 kPa. With appropriate time delay between actuation of the puff valve and triggering the capacitor bank, gas breakdown across the interface of the breach of the PA occurred at pd > 10 torr cm (over the minimum of the Paschen pd-curve). This regime corresponded to the snowplow mode of discharge with a fast rising current through the formed plasma and its subsequent acceleration to the end of the cathode by the $I \times B$ force. The slanting of the current channel, due to the Hall effect, resulted in a so-called anode (breach) current crisis, which limited the duration of axial plasma acceleration to a few microseconds. To mitigate this phenomenon and extend the pulse of the accelerated plasma, we added several (up to four) cable plasma guns near the insulator interface, which fired radially inside the acceleration channel of PA. Using this technique we were able to obtain plasma ion pulses with durations of 40–50 μs, though with lower reproducibility and, on average, a lower plasma velocity.

The injection of the PB into the vessel was done in two configurations: without a collimator through a port

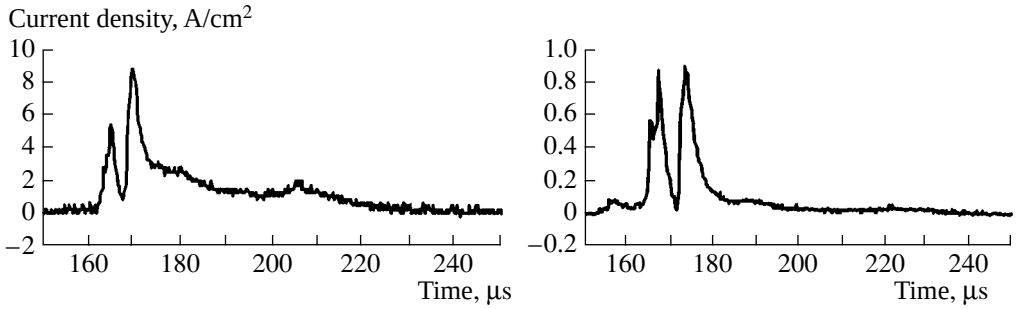

Fig. 3. Typical CFC signal of the PB in vacuum and without a magnetic field: (a) linear CFC array is in position *2* (signal from CFC at $R = 25$ cm; see Fig. 1b) and (b) "showerhead" CFC array is in position *8* (see Fig. 1b).

of 10 cm in diameter and with a collimator 3.8 cm in diameter. In the snowplow regime, when injected into a vacuum without a magnetic field, the typical CFC signals at the mid-plane of the vessel featured two peaks separated by a few to ten microseconds. The first shorter pulse had an amplitude corresponding to 5–10 and 50–70 A/cm^2 for collimated and noncollimated beams, respectively, and average ion energies in the range of 50–100 eV. The second longer pulse of similar amplitude was followed by a trailing tail of lower energy and intensity that corresponded to an average plasma flow energy in the range of 100–20 eV. The PB temperature was estimated to be in the range of 5–10 eV based on the beam's average divergence angle ($\alpha/2 \approx 4°$–$6°$). These values correspond to and reasonably agree with the values deduced from double Langmuir measurements. Typical CFC signals taken at the midplane of the vessel and at the opposite wall along the line of PB injection in vacuum without a magnetic field for the collimated beam are illustrated in Fig. 3.

The ion beam accelerator produced a 2 kA, 60–120 keV, 1-μs duration, ~8-cm-diameter H^+ beam with average half-angle of divergence at the entrance to the vessel of 3° and current density of up to 20–30 A/cm^2. The accelerator consisted of a 120-kV, 1-μs, 1.8-μ Marx generator; a magnetically insulated ballistic focusing diode (MID); a toroidal magnetic lens (TML); and a transport solenoid (TS) for greater efficiency of beam propagation to the entrance port of the vessel. The H^+ plasma source was located at the MID anode and consisted of a fast puff valve, a supersonic Laval nozzle, and a "shock coil" that generated an inductive discharge in the H_2 gas. The distance traveled by the ion beam (IB) to the vessel entrance from the MID was 90 cm. More detailed information on the design and characteristics of the plasma and ion accelerators and the beam parameters can be found in [11, 12].

5. PREVIOUS EXPERIMENTS ON BEAM PROPAGATION (BRIEF OVERLOOK)

In earlier experiments [12], propagation characteristics of an intense PB ($>3 \times 10^{13}$ cm^{-3}) in a background plasma of similar density without a transverse magnetic field were found to be very similar, if not worse, when transporting in vacuum. The latter could be accounted for by beam–plasma instabilities, ion–ion collisions, and charge exchange from neutral ion collisions in the background plasma [12]. In the case of injection across a uniform magnetic field in vacuum, the PB propagated without deflection and suffered a pronounced loss of peripheral layers (see Fig. 4). From the CFCs' signal patterns and time of flight data, in this scenario, only the central core of the PB survived, with considerable "beam braking" and respective bunching resulting in a significant increase core current density (one order and more). This phenomenon could be explained by the diamagnetic mode of propagation of a dense PB with virtual anode formation [13]. When injected across the magnetic field in a magnetized background plasma, the PB still did not deflect as a whole, but displayed significantly less bunching (see Fig. 5). The absence of pronounced slowing of the PB, in this scenario, could indicate the absence of virtual anode formation.

Similar to the behavior of the PB in previous experiments [11], the IB ($(1–3) \times 10^{11}$ cm^{-3}), when propagating in vacuum and transverse magnetic field, did not deflect as a whole. However, differently from the PB, the IB displayed substantial attenuation across its entire cross section without any noticeable bunching or braking of the beam. Such behavior agrees with an $\mathbf{E} \times \mathbf{B}$ collective mode of propagation with a substantial increase in beam divergence and subsequent beam losses.

When propagating in magnetized plasma of 10^{13}-cm^{-3} density, the IB was deflected as a whole following a one-particle Larmor trajectory corresponding to the average ion energy of the IB. Figures 6a and 6b show IB "center of mass" deflection as a function of increasing magnetic field for the 60- and 120-keV IBs, respectively. These graphs signify that there was an efficient shorting of the polarization electric field by the much denser background plasma.

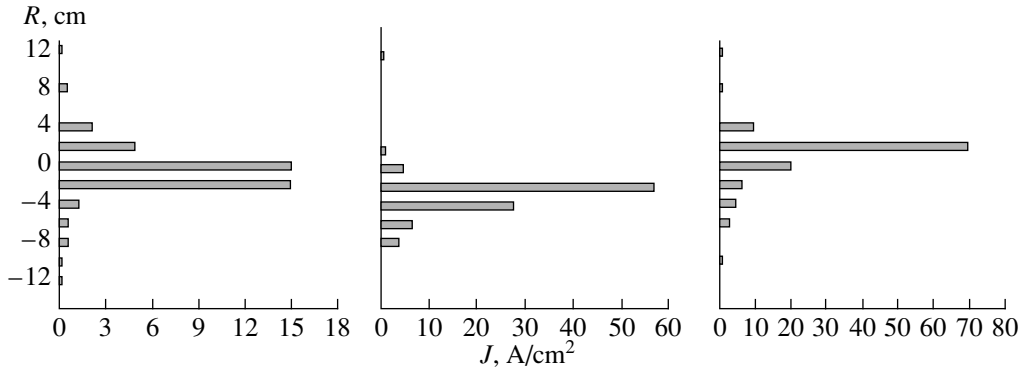

Fig. 4. Typical current density distributions across the collimated PB in vacuum at the vessel midplane for magnetic fields of 0.3 kG (left), 0.8 kG (middle), and 1.2 kG (right). *R* is the (vertical) radial distance of the CFCs from the PB injection axis (linear CFC array is in position *2*; see Fig. 1b).

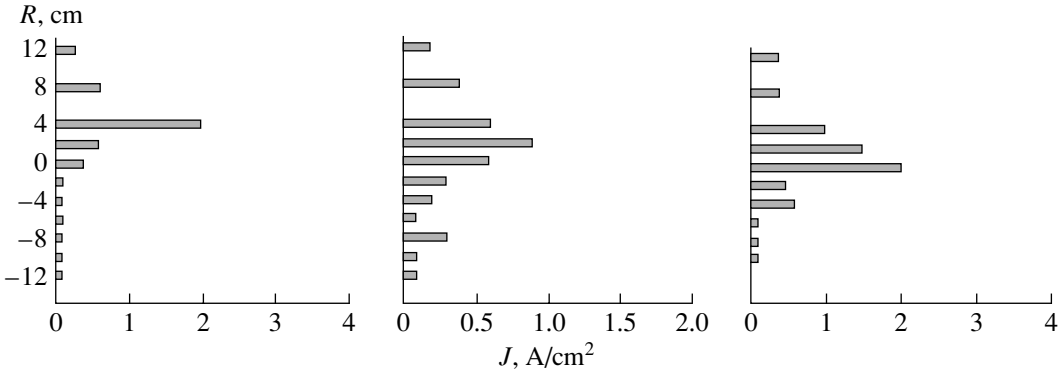

Fig. 5. Typical current density distributions across the collimated PB in a background plasma at the vessel midplane for magnetic fields of 0.3 kG (left), 0.8 kG (middle), and 1.2 kG (right). *R* is the (vertical) radial distance of the CFCs from the PB injection axis (linear CFC array is in position *2*; see Fig. 1b).

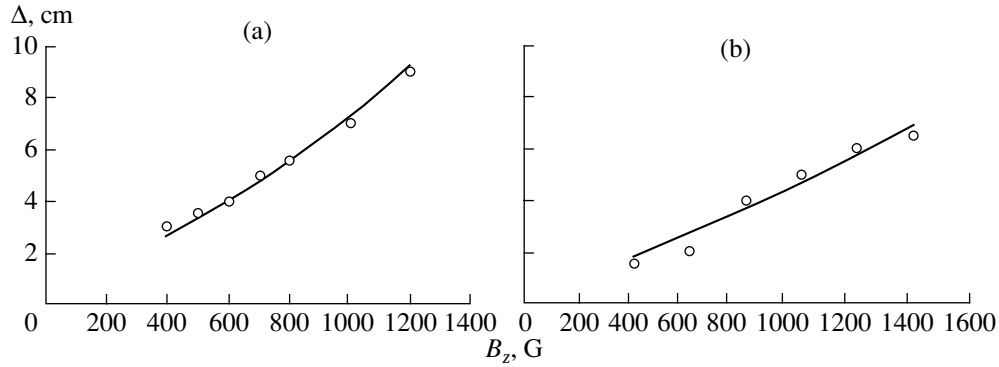

Fig. 6. Radial shift of the current density "center of mass" with respect to the axis of the IB injection as a function of the transverse magnetic field. The circles show the experimental data, and the lines show calculated results for (a) 60- and (b) 120-keV IB, respectively.

6. FRC FORMATION WITHOUT BEAM INJECTION

In most experimental runs, the FRC was formed by firing the background plasma gun arrays 5–20 μs prior to the energizing of both the OS and IS to provide enough time for plasma to build up in the middle part of the vessel. When working with the gas-puff and fast preionizer, the latter was fired with a time delay of 50–80 ms with respect to the puff-valve and a few to 10 μs

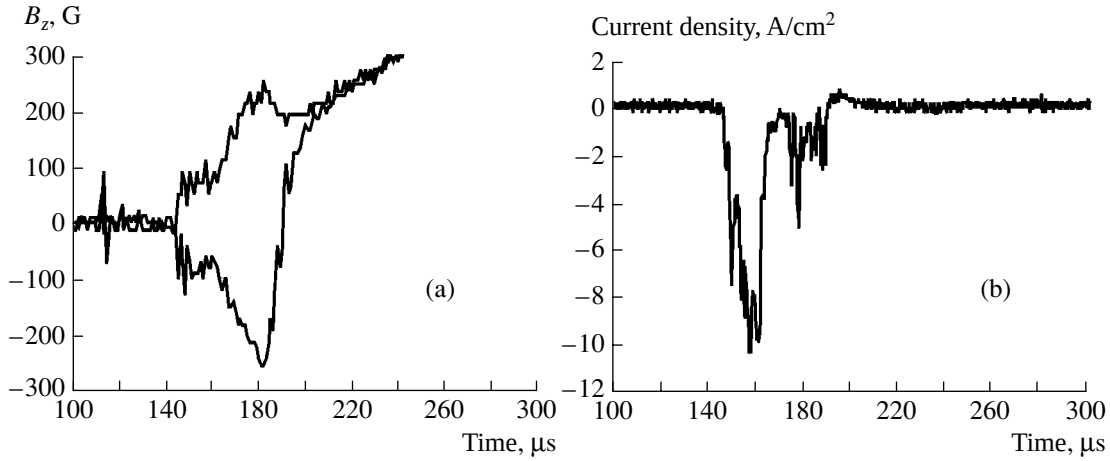

Fig. 7. (a) Typical B_z-dot signals during FRC formation with background plasma only: $Z = 0$, $Z = 0$, $R_{outer} = 40$ cm, and $R_{inner} = 13$ cm; the upper and lower curve correspond to B_z-dot probe arrays in positions *4* and *6* (see Fig. 1b), respectively. (b) Typical CFC signal during FRC formation with background plasma only: –40-V bias and 25-cm radius; linear CFC array is in position *5* (see Fig. 1b).

prior to the OS and IS. The formation of the FRC in this typical scenario occurred when a sufficient inductively driven current in the plasma column was obtained (with $E_{ind} \sim 1$–3 V/cm) due to the rising magnetic flux of the IS. A subsequent decoupling of the OS and IS magnetic fields transpired with magnetic field reversal inside the plasma donut and reconnection of the magnetic field at both ends, closing the configuration. In typical pulses with $V_{OS} \approx 3$–5 kV and $V_{IS} \approx 8$–10 kV, the FRC formed between 5–20 ms after energizing the OS and IS. The FRC reached maximum field reversal in 30–60 μs and lasted up to 100–150 μs, as long as the inductive azimuthal EMF could support the required amplitude of the azimuthal current in the plasma column.

Typical signals from two B_z-dot probes placed at radii 39 and 12 cm in the median cross section of the vessel are shown in Fig. 7a, and respective signals from the linear array of CFCs placed in the same cross section in its upper half are shown in Fig. 7b. The B_z behavior features decoupling of the OS and IS magnetic fields in the early portion of the OS–IS current fronts and a slow decay of the FRC with a lifetime of ~100 μs. Experiments showed that the character of the FRC decay at the end (abrupt or slow) is very sensitive to the tuning the residual B_{res} in the coaxial annulus of the vessel when firing OS and IS without background plasma. Thus, as long as B_{res} is ~0 (zero-field), the magnetic field pressure from the OS and IS on both sides of the FRC remained balanced and enabled the FRC to remain stable with respect to radial motion. Furthermore, by driving the OS or IS too hard or too little (mismatching the magnetic field pressures), we were able to clearly see, from radial B_z probe array data, the FRC move radially inward or outward and collide with the vacuum vessel walls.

As a rule, the CFCs (without or with bias voltages up to –90 V) featured mainly negative signals, corresponding to the fast electrons with current densities ranging in the tens of A/cm^2, which depended on the variable time delay between OS/IS and plasma gun arrays firings. The biggest electron signals were detected at the average radius of the plasma column (≈25 cm). The timing and duration of these negative pulses corresponded in time to the startup and lifetime of the FRC. Typical microwave cutoff and H_α signals and total induced azimuthal current in the plasma are given in Fig. 8.

The FRC decay time clearly corresponded to the decay of the plasma current, duration of the H_α-radiation, and microwave cutoff. The density and temperature of the FRC in the typical range of the parameters ($V_{OS} \approx 3$–5 kV, $V_{IS} \approx 8$–10 kV, and $t_{delay} \sim 20$–30 μs) corresponded to $3 \times 10^{14} > n_e \gg 3 \times 10^{13}$ cm^{-3} and 5–10 eV, respectively.

7. FRC FORMATION WITH PB INJECTION IN VACUUM

In the scenario of FRC formation with only the noncollimated PB, without background plasma prefilling, the beam was injected into the vessel a few to 10 microseconds after or simultaneously with energizing OS and IS. The reverse of the magnetic field occurred during the first few microseconds after energizing OS/IS. The linear array of the negatively biased CFCs, placed in the upper half of the vessel median cross section, usually featured bipolar signals corresponding to current amplitudes in the range of 2–5 A/cm^2 arriving 20–30 μs after firing the plasma accelerator. By the time between successive positive peaks on the upper linear CFC array, the ion captured flow energies were in the range

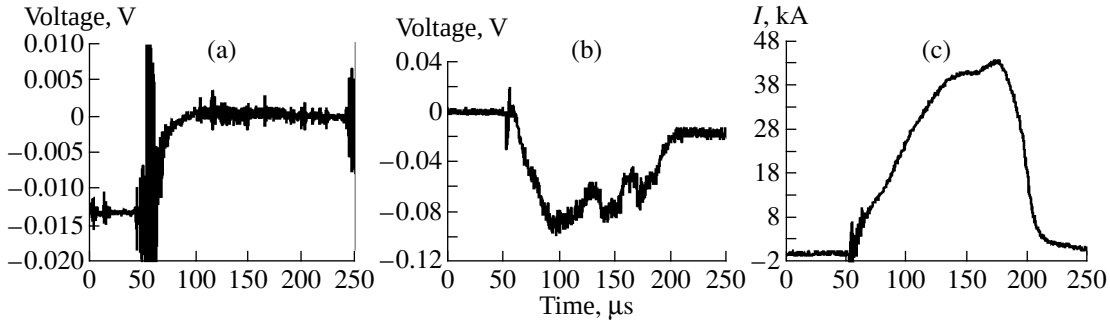

Fig. 8. (a) Typical microwave cutoff signal (detector and receiver are in positions *3a* and *3b*, respectively; see Fig. 1b), (b) typical H_α signal (detector is in position *12*; see Fig. 1b), and (c) total azimuthal current in the FRC plasma measured by a Rogowski coil.

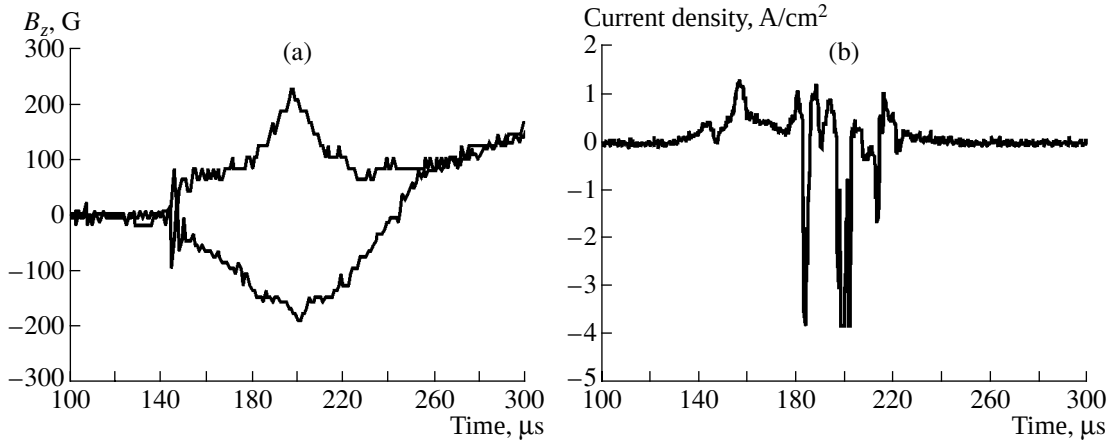

Fig. 9. (a) Typical B_z-dot signals during FRC formation with PB only: $Z = 0$, $R_{outer} = 40$ cm, and $R_{inner} = 13$ cm; the upper and lower curve correspond to B_z-dot probe arrays in positions *4* and *6* (see Fig. 1b), respectively. (b) Typical CFC signal during FRC formation with PB only: –40-V bias and 25-cm radius; linear CFC array is in position *5* (see Fig. 1b).

of 15–30 eV. The negative part of the signal represents fast electron flows with energies higher than the applied bias voltage (E_e > 50–90 eV). It is worth noting the character of the signals registered by the CFC array placed in the line of the PB injection at the opposite vessel wall. The ion signals again featured evident bunching and short ion spikes with amplitudes of up to 10 A/cm^2, which differs from the case of FRC formation without PB injection (<1 A/cm^2). The respective characteristic waveforms of the FRC B_z field and CFC signal are presented in Fig. 9.

8. FRC FORMATION WITH PB INJECTION INTO PREFILLED BACKGROUND PLASMA

In this scenario, the PB was injected 10–30 μs after the background plasma injection into the preformed FRC (usually when the amplitude of the reverse field was ~200 G). Typical signals from the B_z-dot probes and CFC arrays are illustrated at Fig. 10. Similar to the case of the FRC formation with PB only, the CFC placed at the opposite wall along the line of the beam injection featured a structured ion signal preceded by an electron (negative) pulse with amplitudes of a few A/cm^2. By time of flight measurements, these CFC signals can be attributed to the straight propagation of the PB through the FRC. It is worth noting, however, that, when injecting the PB near the end of the FRC lifetime with an "overdriven" OS, the CFCs near the opposite wall along the line of sight of PB injection registered ion current densities >30 A/cm^2, similar to the data in earlier experiments on PB propagation in vacuum and transverse magnetic field. This result suggests that the PB again experienced significant bunching. An explanation of this may be that the plasma column was driven onto the interior vessel wall (surrounding the IS) during PB injection, allowing part of the PB to propagate through the now relatively low density background plasma and strong magnetic field. The signals from the linear array of the CFCs placed in the upper half of the midplane also featured distinct and multiple bipolar signals with large positive amplitudes (up to 10 A/cm^2) as compared to no positive signals when FRC is formed

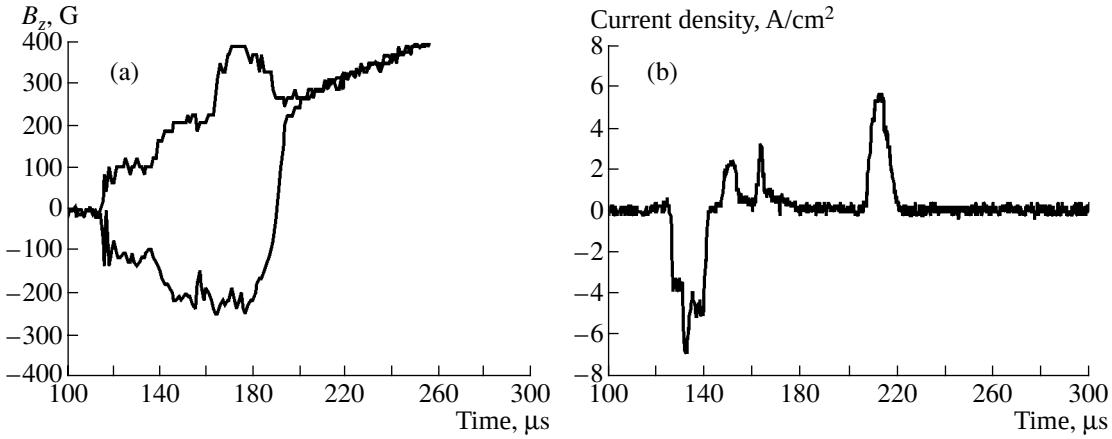

Fig. 10. (a) Typical B_z-dot signal during PB injection into preformed FRC: $Z = 0$, $R_{outer} = 40$ cm, and $R_{inner} = 13$ cm; the upper and lower curve correspond to B_z-dot probe arrays in positions *4* and *6* (see Fig. 1b), respectively. (b) Typical CFC signal during PB injection into a preformed FRC: –40-V bias and 25-cm radius; linear CFC array is in position *5* (see Fig. 1b).

with background plasma only. The appearances of these signals were 20–40 μs after FRC formation and plasma accelerator firing and correspond to ion energies of 10–20 eV.

9. IB INJECTION IN THE FRC

Before going into details, it is worth keeping in mind that the current amplitude and particle density of the injected IB (~2 kA, ~10^{11} cm^{-3}) were at least 10 and 10^2 times lower than the current and particle density values of the FRC plasma (20–30 kA, >10^{13} cm^{-3}). These factors presented a problem in efforts to measure directly the captured IB in the FRC. However, we were able to compare the characteristics of the CFC signals pertinent to the IB injection into preformed FRC by using our earlier data on IB propagation in magnetized plasma of density >10^{13} cm^{-3} at similar magnetic field values. In the previous experiments, at $B \sim 0.6$ kG, the CFC arrays placed at several positions along the propagation path of the IB in magnetized plasma measured current densities in the range of a few A/cm^2 that corresponded to the Larmor trajectory for IB energies in the range of 60–90 keV.

In case of IB injection into the preformed FRC plasma column with similar magnetic field amplitudes, the measured IB current densities at the respective probes were an order less in magnitude on both the CFC array placed along the line of injection at the opposite wall and at the 90°-turn CFC array (see Fig. 1b). These results could be interpreted as a partial trapping of the ion beam in the FRC.

10. IMPACT OF PB INJECTION ON FRC CHARACTERISTICS

The table illustrates the main changes of the FRC characteristics with PB injection compared to the case without PB injection. The resulting amplitude of the magnetic field in the FRC and its duration are given for several time delays Δt between the plasma accelerator firing and the background plasma gun array firing. The data in the table correspond to a regime in which the OS and IS were driven in such a way as to provide magnetic field pressure balance inside and outside the FRC, which generally resulted in the best FRC characteristics. As seen in the table, when the PB was injected (in the same conditions as when the PB was not injected) a longer duration FRC with a higher reverse magnetic field amplitude occurred. The maximum increase in the amplitude of the reversed magnetic field, due to plasma beam injection, was 50% with a >10% increase in the FRC duration.

11. ANALYSIS AND DISCUSSION

The lifetime of the FRC formed by the intense PB alone, injected tangentially across the magnetic field, is the shortest compared to the life time of the preformed FRC supported by the injection of PB or the FRC formed by the background plasma only without PB injection. At the same time, the magnetic field amplitude of the FRC is greatest when both PB and background plasma are involved. This indicates that particle losses from the configuration are the primary limiting cause for our FRC lifetimes accompanied by fast plasma cooling and a subsequent fast decrease of the induced plasma current in the FRC.

The added PB, with greater average translational velocity of the ions compared with the background plasma, serves as an additional reservoir of energy and particles, which results in the extension of the FRC lifetime and longer lifetimes.

At this stage of experiments, there are not enough data to describe in more detail the character and mech-

FRC characteristics for different time delays between background plasma generation and plasma beam injection

Conditions	Background plasma gun arrays (PGAs) only	PGAs & PA, $\Delta t = 90$ μs	PGAs & PA, $\Delta t = 110$ μs	PGAs & PA, $\Delta t = 130$ μs
Average FRC duration, μs	130	148	145	150
Average B_z field, G	200	300	288	260
Average reversed B_z field, G	120	188	150	138

anism of the high energy IB capture in the FRC and IB impact on lifetimes.

Another likely cause of the FRC lifetime limitation in our experimental conditions may be impurities in the background plasma generated by the TiH guns. Spectroscopic studies of this type of guns showed a substantial presence of C^+ and O^+ ions, which represent a large "heat sink" via charge exchange, resulting in the fast cooling of the expanding plasma and a respective loss in plasma conductivity [14].

In accounting for these limitations in the next stage of experiments, we plan to transition to a background plasma source based on electrodeless inductive discharge in H_2 gas (plasma thruster type), similar to what we used in the ion active plasma source in the IB accelerator. Another potential modification would include adding a stronger end-mirror configuration of the magnetic field to aid in decreasing end losses.

12. CONCLUSIONS

Injection of an intense plasma beam with density on the same order as the density of the preformed FRC ($>10^{13}$ cm^{-3}) resulted in an increase in the amplitude of the reversed magnetic field and the extension of FRC lifetimes. This may be due to replenishing of the FRC particle inventory by the captured fast ions of the PB and additional heating of the background plasma, resulting in an increase in plasma conductivity. Modified plasma sources with smaller percentages of impurities are being designed.

The measurements of the injection and propagation of the IB in an FRC can be interpreted as partial beam capture in the FRC. More detailed studies of particle losses and other causes of FRC lifetime limitations are currently under way, including additional diagnostics, such as microwave interferometry and time-resolved imaging.

ACKNOWLEDGMENTS

The authors would like to acknowledge fruitful discussions with, and computational help from, Drs. S. Dettrick and A. Qerushi. The authors also gratefully acknowledge the technical support of S. Armstrong, M. Morehouse, K. Walters, and G. Strashnoy in preparation and maintenance during all experimental runs. This work was carried out at the University of California at Irvine under contract and in cooperation with Tri Alpha Energy, Inc.

REFERENCES

1. M. Tuszewski, Nucl. Fusion **28**, 2033 (1988).
2. Z. A. Pietrzyk, G. Vlases, R. D. R. Brooks, *et al.*, Nucl. Fusion **27**, 1478 (1987).
3. S. Okada, T. Asai, K. Yamanaka, *et al.*, Nucl. Fusion **41**, 625 (2001).
4. H. Y. Guo, A. L. Hoffman, R. D. Brooks, *et al.*, Phys. Plasmas **9**, 185 (2002).
5. S. Okada, K. Yamanaka, S. Yamamoto, *et al.*, Nucl. Fusion **43**, 1140 (2003).
6. J. T. Slough and K. E. Miller, Phys. Rev. Lett. **85**, 1444 (2000).
7. N. Rostoker, A. Qerushi, and M. Binderbauer, J. Fusion Energy **22**, 83 (2003).
8. W. Heidbrink and G. J. Sadler, Nucl. Fusion **34**, 535 (1994).
9. V. Bystritsky, V. Stolupin, and S. Shamsutdinov, Preprint No. LNP-124 (Joint Institute of Nuclear Research, Dubna, 1979).
10. A. I. Morozov and A. K. Vinogradova, in *Physics and Application of Plasma Accelerators*, Ed. by A. I. Morozov (Nauka i Tekhnika, Minsk, 1974) [in Russian].
11. M. Anderson, V. Bystritskii, E. Garate, *et al.*, J. Appl. Phys. **96**, 1249 (2004).
12. M. Anderson, V. Bystritskii, E. Garate, *et al.*, Laser Part. Beams **23**, 117 (2005).
13. F. Wessel, N. Rostoker, A. Fisher, *et al.*, Phys. Fluids **2**, 1467 (1990).
14. C. Barnett, J. Ray, E. Ricci, *et al.*, At. Data Controlled Fusion Res. **1**, A.4.2 (1977).

Plasma Physics Reports, Vol. 31, No. 10, 2005, pp. 818–823. Translated from Fizika Plazmy, Vol. 31, No. 10, 2005, pp. 883–888.

PLASMA OSCILLATIONS AND WAVES

Slow Plasma Waves in a Fine-Stratified Periodic Semiconductor Structure

A. A. Bulgakov and O. V. Shramkova

Usikov Institute of Radiophysics and Electronics, National Academy of Sciences of Ukraine, ul. Akademika Proskury 12, Kharkov, 61085 Ukraine

Received September 6, 2004

Abstract—A study is made of the propagation of electromagnetic waves in an infinite fine-stratified periodic structure composed of alternating layers of two different semiconductors. Such a periodic structure, which can be treated as a uniform uniaxial semiconductor with two different values of the dielectric constant, has four characteristic frequencies: two plasma frequencies of the layers and two hybrid frequencies, which are determined by the parameters of the layers. These frequencies govern the dispersion properties of the eigenwaves of the semiconductor structure. The effect of the dissipative processes on the wave dispersion is considered, and the dependence of the minimum phase velocity on the thickness of the layers and on the collision frequency between charge carriers within them is determined. © *2005 Pleiades Publishing, Inc.*

1. INTRODUCTION

Interest in the electrodynamic properties of artificially produced solid-state structures is growing simultaneously with technological advances in this field. The search for and development of new materials that have properties not possessed by natural crystals are among the most important tasks in solid-state electronics. This can be done on the basis of the experience gained in studying the physical properties of crystals, in particular, by using results that show how the electrodynamic properties of solid-state structures depend on their translational symmetry. The symmetry of complex semiconductor materials largely governs the properties of the electron–hole plasma at frequencies on the order of 10^{12} Hz or higher, i.e., in the millimeter to optical wavelength range [1]. Such investigations opened new scientific directions, among which are photonics [2] and research on bianisotropic and chiral media [3, 4], as well as on Veselago media [5]. At present, however, there are practically no solid-state devices capable of generating and amplifying electromagnetic radiation at millimeter and submillimeter wavelengths [6]. In addition, there remain problems associated with the processing of electromagnetic signals in these wavelength ranges. A possible way to solve these problems is to create stratified periodic semiconductor structures. For the above wavelength ranges, the thicknesses of the layers can be greater than or on the order of 1–2 μm, i.e., they can exceed the Debye radius.

The objective of this paper is to study eigenwaves of a fine-stratified structure composed of alternating layers of two semiconductors with different plasma frequencies and with different densities of charge carriers of different masses. Note that the types of conduction in the two semiconductors may be different. The layers are assumed to be arranged in a periodic fashion, the period being about 1000 times less than the wavelength of the electromagnetic waves. Such a stratified structure can be treated as a continuous uniaxial medium with two different values of the dielectric constant [7, 8]. The plasma properties of the structure are governed by the parameters of both of the semiconductor materials. This paper is aimed at investigating the dispersion parameters of the plasma waves in such a semiconductor material. In order to find out whether the fine-stratified semiconductor media under consideration may be used in active devices in which instability arises as a result of the Cherenkov interaction of waves with drifting charge carriers, the phase velocities of the natural waves and their minimum values are studied as functions of the parameters of the semiconductor structure.

2. FORMULATION OF THE PROBLEM AND BASIC EQUATIONS

We consider an infinite periodic structure composed of alternating layers of two semiconductors having different dielectric constants and different thicknesses, d_1 and d_2 (Fig. 1), and introduce a coordinate system such that the x axis is parallel to the boundaries of the layers and the z axis is perpendicular to the layers, i.e., points in the direction in which the structure is periodic.

The electromagnetic processes in this structure are described by Maxwell's equations and also by the con-

1063-780X/05/3110-0818$26.00

tinuity equations and the equations of motion of charge carriers:

$$\frac{\partial n_{1,2}}{\partial t} + \nabla \cdot (n_{01,02}\mathbf{v}_{1,2}) = 0,$$
$$\frac{\partial \mathbf{v}_{1,2}}{\partial t} + \nu_{1,2}\mathbf{v}_{1,2} = -\frac{e}{m_{1,2}}\mathbf{E}_{1,2}, \quad (1)$$

where n_{01} and n_{02} are the equilibrium densities of the charge carriers in the layers, ν_1 and ν_2 are the frequencies of collisions between charge carriers in the layers, $\mathbf{v}_1$ and $\mathbf{v}_2$ are the velocities of charge carriers, and $m_{1,2}$ are their effective masses. We represent the variables in Eqs. (1) in the form $\exp(ik_x x + ik_{z1,2}z - i\omega t)$, where $k_{z1,2} = \sqrt{\frac{\omega^2}{c^2}\varepsilon_{1,2} - k_x^2}$, $\varepsilon_1 = \varepsilon_{01} - \frac{\omega_{L1}^2}{\omega(\omega + i\nu_1)}$, $\varepsilon_2 = \varepsilon_{02} - \frac{\omega_{L2}^2}{\omega(\omega + i\nu_2)}$, and $\omega_{L1,2}$ are the plasma frequencies. Since the structure is uniform in the y direction, we can set $\partial/\partial y = 0$; in this case, Maxwell's equations split into two sets of equations for two types of waves with different polarizations. In what follows, we will consider the waves polarized in such a way that the only nonzero components of their fields are the E_x, E_z, and H_y components. The boundary conditions imply that the tangential electric field component and the normal component of the magnetic induction are continuous at the boundaries between the layers.

Using the method of the transmission matrix (which relates the fields at the beginning of a wave period and at its end) and applying the Floquet theorem, which takes into account the periodicity of the structure, we obtain the following well-known dispersion relation [9]:

$$\cos\bar{k}d = \cos k_{z1}d_1\cos k_{z2}d_2 - \frac{1}{2}\left[\frac{k_{z1}\varepsilon_2}{k_{z2}\varepsilon_1} + \frac{k_{z2}\varepsilon_1}{k_{z1}\varepsilon_2}\right]\sin k_{z1}d_1\sin k_{z2}d_2, \quad (2)$$

where $d = d_1 + d_2$ and the averaged wavenumber $\bar{k}$ describes the periodicity of the structure.

We investigate dispersion relation (2) for a fine-stratified medium, i.e., we assume that $k_{z1,2}d_{1,2} \ll 1$. In this case, the Bloch wavenumber $\bar{k} = k_z$ is the transverse wavenumber of a uniaxial medium [7, 8] and the dispersion relation for a fine-stratified semiconductor structure has the form

$$\frac{k_x^2}{\varepsilon_{zz}} + \frac{k_z^2}{\varepsilon_{xx}} = \frac{\omega^2}{c^2}, \quad (3)$$

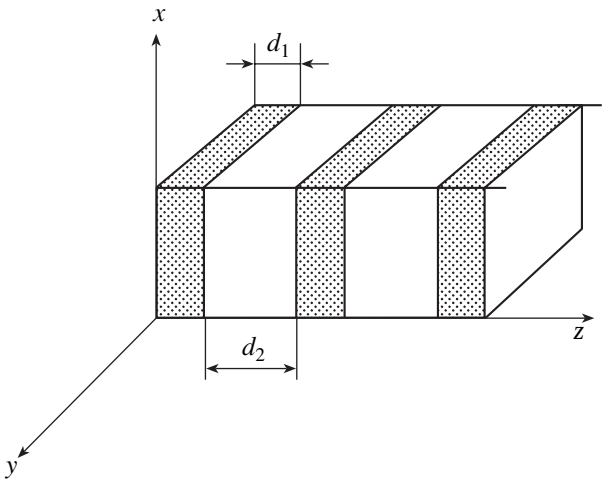

Fig. 1. Geometry of the problem.

where $\varepsilon_{xx} = \frac{\varepsilon_1 d_1 + \varepsilon_2 d_2}{d}$ and $\varepsilon_{zz} = d\left(\frac{d_1}{\varepsilon_1} + \frac{d_2}{\varepsilon_2}\right)^{-1}$.

Since Eq. (3) relates the three quantities ω, k_z, and k_x, it is convenient to regard it as describing either the contours of constant frequency in the plane (k_z, k_x) or the dependence $\omega(k_x)$ at $k_z = \text{const}$.

According to dispersion relation (3), a contour of constant frequency in the (k_z, k_x) plane is a second-order curve. The contours of constant frequency that are shown in Fig. 2 were calculated for $\nu_1 = \nu_2 = 0$. For $\varepsilon_{xx,zz} > 0$, the contour is an ellipse, as in the case of a uniaxial dielectric crystal [2]. This situation corresponds to a frequency ω above the plasma frequencies of both dielectrics (Fig. 1a). For $\varepsilon_{xx} < 0$ and $\varepsilon_{zz} > 0$, the contour is a hyperbola with foci lying on the k_x axis: $k_{xF} = \pm\frac{\omega}{c}\sqrt{\varepsilon_{zz} - \varepsilon_{xx}}$, $k_{zF} = 0$ (Fig. 2b). For $\varepsilon_{zz} < 0$ and $\varepsilon_{xx} > 0$, the foci of the hyperbola are on the k_z axis: $k_{xF} = 0$, $k_{zF} = \pm\frac{\omega}{c}\sqrt{\varepsilon_{xx} - \varepsilon_{zz}}$ (Fig. 2c). Note that these contours make it possible to infer the signs of the dielectric constants.

Let us ignore collisions and analyze dispersion relation (3) in a quasistatic approximation ($c \longrightarrow \infty$). In this case, the dispersion relation takes the form

$$\frac{k_x^2}{k_z^2} = -\frac{\varepsilon_1\varepsilon_2 d^2}{(\varepsilon_1 d_1 + \varepsilon_2 d_2)(\varepsilon_1 d_2 + \varepsilon_2 d_1)}. \quad (4)$$

We denote the right-hand side of the dispersion relation by F_ω and rewrite it as

$$F_\omega = -\frac{\varepsilon_{01}\varepsilon_{02}(\omega^2 - \omega_{p1}^2)(\omega^2 - \omega_{p2}^2)d^2}{(\varepsilon_{01}(\omega^2 - \omega_{p1}^2)d_1 + \varepsilon_{02}(\omega^2 - \omega_{p2}^2)d_2)(\varepsilon_{01}(\omega^2 - \omega_{p1}^2)d_2 + \varepsilon_{02}(\omega^2 - \omega_{p2}^2)d_1)}. \quad (5)$$

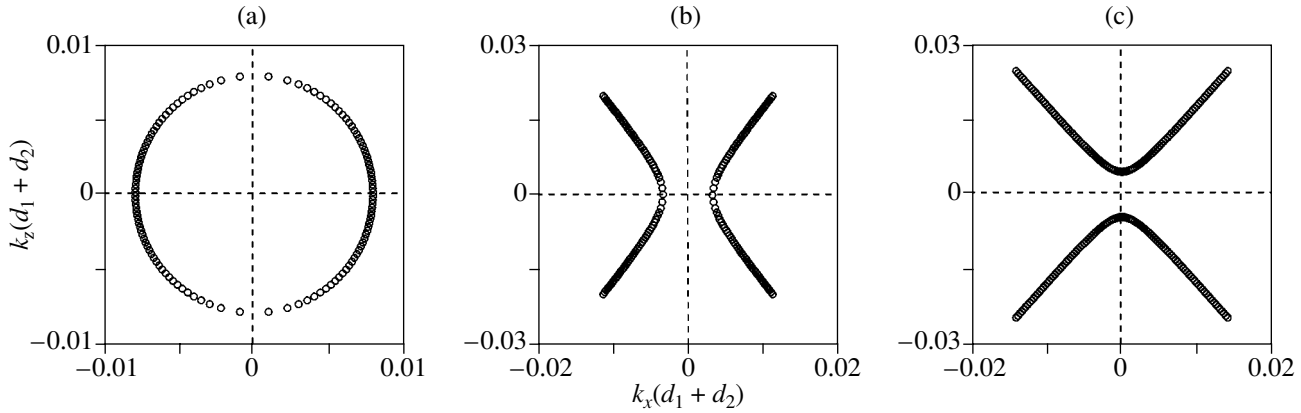

Fig. 2. Dependence of the transverse wavenumber on the longitudinal one for ω = (a) 1.25×10^{12}, (b) 0.92×10^{12}, and (c) 0.6×10^{12} s^{-1}.

The left-hand side of dispersion relation (4) is independent of the frequency and is positive for all values of the longitudinal wavenumber. The right-hand side of dispersion relation (4) is independent of wavenumbers; it should be positive in order for the dispersion relation to have a solution. To solve the dispersion relation, we plot the function $F_\omega(\omega)$ (Fig. 3). This function vanishes at the plasma frequencies ω_{p1} ($\varepsilon_1 = 0$) and ω_{p2} ($\varepsilon_2 = 0$) and has nonremovable discontinuities at the hybrid plasma frequencies

$$\omega_{g1} = \sqrt{\frac{\omega_{01}^2 d_1 + \omega_{02}^2 d_2}{\varepsilon_{01} d_1 + \varepsilon_{02} d_2}} \quad (\varepsilon_{xx} = 0),$$

$$\omega_{g2} = \sqrt{\frac{\omega_{01}^2 d_2 + \omega_{02}^2 d_1}{\varepsilon_{01} d_2 + \varepsilon_{02} d_1}} \quad (\varepsilon_{zz} \longrightarrow \infty).$$

The solution to dispersion relation (4) falls into the frequency range in which the function F_ω is positive. This can be the case only under the following two conditions: the dielectric constant of one of the layers is negative and the denominator in expression (5) is positive. In Fig. 3, the ranges of existence of a solution to the dispersion relation are hatched. Hence, dispersion relation (4) has a solution for $F_\omega > 0$: there exist two oscillation branches corresponding to plasma polari-

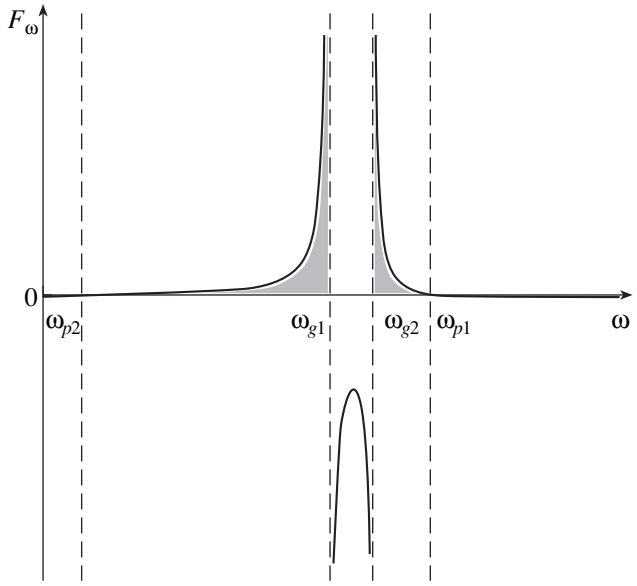

Fig. 3. Frequency dependence of the function F_ω, which describes the time dispersion in a medium.

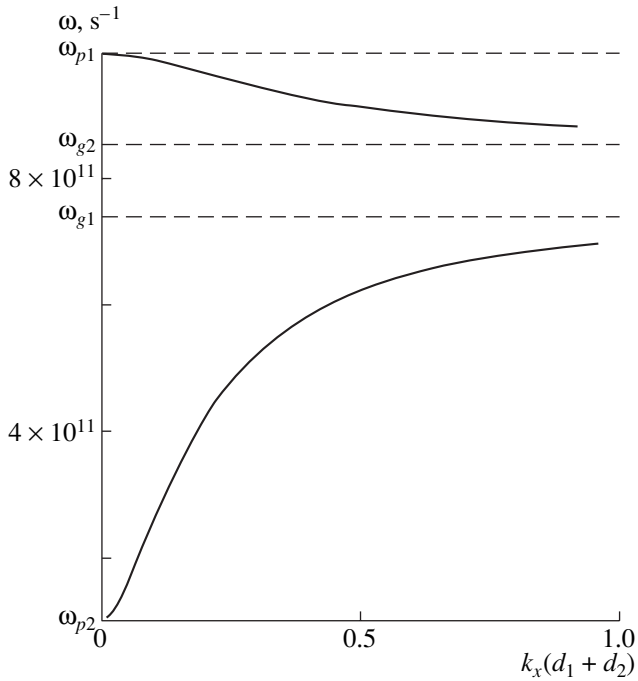

Fig. 4. Dispersion curves of the plasma waves.

tons—one in the frequency range $\omega_{p2} < \omega < \omega_{g1}$ and the other in the frequency range $\omega_{g2} < \omega < \omega_{p1}$.

The results of solving dispersion relation (3) numerically for $\nu_1 = \nu_2 = 0$ are illustrated in Fig. 4. The simulations were carried out for a semiconductor superlattice consisting of alternating layers with the following parameters: layers 1 with $\varepsilon_{01} = 17.8$, $\omega_{p1} = 10^{12}$ s^{-1}, and $d_1 = 2 \times 10^{-4}$ cm and layers 2 with $\varepsilon_{02} = 10$, $\omega_{p2} = 10^{11}$ s^{-1}, and $d_2 = 3 \times 10^{-4}$ cm, the transverse wavenumber being $k_z = 500$ cm^{-1}. Figure 4 shows two branches of plasma polaritons. The first branch emerges from the point with the coordinates $k_x = 0$ and $\omega = \omega_{p2}$ and asymptotically approaches the hybrid plasma frequency $\omega = \omega_{g1}$ as $k_x \longrightarrow \infty$; the group velocity of the wave is positive. The second branch emerges from the point with the coordinates $k_x = 0$ and $\omega = \omega_{p1}$ and asymptotically approaches the hybrid plasma frequency $\omega = \omega_{g2}$ as $k_x \longrightarrow \infty$; the group velocity of the wave is negative. Note that, for $d_1 = d_2$, the hybrid frequencies of the two waves coincide and the dispersion curves approach the same horizontal asymptote. Hence, for $d_1 \neq d_2$, there is a frequency range in which the eigenwaves of the semiconductor structure cannot exist.

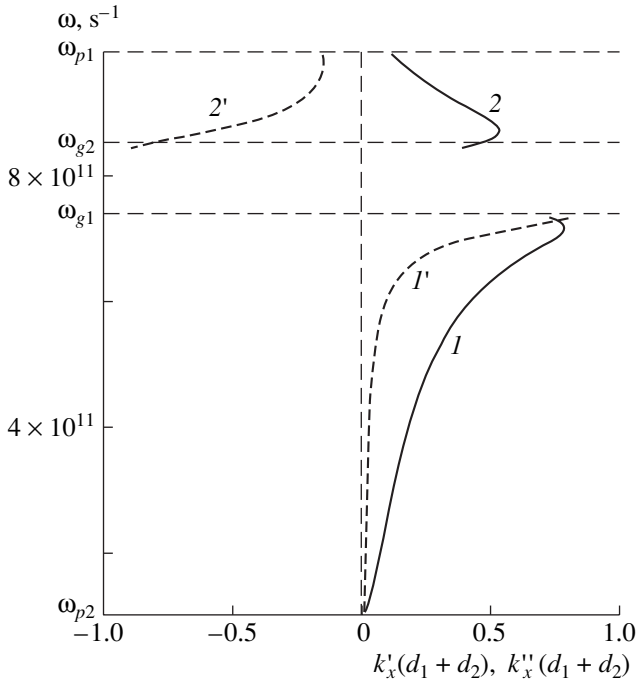

Fig. 5. Dispersion curves with allowance for spatial damping. The solid curves are for $k'_x(\omega)$, and the dashed curves are for $k''_x(\omega)$.

3. ACCOUNTING FOR DISSIPATIVE PROCESSES

Here, we investigate how the dissipative processes affect the properties of the plasma waves in a fine-stratified semiconductor structure. To do this, we take into account the effect of the collision frequencies on the wave dispersion properties and solve dispersion relation (3) numerically for real frequencies ω lying in the ranges revealed in Section 2, assuming that $k_x = k'_x + ik''_x$. In Fig. 5, the dependence of the real part of the wavenumber, $k'_x d$, on ω is shown by solid curves and the dependence $k''_x d\,(\omega)$ is shown by dashed curves. The calculations were carried out for $\nu_1 = 8 \times 10^{10}$ s^{-1} and $\nu_2 = 1 \times 10^8$ s^{-1}. The dispersion curves for waves with a positive and with a negative group velocity are denoted by the numerals *1* and *2*, respectively. The spatial damping of wave *1* (dashed curve *1*') is positive and weak in the range $\omega \approx 1 \times 10^{11}$–$6 \times 10^{11}$ s^{-1}. Beyond this range, the damping is substantially stronger. The spatial damping of wave *2* (dashed curve *2*') is negative. This feature of the polaritons in question is attributed to the negative value of the group velocity: the corresponding eigenwave is damped in the energy propagation direction. If the damping is taken into account, then the dispersion curves have a bend in the range of large values of $k'_x d$. In this range, the value of $|k''_x d|$ is seen to increase considerably. Hence, accounting for the damping restricts possible $k'_x d$ values; in this case, the phase velocity has a minimum [10–14].

For $\nu_1 = \nu_2 = 0$, dispersion relation (4) yields the relationships

$$k'_x \approx k_z d \sqrt{-\varepsilon_{01}\varepsilon_{02} \frac{(\omega^2 - \omega_{p1}^2)(\omega^2 - \omega_{p2}^2)}{(\varepsilon_{01}d_1 + \varepsilon_{02}d_2)(\varepsilon_{01}d_2 + \varepsilon_{02}d_1)(\omega^2 - \omega_{g1}^2)(\omega^2 - \omega_{g2}^2)}}, \qquad (6)$$

$$k''_x \approx 0.$$

When dissipative processes are ignored, we see that $k'_x \longrightarrow \infty$ as $\omega \longrightarrow \omega_{g1,2}$, i.e., as the dispersion curve approaches one of the horizontal asymptotes. With allowance for dissipative processes, we obtain

$$k_x' \approx k_x'' \approx \frac{1}{\sqrt{2}} k_z d \sqrt{-\varepsilon_{01}\varepsilon_{02} \frac{(\omega^2 - \omega_{p1}^2)(\omega^2 - \omega_{p2}^2)}{\omega(\varepsilon_{01}d_1 + \varepsilon_{02}d_2)(\varepsilon_{01}d_2 + \varepsilon_{02}d_1)(\omega^2 - \omega_{g1}^2)(\omega^2 - \omega_{g2}^2)}}$$

$$\times \begin{cases} \sqrt{\dfrac{\nu_1\omega_{L1}^2 d_1 + \nu_2\omega_{L2}^2 d_2}{(\varepsilon_{01}d_1 + \varepsilon_{02}d_2)(\omega^2 - \omega_{g1}^2)}}, & \omega \longrightarrow \omega_{g1}, \\ \sqrt{\dfrac{\nu_1\omega_{L1}^2 d_2 + \nu_2\omega_{L2}^2 d_1}{(\varepsilon_{01}d_2 + \varepsilon_{02}d_1)(\omega^2 - \omega_{g2}^2)}}, & \omega \longrightarrow \omega_{g2}. \end{cases} \quad (7)$$

Figure 6 shows how the minimum phase velocity depends on the relative thickness of the first of the alternating layers. For waves in the frequency range $\omega_{g2} < \omega < \omega_{p1}$ (heavy curve), the minimum phase velocity is approximately equal to $v_{ph\min} \approx 5.2 \times 10^8$ cm/s, and, for waves in the frequency range $\omega_{p2} < \omega < \omega_{g1}$ (light curve), it is about $v_{ph\min} \approx 3.3 \times 10^8$ cm/s. Note that the curves are symmetric with respect to the vertical line $d_1/d = 0.5$. The symmetry of the curves in Fig. 6 can be explained as being due to the symmetry of the right-hand sides of dispersion relation (4) with respect to subscripts *1* and *2*. The minimum value of the phase velocity corresponds to the case where both of the alternating layers have the same thickness.

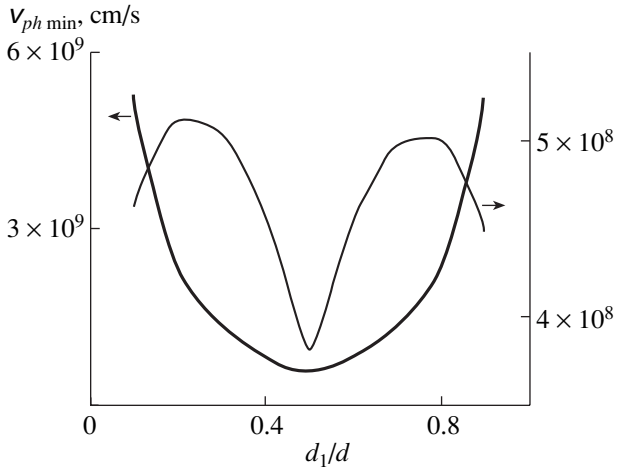

Fig. 6. Dependence of the minimum phase velocity of a plasmon on the relative thickness of the first of the alternating layers for $\nu_1 = 8 \times 10^{10}$ s^{-1}; $\nu_2 = 10^8$ s^{-1}, and $k_z = 500$ cm^{-1}.

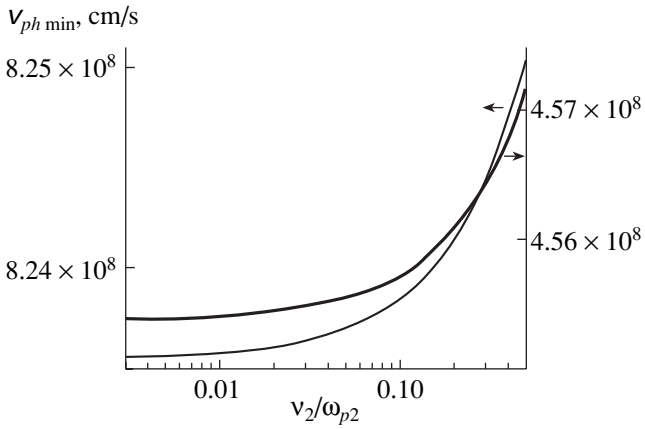

Fig. 7. Dependence of the minimum phase velocity of a plasma wave on the collision frequency in the second of the alternating layers for $d_1 = 2 \times 10^{-4}$ cm, $d_2 = 3 \times 10^{-4}$ cm, $\nu_1 = 8 \times 10^{10}$ s^{-1}, and $k_z = 500$ cm^{-1}.

Figure 7 shows the minimum phase velocity as a function of the ratio ν_2/ω_{p2} for $\nu_1 = 8 \times 10^{10}$ s^{-1}. The light and heavy curves correspond, respectively, to the upper and lower dispersion curves in Fig. 3. It is noteworthy that, as the dissipation rate changes by almost three orders of magnitude, the minimum phase velocity varies by less than 1%.

4. CONCLUSIONS

We have investigated the dispersion of waves in an infinite fine-stratified semiconductor superlattice. We have found that, for a stratified medium, the dependence of the dielectric tensor on the frequency leads to a specific shape of the dispersion curves. We have determined the limiting frequencies of waves in a superlattice. We have shown that accounting for dissipative processes restricts the maximum value of the longitudinal wavenumber at frequencies close to the hybrid plasma frequencies; in this case, the phase velocity has a minimum. We have derived expressions for the maximum value of the longitudinal wavenumber and have numerically calculated the dependence of the minimum phase velocity on the thicknesses of the layers in a semiconductor and on the collision frequencies in them. We have established that the phase velocity is minimum when both of the alternating layers have the same thickness. The minimum phase velocity increases with collision frequencies in the layers. From a practical standpoint, the investigations reported here are important in connection with the prospect of using fine-stratified semiconductor structures to develop various devices for nanoelectronics.

ACKNOWLEDGMENTS

This work was supported in part by the "Nanosystems, Nanomaterials, and Nanotechnologies" program of the National Academy of Sciences of Ukraine.

REFERENCES

1. M. C. Steele and B. Vural, *Wave Interactions in Solid State Plasmas* (McGraw-Hill, New York, 1969; Atomizdat, Moscow, 1973).
2. A. Yariv and P. Yeh, *Optical Waves in Crystals: Propagation and Control of Laser Radiation* (Wiley, New York, 1984; Mir, Moscow, 1987).
3. S. A. Tretyakov, F. Mariotte, C. Simovski, *et al.*, IEEE Trans. Antennas Propag. **44**, 1006 (1996).
4. K. A. Vytovtov, Radiotekh. Élektron. (Moscow) **46**, 1 (2001).
5. K. Yu. Bliokh and Yu. P. Bliokh, Usp. Fiz. Nauk **174**, 439 (2004) [Phys. Usp. **47**, 393 (2004)].
6. A. A. Belyanin, D. Deppe, V. V. Kocharovskiĭ, *et al.*, Usp. Fiz. Nauk **173**, 1015 (2003) [Phys. Usp. **46**, 986 (2003)].
7. Ya. B. Faĭnberg and N. A. Khizhnyak, Zh. Tekh. Fiz. **25**, 711 (1955).
8. S. M. Rytov, Zh. Éksp. Teor. Fiz. **29**, 605 (1955) [Sov. Phys. JETP **2**, 466 (1955)].
9. F. G. Bass, A. A. Bulgakov, and A. P. Tetervov, *High-Frequency Properties of Superlattice Semiconductors* (Nauka, Moscow, 1989) [in Russian].
10. A. A. Bulgakov and Z. E. Eremenko, Opt. Spektrosk. **66**, 1094 (1989) [Opt. Spectrosc. **66**, 640 (1989)].
11. R. R. Alfano, J. Opt. Soc. Am. **60**, 66 (1970).
12. G. R. Kovner, K. W. Alexander, K. J. Beil, *et al.*, Phys. Rev. B **14**, 1458 (1976).
13. A. A. Bulgakov and O. V. Shramkova, Zh. Tekh. Fiz. **73** (3), 87 (2003) [Tech. Phys. **48**, 361 (2003)].
14. O. V. Shramkova, Zh. Tekh. Fiz. **74** (2), 92 (2004) [Tech. Phys. **49**, 232 (2004)].

Translated by O.E. Khadin

Plasma Physics Reports, Vol. 31, No. 10, 2005, pp. 824–842. Translated from Fizika Plazmy, Vol. 31, No. 10, 2005, pp. 889–908.

DUSTY PLASMA

Helical Structures in Complex Plasma II: Collective Interaction

V. N. Tsytovich and N. G. Guseĭn-zade

Prokhorov Institute of General Physics, Russian Academy of Sciences, ul. Vavilova 38, Moscow, 119991 Russia

Received October 21, 2004; in final form, January 24, 2005

Abstract—The conditions for the formation and stability of quasi-crystal helical structures formed of charged dust grains of equal size in a complex plasma are investigated. A study is made of both the transverse confinement of such structures by means of an external parabolic potential well and the possibility of their self-confinement or confinement by the field of the smaller background grains. It is shown that, in the presence of dissipation, any initial random distribution of dust grains in a cylindrical external potential evolves into an equilibrium helical structure with a constant pitch angle. It is found that, when the external control parameter is smoothly varied, the pitch angle of the helix changes abruptly and the structure of the quasi-crystal undergoes bifurcations, during which the number of interwoven helices changes. The smaller the confinement parameter and the weaker the attractive forces between the grains, the larger the number of bifurcations. In addition, it is found that, because of the attraction (both noncollective and collective) between the dust grains, stable helical structures may exist not only at zero value of the external confinement parameter, but also at a negative one, and that the collective interaction between the grains not only increases the number of bifurcations but also changes their character. © *2005 Pleiades Publishing, Inc.*

1. INTRODUCTION

In the present paper, we study the conditions for the formation and stability of helical quasi-crystals formed of charged dust grains of equal size in a complex plasma. By complex plasma, we here mean a partially ionized dusty (or colloidal) plasma containing dust grains of two different sizes. This work is a generalization of [1]: it deals with a more complicated physical situation—the formation of helical structures from larger dust grains in the potential well of smaller grains—and thus takes into account the collective effects that significantly influence the processes under analysis.

The simplest three-dimensional (3D) quasi-crystalline structures (such as helices and their particular type—one-dimensional (1D) linear strings) were observed to form from ultracold atomic ions in different confinement devices (see, e.g., [2]), including Penning and Paul traps, storage rings, and others [2–6].

In most experiments, quasi-crystalline structures were observed to form in an external parabolic confining potential well.

The formation of such 3D quasi-crystals was also observed in experiments with colloids [7, 8] and dusty plasmas (see [9–11]).

In dusty plasmas, 3D crystalline structures (plasma crystals) occur under the conditions of rf discharges and dc glow discharges [9–11]. They differ from clusters in three respects: (i) they contain many grains, (ii) they are three-dimensional, and (iii) the grains in them are subject to collective interactions. As for 3D structures formed of a small number of grains, they differ from plasma crystals in that the interaction between the grains in them is noncollective and is produced by all possible combinations of pairwise interactions. Such structures are 3D clusters.

In our work, theoretical and numerical investigations of the properties of 3D cluster structures were carried out for a simple system of identical grains in a plasma. Plasma dynamics was not considered, and the role of plasma was reduced to specifying the type of intergrain interaction.

Experiments, as well as numerical simulations (see, e.g., [12]), showed that the shells in 3D spherical structures form in much the same way as in two-dimensional (2D) plane structures. Specifically, as the number of grains N increases, the initially formed single spherical shell becomes energetically unfavorable, so a second shell forms inside it; the third shell then forms inside the second; and so on. It is thus possible to speak of an analogue of Mendeleev's periodic table of elements: for a given number of grains N, it is possible to exactly establish how many grains compose each shell for a particular type of intergrain interaction. This structure is similar to that of an atom in the classical atomic model proposed as early as the 19th century by J.J. Thomson.

In a long cylindrical system, the dust grains can be prevented from expanding in a transverse direction by the simplest type of external potential. In a cylindrically symmetric system, the grains can be confined by a parabolic potential well or at the expense of solid walls. In cylindrical geometry, the simplest 3D structure is

1063-780X/05/3110-0824$26.00 © 2005 Pleiades Publishing, Inc.

helical: it has the form of a sequence of plane plasma crystals equally spaced along the cylinder axis in such a manner that each crystal is turned through the same angle relative to the previous one.

One of the objectives of this study is to prove that, for an arbitrary interaction potential between the grains, a steady dust configuration in the form of a helical structure with a fixed pitch angle can exist in cylindrical systems (as well as in large-aspect-ratio toroidal systems). The constant of such a "lattice" is determined by the mean number of grains per unit length of the structure. The limiting case of an extended helical structure is a 1D linear string.

A uniform helical structure formed of N interwoven helices is composed of grains lying in planes that are perpendicular to the symmetry axis of the cylinder and are equally spaced along it, the distance between them being Δ. In each plane, the grains lie at the vertices of a regular N-gon inscribed in a circle of a given radius. For an $N = 2$ helix, this is a "digon" (see Fig. 1). In the general case, this is an N-gon. In each pair of neighboring planes, the polygons are turned relative to one another through the same constant angle φ. For $N = 2$ (Fig. 1), the helical structure resembles the DNA helix.

Similar structures of ultracold atomic ions were observed in linear systems [2] and toroidal traps [3]. In recent years, however, the question of the formation of such structures in dusty plasmas has also begun to be widely discussed. Thus, the first experiments have already been carried out on the injection of dust into the plasma of cylindrical steady-state (unstratified) discharges under microgravity conditions during parabolic flights [13]. In those experiments, dust grains were injected at fairly high speeds, and so the only effects that were observed were the flows of dust clouds and the interaction between them. For higher gas pressures (i.e., stronger friction with neutrals) and for lower dust injection speeds, the injected grains should form helical structures; this is what is expected to be observed in future experiments. Observations of the initial stage of formation of helical structures were also discussed in [14]. As for the problem of the mechanism for their formation, it requires a separate investigation, however.

By varying the external control parameter (e.g., the number of grains per unit length of the helical structure or the parameters of the confining potential), a wide variety of equilibrium configurations can be obtained—from the simplest structures (such as 1D strings) to complex helical structures formed of several interwoven helices.

Another objective of the present study is to numerically investigate the possibility of producing helical structures in a complex plasma (i.e., a plasma with dust grains) in the presence of an external confining parabolic potential in a plane transverse to the symmetry axis. The constant determining the confining potential can be arbitrary. In particular, it can be negative; in this case, however, equilibrium helical structures can exist only when the long-range interaction between the dust grains is attractive and sufficiently intense. The problem to be studied is how various types of intergrain interactions affect different equilibrium configurations and their bifurcations. The investigations were carried out under the assumption that the interaction between all large dust grains can be described by summing all the pairwise interactions (the collective interactions being weak); this is true when the number of grains in a 3D structure is sufficiently small, so that the mean free path of the plasma particles that take part in dust grain charging is much larger than the transverse size of the helical structure.

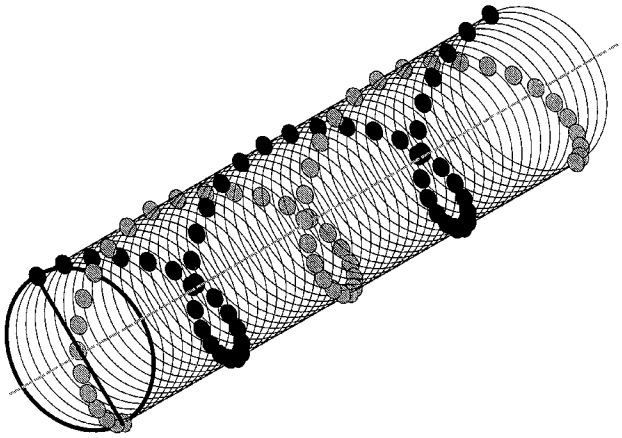

Fig. 1. Two interwoven helices ($N = 2$).

Finite-length helical structures were investigated numerically under the assumption that the confinement in the transverse direction was far better than that along the symmetry axis of the structure. The results of numerical simulations show that, regardless of the type of pairwise interaction, any random distribution of the dust grains evolves into a helical structure.

We begin by discussing the question about the interaction between the grains. We then discuss the results of numerical simulations, in particular, bifurcations of the pitch angle and global bifurcations—the onset of new shells. Finally, we discuss analytic methods for investigating equilibrium helical structures and analyze the role of attraction between the grains in the formation of self-confining structures. All investigations were carried out under the assumption that the interaction between the large grains can be treated as the sum of pairwise interactions.

2. INTERACTION BETWEEN DUST GRAINS IN A COMPLEX PLASMA

Here, we consider the distinguishing features of the interaction between dust grains in a complex plasma containing, in addition to electrons and ions, an appreciable amount of dust.

2.1. Definition of the Terms "Small" and "Large" Dust Grains

Let us consider a complex plasma containing dust grains of two different sizes, namely, "small" and "large" grains. The difference between the small and large grains is characterized by the ratio of the mean free path λ_{id} of the ions with respect to their collisions with grains of each species (in which the ions are absorbed by the grains) to the characteristic size of the structure. The mean free path of the ions with respect to their collisions with small grains is much less than the dimension of the structure, so small grains can be described in a continuous manner in terms of their density n_d. The mean free path of the ions with respect to their collisions with large grains is much greater than both the dimension of the structure and the mean distance between the grains. When small grains accumulate to form a cloud in a certain spatial region, they give rise to a collective ion flux in the direction of their density gradient. The ion flux, in turn, compresses a cloud of small grains and produces self-consistent distributions of the ion density, electron density, dust density, dust charge density, ion drift velocity, and electrostatic potential around the cloud. Large grains interact with one another via a pairwise (grain–grain) interaction potential; they also can be affected by the ion flux generated by the small grains. Moreover, the number of large grains in the structure is usually much less than the number of small grains. This interaction of large grains with small background grains can create conditions such that the external confinement constant (parameter) K, which is positive in the case of a parabolic potential well, can even become negative. This does not mean that large grains in such circumstances may not evolve to a helical structure; as will be shown below, stable helical structures can form even when the external confinement constant is negative (examples of such structures, as well as the corresponding necessary conditions for the magnitude of the attracting forces, will be presented below). In what follows, we will investigate helical structures formed only by the large grains, while treating the small grains merely as a background for the interaction between large grains. The case in which there are no small grains in a plasma may be called the case of helical structures of equal-size grains.

For estimates, we consider parameter values typical of laboratory experiments: the radius of the small grains is about $a_{\text{small}} \approx 8$ μm, the dust density is on the order of 10^4 cm^{-3}, the ion density is 3×10^8 cm^{-3}, the mean free path of the plasma ions absorbed by the small grains is 50–60 μm, and the transverse size of a cylindrical structure is on the order of 400–600 μm. In order for the large grains to be confined in a finer dust background, it is sufficient that they be larger than the small grains (say, the radius of the large grains is twice that of the small ones). As for the confining potential, it is proportional to $(a_{\text{large}}–a_{\text{small}})/a_{\text{small}}$. Under such conditions, the structure is composed of a small number (only a few) of large grains, so the intergrain distance in the structure is far greater than the above mean free path (which equal to about 50–60 μm).

2.2. Potential of the Small Grains

In order to investigate the possibility of the existence of helical structures, we ignore the presence of large grains and consider a complex plasma containing a single species of dust grains of the same size. Numerical simulations show that such a plasma should possess a new simple physical property. Specifically, in contrast to a conventional plasma, a homogeneous dusty plasma is spatially unstable and tends to form dust structures with regions of elevated and of depressed dust density. The instability ends with the separation of the plasma into dust bunches and dust cavities (so-called dust voids) [15]. Steady-state dust bunches (structures) were investigated in detail for very different conditions (e.g., in plane and spherical geometry, in the presence and absence of the surrounding walls, and for different values of the ratio of the mean free paths of the ions with respect to their collisions with grains and with neutral particles) by using simple balance equations for the electron and ion densities, ion drift velocity, and grain charge with allowance for the drag forces exerted on the dust by the ion flow, frictional forces in a neutral gas, and ion diffusion (see [16–20]). The general conclusions reached in these investigations are as follows: such dust structures generate a self-confining potential; their main parameters fall within a limited range, so that all the possible structures can be captured and analyzed numerically; and the maximum depth of the potential well created by a single structure is on the order of $(3–5)T_e$ (where T_e is the electron temperature). The last result is physically natural because the structure itself can be considered as a kind of wall with a floating potential approximately equal to $\approx T_e$, provided that the dimension of the structure is greater than the mean free path. Near the bottom of the potential well, the confining potential can be approximated by a parabola. We will use the simplest approximation for the potential of the structure, keeping in mind that the forces experienced by a dust grain (namely, the electric field force and the ion drag force) are in balance at each point.

If there is a somewhat larger grain in the field of smaller identical background grains (the size of the larger grain may not be very great; it is quite sufficient that it be twice as great as that of the smaller grain), then the balance of the forces acting on it can be expressed as follows: the electric field force increases in proportion to the grain size, while the ion drag force increases to a greater extent, in proportion to the square of the size (accordingly, doubling in the grain size results in a fourfold increase in the drag force). The drag force is driven by an ion flux directed toward the

center of the structure, so the larger grains always remain in a confining potential V_s on the order of

$$V_s \approx Z_d T_e e^2 \rho^2 / \lambda_{id}^2, \quad (1)$$

where ρ is the distance from the center of the structure (in cylindrical geometry, the squared distance from the symmetry axis z is equal to $\rho^2 = x^2 + y^2$).

2.3. Example of a Cylindrical Dust Structure whose Potential Confines Large Grains

As an example, we present here the results of numerical simulations of a cylindrical dust structure whose size is much less than the mean free path of the ions with respect to their collisions with neutrals for the simplest case of a locally quasineutral plasma [21]. In solving the problem numerically, the parameters of the structure, such as the dust, ion, and electron densities, the dust grain charge, and the ion drift velocity, were described by the time-independent force balance equations and the continuity equations for the ion, electron, and dust plasma components (the dust was characterized by the dust number density). The electrons were treated as experiencing two forces—the pressure force and the electrostatic force, whereas the ions were described with allowance for their friction with the dust grains (as a result of the ion-flux-driven drag force) and with the neutral gas particles, their pressure, and their diffusion caused by collisions with neutral atoms. The dust grains were assumed to be charged in a plasma flux, which was regarded as a collective flux, provided that the plasma contained a sufficiently large dust component. The basic equations and the final result of the calculations can be expressed in terms of the following dimensionless parameters: the dimensionless ion density $n = n_i/n_{\text{norm}}$ (with $n_{\text{norm}} = n_0(\lambda_{in}/\lambda_{id})$), the dimensionless electron density $n_e \longrightarrow n_e/n_{\text{norm}}$, the dimensionless Havnes parameter $P = n_d Z_d/n_{\text{norm}}$, the dimensionless electrostatic potential $\phi \longrightarrow e\phi/T_e$, the dimensionless grain charge $z = Z_d e^2/aT_e$, and the dimensionless ion drift velocity $u = u_i/\sqrt{2}\, v_{Ti}$ (with $v_{Ti} = \sqrt{T_i/m_i}$).

The requirements that the plasma be quasineutral, that the drift velocity and diffusive flux both vanish at the cylinder axis, and that the equation for the dust charge have a solution at the center restrict possible central values of the ion density and Havnes parameter. In this case, their values turn out to be such that all possible dust structures can be scanned numerically by varying only one parameter over a limited range. Different structures can be distinguished by the different values of the electrostatic potential drop from the periphery of the structure ($P = 0$) to its center ($P = P_{\max}$).

Figure 2 shows the results of numerical simulations of a cylindrical structure with the maximum potential drop [21]. The parabolic approximation of the potential profile in the central region of the structure yields $\phi = 3.3\rho^2$. The maximum potential drop depends strongly on the sort of gas (the calculations illustrated in Fig. 2 were carried out for argon). For hydrogen, the maximum potential drop is equal to $\phi_{\max} = 2.2$.

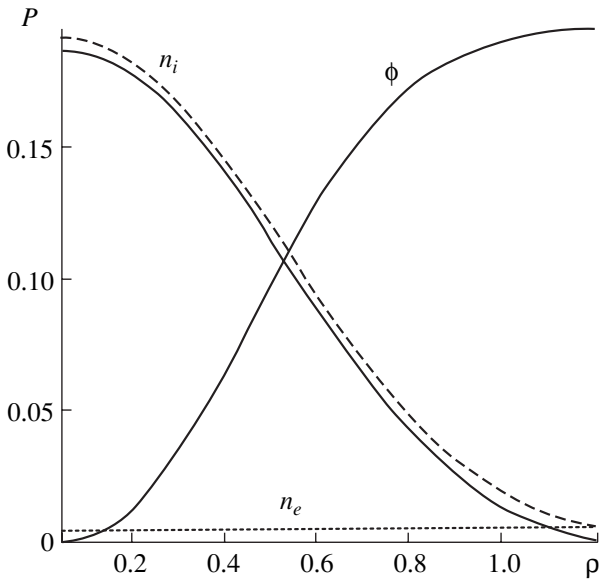

Fig. 2. Example of a self-organized cylindrical dust structure in argon. Here, ρ is the distance from the cylinder axis in units of λ_{in}, the electrostatic potential ϕ is in units of T_e/e, n_e and n_i are the dimensionless electron and ion densities, and P is the Havnes parameter (increased 50-fold for illustrative purposes). The calculations were carried out for the maximum possible potential drop; in the corresponding structure, most of the negative charges are concentrated on the dust grains, the dimensionless grain charge z increases monotonically from 0.64 at the center to 1.1 at the periphery, and the ion drift velocity is directed toward the axis and changes from $u = 0$ at the axis to $u = -2.8$ at the periphery.

2.4. Nonexponential (Non-Debye) Screening

As was mentioned in [1], the Coulomb interaction can be described in terms of the Debye screened potential only when the grain charge is sufficiently small and the ratio of the grain size to the screening length, as well as the ion-to-electron temperature ratio, is not too small.

This is why, in numerical simulations, we used the following relationship (see [22]):

$$\psi = \left(1 - \frac{r-a}{\lambda_{\text{scr}}}\right)^4 \approx (1-Dr)^4 \frac{1}{2}\left(1 + \frac{1-Dr}{|1-Dr|}\right). \quad (2)$$

Here, the distance in the first expression is in dimensional units, and, in the second expression, it is normalized to the spacing Δ between neighboring lattice planes of the quasi-crystal helical structure (see [1] for details).

Simulations were also carried out for a Yukawa potential with the screening factor $\psi_Y = \exp(-D_Y r)$. It should be noted that, in order to compare the nonlinear screening with the Yukawa screening, it is necessary to keep in mind that the screening distance D in the formula for the nonlinear screened potential is ten times less than the Yukawa distance D_Y in the formula for the Yukawa screened potential (at least, for the actual experiments).

2.5. Noncollective Grain Attraction Model

This issue also was discussed in detail in [1]. Although noncollective attraction (the shadow effect) is not, strictly speaking, a screening effect [23–28], the "screening" factor ψ for noncollective attractive interactions may nevertheless be introduced.

The attractive potential is proportional to $1/r$, and the screening factor ψ_{att} is negative, $\psi_{att} = -\alpha$.

The grain noncollective attraction coefficient α may vary for different experimental conditions by many orders of magnitude, e.g., from about 10^6 to values close to unity.

2.6. Collective Confinement and External Dust Confinement

It is thought that large dust grains form a helical structure irrespective of whether or not there is a self-consistent field that is produced by small grains and affects the confinement of large particles. We call this phenomenon collective confinement.[1] The length L of the structure formed by small dust grains is much greater than the mean free path of the ions with respect to collisions with these grains (the density of the small grains is sufficiently high). This is usually the case when the dust can strongly influence the potential distributions, so the potential drop at the center of the structure is on the order of T_e and the confining potential can be approximated by expression (1). The externally produced potential is commonly described by a formula like expression (1), in which λ_{id} is replaced with L. Since $L \gg \lambda_{id}$, the external confining potential is, as a rule, lower than the self-consistent potential created by the dust structure; however, this is not always the case. The helical structures that will be considered below are formed by a few large grains. The intergrain distance in such structures is much larger than the mean free path of the ions with respect to their collisions with the grains, and the collective effects in interaction between the grains are associated only with changes in the background dusty plasma. In numerical simulations, the distance Δ between the planes in the helical structures was taken as the unit of length and the energy was expressed in units of $Z_d e^2/\Delta$. In these units, the self-consistent confining potential has the form

$$V_{\text{self}} = K_s u^2; \quad K_s \approx \frac{T_e \Delta}{e^2}\left(\frac{\Delta^2}{\lambda_{id}^2}\right). \tag{3}$$

where $u = 2R/\Delta$ (the diameter of the structure divided by the distance between the planes in the structure). This expression is presented in order to provide estimates of the self-confining potential for future experiments. In the presence of an external potential with the confinement constant K_{ext}, the constant of the total confining potential is equal to $K = K_s + K_{\text{ext}}$ rather than to K_s.

2.7. Collective Grain Attraction Model

The background of small dust grains influences the interaction between large grains, which in turn perturbs the background. One large grain perturbs the background and thereby influences another large grain. We call this interaction the collective interaction. The dependence of collective interaction on the distance between dust grains was found in [29, 30]. In terms of the dimensionless units used in relationship (2), we can write

$$V_{\text{col.int}} = \frac{\beta}{r}\cos(\gamma r). \tag{4}$$

Here, the collective attraction coefficient is equal to $\gamma \approx Z_d^2 e^2 a_{\text{small}}^2/(\tau\lambda_{Di}^2)$ (see [29, 30]), where $\tau = T_i/T_e$ is the ion-to-electron temperature ratio (for most experiments, it is about $\tau \approx 0.01$), a_{small} is the radius of the small grains, and λ_{Di} is the ion Debye radius. We see that the collective attraction coefficient depends essentially on the grain size and can be much larger than the noncollective attraction coefficient $\alpha \approx Z_d^2 e^2 a_{\text{large}}^2/\lambda_{Di}^2$ because it contains the small parameter τ in the denominator. This coefficient also depends strongly on the background dust density, namely, it is proportional to the squared dust charge density. For a helical structure of large grains against the background of small grains with a charge density on the order of the ion density, the coefficient γ may fall in the range 0.3–0.003, i.e., it may be of the same order of magnitude as the noncollective attraction coefficient for large grains. The coefficient γ can be expressed in terms of the screening distance $D = \Delta/\lambda_{\text{scr}}$. For present-day experiments, it is equal to $\gamma = (0.5–0.2)D$. Other estimates can also be obtained directly from the corresponding formulas of [29]. For

[1] The criterion for the onset of collective interaction due to the presence of small grains has the form $L \gg \lambda_{id}$, where λ_{id} is the mean free path length traveled by an ion before it is absorbed by a grain. It should be noted that the quantity P in the expression for λ_{id}, which is presented in the body of the text, is the Havnes parameter for small grains. This criterion completely determines the density of small grains and can easily be satisfied in modern experiments. Helical structures can only be formed by a small number of large grains when the distance between them exceeds the ion mean free path; this condition also is easy to satisfy experimentally.

our simulations, it was sufficient to know only the order-of-magnitude values of the parameters in question.

2.8. Interaction Potential Model with Allowance for Nonlinear Screening and the Effects of Noncollective Attraction and Collective Interaction

The normalized intergrain interaction potential used in computer simulations and analytic calculations has the form

$$V(r) = \frac{1}{r}\left[(1-Dr)^4\frac{1}{2}\left(1+\frac{1-Dr}{|1-Dr|}\right)-\alpha+\beta\cos(\gamma r)\right]. \quad (5)$$

Here, the potential is in units of $Z_d e^2/\Delta$ and the radial coordinate r is in units of the distance Δ between the planes of the helical structure. The approximation used for the nonlinear screening in this expression implies that the grain sizes are much less than the distance between the planes.

In the limiting case $D = 0$, $\alpha = 0$, and $\beta = 0$, expression (5) describes the Coulomb repulsive interaction.

In what follows, potential (5) will be compared to the Yukawa screened potential of the interaction between the grains with allowance for noncollective attraction ($\alpha \neq 0$) and collective attraction ($\beta \neq 0$):

$$V_Y(r) = \frac{1}{r}\exp(-D_Y r). \quad (6)$$

This comparison is meaningful only for parameter values such that $D \ll D_Y$, e.g., for $D = 0.1D_Y$.

3. NUMERICAL SIMULATIONS

Here, we describe the results from simulations of a system of charged dust grains that are initially distributed in space in a random manner and interact by means of the potentials mentioned above.

We consider a system consisting of a large number of likely charged dust grains (generally of the same radius a) that are prevented from expanding by an external potential $U(\mathbf{r}_\perp)$. Near the bottom of an axisymmetric potential well, the confining potential can always be approximated by a parabolic potential, $U_{\text{foc}} = -\frac{1}{2}K(x^2 + y^2)$, where K is the confinement constant, which depends on the parameters of the trap (in the case of self-confinement of the dust grains by attractive forces, this constant is $K \leq 0$).

In most of the present-day experiments, the grains are confined by an external potential well; however, the confinement constant K can be varied over a wide range, including the range of its zero and negative values, $K \leq 0$.

In simulations, we utilized the standard molecular dynamics method for a one-component plasma. In molecular dynamics, the equations of motion of the nth grain have the form

$$m\frac{\partial^2 \mathbf{r}_n}{\partial t^2} + qK\mathbf{r}_{\perp n} + 2q^2\sum_{n\neq k}F_{nk}(|\mathbf{r}_n - \mathbf{r}_k|) = 0, \quad (7)$$

where $\mathbf{r}_k$ are the coordinates of the kth grain. These equations imply that the interaction between the grains is described by summing all their pairwise interactions and that the collective interactions are ignored.

The initial grain positions were chosen to be random. The temperature was calculated as the mean kinetic energy. In order for the system to be capable of evolving to a steady equilibrium state, we introduced friction into the model.

We simulated the two following experimental situations:

The first is that with a circular toroidal trap, which was calculated under the assumption that the radius of the torus is infinitely large (so the toroidal curvature was ignored); in this case, simulations can be done for a cylindrical system with periodic boundary conditions in the z direction.

The second situation is that with a system of finite length in which the grains are confined in the z direction by a parabolic potential well or at the expense of solid walls.

Simulations of a system with periodic boundary conditions within which the grains interact by means of potentials (5) and (6) with different values of the parameters α, D, β, and (for comparison) D_Y yielded single-shell equilibrium quasi-crystal structures formed of N interwoven helices with a constant pitch angle and a constant spacing Δ between neighboring lattice planes. Other equilibrium single-shell configurations were not observed. It should be noted that, for some values of the external parameter, helical configurations were observed to evolve to different equilibrium configurations, depending on the initial positions of the grains.

In simulations, we decreased the value of the confinement parameter K and observed the following sequence of bifurcations of the steady-state configurations: linear chain $\longrightarrow$ zigzag (a helix with the angle φ equal to π) $\longrightarrow$ helix1 (here, "1" stands for the first stable branch of a helical structure after the first bifurcation; see, e.g., Fig. 5) $\longrightarrow$ tetrahedral configuration (two interwoven helices with $\varphi = \pi/2$), and so on.

For a certain critical value of the external confinement parameter K (each particular interaction potential has its own critical value of K), we observed the appearance of a second shell, i.e., the formation of a linear chain within a helix, followed by the formation of two separate shells, which can also be regarded as two sys-

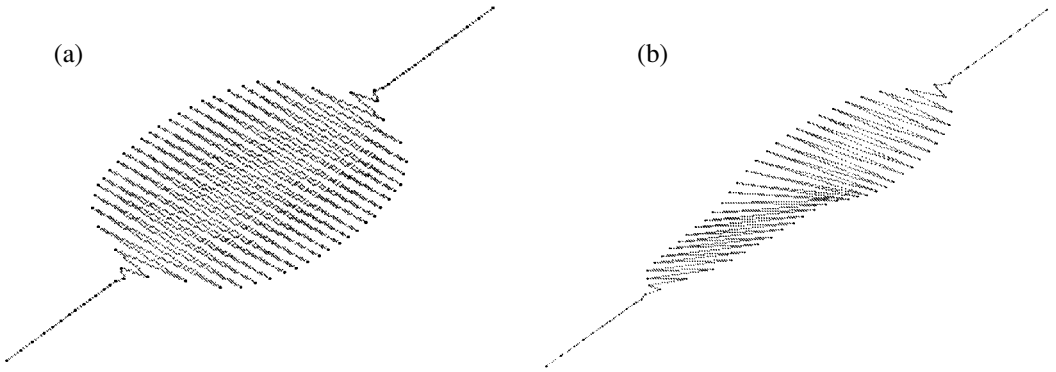

Fig. 3. Results of molecular dynamics simulations for $N = 80$ grains that are confined in the z direction within a cylindrical tube by a parabolic potential and interact through a Yukawa screened potential with $D_Y = 0.1$, the grain noncollective attraction coefficient being $\alpha = 0.1$. The evolution of the system is shown as the depth of the external transverse confining potential well (the external parameter) is decreased. For illustrative purposes, the scales along the axes in the transverse plane are enlarged by a factor of 40 as compared to the z-axis scale.

tems of interwoven helices, one being nested inside the other.

All of the above regular features of systems with periodic boundary conditions should be captured qualitatively in simulations of finite-length systems. Of course, helical structures in finite-length systems are fairly difficult to classify, but it is nevertheless possible to draw an analogy with infinite structures. The system evolves through all the stages: a linear chain changes into a zigzag, which in turn changes into a helix as the external parameter is further decreased, and so on

In simulations, we analyzed the two following models of finite-length systems:

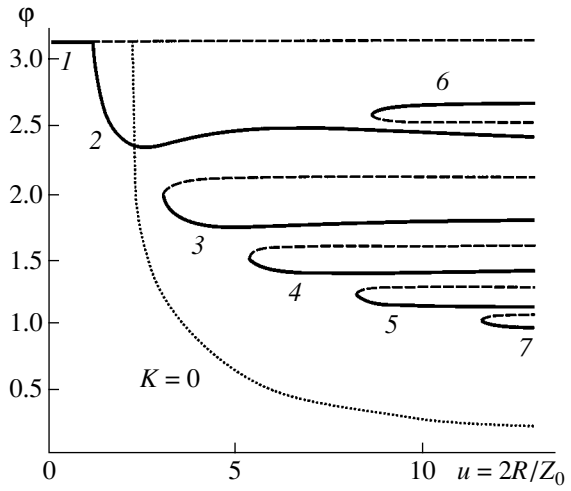

Fig. 4. Extremes of energy and the possibility of self-confinement ($K = 0$) for an $N = 1$ helix in the (φ, u) plane. Here and in the subsequent figures, the dashed curves correspond to the maximum energy of the structure and the dotted curve corresponds to the boundary of the self-confinement region ($K = 0$).

First, we considered an axisymmetric finite-length system in which the grains interacted via potential (5) and were confined in the z direction by a parabolic potential well $U \propto -1/2(d(x^2 + y^2) + z^2)$.

Second, we considered an axisymmetric finite-length system in which the grains interacted via potential (5) and were confined in the z direction at the expense of solid walls, i.e., by means of a potential well $U \propto -1/2(d(x^2 + y^2) + z^{2L})$. The system with solid walls corresponds to the limit $L \gg 1$.

In order to achieve a steady equilibrium state in simulations, as in the case of infinite systems, we introduced friction into the model, assuming that the frictional force was proportional to the particle velocity. The results of simulations are essentially the same as those obtained in [1]. In Fig. 3, we can see all of the evolutionary stages of the system: from a linear string to a structure formed of several interwoven helices. Because of the different line densities of the dust grains (the density per unit length in the z direction), all these stages were often observed to occur simultaneously. In a system in which the grains were confined in the z direction at the expense of solid walls (in contrast to the case of confinement by a parabolic potential well), the grain density near the ends of the cylinder was higher than that in its center. This is why the bifurcation process starts precisely at the cylinder ends.

The results of numerical simulations show that any random distribution of the dust grains interacting by means of potential (5) relaxes to one of the possible single-shell equilibrium configurations in the form of N interwoven helices. For systems with periodic boundary conditions, the result is a quasi-crystal structure formed of N interwoven helices with a constant pitch angle and a constant spacing Δ between neighboring lattice planes. Pursuing the analogy with the plane clusters, we can say that, in a 2D planar case, the simplest

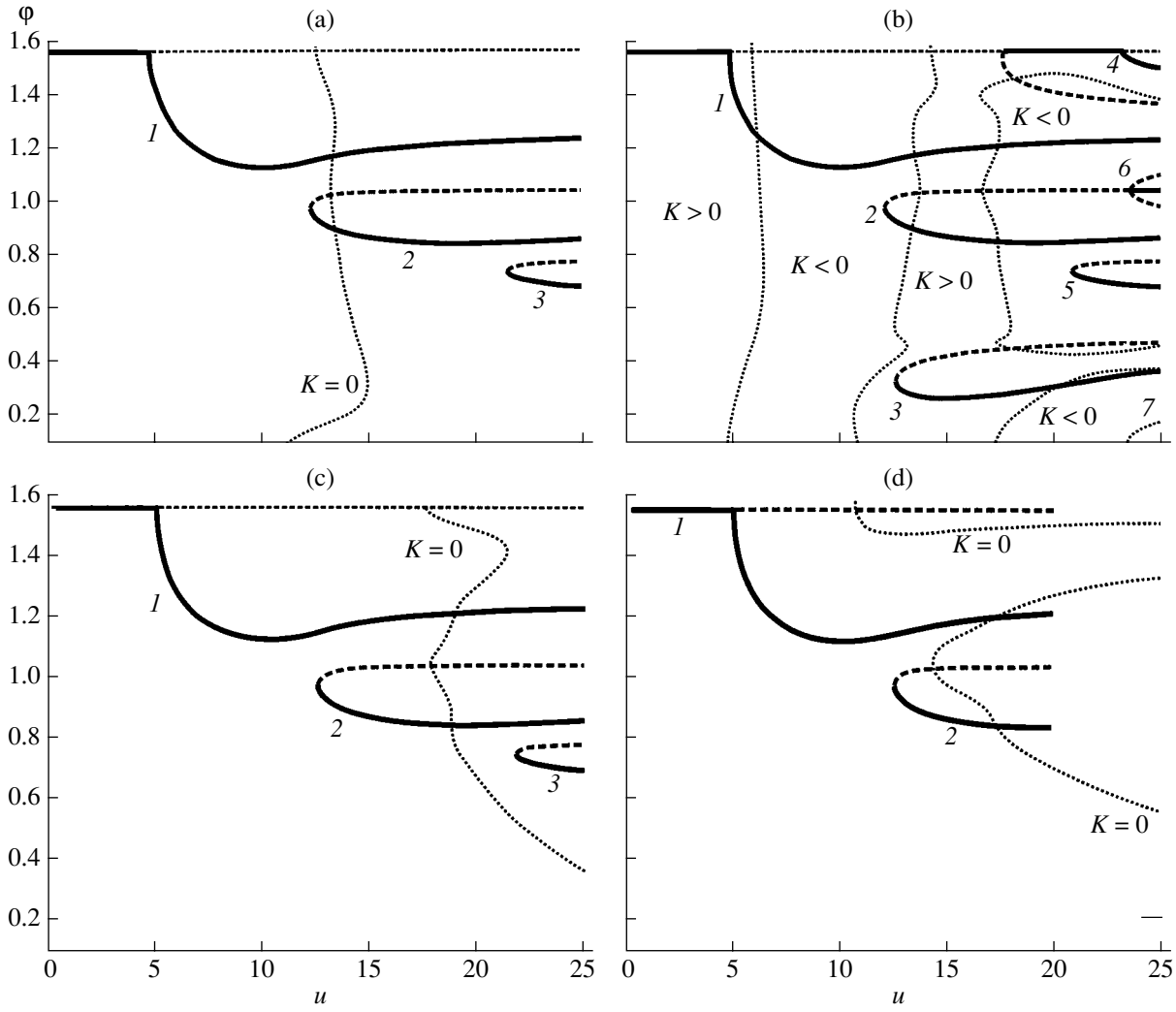

Fig. 5. Positions of extremes of the energy of an $N = 2$ helix and the boundary of the self-confinement region ($K = 0$) in the plane (φ, u) for (a–c) $D_Y = 0.1$ and $\alpha = 0.1$, the remaining parameter values being (a) $\beta = 0.5$ and $\gamma = 0.2$, (b) $\beta = 0.5$ and $\gamma = 0.5$, and (c) $\beta = 0.1$ and $\gamma = 0.1$. Plot (d) corresponds to $D = 0.1$, $\alpha = 0.01$, and $\beta = 0$.

structure is a regular polygon while, in a 3D case, it has the form of a simple helix ($N = 1$) or two, three, etc., interwoven helices.

A decrease in the external confinement constant is accompanied by bifurcations in the (u, φ) plane (see Section 5). The mechanisms for such discontinuous transitions from one type of helix to another are not completely clear.

When the long-range interaction between the dust grains is attractive, they can form steady helical structures in the absence of an external confining potential and even in the presence of a parabolic repulsive potential.

Hence, as the confinement parameter K decreases, interactions with remote grains begin to play an increasingly important role, so the bifurcations can be strongly influenced by the character of screening (either the Yukawa or nonlinear screening) and also by the collective and noncollective attractions.

In our simulations, it was found, however, that the collective interaction substantially changes the bifurcational picture; specifically, it not only increases the number of bifurcations (i.e., decreases the difference between the values of the confinement parameter at which two subsequent bifurcations occur) but also alters the character of the structural transitions.

4. HELICES

In experiments and numerical simulations, steady configurations in the form of a helix with constant values of Δ and φ have been observed. It is therefore reasonable to analyze only this type of configurations.

Let us consider all the possible structures formed of N interwoven helices.

To do this, we substitute into general equations of motion (7) the coordinates of the grains that have already formed a quasi-crystal helical structure with a constant spacing between neighboring lattice planes.

In this case, several different equilibrium states are possible. It can be shown, however, that, among all possible equilibrium configurations, the one in which the grains in the (x, y) plane are at the vertices of a regular polygon possesses a minimum energy and, accordingly, is most stable. This is why we restrict ourselves to considering only such configurations.

The configurations of interest can be represented as follows:

$$\mathbf{r}_{1,n} = (x_{1,n}, y_{1,n}, z_{1,n}) = (R_{1,n}\cos\varphi_{1,n}, R_{1,n}\sin\varphi_{1,n}, z_{1,n}),$$

$$\mathbf{r}_{2,n} = (x_{2,n}, y_{2,n}, z_{2,n}) = [R_{2,n}\cos(\alpha+\varphi_{2,n}), R_{2,n}\sin(\alpha+\varphi_{2,n}), z_{2,n}],$$

$$\mathbf{r}_{3,n} = (x_{3,n}, y_{3,n}, z_{3,n}) = [R_{3,n}\cos(2\alpha+\varphi_{3,n}), R_{3,n}\sin(2\alpha+\varphi_{3,n}), z_{3,n}],$$

$$\ldots\ldots\ldots\ldots\ldots\ldots\ldots\ldots\ldots\ldots\ldots\ldots$$

$$\mathbf{r}_{N,n} = (x_{N,n}, y_{N,n}, z_{N,n}) = [R_{N,n}\cos((N-1)\alpha+\varphi_{N,n}), R_{N,n}\sin((N-1)\alpha+\varphi_{N,n}), z_{N,n}],$$

where $z_{1,n} = z_{2,n} = z_{3,n} = \ldots = z_{N,n} = z_0(Nn)$.

Hereafter, it is assumed that the grain density along the z axis is constant, i.e., that there are N_0 grains over an interval of length L; so, for an $N=1$ helix, we have $z_0 = L/N_0$. In a structure formed of N interwoven helices, the charged grains are separated by the distance Nz_0 along the z axis, the linear grain density being the same as that in an $N = 1$ helix. The rest of the notation is as follows: $R_{1,n} = R_{2,n} = R_{3,n} = \ldots = R_{N,n} = R = \text{const}$ is the radius of a structure formed of N interwoven helices, $\alpha = 2\pi/N$ is the angle between each two neighboring grains at the vertices of a regular N-gon in the same (x, y) plane, and $\varphi_{1,n} = \varphi_{2,n} = \varphi_{3,n} = \ldots = \varphi_{N,n} = \varphi n$ is the angle through which the polygons formed by the grains in the neighboring (x, y) planes are turned relative to one another.

We are considering the equilibrium conditions for a helical structure that does not rotate as a whole ($\dot{\varphi} = 0$) because it is always possible to pass over to a frame of reference in which the structure is nonrotating.

The conditions for the existence of a steady equilibrium state have the form

$$\frac{\partial U}{\partial \varphi_n} = 0; \quad \frac{\partial U}{\partial R_n} = 0; \quad \frac{\partial U}{\partial z_n} = 0. \tag{8}$$

Since the line densities z_n and angles φ_n always satisfy the force balance equation, we are left with only one of the three equilibrium conditions:

$$\frac{\partial U}{\partial R_n} = 0. \tag{8a}$$

A full analysis of the properties of a helix and its linear stability is a fairly complicated task and is to be done separately. This is why we perform here only a qualitative analysis of the possible types of stable configurations and the evolution from one structure to another when one or several external parameters are varied.

In order to study this problem, we utilize the following familiar mechanical principle: in a stable equilibrium state, the system has a minimum potential energy. This is indeed the case for systems with dissipation.

When the grains in such configurations interact through potential (5), the energy of each grain can be written as

$$E = Ku^2 + (1-\delta_{N,1}) \times \sum_{k=1}^{N-1} \frac{1}{\Delta r_{0,k}}\left[(1-D\Delta r_{0,k})^4 \frac{1}{2}\left(1+\frac{1-D\Delta r_{0,k}}{|1-D\Delta r_{0,k}|}\right) - \alpha + \beta\cos(\gamma\Delta r_{0,k})\right] + \sum_{k=0}^{N-1}\sum_{l=1}^{\infty} \frac{2}{\Delta r_{l,k}}\left[(1-D\Delta r_{l,k})^4 \frac{1}{2}\left(1+\frac{1-D\Delta r_{l,k}}{|1-D\Delta r_{l,k}|}\right) - \alpha + \beta\cos(\gamma\Delta r_{l,k})\right]. \tag{9}$$

Here,

$$\Delta r_{l,k} = \left[N^2 l^2 + u^2 \sin^2\left(\frac{l\varphi}{2} + \frac{\pi k}{N}\right)\right]^{1/2},$$

where $\delta_{N,1}$ is the Kronecker delta and $u = 2R/z_0$ is the diameter of the quasi-crystal helical structure normalized to the spacing z_0 between neighboring lattice planes.

Accordingly, for interactions through Yukawa screened potential (6), the energy per grain is equal to

$$E = Ku^2 + (1-\delta_{N,1}) \times \sum_{k=1}^{N-1} \frac{\exp(-D\Delta r_{0,k}) - \alpha + \beta\cos(\gamma\Delta r_{0,k})}{\Delta r_{0,k}} + 2\sum_{k=0}^{N-1}\sum_{l=1}^{\infty} \frac{\exp(-D\Delta r_{l,k}) - \alpha + \beta\cos(\gamma\Delta r_{l,k})}{\Delta r_{l,k}}. \tag{10}$$

Since the infinite sums in expressions (9) and (10) for the grain energy diverge, it is meaningful to calcu-

late only the difference between the energy of a structure formed of N interwoven helices and the energy of a linear string, $E_{\mathrm{Nhelix}} - E_{\mathrm{string}}$. This allows us to set aside problems associated with the divergence of the infinite sums.

For a helix, the condition under which the energy takes an extremal value has the form

$$\frac{\partial E}{\partial \varphi} = 0. \tag{11}$$

The stability analysis requires knowledge not only of the extreme value of the energy but also of its minimum value. The corresponding criterion has a definite physical meaning: it gives nothing more than the minimum energy per elementary cell, or, in other words, a minimum in the Madelung energy.

Condition (11) yields phase diagrams in the (u, φ) plane. The situation in which two or more different values of the variables (u, φ) correspond to one value of the external parameter K will be regarded as a bifurcation. As will be shown below, the smaller the confinement parameter K, the larger the number of possible bifurcations.

On the other hand, the expression for the external parameter K is determined by radial force balance equation (8a). Consequently, the parameter K depends more significantly on the radius of the structure and on the type of the intergrain interaction potential. In the simplest cases, the dimensionless diameter u of the structure is inversely proportional to the parameter K, so it is convenient to classify bifurcations in terms of this parameter:

$$\begin{aligned} K &= \frac{1}{2}(1-\delta_{N,1})\sum_{k=1}^{N-1} V_1(\Delta r_{l,k})\sin^2\left(\frac{\pi k}{N}\right) \\ &+ \sum_{k=0}^{N-1}\sum_{l=1}^{\infty} V_1(\Delta r_{l,k})\sin^2\left(\frac{l\varphi}{2}+\frac{\pi k}{N}\right), \end{aligned} \tag{12}$$

where

$$\begin{aligned} V_1(r) &= \frac{1}{r^3}\Big[(1-Dr)^3(1+3Dr)\frac{1}{2}\left(1+\frac{1-Dr}{|1-Dr|}\right) \\ &- \alpha + \beta(\cos(\gamma r) + \gamma r\sin(\gamma r))\Big]. \end{aligned}$$

This is why, in contrast to molecular dynamics simulations, in which the equilibrium values of the variables (u, φ) were calculated from the preset values of K, it is now expedient to carry out simulations in exactly the opposite way, i.e., to calculate the external parameter K from formula (12) with the preset equilibrium values of (u, φ).

As was noted above, the intergrain interaction potentials can be not only repulsive but also attractive; therefore, we can also obtain equilibrium structures for negative K values.

If, under radial force balance condition (8a) and under condition (11) for the existence of an extremum, the equilibrium values of (u, φ) are possible for which $K \le 0$, then self-confining structures are possible too. The value $K = 0$ indicates that a structure can be in equilibrium in the absence of any external potential, so a self-confining helical structure also can exist.

The stability condition for a configuration is the condition for its energy to be minimal. Accordingly, for a two-parameter equation, the minimum-energy conditions have the form

$$\begin{aligned} E_{\varphi\varphi}E_{uu} - E_{u\varphi}E_{\varphi u} \equiv K'(u,\varphi) > 0, \\ E_{\varphi\varphi} \equiv F'(u,\varphi) > 0, \end{aligned} \tag{13}$$

where

$$\begin{aligned} F'(u,\varphi) &= \sum_{k=0}^{N-1}\sum_{l=1}^{\infty} -\frac{1}{2}V_1(\Delta r_{l,k})u^2 l^2 \\ &\times\left[1-\sin^2\left(\frac{l\varphi}{2}+\frac{\pi k}{N}\right)\right] \\ &+ \frac{1}{2}V_2(\Delta r_{l,k})\left[u^2 l\sin\left(\frac{l\varphi}{2}+\frac{\pi k}{N}\right)\cos\left(\frac{l\varphi}{2}+\frac{\pi k}{N}\right)\right]^2, \\ V_2(r) &= \frac{3}{r^5}\Big[(1-Dr)^2(1+2Dr+D^2r^2) \\ &\times\frac{1}{2}\left(1+\frac{1-Dr}{|1-Dr|}\right) \\ &- \alpha + \beta((3-\gamma^2r^2)\cos(\gamma r) + 3\gamma r\sin(\gamma r))\Big]. \end{aligned} \tag{14}$$

This finally yields

$$\begin{aligned} K'(u,\varphi) &= F'(u,\varphi)\Big[-2K(u,\varphi) \\ &+ (1-\delta_{N,1})u^2\sum_{k=1}^{N-1} V_2(\Delta r_{0,k})\sin^4\left(\frac{\pi k}{N}\right) \\ &+ 2u^2\sum_{k=0}^{N-1}\sum_{l=1}^{\infty} V_2(\Delta r_{l,k})\sin^4\left(\frac{l\varphi}{2}+\frac{\pi k}{N}\right)\Big] \\ &+ \Big[\sum_{k=0}^{N-1}\sum_{l=1}^{\infty}[2V_1(\Delta r_{l,k}) \end{aligned} \tag{15}$$

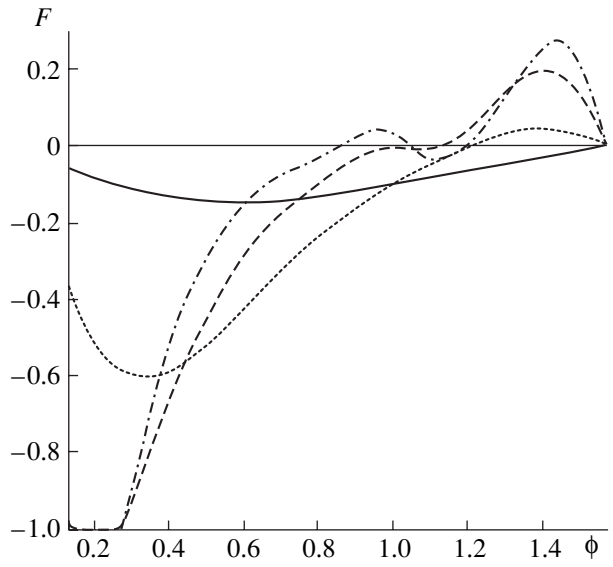

Fig. 6. Onset of bifurcations in an $N = 2$ helix in the case of a nonlinear screened potential for $D = 0.1$ and $\alpha = \beta = 0$.

$$- V_2(\Delta r_{l,k})u^2 \sin^2\left(\frac{l\varphi}{2} + \frac{\pi k}{N}\right)\Bigg]$$

$$\times lu \sin\left(\frac{l\varphi}{2} + \frac{\pi k}{N}\right)\cos\left(\frac{l\varphi}{2} + \frac{\pi k}{N}\right)\Bigg]^2.$$

We thus have determined the minimum of the Madelung energy.

5. NUMERICAL SIMULATIONS OF EQUILIBRIUM HELICAL STRUCTURES

A decrease in the external confinement constant is accompanied by bifurcations of the phase diagrams in the (u, φ) plane.

A typical dependence of φ on $u = 2R/z_0$ for an $N = 1$ helix is shown in Fig. 4. The numerals by the curves label different branches of the equilibrium solutions describing an $N = 1$ helix, zigzag, helix1, helix2, helix3, etc. As the external confinement parameter K decreases, a pair of new equilibrium states appear, one of which (as well as the corresponding branch of the solutions) is unstable (dashed curves) and the other is stable (solid curves).

In order to provide a complete graphic description of the grain system, it is convenient to plot these bifurcation curves and the family of the characteristic curves of equilibrium equation (8a) in the same figure. The resulting plot can thus be scaled by the value of the external confinement parameter of the system. In the case under consideration, the equilibrium condition has the form (hereafter, we use dimensionless variables)

$$K = \sum_{l=1}^{\infty}\Bigg[\frac{\exp(-D\Delta r) - \alpha + \beta\cos(\gamma\Delta r)}{\Delta r}$$

$$+ D\exp(-D\Delta r) + \gamma\beta\sin(\gamma\Delta r)\Bigg]\frac{\sin^2(l\varphi/2)}{(\Delta r)^2}.$$

This condition clearly demonstrates the great difference between different types of interaction potentials with different values of D, α, and β. We see that there are several regions in which the external confinement parameter K has different signs. Accordingly, there are K values at which the grains can evolve to a stable structure in the absence of an external confining potential (Fig. 4, dotted curve).

Figure 5, which illustrates an $N = 2$ helix, also shows several values of the external parameter K at which a stable equilibrium structure can arise in the absence of any external confining potential. (It can be seen from Fig. 8 that the parameters of the helix at which this configuration is possible depend strongly on the type of the interaction potential.) However, the question of the stability of such structures remains open and requires a separate consideration.

5.1. Dynamics of the Onset of Bifurcations

The results of computer simulations show that, for the same value of the external parameter K, several equilibrium conditions can be satisfied (see, e.g., Figs. 4, 5). The smaller the external parameter, the larger the radius of the helix and the larger the number of possible equilibrium conditions. At the same time, the larger the number N of interwoven helices, the smaller the value of the external parameter K at which bifurcations occur.

It is likely that the grain system will "try" to evolve to a configuration that is most favorable from the energy standpoint, but whether or not this will occur depends, of course, on the initial grain distribution and other parameters of the system. This will inevitably happen, however, in the presence of dissipation.

Taking now an $N = 2$ helix as an example, we analyze the onset of bifurcations in more detail and illustrate the difference between the nonlinear screening and the Debye screening (see Fig. 6).

According to the above estimates, we set the nonlinear screening factor D to be ten times smaller than the Yukawa screening factor D_Y. Figure 6 shows the evolution of the function $F(\varphi)$ for different values of u in the case of grains that interact through a nonlinear screened potential with $D = 0.1$ and experience no attraction ($\alpha = \beta = 0$).

Until $u = 2.8$ (i.e., along the solid curve), the function $F(\varphi)$ is always negative and has two equilibrium points ($u = 0$; $\varphi = \pi/2$) and ($u = 0$, $\varphi = 0$), of which the latter is unstable because the derivative of the function

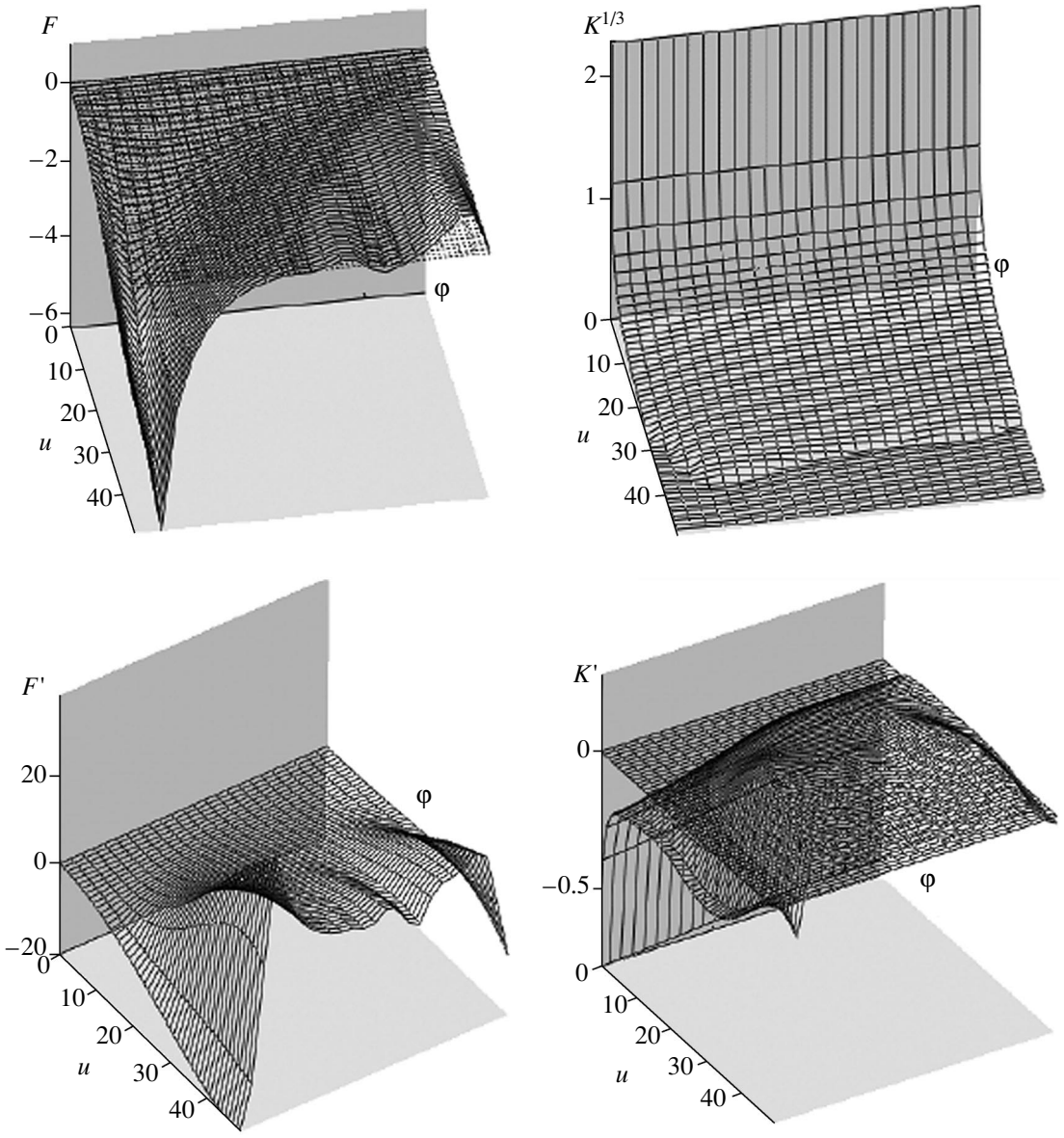

Fig. 7. Reliefs of the functions F, F', $K^{1/3}$, and K' for an $N = 2$ helix in the case of nonlinear screening ($D = 0.1$), weak noncollective attraction ($\alpha = 0.01$), and strong collective interactions ($\beta = 0.5$, $\gamma = 0.2$).

with respect to φ is negative there. The only stable value of φ is π/2. For $u > 2.8$, the function along a small portion of the curve near φ/2 becomes positive. As u increases further, this portion of the curve (along which the function F is positive) rises upward and extends, the curve itself intersects the abscissa at two points, indicating a bifurcation, and the second point of intersection shifts toward the smaller φ values. It can be seen that, as u increases to the value $u = 8.8$ (the dotted curve), the second point of intersection is stable and the intersection point at $\varphi = \pi/2$ is unstable. The curve becomes straighter and, at $u = 12$ (the dashed curve), it is seen to have an additional intersection with the abscissa. The next maximum can be seen at the dashed-and-dotted curve, which refers to $u = 16$ and describes well a bifurcation characterized by two new branches, one being stable and the other unstable. It should be noted that the bifurcation points $u = 2.8$ and 12, which were obtained for the nonlinear screening, differ somewhat from those obtained for the Debye screening, namely, $u = 6$ and 12.5 (Fig. 5).

We thus see that the nonlinear screening and the Debye (Yukawa) screening differ not only quantitatively but also qualitatively. Moreover, this difference increases substantially for stronger noncollective attraction and/or collective interaction.

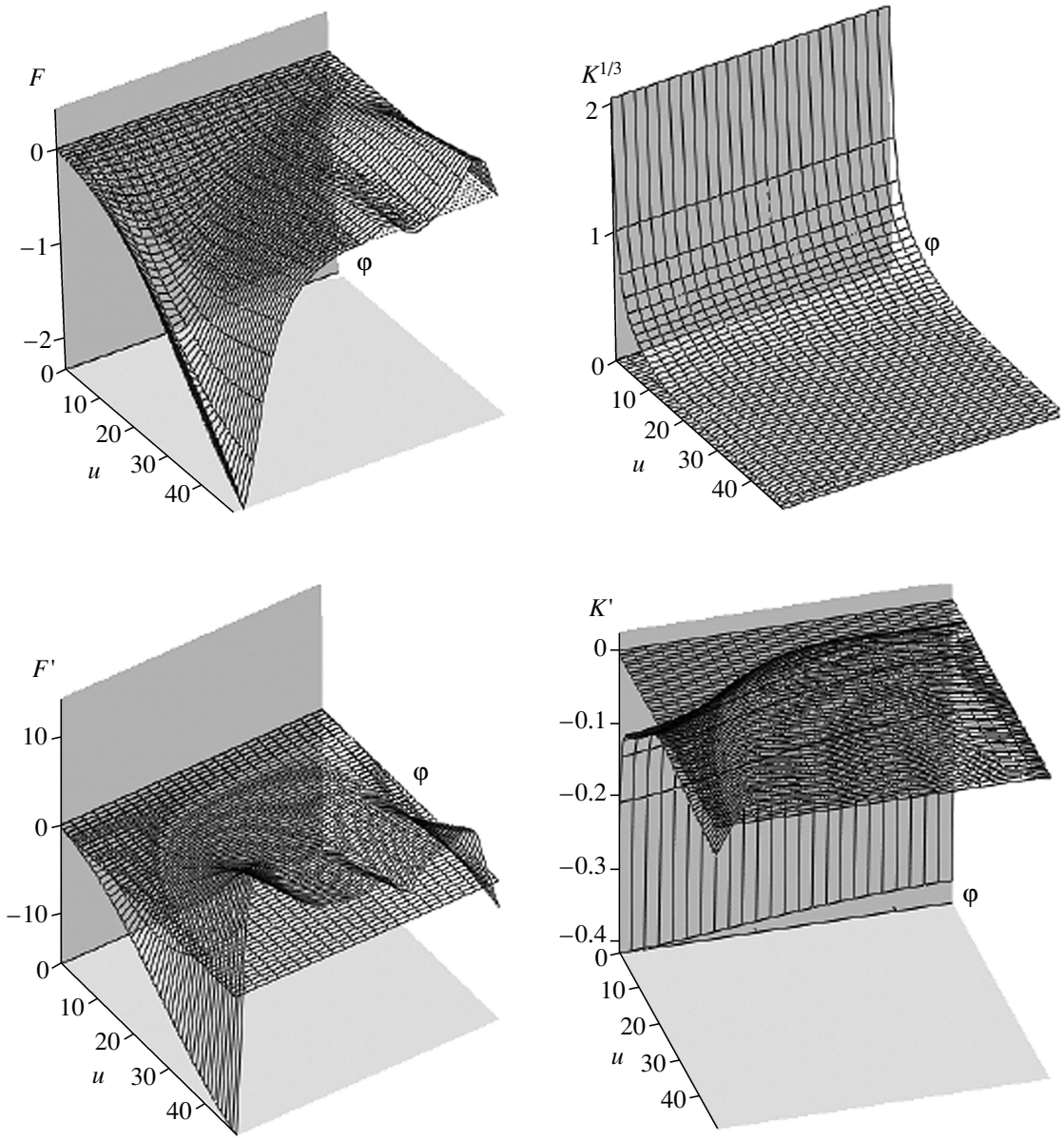

Fig. 8. Reliefs of the functions F, F', $K^{1/3}$, and K' for an $N = 2$ helix in the case of nonlinear screening ($D = 0.1$), weak noncollective attraction ($\alpha = 0.01$), and weak collective interactions ($\beta = \gamma = 0.1$).

5.2. Linear String

Now, we analyze how a string bifurcates into a helix.

To do this, we consider an infinitely long chain of charged grains separated by the same distance z_0. In this case, Eqs. (7) has the solution

$$\mathbf{r}_n = (0, 0, z_n) = (0, 0, z_0 n).$$

In Fig. 6, our analysis begins immediately with a zigzag—a particular case of a helical structure in which two grains in the neighboring (x, y) planes are turned relative to one another through the angle $\varphi = \pi$.

We see that a linear chain bifurcates into a zigzag in the same manner as was described above. The bifurcation occurs when the energy per grain in a linear chain becomes equal to that in a zigzag:

$$E_{\text{zigzag}} - E_{\text{string}} = 0.$$

From this we can obtain the instability criterion, i.e., the value of the external parameter K at which the linear chain becomes unstable:

$$K = \sum_{k}^{\infty}\left[\frac{\exp(-D(2k+1)) - \alpha + \beta\cos(\gamma(2k+1))}{u^2(2k+1)}\right.$$
$$\left. - \frac{\exp(-D\sqrt{(2k+1)^2+u^2}) - \alpha + \beta\cos(\gamma\sqrt{(2k+1)^2+u^2})}{u^2\sqrt{(2k+1)^2+u^2}}\right]. \quad (16)$$

For particular values of D, α, β, and γ, it is an easy matter to compare this K value with that found from an analytic formula in accordance with [31].

5.3. Zigzag

A zigzag is seen to bifurcate into a helix of general form in the same way as in the case of purely Coulombic interaction. The minimum point of the potential energy, given by the conditions $E_{\varphi\varphi}E_{uu} - E_{u\varphi}E_{\varphi u} > 0$ and $E_{\varphi\varphi} > 0$, becomes the inflection point, $E_{\varphi\varphi}E_{uu} - E_{u\varphi}E_{\varphi u} < 0$. Applying the last formula to each particular type of interaction, we can then find the values of u and, consequently, the values of the external parameter K', at which a bifurcation occurs [31].

We can see that an evolving $N = 1$ helix actually loses its stability only when it undergoes a Y-type bifurcation, namely, a zigzag $\longrightarrow$ helix1 bifurcation. In this case, the solution $\varphi = \pi$ becomes unstable and splits into two symmetric stable branches.

As for transitions like helix1 $\longrightarrow$ helix3, they are nothing more than discontinuous transitions of the system from one stable state to another, provided that the latter is more favorable energetically. In other words, the system tends to change to a configuration that possesses a minimum energy at a fixed value of the external confinement parameter. This process, however, depends on the initial grain distribution. It is often the case that configurations differ in energy by only small fractions of 1%; so, in actual experiments, there may be several (rather than one) different stable grain configurations.

This is why, for certain values of the external confinement parameter, our numerical simulations yielded different steady configurations of grains, depending on their initial distribution.

5.4. Structures formed of N Helices

Recall that, as the external confinement parameter K decreases, the formation of an $N = 1$ helix can be followed by the formation of $N = 2$, 3, etc., steady helical configurations.

Of course, structures formed of N helices possess the same regular features as $N = 1$ helices. For instance, for an $N = 2$ helical structure, the bifurcation process begins with a "limiting" tetrahedral configuration (an $N = 2$ helix with an angle φ equal to $\pi/2$), which then (at a certain value of the external parameter) changes into a structure with a larger number of interwoven helices (see Fig. 4).

Figures 7–10 show the calculated surfaces of the functions $F(u, \varphi)$, $K(u, \varphi)$, $F'(u, \varphi)$, and $K'(u, \varphi)$ for an $N = 2$ helix in the case of nonlinear screening ($D = 0.1$) with different combinations of weak and strong collective interactions and weak and strong noncollective attractions.

These figures also show the planes $F = 0$, $K = 0$, $F' = 0$, and $K' = 0$. The intersections of the surfaces of the functions with the planes have the following meaning. On one side of the intersection of the surface K with the plane $K = 0$, the confinement is provided by an external attractive potential ($K > 0$) and on the other side, by the repulsive one ($K < 0$). The intersection with the $F = 0$ plane is the equilibrium curve. Finally, the intersections with the $F' = K' = 0$ planes are the boundaries between the stable ($F' < 0$, $K' < 0$) and unstable ($F' > 0$, $K' > 0$) regions of the planes.

Numerical simulations were carried out for different types of interaction, i.e., for different values of the parameters D, α, β, and γ. For collective interaction ($\beta \neq 0$), the values of the structure diameter ($u = 2R/z_0$) and the angle φ that correspond to the minimum Madelung energy can differ substantially for different values of D, α, β, and γ, showing the onset of new bifurcations and new stable equilibrium states.

The curves in Fig. 11 represent the positions of extremes of energy for $\gamma = 0.5$ and different β values. Figure 12 illustrates how the branches of the solutions change as the parameter γ is varied, the values of D, α, and β being fixed. These figures, too, show the onset of new bifurcations and new stable equilibrium states.

They also show how the position of the energy minimum changes when the values of the parameters determining the type of interaction are varied.

The simplest possible structure into which an $N = 2$ helical configuration can bifurcate is an $N = 3$ helix. Similar structures were observed to form in experiments with ultracold atomic ions interacting by means of Coulomb repulsive forces [2]. More precisely, the structures observed in those experiments were a limiting case of an $N = 3$ helix—an octahedral configuration, in which the triangles formed by the grains in the neighboring (x, y) planes are turned relative to one another

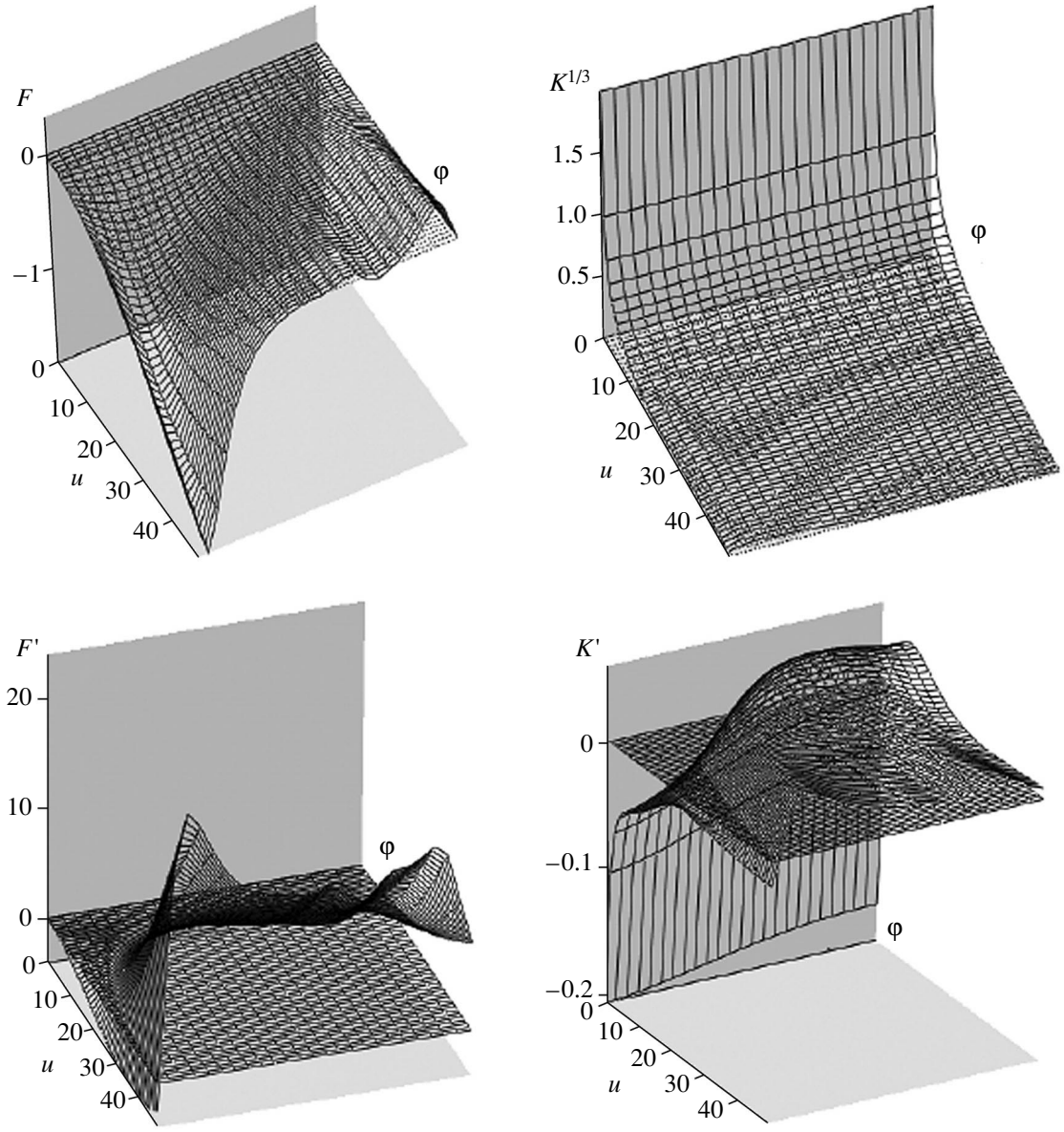

Fig. 9. Reliefs of the functions F, F', $K^{1/3}$, and K' for an $N = 2$ helix in the case of nonlinear screening ($D = 0.1$), strong noncollective attraction ($\alpha = 0.1$), and weak collective interactions ($\beta = \gamma = 0.1$).

through the angle $\varphi = \pi/3$. In this case, as in the cases of a linear string, a zigzag, and a tetrahedral configuration, it is also possible to obtain the values u_{crit} at which the octahedral configuration loses its stability.

The results of numerical simulations and the data from experiments with purely Coulomb systems show that there are only a few possible types of structures formed of several interwoven helices. The particles often form a two-shell structure that is energetically more favorable than a one-sell structure. In the planar case, this corresponds to a transition from five particles at the vertices of a regular pentagon to four particles at the vertices of a square and one particle at the center of the square. The situation with dust structures is, in a sense, similar, the only difference being that, along with $N = 2$ structures, structures with a larger number of interwoven helices can be energetically favorable. Most frequently, the results depend strongly on the type of screened potential and on the efficiency with which the grains are attracted to one another In the case of Yukawa screening, the final results differ radically from those in the case of nonlinear screening, especially when the screening parameters are close to certain critical values. These critical values, in turn, are determined by the number of grains per unit length of the

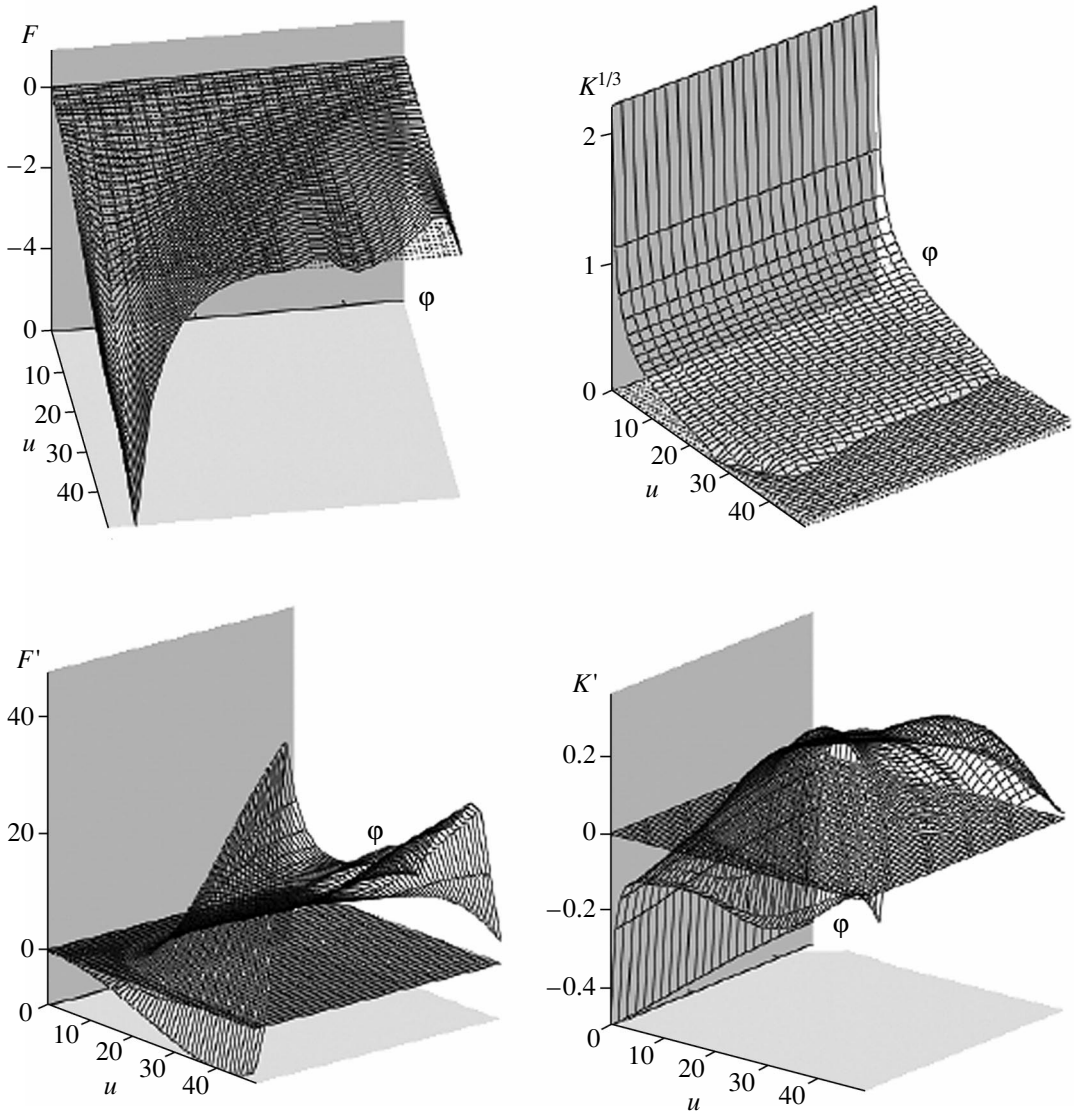

Fig. 10. Reliefs of the functions F, F', $K^{1/3}$, and K' for an $N = 2$ helix in the case of nonlinear screening ($D = 0.1$), strong noncollective attraction ($\alpha = 0.1$), and strong collective interactions ($\beta = 0.5$, $\gamma = 0.2$).

system and can easily be achieved in actual laboratory experiments, as well as under microgravity conditions.

5.5. Formation of the Second Shell

The formation of the second shell begins with the onset of a "degenerate" helical structure—a linear string at the axis of an $N = 1$ helix.

As time elapses, the pitch of the string decreases and the chain can bifurcate into a configuration of two $N = 1$ helices, one being inside another. In numerical simulations, such a configuration was not observed, however. The external shell in the form of an $N = 1$ helix then evolves into a structure formed of several interwoven helices, or, more precisely, into an $N = 6$ helix, containing within itself a linear string. As the external parameter is further changed, two nested shells form, followed by the formation of a linear string inside them, and later by the formation of three nested shells, and so on. We thus can again draw an analogy with the planar case: as the external parameter is changed, a particle appears at the center of the ring, inside which the second ring then forms, followed by the appearance of a particle at its center, and later by the formation of the third ring inside it, and so on.

We are interested here in the formation of the second shell merely in order to determine the parameter range corresponding to one-shell structures.

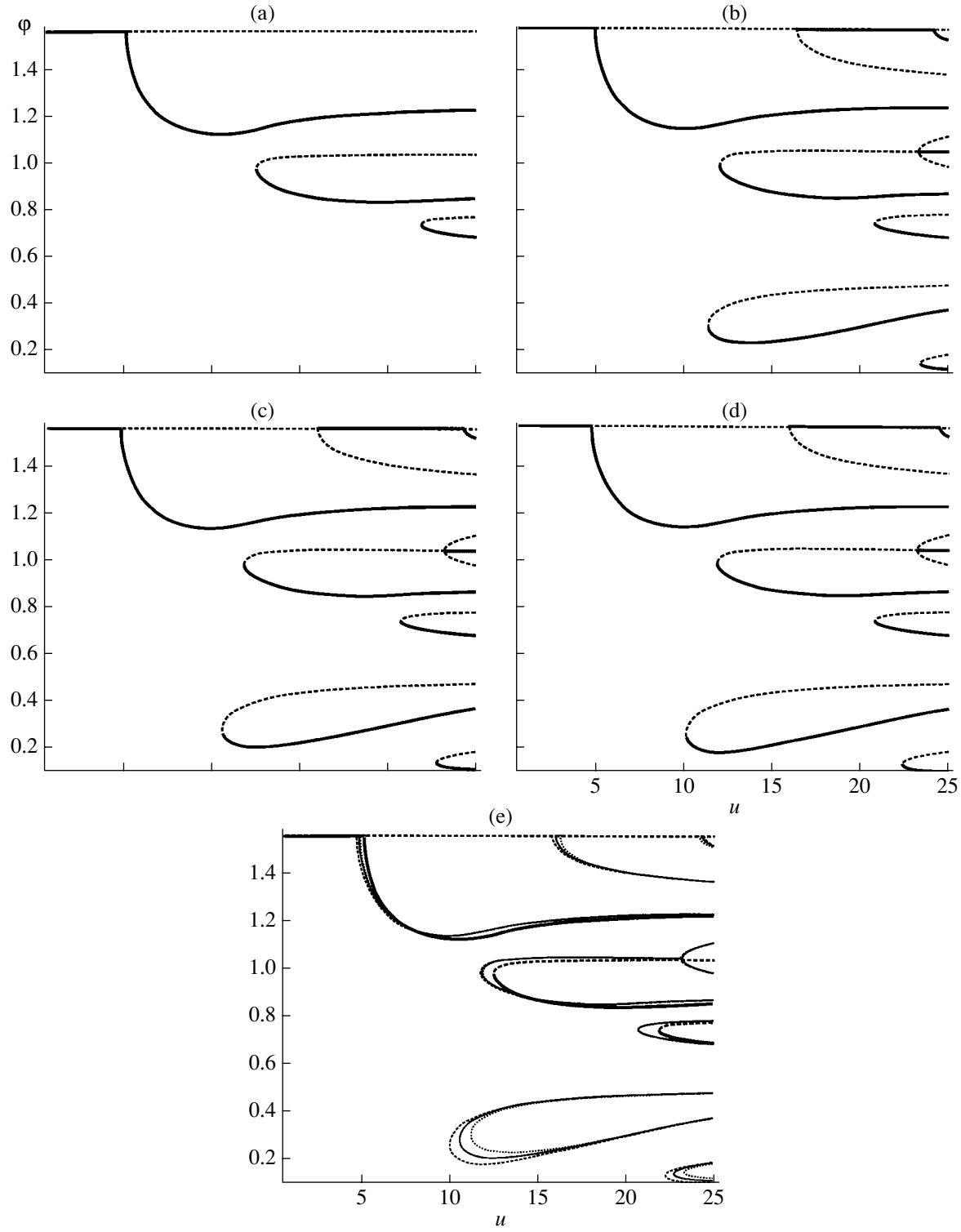

Fig. 11. Positions of extremes of the energy of an $N = 2$ helix and the boundary of the self-confinement region ($K = 0$) in the plane (φ, u) in the case of collective interactions for $D = 1$, $\alpha = 0$, $\gamma = 0.5$, and different β values: β = (a) 0, (b) 0.2, (c) 0.4, and (d) 1.0. Plot (e) summarizes all the curves shown in plots (a)–(d).

5.6. Comparison of Energies

It can be seen that, as the external confinement parameter is varied, a dust structure evolves through the following configurations: string ⟶ zigzag ⟶ helix1 ⟶ tetrahedral configuration, etc. Since the energies of some configurations differ by only a few percent, it is possible to experimentally observe stable

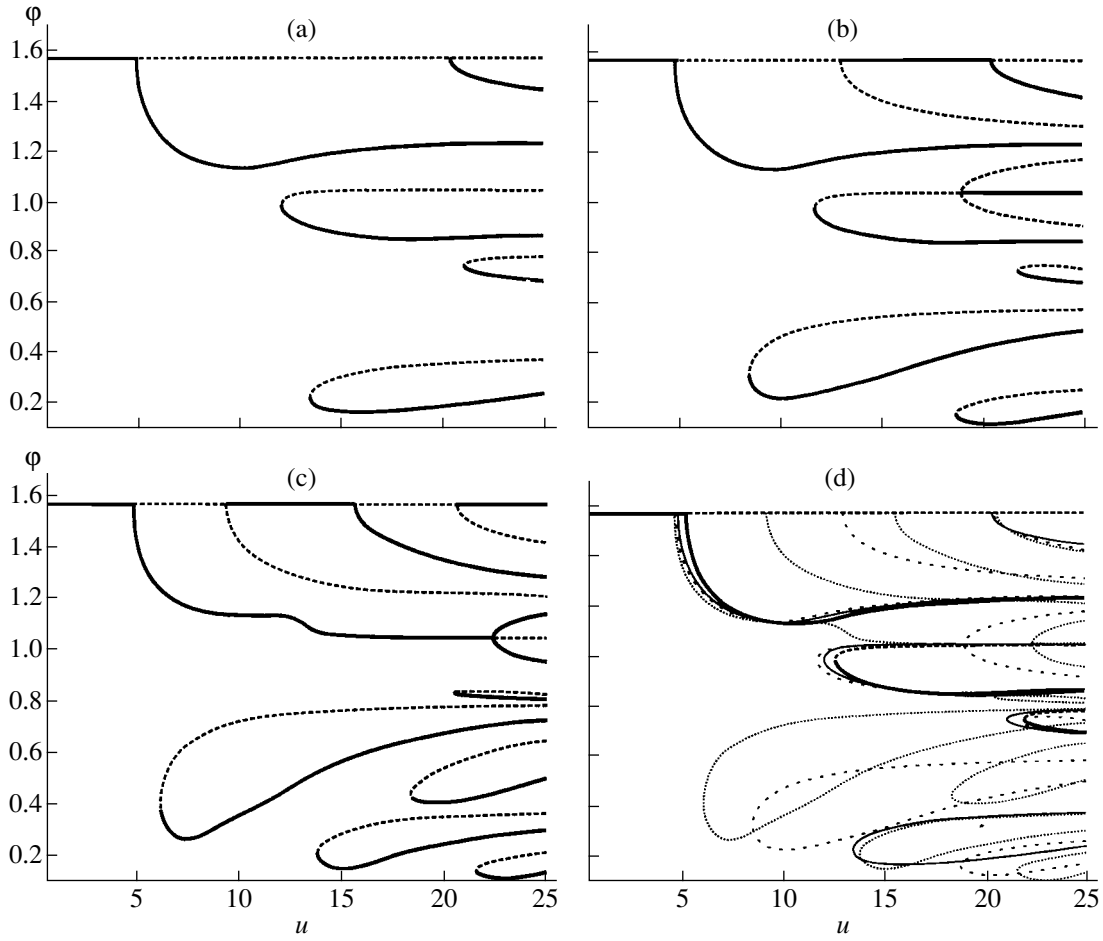

Fig. 12. Extremes of the energy of an $N = 2$ helix and the boundary of the self-confinement region ($K = 0$) in the plane (φ, u) in the case of collective interactions for $D = 1$, $\alpha = 0$, $\beta = 0.5$, and different γ values: γ = (a) 0.4, (b) 0.6, and (c) 0.8. Plot (d) compares all the cases of collective interaction illustrated in plots (a)–(c) to the case $\beta = 0$.

equilibrium configurations with energies slightly exceeding the minimum energy. This was indeed observed in numerical simulations: for the same value of the external parameter, they yielded different configurations, depending on the initial grain positions. Collective attraction is found to considerably complicate the bifurcational picture because it leads to many new "competing" equilibrium configurations with nearly the same energies.

On the whole, the results of numerical simulations agree well with our analytical estimates, which in turn are physically more transparent and explain all phase transitions from one configuration to another. We stress that, for different configurations, we are comparing the energies per grain, because the structures under analysis are infinitely long in the z direction and thereby have infinite total energies.

6. CONCLUSIONS

We have investigated typical equilibrium configurations of a system of correlated likely charged dust grains. We have derived stability criteria for several configurations (such as a string and a zigzag). When the external confinement parameter K is smoothly varied, the structure can make either a smooth or a discontinuous transition to a new state. Consequently, it may be said that, whereas transitions of a string into a zigzag and of a zigzag into an $N = 1$ helix are analogues of second-order phase transitions, transitions between different types of helical configurations resemble first-order phase transitions.

We have carried out a comparative analysis of the energies of each of the configurations under study. All analytical estimates are fully confirmed by the results of numerical simulations.

We have shown that finite-length systems should possess all of the regular features revealed in our investigations of infinite systems. We have described a scheme whereby instability should develop in its initial stage. With the results obtained for an infinitely long linear chain, it is possible to correctly estimate the values of the external confinement parameter at which the

configuration undergoes transitions from one state to another.

In actual systems, a suspended dust grain can gain kinetic energy in collisions with plasma ions and electrons. As a result, the grain begins to oscillate about its equilibrium position and can even escape from the potential well. Our results take on special meaning in this context. If the system has acquired sufficient energy, then it evolves into a new steady configuration with a minimum kinetic energy. If, however, the energy acquired by the system is insufficient for it to evolve into another steady configuration, then the grains in it begin to oscillate about their previous steady-state positions.

It is important to emphasize the general features that have been revealed in our numerical simulations:

(i) It was found that any random distribution of the grains evolves into one of the possible steady helical configurations. No final configurations other than helical ones were observed.

(ii) When the long-range interaction between the dust grains is attractive, they can form steady helical structures in the absence of an external confining potential and even in the presence of a parabolic repulsive potential.

(iii) In helical configurations, the dust grain distribution has a shell structure.

ACKNOWLEDGMENTS

This work was supported in part by the Russian Foundation for Basic Research, project no. 02-02-16439.

REFERENCES

1. N. G. Guseĭn-zade and V. N. Tsytovich, Fiz. Plazmy **31**, 432 (2005) [Plasma Phys. Rep. **31**, 392 (2005)].
2. J. J. Bolinger, D. J. Wineland, and D. H. E. Dubin, Phys. Plasmas **1**, 1403 (1994).
3. G. Birkl, S. Kassner, and H. Walther, Nature **357**, 310 (1992).
4. J. D. Prestage, G. J. Dick, and L. Maleki, J. Appl. Phys. **66**, 1013 (1989).
5. M. G. Raizen, J. M. Gilligan, J. C. Bergquist, *et al.*, Phys. Rev. A **45**, 6493 (1992).
6. S. L. Gilbert, J. J. Bollinger, and D. J. Wineland, Phys. Rev. Lett. **60**, 2022 (1988).
7. N. A. Clark, A. J. Hurd, and B. J. Ackerson, Nature **281**, 57 (1979).
8. S. Neser, T. Palberg, C. Blechinger, and P. Leiderer, Prog. Colloid. Polim. Sci. **104**, 194 (1997).
9. V. N. Tsytovich, Usp. Fiz. Nauk **167**, 57 (1997) [Phys. Usp. **40**, 53 (1997)].
10. A. P. Nefedov, O. F. Petrov, and V. E. Fortov, Usp. Fiz. Nauk **167**, 1215 (1997) [Phys. Usp. **40**, 1163 (1997)].
11. H. Thomas, G. E. Morfill, and V. N. Tsytovich, Fiz. Plazmy **29**, 963 (2003) [Plasma Phys. Rep. **29**, 895 (2003)].
12. V. Schweigert and F. Peters, Phys. Rev. B **51**, 7700 (1995).
13. H. Thomas, U. Konopka, G. Morfill, *et al.*, Phys. Rev. Lett. (2005) (in press).
14. N. Sato, G. Ushida, R. Ozaki, *et al.*, in *Proceedings of the 2nd International Conference on Physics of Dusty Plasmas, Hakone, 1999* (Elsevier, Amsterdam, 2000), p. 329.
15. G. E. Morfill and V. N. Tsytovich, Fiz. Plazmy **26**, 727 (2000) [Plasma Phys. Rep. **26**, 682 (2000)].
16. V. N. Tsytovich, Fiz. Plazmy **26**, 712 (2005) [Plasma Phys. Rep. **26**, 668 (2005)].
17. V. N. Tsytovich, Phys. Scr. **89**, 89 (2001).
18. J. Goree, G. E. Morfill, V. N. Tsytovich, and S. V. Vladimirov, Phys. Rev. E **59**, 7055 (1999).
19. V. N. Tsytovich, S. V. Vladimirov, G. E. Morfill, and J. Gorre, Phys. Rev. E **63**, 056609 (2001).
20. G. E. Morfill and V. N. Tsytovich, Phys. Plasmas **9**, 235 (2002).
21. V. N. Tsytovich, Fiz. Plazmy **31**, 157 (2005) [Plasma Phys. Rep. **31**, 133 (2005)].
22. V. N. Tsytovich, Pis'ma Zh. Éksp. Teor. Fiz. **78**, 1283 (2003) [JETP Lett. **78**, 763 (2003)].
23. Ya. Khodataev, R. Bingkham, V. Tarakanov, and V. Tsytovich, Fiz. Plazmy **22**, 1028 (1996) [Plasma Phys. Rep. **22**, 932 (1996)].
24. V. N. Tsytovich, Ya. K. Khodataev, and R. Bingham, Comm. Plasma Phys. Controlled Fusion **17**, 249 (1996).
25. A. M. Ignatov, Kratk. Soobshch. Fiz., No. 58, 1 (1995).
26. Ya. K. Khodataev, G. E. Morfill, and V. N. Tsytovich, J. Plasma Phys. **65**, 257 (2001).
27. M. Lampe, G. Joyce, and G. Ganguli, Phys. Scr. **T89**, 106 (2001).
28. M. Lampe, V. Gavrishchaka, G. Ganguli, and G. Joyce, Phys. Rev. Lett. **86**, 5278 (2001).
29. V. N. Tsytovich and G. E. Morfill, Fiz. Plazmy **28**, 195 (2002) [Plasma Phys. Rep. **28**, 171 (2002)].
30. G. E. Morfill, V. N. Tsytovich, and H. Thomas, Fiz. Plazmy **29**, 3 (2003) [Plasma Phys. Rep. **29**, 1 (2003)].
31. N. G. Guseĭn-zade and A. M. Ignatov, Kratk. Soobshch. Fiz., No. 11, 13 (2002).
32. N. G. Guseĭn-zade and A. M. Ignatov, Fiz. Plazmy **29**, 521 (2003) [Plasma Phys. Rep. **29**, 485 (2003)].

Translated by I.A. Kalabalyk

Plasma Physics Reports, Vol. 31, No. 10, 2005, pp. 843–854. Translated from Fizika Plazmy, Vol. 31, No. 10, 2005, pp. 909–922.

PLASMA DYNAMICS

Formation of a Micropinch and Generation of Multiply Charged Ions at the Front of a Current-Carrying Plasma Jet

E. A. Zverev[2], V. I. Krasov[1], I. A. Krinberg[1], and V. L. Papernyĭ[1]

[1] *Irkutsk State University, Irkutsk, 664003 Russia*

[2] *Institute of Solar–Terrestrial Physics, Siberian Division, Russian Academy of Sciences, Irkutsk, 664033 Russia*

Received August 18, 2004; in final form, December 2, 2004

Abstract—The formation of a neck in the cathode plasma jet in the initial stage of a low-voltage vacuum spark is investigated experimentally and theoretically. X-ray bursts corresponding to an electron temperature of 150–300 eV are detected. With the use of a pinhole camera, it is found that an emitting region less than 1 mm in size is located near the cathode. The free expansion of a current-carrying cathode plasma jet with a current growing in accordance with the experimentally observed time dependence is simulated using a hydrodynamic model. It is shown that the neck forms at the front of the plasma jet due to the plasma compression by the magnetic self-field. In the constriction region, the plasma is rapidly heated and multiply charged ions are generated. The calculated spatial and temporal variations in the electron temperature and average ion charge are close to the measured dependences over a wide range of the discharge parameters. © *2005 Pleiades Publishing, Inc.*

1. INTRODUCTION

It is well known that high-current vacuum sparks, in which plasma is produced due to electrode erosion, are sources of the characteristic X-ray emission from multiply charged ions (see, e.g., [1, 2]). According to the current notion, these ions are generated in micron-size regions of a high-temperature plasma with an electron temperature of up to several kiloelectronvolts [3, 4]. The formation of such regions is attributed to plasma pinching that occurs in the plasma jet closing the interelectrode gap when the discharge current reaches its maximum. Under these conditions, micropinches form at a sufficiently high voltage (a few tens of kilovolts) and high current (about 100 kA) [3–5] and the plasma is produced from the erosion material of the anode [6].

However, the processes occurring in the initial stage of a pulsed vacuum discharge (vacuum breakdown), when the plasma has the form of a jet emerging from the cathode, are still poorly understood. This stage is characterized by the presence of a free boundary of the cathode plasma expanding into the interelectrode gap and the rapid growth of the discharge current, which leads to specific effects. It is in the initial stage that the beams of multiply charged ions of the cathode material were observed both in early experiments with high-voltage discharges (Al^{+6}, W^{+6} [7]) and in recent experiments with low-voltage discharges with currents of a few kiloamperes (Cu^{+19}, Ta^{+50} [8, 9]). The generation of multiply charged ions is presumably related to the formation of a neck at the front of the cathode plasma jet. The results of numerical simulations [10, 11] show that such a neck can develop when the discharge current rapidly increases to about 1 kA. It was found in recent experiments [12] that so-called "hot spots" emitting X radiation are generated at the front of the cathode plasma jet during a laser-induced vacuum discharge with a current of several amperes.

The objective of the present paper is to investigate (both theoretically and experimentally) conditions for the formation of micropinch structures in a macroscopic cathode plasma jet in the initial stage of a vacuum spark discharge. These investigations, which are certainly of general interest, are also important for applications, namely, a low-voltage vacuum spark can be used to create a simple and compact source of soft X-ray emission and multiply charged metal ions.

To solve the problem, we use not only the results of recent X-ray measurements, but also of our previous studies of the ion component of the discharge plasma. The experimental data are compared to the results of simulations of a current-carrying plasma jet by an MHD model. In contrast to our preliminary simulations [10, 11], the parameters of the model are chosen to be close to the experimental conditions.

Most of the available MHD models apply to fast Z-pinches with a characteristic current of $I \approx 10^5$–10^6 A and current growth rate of $dI/dt \approx 10^{11}$–10^{13} A/s [13–15]. As regards a vacuum spark, the final stage of a micropinch was studied in [3] under the assumption that there was radial equilibrium between the plasma pressure and magnetic pressure and that the constriction region was cylindrical in shape.

Our model deals with moderate discharge parameters: $I \approx 10^3$–10^4 A and $dI/dt \approx 10^9$–10^{10} A/s. The model differs substantially from the previous ones in some respects concerning the specific features of the experiments to be described. In particular, the model considers a plasma jet that emerges from the cathode and

1063-780X/05/3110-0843$26.00

expands into a vacuum, the jet current growing with time, and a fresh plasma being continuously supplied into the jet channel from the cathode surface. We do not assume a priori that there is equilibrium between the plasma pressure and magnetic pressure, and the shape and localization of the neck are governed by the discharge parameters and are calculated self-consistently.

2. EXPERIMENTAL

The experiments with a low-inductance vacuum spark were performed at a storage voltage U of up to 2.5 kV. The electrode system consisted of a conical copper cathode1 mm in diameter and a plane grounded grid anode located at a distance of 9 mm from the cathode end. The electrode system was placed in a chamber evacuated to a pressure on the order of $(5–8) \times 10^{-6}$ torr. A discharge at the cathode end was initiated by means of breakdown produced along the surface of a dielectric inserted between the cathode and the igniting electrode. The discharge current was maintained by a capacitor ($C = 2$ μF) and was measured by a Rogowski coil immediately in the cathode circuit. The total inductance of the discharge circuit was no higher than 40 nH. Before measurements, a series of 10^3 preliminary shots were produced in order to train the cathode surface; after training, the discharge parameters in different shots differed by no more than 20%. The waveform of the discharge current was a decaying sinusoid with a half-period of about 1.5 μs.

In our studies, we used two X-ray diagnostics. In both of them, microchannel plates (MCPs) were used as radiation detectors. The temporal and energy characteristics of X-ray emission from the discharge were measured with the help of a three-channel detector similar to that described in [16, 17]. The hardness of the X-ray spectrum was estimated using absorbing filters—polypropylene films of thickness 3.7, 7.4, and 11.1 μm installed in the first, second, and third channels, respectively. The films protected the detector from UV radiation and plasma particles but were transparent to X rays in a certain spectral range dependent on the film thickness. The geometry of measurements was such that only the cathode region of the discharge gap fell into the detector's field of view; this prevented the detector from the anode X-ray bremsstrahlung.

The second X-ray diagnostics used a pinhole chamber equipped with an MCP. The plasma jet was imaged onto the detector surface through a pinhole 0.4 mm in diameter. As in the first diagnostics, the anode region of the discharge did not fall into the detector's field of view. The spatial resolution of the pinhole camera at the surface of the plasma jet was 1 mm. A luminescent screen placed behind the MCP converted the electron flux into a visible image recorded by a digital camera. The detector operated in the integral mode; i.e., the signal was averaged over the discharge pulse. Both of the X-ray diagnostics are described in detail in [18, 19].

In addition to X-ray measurements, we also measured the ion energy distribution and the ion charge composition by the time-of-flight technique using a plane-capacitor-type electrostatic analyzer with an energy resolution of $\Delta E/E \approx 2 \times 10^{-2}$ and a time resolution of about 40 ns. An MCP was used as an ion detector. The MCP sensitivity to ions with different energies and charges was corrected using the data from [20]. The analyzer was installed behind both the grid anode and the drift gap and received the ions emitted from the cathode jet and moving along the discharge axis toward the anode. With the time-of-flight technique, the ratio μ/Z (where μ is the atomic mass and eZ is the ion charge number) could be determined for each ion species by analyzing the delay time of the corresponding signal from the detector.

3. MODEL OF A NONSTATIONARY PLASMA JET

3.1. Basic Equations

Without allowance for viscosity, the plasma motion is described by the following set of MHD equations [21]:

$$\frac{\partial \rho}{\partial t} + \nabla \cdot (\rho \mathbf{V}) = 0, \tag{1}$$

$$\frac{\partial (\rho \mathbf{V})}{\partial t} + \nabla \cdot (\rho \mathbf{V}\mathbf{V}) = -\nabla P + \frac{1}{c}\mathbf{j} + \mathbf{B}, \tag{2}$$

$$\frac{\mathbf{j}}{\sigma} = \mathbf{E} + \frac{1}{c}\mathbf{V} \times \mathbf{B} + \frac{1}{eN_e}\nabla P_e - \frac{1}{ceN_e}\mathbf{j} \times \mathbf{B}, \tag{3}$$

$$\nabla \cdot \mathbf{j} = 0, \tag{4}$$

$$\nabla \times \mathbf{B} = \frac{4\pi}{c}\mathbf{j}, \tag{5}$$

$$\nabla \cdot \mathbf{B} = 0. \tag{6}$$

where $\rho = mN_i$ and $P = P_e + P_i$ are the mass density and pressure of the plasma; N_e, N_i, T_e, T_i, P_e, P_i, $\mathbf{V}_e$, and $\mathbf{V}$ are the density, temperature (in energy units), pressure, and the electron and ion velocities, respectively; m is the ion mass; c is the speed of light; $\mathbf{E}$ and $\mathbf{B}$ are the electric and magnetic fields; $\mathbf{j} = eN_e(\mathbf{V} - \mathbf{V}_e)$ is the current density; $\sigma = k_\sigma T_e^{3/2}/Z$ is the plasma conductivity; and $Z = N_e/N_i$ is the average ion charge number.

Taking into account that, in the plasma emitted from the cathode spots, the inequality $T_e \gg T_i$ holds [22, 23] and that the Joule heat is released predominantly in the electron gas, we will use the cold-ion approximation, assuming $P = P_e$. In this case, in order to close set of Eqs. (1)–(6), it is sufficient to supplement it with the

electron heat balance equation. Without allowance for heat conduction, this equation has the form [21]

$$\frac{3}{2}\frac{\partial P_e}{\partial t} + \frac{3}{2}\nabla \cdot (P_e \mathbf{V}_e) + P_e \nabla \cdot \mathbf{V}_e = \frac{j^2}{\sigma} - Q \qquad (7)$$

Here, $Q = Q_{ei} + Q_{ex} + Q_{ion} + Q_{br}$ is the rate of the electron energy loss in collisions with ions, which is the sum of the loss in elastic collisions (Q_{ei}), losses for the excitation (Q_{ex}) and ionization (Q_{ion}) of ions, and bremsstrahlung loss (Q_{br}) [24]. The energy losses for the line and recombination radiation do not enter explicitly into the heat balance equation but only influence the values of Q_{ex} and Q_{ion}, because a fraction of the ion internal energy may again return to the electron gas via the deexcitation of electronic levels and via recombination [24].

In what follows, we use cylindrical coordinates r, φ, and z (the z axis being directed from the cathode to the anode) and assume that the plasma jet is axisymmetric. In this case, the vectors entering into the equations have the components $\mathbf{V} = (V_r, 0, V_z)$, $\mathbf{j} = (j_r, 0, j_z)$, and $\mathbf{B} = (0, B_\varphi, 0)$.

3.2. Quasi-One-Dimensional Approximation

To solve set of Eqs. (1)–(7), we used the profiling method [15], which allows one to reduce a two-dimensional problem to a one-dimensional one, i.e., to study the dependence of the plasma parameters on z and t only. This approach is physically justified if the length of the plasma jet is much larger than its diameter. As in [25] (where a stationary case was considered), we assume that the particle and current densities decrease to zero in a narrow transition region at the jet periphery, whereas, in the bulk of the jet, the parameters ρ, P, T, N, V_z, and j_z are constant. We will also use a similarity condition for the plasma and current channels, $\mathbf{V} \times \mathbf{j} = 0$ [26], assuming that the boundary of the current channel coincides with the jet boundary.

Under these assumptions, the two components of the current density can be expressed in terms of the current I and jet radius $R(z, t)$ using continuity equation (4) [25],

$$j_r(z) = j_z \frac{\partial R}{\partial z}\frac{r}{R}, \qquad (8)$$

$$j_z = -I/S, \qquad (9)$$

where $S = \pi R^2$ is the cross-sectional area of the jet. From Eq. (5), we then find

$$B_\varphi(r, z) = -B_R \frac{r}{R}, \qquad (10)$$

where $B_R = 2I/(cR)$ is the magnetic field at the jet boundary.

From Eq. (1), we also obtain a similar linear dependence on r for the radial velocity $V_r(r, z) = V_R r/R$, where $V_R(z, t)$ is the radial expansion velocity of the jet,

$$V_R = \frac{\partial R}{\partial t} + V_z \frac{\partial R}{\partial z}. \qquad (11)$$

Multiplying Eqs. (1) and (2), written in cylindrical coordinates, by $dS = 2\pi r dr$; integrating the product from 0 to ∞; and taking into account Eqs. (8)–(11), we obtain quasi-one-dimensional equations of conservation of mass and momentum,

$$\frac{\partial(\rho S)}{\partial t} + \frac{\partial}{\partial z}(\rho S V_z) = 0, \qquad (12)$$

$$\frac{\partial}{\partial t}(\rho S V_z) + \frac{\partial}{\partial z}(\rho S V_z^2) = -\frac{\partial(PS)}{\partial z} + \left(\frac{I}{c}\right)^2 \frac{\partial \ln R}{\partial z}, \qquad (13)$$

$$\frac{\partial}{\partial t}(\rho S V_R) + \frac{\partial}{\partial z}(\rho S V_R V_z) = \frac{3PS}{R} - \frac{2}{R}\left(\frac{I}{c}\right)^2, \qquad (14)$$

and the electron heat balance equation

$$\frac{\partial}{\partial t}\left(\frac{PS}{\rho^{2/3}}\right) + \frac{\partial}{\partial z}\left(\frac{PS}{\rho^{2/3}} V_z\right) = \frac{2I^2}{3\sigma S \rho^{2/3}}\left(1 + \frac{1}{2}\left(\frac{dR}{dz}\right)^2\right) - \frac{I}{e}\left(\frac{N_e}{\rho}\right)^{2/3} \frac{\partial}{\partial z}\left(\frac{T_e}{N_e^{2/3}}\right) - \frac{2QS}{3\rho^{2/3}}, \qquad (15)$$

where $P = P_e = T_e N_e$ and e is the elementary charge. In deriving Eq. (15), we used Eqs. (8), (9), and (12) and the relationship $\mathbf{V}_e = \mathbf{V} - \mathbf{j}/(eN_e)$.

Equation (13), which describes plasma motion along the jet, coincides with that from [15], whereas equation of radial motion (14) differs from the corresponding equation obtained in [15] by a numerical factor because of the different assumptions on the current density distributions over the jet cross section.

3.3. Account for the Ionization Effect

It is known [22] that, in vacuum discharges, the cathode surface emits a dense plasma propagating toward the anode at a velocity of $V_0 \approx (1–3) \times 10^6$ cm/s. Because of the high plasma density ($N_e \geq 10^{18}$–10^{19} cm^{-3}), the ion distribution over charge states approximately corresponds to a local thermodynamic equilibrium [27]. As the plasma expands into the interelectrode gap, its density rapidly decreases and the ionization–recombination balance becomes disturbed. At low currents ($I \leq 500$ A), the ion composition of the expanding plasma remains unchanged and corresponds to that in the cathode spot. At $I \geq 1$ kA, the ion charge can further increase; this process is governed by the rate of electron-impact ionization (i.e., by the electron temperature and density) and by the time during which the ions stay in the discharge gap, $\tau_i \approx L/V_0 \approx 1$ μs (where $L \approx 1$ cm is the gap length). In this case, the recombination pro-

cesses are of minor importance, because the recombination time is much longer than the ionization time, $\tau_R \gg \tau_i$. In [11, 28], it was shown that three-body recombination can be ignored at $N_e < 10^{18}$ cm^{-3} and $T_e \approx$ 10–100 eV. Estimation of the photorecombination time at the same plasma parameters yields $\tau_R \approx 1/(\alpha_R N_e) \geq$ 10 μs, where $\alpha_R \approx 10^{-12}/\sqrt{T_e}$ cm^{-3} s^{-1} (here, T_e is in eV [29]).

For this reason, the equations for the ionization balance can be written in the form [11, 28]

$$\frac{\partial f_n}{\partial t} + V\frac{\partial f_n}{\partial r} = k_n f_{n-1} N_e - k_{n+1} f_n N_e. \qquad (16)$$

Here, $f_n = N_n/N_i$ is the fraction of ions with the charge n and density N_n, and E_{n+1} and k_{n+1} are the ionization energy and the ionization coefficient for the generation of an ion with the charge $n + 1$. The average ion charge number is then defined as $Z = \sum_{n=1} n f_n$ or $Z = N_e/N_i$, where $N_i = \sum_{n=1} N_n$ is the total ion density. The values of coefficients $k_n(T_e)$ are given in [11, 28].

The rate of the electron energy loss for the ionization of ions is defined by the expression

$$Q_{\text{ion}} = N_e N_i \sum_{n=1} E_{n+1} k_{n+1} f_n. \qquad (17)$$

Below, in most of the calculations, we assume that $Q_{ei} = 0$, $Q_{\text{ex}} = 0$, and $Q_{\text{br}} = 0$; i.e., ionizing collisions with ions are considered to be a dominant mechanism for electron energy losses ($Q = Q_{\text{ion}}$). The validity of this assumption is discussed in Section 5.

3.4. Initial and Boundary Conditions

Equations (12)–(15), represented in a divergent form, were solved numerically by the particle-in-cell method [3]. To compare the results of numerical simulations with experimental data, the growth in the discharge current was described by the formula $I(t) = I_0 + I_a \sin(\pi t/\tau)$, where the current amplitude (I_a = 1–10 kA) and the half-period (τ = 1 μs) were taken to be close to their actual values. The initial spatial distributions of the plasma parameters (at $t = 0$) were calculated by the steady-state arc model [31] for a current of I_0 = 100 A. It was assumed that, at the initial instant, the plasma expanded from a cathode spot within a cone with a half-angle of $\alpha_0 \approx \pi/6$ and that the plasma front was almost spherical [31]. Thus, the presence of a low-density foreplasma in the discharge gap was roughly taken into account. This plasma was produced by the ignition current and provided the closing of the discharge current as the cathode jet propagated toward the anode. As boundary conditions for the plasma jet at $z = z_0$ (near the surface of the copper cathode), we used the velocity and the ion compositions measured in low-current arcs and approximately corresponding to the plasma parameters in the initial microjets: $V_0 = 1.3 \times 10^6$ cm/s [32], $f_1^0 =$ 0.11, $f_2^0 = 0.72$, and $f_3^0 = 0.17$, the average ion charge number being $Z_{i0} = 2.06$ [27]. The electron temperature was taken to be $T_{e0} \approx 1$ eV. It was assumed that the cross-sectional area $S_0 = \pi R_0^2$ of the plasma jet did not change over time. This agreed with the experimental data of [33], where it was shown that, in a short high-current pulse (I = 1–3 kA, $\tau \leq 1$ μs), the plasma was entirely emitted from a single macroscopic spot. For a copper cathode, the spot radius is equal to $R_0 \approx 0.15$ mm [34].

The mass flux through the cross-sectional area S_0 can be calculated by the formula $G_0(t) = \eta_0 mI(t)/(Z_{i0}e)$, where $\eta_0 \approx 0.1$ is the ratio between the ion and total currents through the cathode spot [22]. The boundary values of the mass plasma density and the electron density were then defined as $\rho_0(t) = \eta_0 mI(t)/(Z_{i0}eV_0S_0)$ and $N_{e0}(t) = Z_{i0}\rho_0/m$. Thus, in the initial part of the plasma jet, the charged particle density steadily increased with increasing current $I(t)$; this resulted in a nonuniform plasma distribution along the discharge gap.

4. FORMATION OF A MICROPINCH REGION

4.1. Formation of a Plasma Neck

Figure 1 shows the calculated distributions of the main plasma parameters along the jet axis. It can be seen that a neck forms in the jet (Fig. 1a). Due to magnetic compression, the longitudinal plasma velocity V_z near the left boundary of the neck decreases and then vanishes at a certain point at the jet axis (Fig. 1b). At this point, the plasma stops, and the neck breaks down into two fragments. After this instant, the computation was terminated.

As the cross-sectional area of the neck decreases, the plasma density and the electron temperature rapidly increase (Figs. 1c, 1d). This, in turn, leads to a substantial increase in the average ion charge (Fig. 1e). Hence, as in the classical Z-pinch, the development of a constriction in the expanding plasma jet results in the formation of a micropinch structure with a hot, highly ionized plasma.

It can also be seen from Figs. 1c–1e that, when the neck breaks down, the plasma parameters (the density, electron temperature, and average ion charge) reach their maximum values. Test calculations for the subsequent period of time showed that two fragments of the neck move in opposite directions and the plasma density and temperature in them slowly decrease. The dynamics of the micropinch formation is illustrated in more detail in Fig. 2. It can be seen that the decrease in the jet cross-sectional area and the accompanying substantial increase in the plasma density (by more than two orders of magnitude) occur relatively slowly, whereas the electron temperature and the ion charge increase over a much shorter time (about 5 ns).

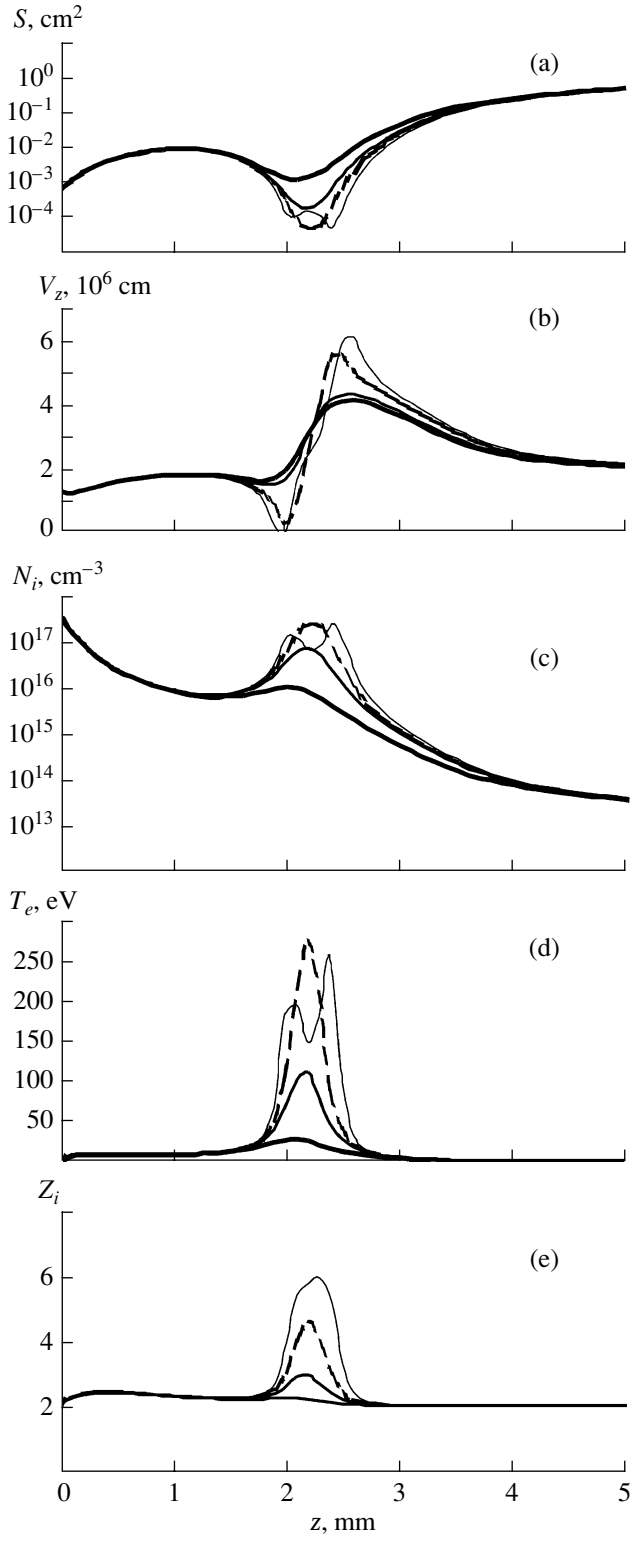

Fig. 1. Calculated distributions of the plasma parameters along the axis of the cathode jet for a discharge current amplitude of I_a = 3 kA: (a) jet cross-sectional area, (b) longitudinal plasma velocity, (c) ion density, (d) electron temperature, and (e) average ion charge number at the instants of 116 (heavy line), 119 (solid line), 120 (dashed line) and 121 (light line) ns from the beginning of the discharge.

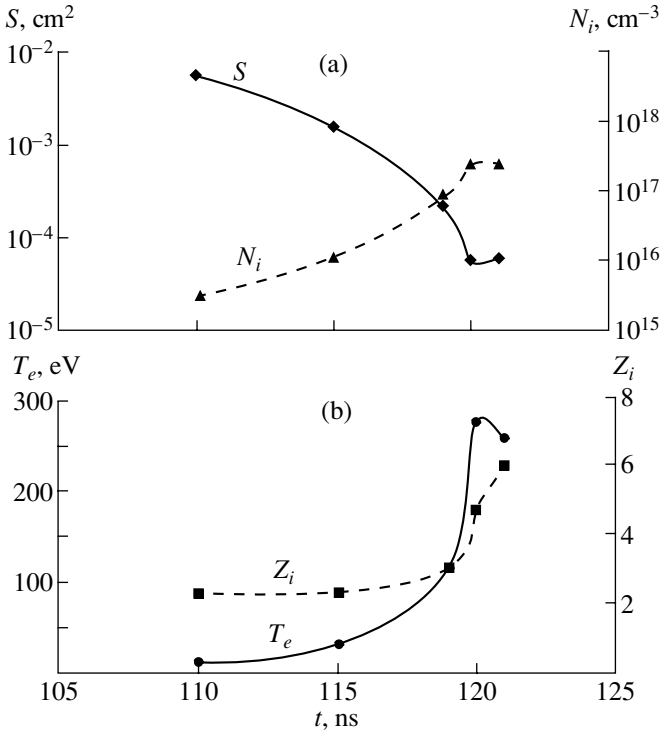

Fig. 2. Time dependence of (a) the cross-sectional area and ion density in the constriction region and (b) the electron temperature and average ion charge number.

Note that, the development of the constriction is accompanied by a sharp increase in the electric and hydrodynamic resistances of the jet. Since the dense cold cathode plasma is unmagnetized, this may provoke the formation of a new jet with its own current channel. Presumably, it is this effect that was responsible for the appearance of a peculiarity in the current derivative signal (see Fig. 4b) and spikes in the current waveform in experiments by Plyutto [7].

The results of calculations allowed us to investigate the development of a constriction in an expanding current-carrying plasma jet in more detail. Figure 3a shows the longitudinal profile of the ratio of the plasma pressure to the pressure of the magnetic self-field, $\beta = 8\pi P/B_R^2 = 2c^2PS/I^2$, at different times. It can be seen that, at the initial instant, when the plasma current is 100 A, the plasma pressure is everywhere higher than the magnetic pressure ($\beta > 1$), so the influence of the magnetic self-field on the plasma flow can be ignored. Because of the rapid current growth, the system passes through the equilibrium state with $\beta = 1$, and, 20 ns later, the magnetic pressure exceeds the plasma pressure over the entire jet. This causes plasma compression toward the axis by the magnetic self-field. However, different regions of the jet move toward the axis with different accelerations, which, according to Eq. (14), are approximately equal to $dV_R/dt \approx I^2/(\rho c^2 R^3)$. Near the cathode, the acceleration is small

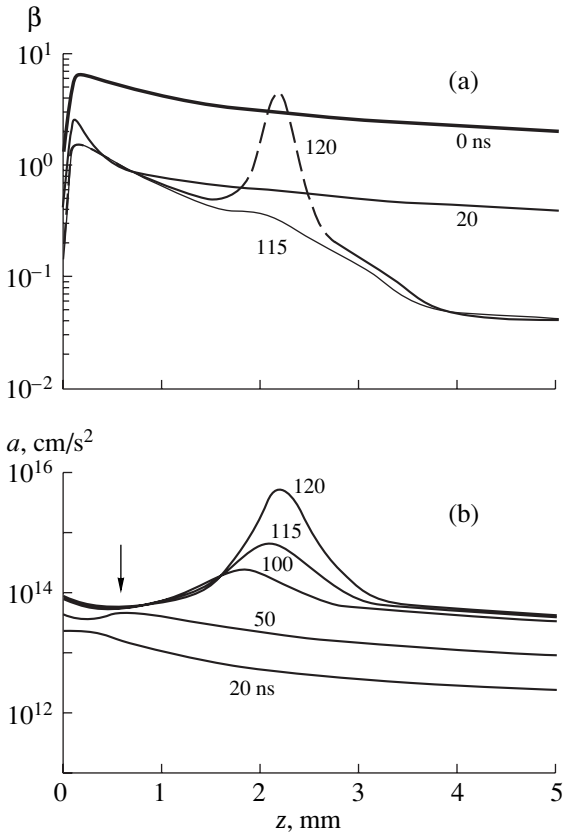

Fig. 3. Longitudinal profile of (a) the ratio of the plasma pressure to the magnetic pressure $\beta = 8\pi P/B_R^2 = 2c^2PS/I^2$ and (b) the radial acceleration of the cylindrical boundary of the plasma jet $a = dV_R/dt$ at different instants for a discharge current amplitude of 3 kA. The arrow indicates the point at which the neck starts to develop.

because of the high mass density ρ of the plasma arriving from the cathode surface, and it is also small at large distances because of the low gradient of the magnetic field, $\nabla B^2 \propto I^2/R^3$. Hence, in a certain cross section of the jet, the jet boundary moves toward the axis with the maximum acceleration. It is in this cross section that the constriction begins to form. This is illustrated in Fig. 3b, which shows the longitudinal profile of the transverse acceleration of the plasma boundary, dV_R/dt. It can be seen that the constriction begins to develop at a distance of about 0.7 mm from the cathode, where the transverse acceleration has a pronounced maximum as early as at $t = 50$ ns. This region is entrained by the plasma flow, and, as the neck radius decreases, the magnetic pressure force increases rapidly; as a result, the compression in the final stage occurs very rapidly. Figure 3a also shows that, during almost the entire phase of compression, the magnetic pressure exceeds the plasma pressure. Only in the final stage does the plasma pressure exceed the magnetic pressure ($\beta > 1$) in the region of maximum compression.

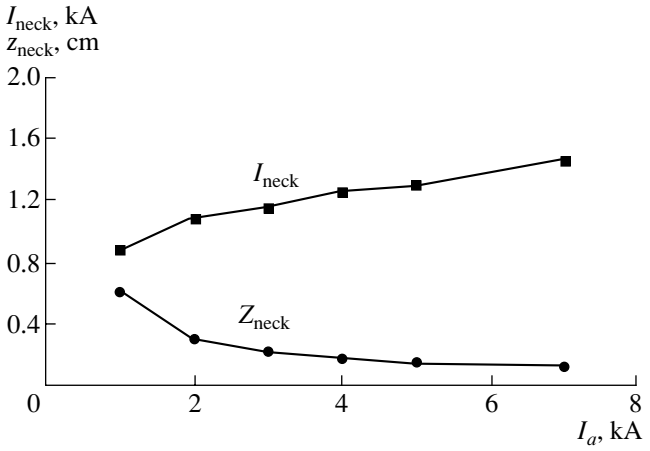

Fig. 4. Threshold current for the micropinch formation and the distance from the cathode to the micropinch as functions of the discharge current amplitude.

4.2. Spatial and Temporal Characteristics of the Micropinch

Important characteristics of the micropinch are the time t_{neck} (from the beginning of the discharge) and location z_{neck} (the distance from the cathode) of its formation. Calculations performed for different amplitudes of the discharge current show (see Fig. 4) that, as the current amplitude increases sevenfold, the threshold current at which the process of pinching begins, $I_{neck} \approx$ 1 kA, increases by only 50%. This means that the larger the discharge current amplitude (i.e., the larger the current growth rate at the same oscillation period), the shorter the time (with respect to the beginning of the current pulse) during which the micropinch forms. At large amplitudes, the micropinch forms well before the current reaches its maximum. Indeed, in the initial stage of the current pulse, we have $dI/dt \approx \pi I_a/\tau$, so the time during which the micropinch forms can be defined as $t_{neck} = I/(dI/dt) \approx I\tau/(\pi I_a)$. Estimates by this formula (with $\tau = 1$ μs) yield $t_{neck} \approx$ 40–300 ns and $z_{neck} \approx V_0 t_{neck} \approx$ 0.4–3 mm for amplitudes varying from 7 to 1 kA. It follows from this that the key factor governing the formation of a micropinch in the cathode jet is the growth rate of the discharge current (rather than its maximum value). This means that the formation of a micropinch in a plasma jet expanding into a vacuum differs substantially from the classical Z-pinch, in which this process is determined by the amplitude of the discharge current [1, 5].

Let us now compare the results of calculations to experimental data. Figure 5 shows the waveforms of the discharge current and its derivative, as well as signals from one of the channels of the X-ray detector for two amplitudes of the discharge current. It can be seen that X-ray signals are observed over a wide range of the current amplitudes; however, the parameters of the signals vary substantially as the current increases. At relatively

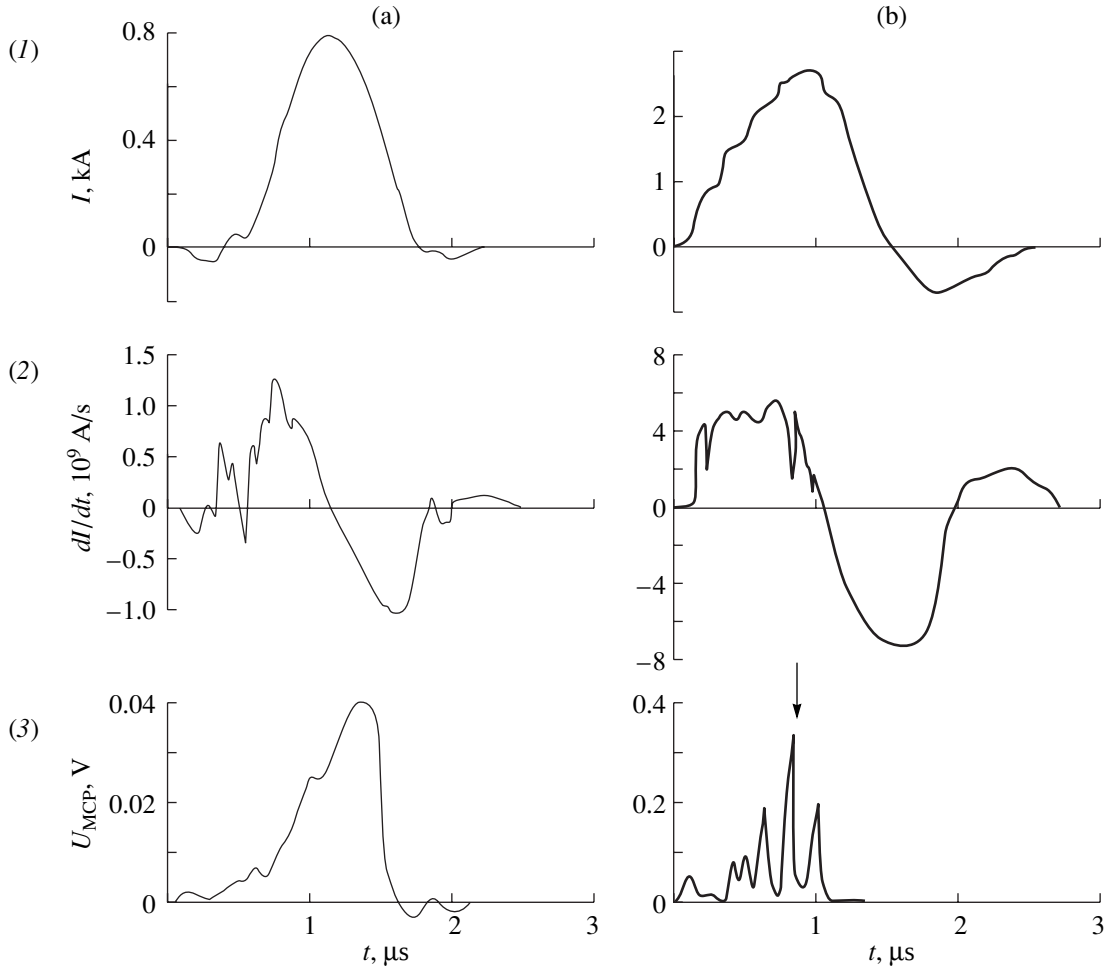

Fig. 5. Waveforms of (*1*) the discharge current, (*2*) the signal from the Rogowski coil, and (*3*) the signal from the X-ray detector for discharge current amplitudes of (a) 0.8 and (b) 3.0 kA. The arrow indicates the peak from which the electron temperature was estimated.

low currents (see Fig. 5a), the X-ray signal has the shape of a smooth small-amplitude peak with a microsecond duration and a gently sloping leading edge. The maximum of the signal lies behind the maximum of the discharge current. These data show that a hot plasma emitting X rays appears in the discharge gap at currents lower than 1 kA. Since the duration of the X-ray signal fairly coincides with that of the current pulse, we may suppose that the plasma jet emits as a whole. The low level of the signal does not allow us to estimate the plasma temperature but indicates that it is rather low.

As the discharge current amplitude increases to several kiloamperes, the character of the X-ray signal changes markedly. First, the signal appears as a sequence of bursts, the duration of individual busts δt being several tens of nanoseconds, which is much shorter than the rise time of the discharge current. This indicates the small size of the emitting region δz, which can be estimated by using the measured value of δt: $\delta z \approx V_0 \delta t < 0.1$ cm. It should be noted that X-ray bursts correlate with peculiarities in the waveform of the current derivative, whereas there are no peculiarities in the waveform of the current itself (see Fig. 5b).

Second, X-ray emission at large current amplitudes is observed in the initial stage of the discharge, before the current reaches its maximum value. We can estimate the distance z_1 between the cathode and the source of X-ray bursts at the time corresponding their maximum brightness. It can be seen from Fig. 4b that the brightness is maximum at $t_1 = 400$ ns after the beginning of the discharge current, so we find $z_1 \approx V_0 t_1 \approx 0.5$ cm, which is smaller than the length of the discharge gap but larger than the length δz of the X-ray generation region. Therefore, it may be supposed that X rays are emitted from the front of the cathode jet expanding into a vacuum. This estimate of z_1 agrees with calculations of the distance z_{neck} between the neck and the cathode (see Fig. 4).

To determine of the micropinch location, let us consider pinhole images shown in Fig. 6 for two values of the discharge current. It can be seen from Fig. 6a that,

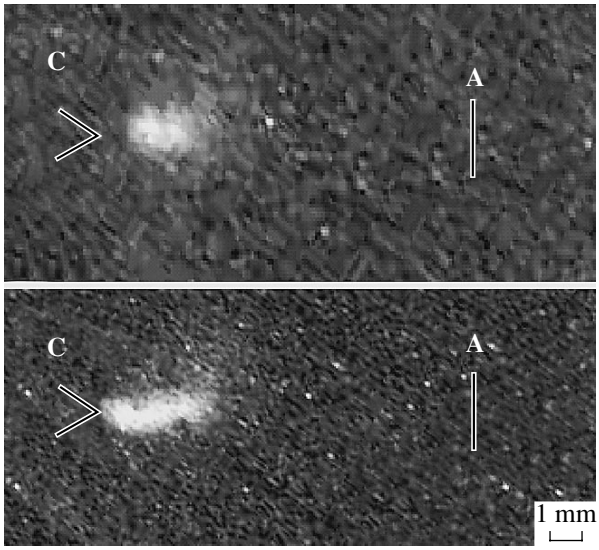

Fig. 6. X-ray pinhole images of a cold cathode jet for discharge current amplitudes of (a) 3 and (b) 10 kA: (C) cathode, (A) anode.

at a current of 3 kA, the emission source appears as a bright core less than 1 mm in size, which is located at a distance of 2–3 mm from the cathode. Taking into account that the pinhole resolution is also about 1 mm, we may suppose that the size of the hot plasma region emitting X rays is substantially smaller than this value. As the current amplitude increases to 10 kA, the parameters of the emission source change (Fig. 6b). First, the emitting region is somewhat displaced toward the cathode, which is consistent with calculations (Fig. 4). Second, the brightness of this region increases and its image takes the form of a bright strip with sharp boundaries near the cathode. That the emitting region is extended toward the anode may be attributed to the downstream propagation of a hot spot along the jet, which leads to the spreading of its image. Note that a similar effect—the propagation of the region of a compressed high-temperature plasma emitting X radiation along the discharge axis—was recently observed in a high-current plasma-focus discharge [35].

Let us now discuss the data from measurements of the ion composition of the cathode plasma jet that were performed earlier by us under the same experimental conditions [8, 9]. Figure 7c shows the signal from the electrostatic energy analyzer measuring accelerated ions moving toward the anode. The charge spectrum of ions and the time of their generation (indicated by the arrow in the figure) were calculated from the measured values of their energy and flight time. It can be seen from Fig. 7c that, at a certain instant, the cathode jet generates short-duration beams of multiply charged ions of the cathode material. Their duration and the generation time are close to the corresponding parameters of X-ray bursts (see Fig. 5b, curve *3*). Since multiply charged ions of the cathode material are generated in the high-temperature plasma emitting X radiation, the data from the ion measurements are consistent with X-ray measurements. Moreover, previous experiments [36] showed that the duration of the ion signals decreased with increasing discharge current amplitude. This also correlates with the data from X-ray measurements.

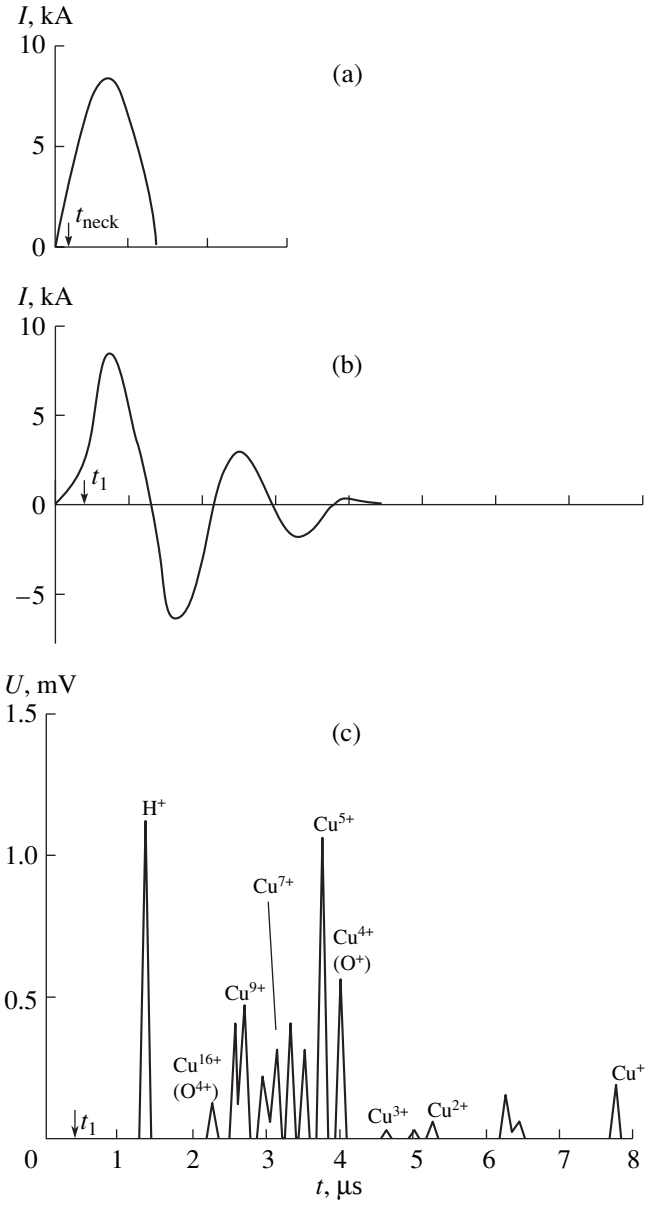

Fig. 7. (a) Calculated and (b) measured time dependences of the discharge current and (c) the signal from the electrostatic ion analyzer for $E/Z = 2.1$ keV. Arrow t_1 indicates the instant at which all the ion species escape from the cathode jet, and arrow t_{neck} indicates the calculated time of the micropinch formation.

It can also be seen from Fig. 7c that, besides the ions of the cathode material in different ionization states, the experiment shows the presence of a pronounced peak of

H^+ ions. In addition, ions of other light impurities desorbed from the cathode surface and from the dielectric insert (O^{n+}, C^{n+}, N^{n+}, where $n = 1, 2, \ldots$) may also contribute to the signal if the ratios μ/Z of these ions are close to those of copper ions (e.g., O^+ for Cu^{4+}, O^{2+} for Cu^{8+}, etc.). In Fig. 8c, the impurity ions that may contribute to the signal are indicated in brackets. Noted that it is more reasonable to ascribe the $\mu/Z = 4$ peak to O^{4+} ions, rather than to Cu^{16+}, because there are no peaks of the copper ions in close intermediate charge states (such as Cu^{15+}, Cu^{14+}, etc.). It should also be noted that there was a considerable scatter in the signal amplitudes in different shots. To exclude this effect, the signals recorded at fixed discharge parameters were averaged over a series of shots and only these average values corresponding to different ion species were used in the subsequent processing of the experimental results.

Figure 7a compares the experimental data to the results of calculations of the dynamics of the neck formation for the same amplitude of the discharge current. The calculated time of the micropinch formation is indicated by the arrow. This time is close to the instant of generation of multiply charged ions observed in the experiment (Fig. 7b).

4.3. Parameters of the Micropinch Plasma at Different Amplitudes of the Discharge Current

Let us now consider the measured values of the plasma parameters in the micropinch and compare them to the simulation results. The plasma parameters in the emitting region were estimated using the following procedure. In an X-ray signal, we chose a peak with a maximal amplitude, which apparently corresponded to maximal values of the plasma temperature and density that were reached by the time of the micropinch formation. Signals recorded in this detector channel during different shots at a fixed amplitude of the discharge current were structurally similar to one another but had markedly different amplitudes. To obtain a statistically valid result, the peak amplitude was averaged over a series of ten shots. From the ratio of the averaged amplitudes for two channels (which differed from one another by the filter thickness), we estimated the hardness of the emission spectrum at a given amplitude of the discharge current. Since the time resolution of the recording system (about 30 ns) far exceeded the characteristic time of plasma heating in the neck (a few nanoseconds, see Fig. 3b), this procedure allowed us to estimate the time-averaged plasma parameters by the time of the micropinch formation.

In order to determine the parameters of the emitting plasma (e.g., the electron temperature) from these data, it is necessary to have information on the relationship between the bremsstrahlung, characteristic, and recombination components of the spectrum. The line emission in this case is directly related to the presence of multiply charged ions of the cathode material in the jet plasma. Previously, such ions were detected using time-of-flight diagnostics [8, 9]. However, X-ray measurements could not help us in deciding which of the spectral components was prevalent. For this reason, when processing the experimental data, we assumed that the plasma bremsstrahlung made a major contribution to the signal and that the energy distribution of emitting electrons was Maxwellian with a temperature T_e. Note that, for the given filter thicknesses, the electron temperature range within which this method provides a reasonable accuracy (about 30%) spans from 0.1 to 1.2 keV.

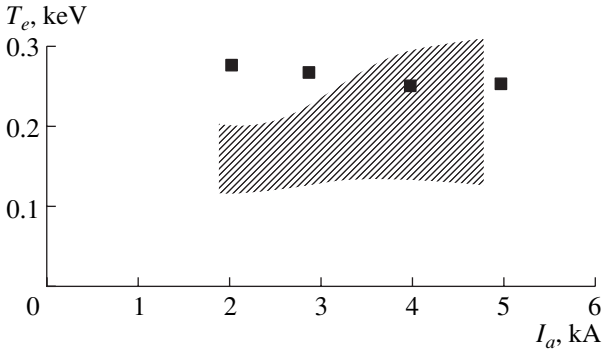

Fig. 8. Calculated electron temperature (symbols) and that estimated from X-ray detector signals (shaded domain) vs. discharge current amplitude.

Figure 8 shows the electron temperature versus the discharge current amplitude. The temperature was estimated from the signal ratio for two pairs of filters. It can be seen that the temperature varies in the range 150–300 eV and increases with increasing discharge current. The temperatures determined with different pairs of filters are close to one another; this confirms our assumption that the bremsstrahlung component is dominant in the emission spectrum. Fig. 8 also demonstrates fair agreement between the experimental data and the calculated results over the entire current range under study.

The parameters of the ion component of the pinch plasma were determined as follows. From the average amplitudes of the signals corresponding to ions in a given charge state Cu^{n+} and measured at different values of E/Z, we constructed the energy spectrum of these ions. Integrating the spectra of different ion species, we determined the fractions of these species in the ion beam for a given amplitude of the discharge current. From the charge composition found in this way, we calculated the average ion charge number, which is shown as a function of the current amplitude in Fig. 9. The figure also shows the dependence of the average ion charge number on the current amplitude obtained from model calculations for two instants: just before and just after the neck breaks down into two fragments (which correspond to 120 and 121 ns in Fig. 1 for $I_a = 3$ kA). It can be seen from Fig. 9 that both experimental and calculated values of the average ion charge number increase with increasing discharge current amplitude

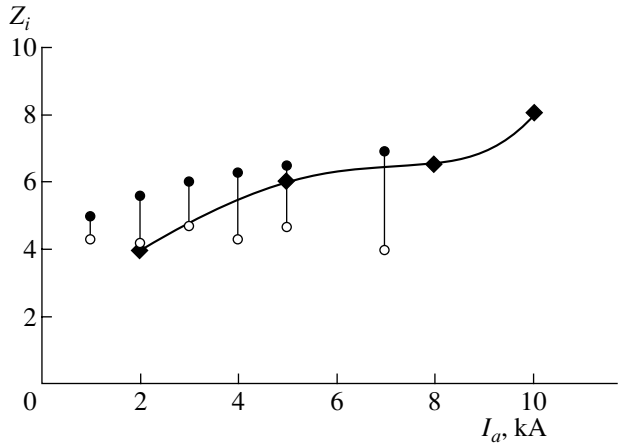

Fig. 9. Average charge number of copper ions in the micropinch plasma as a function of the discharge current amplitude: the rhombuses show the measured values, while the closed and open circles show the maximum computed values and the values obtained at the next computation step, respectively.

and that these values are close to one another over the entire current range under study. Calculations also show that the plasma density in the neck increases with current amplitude. Since the electron temperature in this region varies only slightly (see Fig. 8), the observed increase in the average ion charge number is evidently related to an increase in the plasma density.

As was pointed out in Section 3.3, the production of multiply charged ions in the expanding plasma jet is governed by three parameters: the electron temperature and density and the plasma velocity, which determines the time during which the ions stay in the micropinch region. In a moving jet, the time during the ions undergo additional ionization is substantially shorter than in a stationary plasma. This is why the average ion charge in our case is substantially lower than that calculated for a stationary plasma with the same values of the electron temperature and density [37].

4.4. Effect of the Discharge Gap Length on the Micropinch Formation

The simulation results show that, as the amplitude of the discharge current decreases, the region where the neck forms is displaced away from the cathode (see Fig. 4). The reason for this is that the current grows more slowly and, consequently, the time during which the neck develops increases. During this phase, the neck is entrained by the expanding plasma downstream from the cathode (see Fig. 2b). For discharge current amplitudes below a certain critical value, the neck is displaced outside the discharge gap; i.e., a micropinch has no time to develop. Hence, the formation of a micropinch and the accompanying phenomena (such as X-ray bursts and the generation of multiply charged ions) should occur only when the amplitude of the discharge current exceeds this critical value, which depends on the length of the interelectrode gap. This is confirmed by the data from X-ray measurements, which show that short emission bursts are observed only at current amplitudes of higher than 1 kA.

Our analysis has shown that the micropinch parameters deduced from X-ray and ion measurements agree with the simulation results over a wide range of discharge currents. This indicates that the proposed model adequately describes the formation of a high-temperature micropinch plasma in the cathode jet in the initial stage of the discharge and the generation of multiply charged ions of the cathode material by this plasma.

5. DISCUSSION

Using the calculated values of the plasma parameters, let us now estimate how the processes that were ignored in the energy balance equation may affect the formation of a micropinch. We compare the time of the micropinch formation τ_p to the characteristic time $\tau_\kappa \approx l_p^2 N_e/\kappa$ of energy losses by heat conduction from the heating region [38] (here, l_p is the length of the constriction region and κ is the electron thermal conductivity). Since the φ component of the magnetic field $B_\varphi \approx B_R = 2I/(cR_p)$ (where R_p is the neck radius) is nonzero almost over the entire cross section of the plasma jet, we have to do with heat transport across the magnetic field. In this case, the electron thermal conductivity is $\kappa \approx 4N_eT_e/(m_e\omega_e^2\tau_e)$, where ω_e is the electron plasma frequency and $\tau_e \approx 10^4 T_e^{3/2}/N_e$ is the electron–electron collision time (here, T_e is in eV and N_e is in cm^{-3}) [38]. From Figs. 1a, 1c, and 1d, we have: $l_p/R_p \approx 5$, $T_e \approx 10^2$ eV, and $N_e \approx 10^{17}$ cm^{-3} for $I \approx 3$ kA. Thus, we find that the heat loss time is $\tau_\kappa \propto (l_pI/R_p)^2\sqrt{T_e}/N_e \approx 100$ ns, whereas the characteristic time during which the micropinch parameters vary, $\tau_p \approx 10$–30 ns, is substantially shorter. Therefore, heat conduction insignificantly affects the development of the plasma constriction. However, taking it into account would smooth the temperature distribution and decrease the maximum electron temperature.

Let us now compare electron energy losses for bremsstrahlung (Q_{br}) and ion excitation (Q_{ex}) to losses for ionization (Q_{ion}). According to [39], we have $Q_{br}/(Q_{ex} + Q_{ion}) \ll 1$ at $T_e \approx 10^1$–10^3 eV; i.e., bremsstrahlung losses are small. In all cases under consideration, energy losses due to elastic collisions (Q_{ei}) also are insignificant. In [40], the effect of excitation losses for a vacuum arc with an aluminum cathode at currents on the order of 1 kA was analyzed. It was shown that $Q_{ex}/Q_{ion} < 1$ at temperatures of $T_e < 20$ eV. Taking into account losses for ion excitation (i.e., for line emission at plasma temperatures of several hundred electronvolts; see Fig. 1) is a rather complicated

problem, because it is necessary to consider a great number of elementary processes, whereas the values of the effective cross sections for many of them are unknown. Rough estimates can be made by invoking the concept of an average energy W of the formation of an electron–ion pair (the difference $W - E_i$ corresponds to electron energy losses for excitation, where E_i is the ionization energy). Experimental data for several gases show that $\alpha = W/E_i \approx 2$ [39]. Theoretical calculations for multiply charged ions in a hydrogen-like ion approximation yield $\alpha \approx 1.5$–4 [24] for $N_e \approx 10^{15}$–10^{17} and $T_e/E_i \approx$ 0.3–1. For this range of α values, the micropinch parameters were calculated assuming that the total collision losses are equal to $Q = Q_{ex} + Q_{ion} = \alpha Q_{ion}$. It turns out that, even for $\alpha = 4$, a decrease in the peak value of the electron temperature (in comparison to the case $\alpha = 1$) is about 10%. This means that collision losses are of minor importance during the fast development of the plasma neck ($\Delta t \approx 1$ ns), when the work of the magnetic pressure force goes almost entirely to an increase in the electron kinetic energy. Of course, these losses may become important in the late stage of the formation a quasi-equilibrium pinch [3]. However, a detailed discussion of this problem goes beyond the scope of our study.

As regards the assumption on the composition of the X-ray spectrum (see Section 4.3), it is worth noting that the literature data concerning the character of emission of high-temperature metal plasma are contradictory. Calculations show that the line emission from multiply charged metal ions makes the major contribution to the emission spectrum at electron temperatures of 10^2–10^3 eV [5]. However, an analysis of measurements of X-ray emission from a micropinch plasma [5] showed that the effect of the line and photorecombination emission could be ignored. Experimental results obtained with the use of Ross filters [41] also indicate that bremsstrahlung is dominant in the X-ray emission spectrum of the spark plasma. Note that, in experiments with laser plasma, where (as in our case) multiply charged ions were produced from the target material, the emission spectrum of the plasma jet was also ascribed to bremsstrahlung and the filter method was successfully used to measure the electron temperature in the range 0.3–2.5 keV [42].

The X-ray emission spectrum of a plasma may also be modified by the beams of runaway electrons generated at the instant of the micropinch formation [43]. Model calculations [44] show that the energy of runaway electrons depends on the discharge current. Figure 8 shows, however, that, in our case, this dependence is weak. We believe that, under our experimental conditions, the effect of X-ray emission from runaways on the estimate of the electron temperature is insignificant, because this temperature itself is evaluated to within a factor of 2–2.5.

6. CONCLUSIONS

The results of our experimental and theoretical investigations allow us to propose the following scenario for the formation of a micropinch structure in the cathode jet of a vacuum spark discharge at currents of 1–10 kA. In the early stage of the discharge, a neck forms at the front of the expanding cathode jet (at a distance of a few millimeters from the cathode) as a result of plasma compression by the magnetic self-field. The time during which the constriction develops and its location in the interelectrode gap depend on the growth rate of the discharge current. However, the further evolution of the formed micropinch is governed by its own parameters. In the constriction region, the radius of the current channel is less than 0.1 mm; as a result, the density increases to 10^{17} cm^{-3}, the electron component is rapidly heated to a temperature on the order of 10^2 eV, and the averaged ion charge increases substantially. The calculated spatial and temporal variations in the electron temperature and average ion charge are close to the measured dependences over a wide range of the discharge parameters.

It should be noted that, as the cathode jet generated in a spark discharge with a rapidly growing current expands into a vacuum, it demonstrates features typical of different plasma objects:

(i) At small (less that 1 mm) distances from the cathode, the action of the magnetic field on a dense, relatively cold plasma jet can be ignored and the plasma parameters in the jet are close to those in a steady-state vacuum arc.

(ii) As the plasma jet expands further, a micropinch forms at its front. The micropinch plasma is heated to a high temperature, which leads to the generation of multiply charged ions of the cathode material. In this case, the parameters of the micropinch plasma are comparable to those in high-current vacuum sparks, which, however, are characterized by a substantially higher energy.

(iii) The multiply charged ions generated in the micropinch move toward the anode. A similar emission of multiply charged ions from a current-free plasma jet was observed when a target was irradiated by high-power laser radiation (see, e.g., [45]). We emphasize that, in both cases, the generation of multiply charged ions occurs just at the front of the plasma expanding into a vacuum. This allows one to directly measure multiply charged ions. Such a situation is quite different from that occurring in the pinch structures of high-current sparks [2], in which multiply charged ions are generated in a local region of the plasma column bridging the interelectrode gap. In this case, the ions passing through the surrounding cold plasma undergo charge exchange and their charge decreases substantially. Presumably for this reason, the cathode-material ions escaping from the plasma column are in low charge states [46].

ACKNOWLEDGMENTS

This work was supported in part by the "Universities of Russia" program (project no. UR.01.01.008) and the Russian Foundation for Basic Research (project no. 04-02-16431).

REFERENCES

1. K. N. Koshelev and N. R. Pereira, J. Appl. Phys. **69**, R21 (1991).
2. C. R. Negus and N. J. Peacock, J. Phys. D **12**, 91 (1979).
3. V. V. Vikhrev and V. V. Ivanov, Fiz. Plazmy **8**, 1211 (1982) [Sov. J. Plasma Phys. **8**, 688 (1982)].
4. K. N. Koshelev, Yu. V. Sidel'nikov, V. V. Vikhrev, and V. V. Ivanov, *Spectroscopy of Multiply Charged Ions in Hot Plasma* (Nauka, Moscow, 1991), p. 116 [in Russian].
5. M. A. Gulin, A. N. Dolgov, N. N. Kirichenko, and A. S. Savelov, Zh. Éksp. Teor. Fiz. **108**, 1309 (1995) [JETP **81**, 719 (1995)].
6. A. N. Dolgov and G. Kh. Salakhutdinov, Fiz. Plazmy **29**, 818 (2003) [Plasma Phys. Rep. **29**, 757 (2003)].
7. E. D. Korop and A. A. Plyutto, Zh. Tekh. Fiz. **40**, 2534 (1970) [Sov. Phys. Tech. Phys. **15**, 1976 (1970)].
8. M. F. Artamonov, V. I. Krasov, and V. L. Papernyĭ, Zh. Éksp. Teor. Fiz. **120**, 1404 (2001) [JETP **93**, 1216 (2001)].
9. M. F. Artamonov, V. I. Krasov, and V. L. Paperny, J. Phys. D **34**, 645 (2001).
10. E. A. Zverev and I. A. Krinberg, Pis'ma Zh. Tekh. Fiz. **24** (18), 50 (1998) [Tech. Phys. Lett. **24**, 728 (1998)].
11. E. A. Zverev and I. A. Krinberg, Prikl. Fiz., No. 5, 50 (2002).
12. N. Vogel, Pis'ma Zh. Éksp. Teor. Fiz. **67**, 622 (1998) [JETP Lett. **67**, 647 (1998)].
13. V. F. D'yachenko and V. S. Imshennik, in *Reviews of Plasma Physics*, Ed. by M. A. Leontovich (Atomizdat, Moscow, 1967; Consultants Bureau, New York, 1970), Vol. 5.
14. V. F. D'yachenko and V. S. Imshennik, in *Reviews of Plasma Physics*, Ed. by M. A. Leontovich (Atomizdat, Moscow, 1974; Consultants Bureau, New York, 1980), Vol. 8.
15. V. V. Vikhrev and S. I. Braginskii, in *Reviews of Plasma Physics*, Ed. by M. A. Leontovich (Atomizdat, Moscow, 1980; Consultants Bureau, New York, 1986), Vol. 10.
16. A. T. Altyntsev, V. I. Krasov, N. V. Lebedev, *et al.*, Prib. Tekh. Éksp., No. 6, 177 (1983).
17. V. D. Dmitriev, S. M. Luk'yanov, Yu. É. Peniozhkevich, *et al.*, Prib. Tekh. Éksp., No. 2, 7 (1982).
18. M. F. Artamonov, V. I. Krasov, and V. L. Papernyĭ, Prikl. Fiz., No. 5, 69 (2002).
19. M. F. Artamonov, V. I. Krasov, and V. L. Papernyĭ, Prikl. Fiz., No. 5, 34 (2003).
20. M. P. Stockli and D. Fry, Rev. Sci. Instrum. **68**, 3053 (1997).
21. K. V. Brushlinskiĭ and A. I. Morozov, in *Reviews of Plasma Physics*, Ed. by M. A. Leontovich (Atomizdat, Moscow, 1974; Consultants Bureau, New York, 1980), Vol. 8.
22. G. A. Mesyats and S. A. Barengol'ts, Usp. Fiz. Nauk **172**, 1113 (2002) [Phys. Usp. **45**, 1101 (2002)].
23. I. A. Krinberg, Zh. Tekh. Fiz. **71** (11), 25 (2001) [Tech. Phys. **46**, 1371 (2001)].
24. V. I. Derzhiev, A. G. Zhidkov, and S. I. Yakovlenko, *Radiation from Ions in a Nonequlibrium Dense Plasma* (Énergoatomizdat, Moscow, 1986), p. 74 [in Russian].
25. I. A. Krinberg, Prikl. Fiz., No. 6, 77 (2004).
26. V. A. Nemchinskiĭ, Zh. Tekh. Fiz. **53**, 235 (1983) [Sov. Phys. Tech. Phys. **28**, 146 (1983)].
27. A. Anders, Phys. Rev. E **55**, 969 (1997).
28. I. A. Krinberg and E. A. Zverev, Plasma Sources Sci. Technol. **12**, 372 (2003).
29. C. W. Allen, *Astrophysical Quantities* (Athlone, London, 1973; Mir, Moscow, 1977).
30. O. M. Belotserkovskiĭ and Yu. M. Davydov, *Particle-in-Cell Method in Gas Dynamics* (Nauka, Moscow, 1982) [in Russian].
31. I. A. Krinberg and E. A. Zverev, Fiz. Plazmy **25**, 88 (1999) [Plasma Phys. Rep. **25**, 82 (1999)].
32. A. Anders and G. Y. Yushkov, J. Appl. Phys. **91**, 4824 (2002).
33. D. F. Alferov, N. I. Korobova, and I. O. Sibiryak, Fiz. Plazmy **19**, 399 (1993) [Plasma Phys. Rep. **19**, 207 (1993)].
34. P. Siemroth, T. Schulke, and T. Witke, IEEE Trans. Plasma Sci. **25**, 571 (1997).
35. N. V. Fillipov, M. A. Karakin, V. I. Krauz, *et al.*, Prikl. Fiz., No. 5, 43 (1999).
36. N. V. Astrakhantsev, V. I. Krasov, and V. L. Paperny, J. Phys. D **28**, 1922 (1995).
37. G. A. Vergunova, E. M. Ivanov, and V. B. Rozanov, Preprint No. 74 (Lebedev Physical Inst., Russ. Acad. Sci., Moscow, 1999).
38. S. I. Braginskii, in *Reviews of Plasma Physics*, Ed. by M. A. Leontovich (Gosatomizdat, Moscow, 1963; Consultants Bureau, New York, 1965), Vol. 1.
39. A. Dalgarno, in *Atomic and Molecular Processes*, Ed. by D. R. Bates (Academic, New York, 1962; Mir, Moscow, 1964).
40. S. Goldsmith and R. L. Boxman, J. Appl. Phys. **51**, 3649 (1980).
41. N. V. Averkiev, A. N. Dolgov, V. K. Lyapidevskiĭ, *et al.*, Fiz. Plazmy **18**, 724 (1992) [Sov. J. Plasma Phys. **18**, 374 (1992)].
42. N. Vogel and D. Nikitine, in *Proceedings of the 13th International Symposium on High-Current Electronics, Tomsk, 2004*, p. 333.
43. A. N. Dolgov, N. N. Kirichenko, V. K. Lyapidevskiĭ, *et al.*, Fiz. Plazmy **19**, 97 (1993) [Plasma Phys. Rep. **19**, 50 (1993)].
44. V. V. Vikhrev and E. O. Baronova, Prikl. Fiz., No. 5, 71 (1999).
45. K. N. Makarov, Yu. A. Satov, A. P. Strel'tsov, *et al.*, Zh. Éksp. Teor. Fiz. **106**, 1649 (1994) [JETP **79**, 891 (1994)].
46. V. A. Veretennikov, A. E. Gureĭ, A. N. Dolgov, *et al.*, Pis'ma Zh. Tekh. Fiz. **21** (22), 78 (1995) [Tech. Phys. Lett. **21**, 940 (1995)].

Translated by N.F. Larionova

Plasma Physics Reports, Vol. 31, No. 10, 2005, pp. 855–859. Translated from Fizika Plazmy, Vol. 31, No. 10, 2005, pp. 923–927.

PLASMA OPTICS

Space-Charge Lens for Focusing Negative Ion Beams by Means of an Additional Electron Ionizer

V. P. Goretskiĭ, A. M. Zavalov, and I. A. Soloshenko

Institute of Physics, National Academy of Sciences of Ukraine, pr. Nauki 144, Kiev, 03028 Ukraine

Received September 15, 2004; in final form, December 29, 2004

Abstract—A space-charge lens created at the Institute of Physics, National Academy of Sciences of Ukraine, to focus negative ion beams using an additional electron ionizer is investigated. In the previous version of the lens, in which the gas was ionized by the ion beam itself, the focal power was quite high (the focal length was $f \le 20$ cm) but the gas pressure was too great ($P \sim 10^{-3}$ torr), which resulted in significant charge-exchange losses of the beam ions. The experimental and theoretical study reported here shows that the use of a 100-eV electron beam as an auxiliary ionizer allows the working pressure in the lens to be significantly reduced. As a result, a simple, inexpensive, and efficient lens has been developed that can be used in systems for transportation of negative ion beams. © *2005 Pleiades Publishing, Inc.*

1. INTRODUCTION

The concept of a space-charge lens for focusing positive ion beams was first proposed by Gabor [1] and was then developed in a number of studies (see, e.g., [2–4]). In such a lens, the negative space charge is produced by injecting electrons, which are confined in the lens volume by an external magnetic field. The radial profile of the electric field is controlled by specifying the electric potentials of the ring electrodes. It is evident that this type of lens cannot, in principle, be used to focus negative ion beams, because this can be done only by means of a positive space charge. A concept of a space-charge lens for focusing negative ion beams was first formulated in [5]. In this lens, the space charge is created by positive ions produced via direct ionization of the working gas by the negative ion beam itself. The electrons created in the course of ionization are removed from the system by applying a longitudinal electric field. The use of easily ionized high-Z gases (such as argon, krypton, and xenon) allowed us to create a lens with a focal length of $f \le 20$ cm, which is comparable to the focal lengths of electrostatic and magnetic lenses. Note that the potentials of the main electrodes of electrostatic lenses are comparable to the potential of the ion source; this increases energy consumption and, most importantly, leads to aberrations and loss of the beam ions at the electrodes due to intense deceleration of the beam. The role of these negative effects increases with the beam current; therefore, as is known from practice, electrostatic lenses can be used only at beam currents of less than 10 mA. Magnetic lenses are free of these drawbacks, so they are widely used in practice. However, to focus a 10-keV hydrogen ion beam at a focal length of $f \approx 20$ cm with an ordinary 10-cm-diameter coil, the latter should have $\sim 2 \times 10^4$ ampere turns. In this case, the power consumption exceeds 10 kW. Note that the power dissipated in a space-charge lens with an external electron source is ~100 W, and it is as low as a few watts without an external source.

The space-charge lens is a rather simple and compact device consisting of three electrodes with interelectrode voltages a few tens of times lower than the potential of the ion source. However, the lens proposed in [5, 6] has a significant drawback: since the gas pressure in the lens is rather high (~10^{-3} torr), a significant fraction of the beam ions is lost due to charge exchange with neutral gas atoms.

Here, we propose a space-charge lens of alternative design in which the gas is ionized not only by the ion beam itself but also by an auxiliary 100-eV electron beam. The use of an auxiliary ionizer allowed us to decrease the working gas pressure severalfold and, thereby, to substantially reduce charge-exchange losses of the beam ions.

The focal power of the lens is measured as a function of the electron ionizer current. The results of the corresponding numerical simulations by the particle-in-cell method agree well with the experimental data.

2. EXPERIMENTAL SETUP AND RESULTS

A scheme of the experiment with a space-charge lens is shown in Fig. 1. A beam of H^- ions with an energy of 10–12 keV and a current of 10–30 mA was output from surface plasma source *1* through a 0.5 × 15.0-mm slit. The beam was formed and deflected with the help of a 2-kG magnetic field created by electromagnet *2*. After passing through the lens electrodes (*3*, *4*), the beam fell onto measuring collectors (*7*, *8*). Collector *7* (10 cm in diameter) was used to measure the total beam current, whereas collector *8* (2 cm in diameter) was used to measure the beam compression ratio

1063-780X/05/3110-0855$26.00

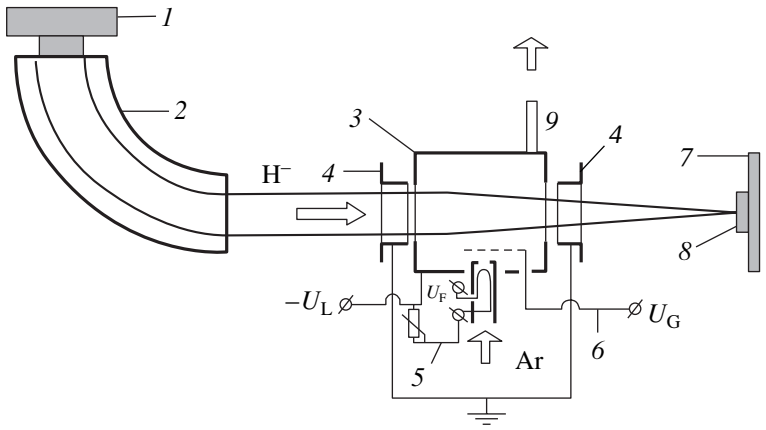

Fig. 1. Scheme of the experiment: (*1*) pulsed source of H^- ions, (*2*) deflecting magnets, (*3*) central electrode, (*4*) grounded end electrodes, (*5*) filament circuit of the electron emitter, (*6*) control grid circuit, (*7*) beam current collector, and (*8*) collector for measuring the beam current density. The gas is supplied through the output aperture of the electron emitter and is fed to a pressure gauge through pipe *9*.

(the ratio of the maximum beam current measured by collector *8* in the focusing regime to the maximum current measured without focusing). The lens was placed ~20 cm away from the slit of the ion source. The distance between the outlet plane of the lens and the collector was ~30 cm.

The lens consisted of three electrodes: a central cylindrical electrode 15 cm in diameter and 10 cm in length (the diameters of the inlet and outlet apertures being 5 cm) and two 1.5-cm-long 5-cm-diameter end electrodes, placed a distance of 0.5-cm from the central electrode. The end electrodes were grounded, while the central electrode was at a negative potential, which could be varied from 0 to –2000 V. The working gas (argon) was supplied either through a pipe at the wall of the central electrode or through the outlet aperture of the electron emitter (see Fig. 1). The gas pressure in the lens could be varied in the range $(0.1–1.5) \times 10^{-3}$ torr, the pressure in the beam drift chamber being one order of magnitude lower.

Two types of electron emitter were used. The first type was a 7-cm-long 0.03-cm-diameter incandescent tungsten filament set parallel to the lens axis along the wall of the central electrode. The electrons were extracted by the electric field of grid *6* (Fig. 1), whose potential was varied from 0 to 100 V. The emission current was limited by the electron space charge and reached its maximum value of 25 mA at a grid potential of 100 V.

The second type of emitter was a 1-cm-long spiral made of 7-cm-long 0.03-cm-diameter tungsten wire. It was set in the middle of the central electrode wall, inside a metal cylinder with an outlet aperture of 1 cm. The electrons were extracted by applying a positive potential to the grid. Since the gas was supplied through the electron emitter, a non-self-sustained discharge was ignited between the cathode and the grid. This discharge partially removed the space charge that limited the emission current. As a result, the electron current injected into the lens could reach 200 mA.

The positive space charge in the lens was created via gas ionization by both the negative ion beam and the electrons arriving from the emitter. Special experiments and numerical simulations showed that the electrons produced due to ionization and charge exchange escaped either to the grid or to the end electrodes under the action of the longitudinal electric field. The ions, which were inertially confined in the lens, eventually escaped to the central electrode. It was shown in [6] that, when the gas was ionized by the ion beam only, the density of positive ions could be a few orders of magnitude higher than the electron density.

The effect of an additional ionizer is illustrated in Fig. 2 by the dependences of the beam compression ratio on the emitter current for different gas pressures.

As was noted in the Introduction, in the absence of additional electron-impact ionization, the optimal compression ratio (sixfold increase in the current density) was observed at a pressure of $\sim 10^{-3}$ torr. It can be seen from Fig. 2 that, with the additional ionizer, the beam compression ratio increases appreciably at pressures as low as $P \sim 0.1 \times 10^{-3}$ torr. The optimal compression is achieved at a pressure of $\approx 0.3 \times 10^{-3}$ torr. The physical picture of the processes occurring in the lens will be analyzed in the next section using results of numerical simulations. To make the comparison between the experimental and numerical results more convenient, the data presented in Fig. 2 are replotted in Fig. 3 using other variables. Here, the ratio of the lens focal length to the optimal focal length corresponding to the maximum beam compression ratio is plotted on the ordinate.

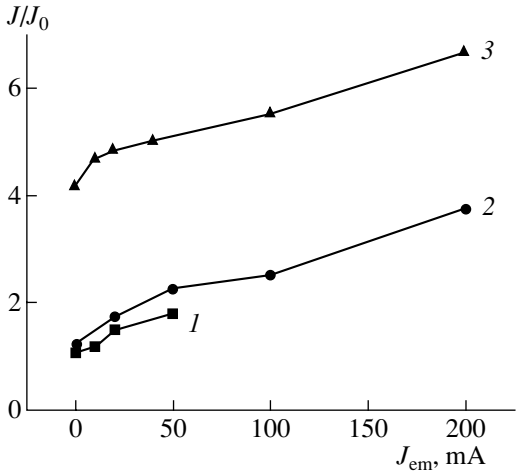

Fig. 2. Compression ratio J/J_0 of a 12-keV H^- beam vs. electron emission current for different gas (argon–air mixture) pressures in the lens: P = (*1*) 2.2×10^{-4}, (*2*) 2.9×10^{-4}, and (*3*) 7.2×10^{-4} torr. The gas is supplied through the output aperture of the electron emitter. The lens potential is U_L = –1400 V, and the ion beam current is 15 mA.

3. NUMERICAL RESULTS

The processes occurring in the lens were simulated by the particle-in-cell method [7]. The geometrical parameters of the simulated system corresponded to the actual experimental parameters (Fig. 1). The voltage between the central electrode and the end electrodes was assumed to be constant and equal to U_L = –1500 V. The electron emitter was an incandescent filament wound to form a 14-cm-diameter spiral. A 2-cm-long 12-cm-diameter grid electrode was placed 1 cm away from the electron emitter. A voltage of 100 V was applied between the electron emitter and the grid electrode, so the initial electron energy was optimal for gas ionization.

In our simulations, the gas pressure was varied in the range $(0.2–1.5) \times 10^{-3}$ torr. The current of the 15-keV H^- ion beam was 15 mA. The computational procedure is described in detail in [6]. The only difference was that here we took into account ionization produced by the electrons arriving from the electron emitter.

The results of simulations allowed us not only to determine all the parameters of the system in a steady state (the particle trajectories and the spatial distributions of the electric potential, electric field, and particle densities), but also to trace their dynamics during the transient process. For brevity, we present here only the most important results that are necessary to understand the physical picture of the processes occurring in the lens and to make a comparison with the experimental data. The characteristic parameters of the system are as follows: the time during which a steady state is established is a few microseconds, the radial electric field

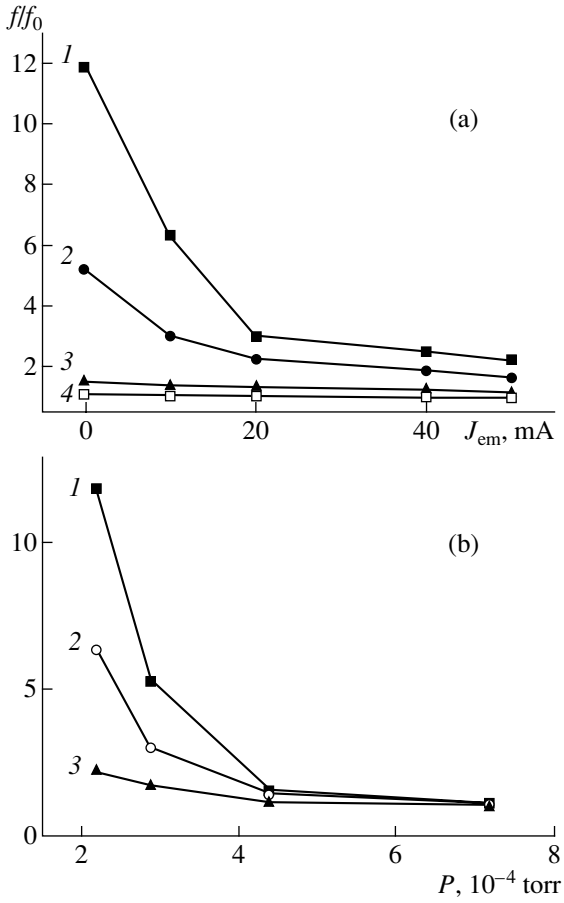

Fig. 3. Relative focal length of the lens for a 12-keV H^- beam (a) as a function of the electron emitter current at different gas pressures in the lens (P = (*1*) 2.2×10^{-4}, (*2*) 2.9×10^{-4}, (*3*) 4.4×10^{-4}, and (*4*) 7.2×10^{-4} torr) and (b) as a function of the gas pressure at different electron emission currents (J_{em} = (*1*) 0, (*2*) 10, and (*3*) 50 mA). The lens potential is U_L = –1400 V, and the ion beam current is 15 mA.

attains ~100 V/cm, and the positive ion density is as high as ~10^8 cm^{-3}.

Let us consider in more detail how steady-state operating conditions are established in the lens at an emission current of 100 mA and a gas pressure of 0.7×10^{-3} torr. Figure 4 shows the time evolution of the potential at the center of the lens. In the initial stage, which lasts from t = 0 to $t = 0.5 \times 10^{-6}$ s (the so-called initial filling stage), the potential decreases. The reason for this is that all the newly born particles are accumulated in the volume and the number of the positive ions produced due to ionization is less than the number of electrons created via both gas ionization and the detachment from negative ions in their collisions with neutral atoms. In this stage, the potential at the center of the lens becomes lower than the grid potential U_G and even than the potential of the central electrode U_L, so

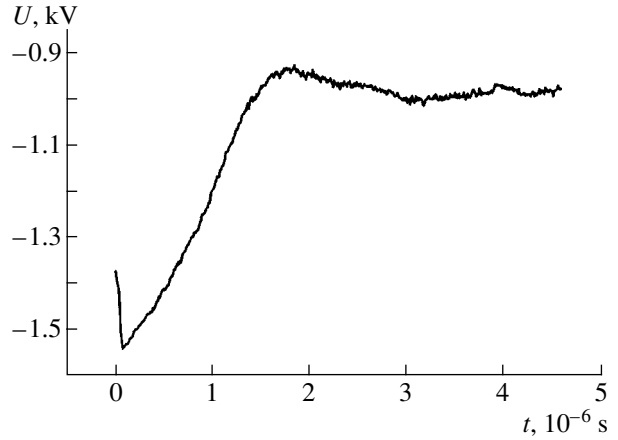

Fig. 4. Calculated time evolution of the potential at the center of the lens.

the lens is defocusing. The electrons arriving from the emitter play a minor role because, in this stage, they do not penetrate into the central region of the lens.

As time elapses, the electrons escape to the end electrodes and partially to the grid, whereas the positive ions continue to be accumulated in the lens volume. This leads to an increase in the potential at the center of the lens and, consequently, to an increase in the rate of gas ionization by the electrons arriving from the emitter. The time evolution of the logarithm of the ratio of the positive ion density to the electron density in the lens, $\log(n_{\text{ion}}/n_{\text{ion}})$, is shown in Fig. 5a. It can be seen that, 0.5 μs after the beginning of the process, the ion density becomes equal to the electron density and then exceeds it. The steady state is established over a time of about 1 μs. In this regime, the electrons arriving from the emitter efficiently ionize gas atoms. They have time to perform several oscillations in the lens before escaping to either the grid or the end electrodes. Note that the electrons born in the interaction between the beam and the gas atoms escape from the lens only to the end electrodes.

It should be noted that, in a steady state with additional electron injection, $\log(n_{\text{ion}}/n_{\text{ion}})$ is equal to 0.5 (Fig. 5a), whereas without electron injection, it is ~2.0.

In the steady state, the radial profile of the potential in the lens is close to parabolic (Fig. 5b, upper curve). In this case, as follows from Fig. 6, the beam is efficiently focused by the lens, the focal length being 25 cm.

We performed calculations for different electron emission currents and gas pressures. The results obtained are presented in Fig. 6 in the form of pressure dependences of the relative focal length (the ratio of the focal length f to the optimal focal length f_0) for different electron emission currents. Here, the optimal focal length is the focal length at a pressure of $P = 1.5 \times 10^{-3}$ torr. It can be seen that an increase in the electron

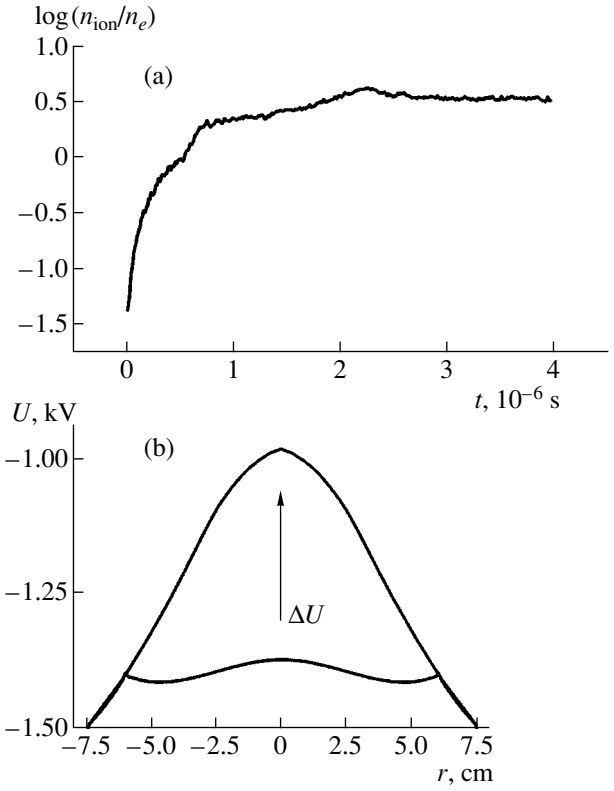

Fig. 5. (a) Calculated time evolution of the logarithm of the ratio of the positive ion density to the electron density in the lens and (b) radial profiles of the potential in the central cross section of the lens at the initial instant (lower curve) and in a steady-state operating mode (upper curve). The increase in the potential at $r = 0$ is $\Delta U \approx 400$ V.

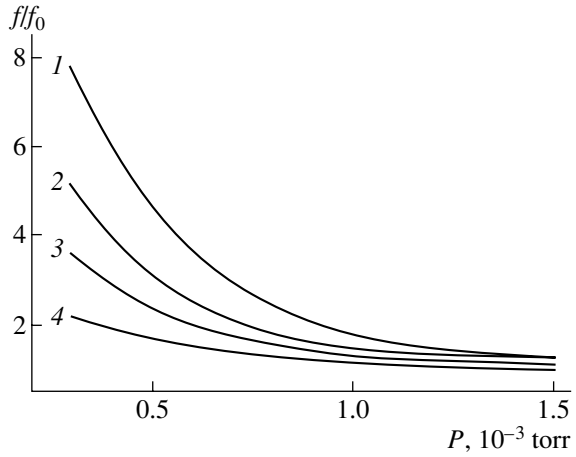

Fig. 6. Calculated relative focal length of the lens (f_0 = 20.0 cm) vs. gas pressure for different electron emission currents: J_{em} = (*1*) 0, (*2*) 20, (*3*) 50, and (*4*) 100 mA.

current leads to a significant decrease in the focal length (an increase in the lens power). This effect is more pronounced at low gas pressures. At the maximum electron current, the focal length at a pressure of 0.3×10^{-3} torr

is only twice as large as that at a pressure of $P = 1.5 \times 10^{-3}$ torr. A comparison of Fig. 3 to Fig. 6 shows that the simulation results agree well with the experimental data.

4. CONCLUSIONS

Our experimental and theoretical study has shown that the use of an auxiliary electron ionizer with an electron energy that is optimal for ionizing the working gas in a space-charge lens allows one to decrease the gas pressure severalfold and, thereby, to substantially reduce charge-exchange losses of the beam ions. Therefore, such a lens is a simple and efficient means for focusing intense negative ion beams.

ACKNOWLEDGMENTS

This work was supported by the Ukrainian Foundation for Basic Research at the Ministry of Science of Ukraine, grant no. F7/297-2001.

REFERENCES

1. D. Gabor, Nature **160**, 89 (1947).
2. A. I. Morozov, Dokl. Akad. Nauk SSSR **163**, 1363 (1965) [Sov. Phys. Dokl. **10**, 775 (1965)].
3. A. I. Morozov and S. V. Lebedev, in *Reviews of Plasma Physics*, Ed. by M. A. Leontovich (Atomizdat, Moscow, 1974; Consultants Bureau, New York, 1980), Vol. 8.
4. A. A. Goncharov, A. N. Dobrovol'skiĭ, A. N. Kotsarenko, *et al.*, Fiz. Plazmy **20**, 499 (1994) [Plasma Phys. Rep. **20**, 449 (1994)].
5. V. P. Goretskiĭ, I. A. Soloshenko, and A. I. Shchedrin, Fiz. Plazmy **27**, 356 (2001) [Plasma Phys. Rep. **27**, 335 (2001)].
6. A. M. Zavalov, V. N. Gorshkov, V. P. Goretskiĭ, and I. A. Soloshenko, Fiz. Plazmy **29**, 516 (2003) [Plasma Phys. Rep. **29**, 480 (2003)].
7. D. E. Potter, *Computational Physics* (Mir, Moscow, 1975; Wiley, New York, 1973).

Translated by N.N. Ustinovskiĭ

Plasma Physics Reports, Vol. 31, No. 10, 2005, pp. 860–864. Translated from Fizika Plazmy, Vol. 31, No. 10, 2005, pp. 928–932.

NONLINEAR PHENOMENA

Inertial Alfvén-Wave-Driven Convective Cells in Low-Density Plasmas

O. A. Pokhotelov[1, 2], O. G. Onishchenko[1], R. Z. Sagdeev[3], L. Stenflo[4], and M. A. Balikhin[2]

[1] *Schmidt Institute of Physics of the Earth, Russian Academy of Sciences, ul. Bol'shaya Gruzinskaya 10, Moscow, 123995 Russia*

[2] *University of Sheffield, Sheffield, UK*

[3] *University of Maryland, College Park, MD, USA*

[4] *Umeå University, Umeå, Sweden*

Received July 10, 2004; in final form, January 12, 2005

Abstract—The parametric interaction of inertial Alfvén waves with large-scale convective cells in a low-density plasma is investigated. It is shown that, in plasmas where the Alfvén velocity is comparable to or exceeds the speed of light, the parametric interaction is substantially suppressed. A compact expression for the optimal scale and instability growth rate of the fastest growing mode is obtained. The relevance of our theory to spacecraft measurements in the Earth's ionosphere is discussed. © *2005 Pleiades Publishing, Inc.*

1. INTRODUCTION

The generation and nonlinear evolution of convective cells in magnetized plasmas and geophysical fluids have been the subject of a great deal of research in recent years [1–9]. Convective cells driven by the parametric decay of inertial Alfvén waves (IAWs) in the topside ionosphere have recently been discussed in [10]. It has been shown that this instability can provide an efficient mechanism for the excitation of nonlinear large-scale electrostatic structures. This may lead to the formation of a turbulent boundary Alfvén layer in the Earth's ionosphere. Such a mechanism represents an inverse cascade in plasma turbulence and can therefore result in energy transfer from small-scale Alfvénic perturbations to large-scale convective motions. Furthermore, in this scenario, one can expect efficient particle acceleration perpendicular to the external magnetic field.

Some of the plasmas existing around magnetized space objects contain regions where the plasma density is substantially decreased (plasma cavities) relative to the background environment. Therefore, it is of interest to investigate the parametric instability of Alfvén waves in a low-density plasma in which the Alfvén velocity is on the order of the speed of light and the magnetic pressure is on the order of the plasma energy density at rest. This applies, first of all, to the auroral region, where the plasma density decreases exponentially with height above the ionosphere, while the magnetic field changes more slowly. The Alfvén velocity in this region increases sharply toward the magnetosphere and attains its maximum value at an altitude on the order of the Earth's radius. According to observations [11, 12], the Alfvén velocity in this region is on the order of 2×10^5 km/s or larger and thus becomes relativistic, i.e., comparable to the speed of light. This effect was not included in the analysis of [10].

The aim of the present paper is to generalize the theory of the IAW parametric instability developed in [10] to the case of a low-density plasma, accounting for effects of a nonzero ratio between the Alfvén velocity and the speed of light.

The paper is organized as follows: In Section 2, we derive the basic nonlinear equations describing the nonlinear dynamics of IAWs, taking into account the nonzero ratio of the Alfvén velocity to the speed of light. Section 3 is devoted to the derivation and analysis of a general dispersion relation for convective modes. A discussion of our results and their relevance to space observations is presented in Section 4.

2. BASIC EQUATIONS

IAWs correspond to shear ($k_\perp \gg k_z$) electromagnetic waves in low-β ($\beta \ll m_e/m_i$, where $m_{e(i)}$ is the electron (ion) mass) plasmas. In the linear approximation, they obey the dispersion relation

$$\omega_{\mathbf{k}} = k_z v_A \beta_A^{1/2} \Lambda_{\mathbf{k}}^{-1/2}, \qquad (1)$$

where $\omega_{\mathbf{k}}$ and $\mathbf{k}$ are the wave frequency and wave vector; k_z and $k_\perp$ are the components of the wave vector along and perpendicular to the external magnetic field $\mathbf{B}_0$, respectively; $v_A = B_0/(\mu_0\rho)^{1/2}$ is the Alfvén velocity; μ_0 is the permeability of free space; and $\rho = nm_i$ is the plasma mass density. Furthermore, $\Lambda_{\mathbf{k}} \equiv 1 + \lambda_e^2 k_\perp^2$ is a factor accounting for the wave dispersion, $\lambda_e = c/\omega_{pe}$ is the collisionless electron skin depth, c is the speed of light, $\omega_{pe} = (ne^2/\varepsilon_0 m_e)^{1/2}$ is the plasma frequency, n is

1063-780X/05/3110-0860$26.00 © 2005 Pleiades Publishing, Inc.

the plasma density, e is the elementary charge, ε_0 is the permittivity of free space, and $\beta_A = 1/(1 + v_A^2/c^2)$ is the factor accounting for the finite ratio between the Alfvén velocity and the speed of light. In a plasma with a weakly relativistic Alfvén velocity, we have $\beta_A \simeq 1 - v_A^2/c^2$. In the limit $v_A \gg c$, dispersion relation (1) reduces to the ordinary IAW dispersion relation. In the case of very small plasma density, i.e., when the magnetic field pressure substantially exceeds the plasma energy density at rest, we have $v_A \gg c$. According to Eq. (1), the dispersion relation in this case is $\omega_\mathbf{k} = k_z c \Lambda_\mathbf{k}^{-1/2}$, and thus the IAW's phase and group velocities along the external magnetic field are lower than the speed of light.

The nonlinear IAWs can be described in terms of the two-potential representation [10]: $E_z = -\partial_z\varphi - \partial_t A$, $\mathbf{E}_\perp = -\nabla_\perp\varphi$, and $\mathbf{B}_\perp = \nabla_\perp A \times \hat{\mathbf{z}}$, where $\mathbf{E}$ and $\mathbf{B}$ are the wave electric and magnetic fields and $\hat{\mathbf{z}}$ is the unit vector along the ambient magnetic field $\mathbf{B}_0$. Here, the subscripts z and $\perp$ denote the components along and perpendicular to $\mathbf{B}_0$, respectively; $\partial_t \equiv \partial/\partial t$; $\partial_z \equiv \partial/\partial z$; φ is the scalar potential of the electric field; and A is the z component of the vector potential.

We next adopt the equation for the parallel electron motion, $E_z + (\mathbf{v}_E \times \mathbf{B})_z = -(m_e/e)d_t v_{ze}$, where $\mathbf{v}_E = B_0^{-1}\hat{\mathbf{z}} \times \nabla\varphi$ is the electric drift velocity, $d_t \equiv \partial_t + \mathbf{v}_E \cdot \nabla$, and $\nabla_\perp = \nabla - \hat{\mathbf{z}}\,\cdot\nabla$. Here, $v_{ze} = -j_z/en$ and $j_z = -\mu_0^{-1}\nabla_\perp^2 A$ are the parallel electron velocity and electric current, respectively. We then obtain the gauge condition relating the electrostatic potential φ to the vector potential A,

$$d_t(1 - \lambda_e^2\nabla_\perp^2)A + \partial_z\varphi = 0. \quad (2)$$

Taking into account that the perpendicular current is related solely to the ion inertia, $\mathbf{j}_\perp = \mathbf{j}_{\perp i} = -\mu_0^{-1} d_t \nabla_\perp \varphi$, and substituting the explicit expressions for the perpendicular and parallel electric currents into the equation $\varepsilon_0^{-1}\nabla\,\cdot\mathbf{j} + \partial_t \nabla\cdot\mathbf{E} = 0$, we obtain

$$\frac{v_A^2}{c^2}\partial_t\nabla_\perp^2\varphi + d_t\nabla_\perp^2\varphi + v_A^2 d_z\nabla_\perp^2 A = 0, \quad (3)$$

where $d_z = \partial_z + B_0^{-1}\mathbf{B}_\perp\cdot\nabla = \partial_z + B_0^{-1}\{A, \ldots\}$ is the operator of differentiation along the total magnetic field and $\{A, \ldots\} \equiv (\partial_x A)\partial_y - (\partial_y A)\partial_x$ denotes the Poisson bracket. The term proportional to v_A^2/c^2 on the left-hand side of Eq. (3) is due to the displacement current in Ampére's law. The system of Eqs. (2) and (3) constitutes a closed set of equations that describes the nonlinear dynamics of IAWs and represents the generalization of the equations used in [10] to the case of relativistic Alfvén velocities.

3. EXCITATION OF CONVECTIVE CELLS

Following [10], we decompose the scalar and vector potentials (φ and A) into their low- and high-frequency parts: $\varphi = \phi + \psi$ and $A = a + A_h$, where ϕ and a are the electro- and magnetostatic potentials of the convective mode that vary slowly with time and do not depend on the z coordinate.

Averaging Eqs. (2) and (3) over the fast time and short spatial scales of the IAWs, we obtain a set of equations describing the evolution of convective cells,

$$\partial_t\nabla_\perp^2\phi = -B_0^{-1}\beta_A(\overline{\{\psi, \nabla_\perp^2\psi\}} - v_A^2\overline{\{A, \nabla_\perp^2 A\}}), \quad (4)$$

$$\partial_t(1 - \lambda_e^2\nabla_\perp^2)a = -B_0^{-1}\overline{(\{\psi, (1 - \lambda_e^2\nabla_\perp^2)A\}}, \quad (5)$$

where the overbar denotes averaging. Hereafter, for notational convenience, the subscript h in the definition of the high-frequency part of the vector potential is omitted.

The coupling of IAWs with convective cells is governed by the equations

$$\begin{aligned}&\partial_t\nabla_\perp^2\psi + v_A^2\beta_A\partial_z\nabla_\perp^2 A \\ &= -B_0^{-1}\beta_A[\{\phi, \nabla_\perp^2\psi\} + \{\psi, \nabla_\perp^2\phi\} \\ &\quad - v_A^2(\{a, \nabla_\perp^2 A\} + \{A, \nabla_\perp^2 a\})],\end{aligned} \quad (6)$$

$$\begin{aligned}&\partial_t(1 - \lambda_e^2\nabla_\perp^2)A + \partial_z\psi \\ &= -B_0^{-1}(\{\phi, (1 - \lambda_e^2\nabla_\perp^2)A\} + \{\psi, (1 - \lambda_e^2\nabla_\perp^2)a\}).\end{aligned} \quad (7)$$

We choose the potentials of the convective mode in the form $\phi = \phi_\mathbf{q}\exp[i(\mathbf{q}\cdot\mathbf{r} - \Omega t)] + \text{c.c.}$ and $a = a_\mathbf{q}\exp[i(\mathbf{q}\cdot\mathbf{r} - \Omega t)] + \text{c.c.}$, where $\phi_\mathbf{q}$ and $a_\mathbf{q}$ are the slowly varying Fourier amplitudes of the convective potentials; $\mathbf{q} \equiv \mathbf{q}_\perp$ and Ω are the wave vector and wave frequency of the convective mode, respectively; and c.c. denotes complex conjugate. The high frequency potentials are then represented as a superposition of the pump wave and two sidebands: $\psi = \psi_0 + \psi_+ + \psi_-$ and $A = A_0 + A_+ + A_-$. The potentials $\psi_0 = \psi_\mathbf{k}\exp[i(\mathbf{k}\cdot\mathbf{r} - \omega_\mathbf{k} t)] + \text{c.c.}$ and $A_0 = A_\mathbf{k}\exp[i(\mathbf{k}\cdot\mathbf{r} - \omega_\mathbf{k} t)] + \text{c.c.}$ correspond to the pump Alfvén wave with the frequency $\omega_\mathbf{k}$ determined by Eq. (1). The two sidebands are written in the form $\psi_\pm = \psi_{\mathbf{k}_\pm}\exp[i(\mathbf{k}_\pm\cdot\mathbf{r} - \omega_{\mathbf{k}_\pm} t)] + \text{c.c.}$ and $A_\pm = A_{\mathbf{k}_\pm}\exp[i(\mathbf{k}_\pm\cdot\mathbf{r} -$

$\omega_{\mathbf{k}_\pm} t)]$ + c.c., where $\omega_{\mathbf{k}_\pm} = k_z v_A \beta_A \Lambda_{\mathbf{k}}^{-1/2} \pm \Omega$ and $\mathbf{k}_\pm = \mathbf{k} \pm \mathbf{q}$. As a result, from Eqs. (4) and (5) we obtain

$$\begin{aligned} i\Omega q^2 \phi_{\mathbf{q}} &= -B_0^{-1} \beta_A (\mathbf{q}\times\mathbf{k})_z [(k_+^2 - k^2)(\psi_{\mathbf{k}}^* \psi_{\mathbf{k}_+} - v_A^2 A_{\mathbf{k}}^* A_{\mathbf{k}_+}) \\ &+ (k^2 - k_-^2)(\psi_{\mathbf{k}} \psi_{\mathbf{k}_-}^* - v_A^2 A_{\mathbf{k}} A_{\mathbf{k}_-}^*)] \end{aligned} \quad (8)$$

$$\begin{aligned} i\Omega \Lambda_{\mathbf{q}} a_{\mathbf{q}} &= -B_0^{-1} (\mathbf{q}\times\mathbf{k})_z (\Lambda_{\mathbf{k}_+} \psi_{\mathbf{k}}^* A_{\mathbf{k}_+} \\ &- \Lambda_{\mathbf{k}} \psi_{\mathbf{k}_+} A_{\mathbf{k}}^* + \Lambda_{\mathbf{k}} \psi_{\mathbf{k}_-}^* A_{\mathbf{k}} - \Lambda_{\mathbf{k}_-} \psi_{\mathbf{k}} A_{\mathbf{k}_-}^*), \end{aligned} \quad (9)$$

where $\Lambda_{\mathbf{q}} = 1 + q^2 \lambda_e^2$ and $\Lambda_{\mathbf{k}_\pm} = 1 + k_\pm^2 \lambda_e^2$. Using Eqs. (6) and (7), we obtain the expressions for the Fourier amplitudes of the sidebands

$$\psi_{\mathbf{k}_+} = i \frac{(\mathbf{q}\times\mathbf{k})_z}{(\Omega + \delta\omega_+) B_0} \frac{k^2 - q^2}{k_+^2} \beta_A [\psi_{\mathbf{k}} \phi_{\mathbf{q}} - v_A^2 A_{\mathbf{k}} a_{\mathbf{q}}], \quad (10)$$

$$\begin{aligned} &\psi_{\mathbf{k}_-}^* \\ &= -i \frac{(\mathbf{q}\times\mathbf{k})_z}{(\Omega - \delta\omega_-) B_0} \frac{k^2 - q^2}{k_-^2} \beta_A [\psi_{\mathbf{k}}^* \phi_{\mathbf{q}} - v_A^2 A_{\mathbf{k}}^* a_{\mathbf{q}}], \end{aligned} \quad (11)$$

$$A_{\mathbf{k}_+} = i \frac{(\mathbf{q}\times\mathbf{k})_z}{(\Omega + \delta\omega_+) B_0} \frac{\Lambda_{\mathbf{k}} A_{\mathbf{k}} \phi_{\mathbf{q}} - \Lambda_{\mathbf{q}} \psi_{\mathbf{k}} a_{\mathbf{q}}}{\Lambda_{\mathbf{k}_+}}, \quad (12)$$

$$A_{\mathbf{k}_-}^* = -i \frac{(\mathbf{q}\times\mathbf{k})_z}{(\Omega - \delta\omega_-) B_0} \frac{\Lambda_{\mathbf{k}} A_{\mathbf{k}}^* \phi_{\mathbf{q}} - \Lambda_{\mathbf{q}} \psi_{\mathbf{k}}^* a_{\mathbf{q}}}{\Lambda_{\mathbf{k}_+}}, \quad (13)$$

where $\delta\omega_\pm = k_z v_A \beta_A (\Lambda_{\mathbf{k}}^{1/2} - \Lambda_{\mathbf{k}_\pm}^{1/2})$. Substituting expressions (10)–(13) into Eqs. (8) and (9), we find the dispersion relation for convective cells

$$\begin{pmatrix} \Omega + A_1 & B_1 \\ A_2 & \Omega + B_2 \end{pmatrix} \begin{pmatrix} \phi_{\mathbf{q}} \\ \hat{a}_{\mathbf{q}} \end{pmatrix} = 0, \quad (14)$$

where $\hat{a}_{\mathbf{q}} = a_{\mathbf{q}} v_A \beta_A \Lambda_{\mathbf{q}}^{1/2}$. The matrix elements $A_{1,2}$ and $B_{1,2}$ are

$$\begin{aligned} A_1 &= \frac{(\mathbf{q}\times\mathbf{k})_z^2 |\psi_{\mathbf{k}}|^2}{B_0^2} \\ &\times \left\{ \frac{k_+^2 - k^2}{q^2} \left(\frac{k^2 - q^2}{k_+^2} \beta_A^2 - \frac{1}{\Lambda_{\mathbf{k}_+}} \right) \frac{1}{\Omega + \delta\omega_+} \right. \\ &\left. + \frac{k_-^2 - k^2}{q^2} \left(\frac{k^2 - q^2}{k_-^2} \beta_A^2 - \frac{1}{\Lambda_{\mathbf{k}_-}} \right) \frac{1}{\Omega - \delta\omega_-} \right\}, \end{aligned} \quad (15)$$

$$\begin{aligned} B_1 &= -\frac{(\mathbf{q}\times\mathbf{k})_z^2 |\psi_{\mathbf{k}}|^2}{B_0^2 \Lambda_{\mathbf{k}}^{1/2} \Lambda_{\mathbf{q}}^{1/2}} \\ &\times \left\{ \frac{k_+^2 - k^2}{q^2} \left(\frac{k^2 - q^2}{k_+^2} \beta_A - \frac{\Lambda_{\mathbf{q}}^{1/2}}{\Lambda_{\mathbf{k}_+}} \right) \frac{1}{\Omega + \delta\omega_+} \right. \\ &\left. + \frac{k_-^2 - k^2}{q^2} \left(\frac{k^2 - q^2}{k_-^2} \beta_A - \frac{\Lambda_{\mathbf{q}}^{1/2}}{\Lambda_{\mathbf{k}_-}} \right) \frac{1}{\Omega - \delta\omega_-} \right\}, \end{aligned} \quad (16)$$

$$\begin{aligned} A_2 &= \frac{(\mathbf{q}\times\mathbf{k})_z^2 |\psi_{\mathbf{k}}|^2 \Lambda_{\mathbf{k}}^{1/2}}{B_0^2 \Lambda_{\mathbf{q}}^{1/2}} \left\{ \left(1 - \beta_A \frac{k^2 - q^2}{k_+^2} \right) \frac{1}{\Omega + \delta\omega_+} \right. \\ &\left. + \left(1 - \beta_A \frac{k^2 - q^2}{k_-^2} \right) \frac{1}{\Omega - \delta\omega_-} \right\}, \end{aligned} \quad (17)$$

$$\begin{aligned} B_2 &= -\frac{(\mathbf{q}\times\mathbf{k})_z^2 |\psi_{\mathbf{k}}|^2}{B_0^2} \left\{ \left(1 - \frac{k^2 - q^2}{k_+^2 \Lambda_{\mathbf{q}}} \right) \frac{1}{\Omega + \delta\omega_+} \right. \\ &\left. + \left(1 - \frac{k^2 - q^2}{k_-^2 \Lambda_{\mathbf{q}}} \right) \frac{1}{\Omega - \delta\omega_-} \right\}. \end{aligned} \quad (18)$$

In analogy with [10], considering solely large-scale convective cells ($q^2 \lambda_e^2 \ll 1$) and keeping in mind that the strongest interaction of IAWs corresponds to the case $q \ll k$ and $\mathbf{q} \perp \mathbf{k}$, matrix elements (15)–(18) are reduced to the form

$$A_1^{(0)} \approx q^2 |v_E|^2 \frac{2\Omega}{\Omega^2 - \delta\omega^2} [b - \alpha(1 + \beta_A)], \quad (19)$$

$$B_1^{(0)} \approx -q^2 |v_E|^2 \frac{2\Omega}{\Omega^2 - \delta\omega^2} \frac{1}{\Lambda_{\mathbf{k}}^{1/2}} (b - \alpha), \quad (20)$$

$$A_2^{(0)} \approx q^2 |v_E|^2 \frac{2\Omega}{\Omega^2 - \delta\omega^2} \Lambda_{\mathbf{k}}^{1/2} \left(\alpha - 2\beta_A \frac{q^2}{k^2} \right), \quad (21)$$

$$B_2^{(0)} \approx -q^2 |v_E|^2 \frac{4\Omega}{\Omega^2 - \delta\omega^2} \frac{q^2}{k^2}, \quad (22)$$

where $|v_E|^2 = |\psi_{\mathbf{k}}|^2 k^2 B_0^{-2}$, $\delta\omega = \omega_{\mathbf{k}} b (q^2/2k^2)$, $b = k^2 \lambda_e^2 / (1 + k^2 \lambda_e^2)$, and $\alpha = v_A^2 / (v_A^2 + c^2)$. In the nonrelativistic case, where $\beta_A \longrightarrow 1$ and $\alpha \longrightarrow 0$, matrix elements (14)–(22) are reduced to their values obtained in [10].

From Eq. (14) with matrix elements (19)–(22), one finds that parametric instability occurs if

$$b - 2q^2/k^2 > \alpha(1 + \beta_A). \quad (23)$$

Note that this condition is not satisfied (and thus the instability is suppressed) in a plasma with ultrarelativistic Alfvén velocities, when $v_A \gg c$, $\beta_A \longrightarrow 0$, and $\alpha \longrightarrow 1$.

Dispersion relation (14) with matrix elements (19)–(22) allows us to investigate the parametric instability of IAWs in the general case of arbitrary values of v_A^2/c^2 and $k\lambda_e$. The analysis of the dispersion relation in the general case reduces to an investigation of the roots of a biquadratic equation for the frequency Ω. In order to make our analysis more transparent, we restrict our consideration to the most important case in which $k\lambda_e \approx 1$ and $v_A^2/c^2 \ll 1$. In such a plasma, b is on the order of unity, $\alpha \approx v_A^2/c^2$, and $\beta_A \approx 1 - v_A^2/c^2$. From expressions (19)–(22) one realizes that the matrix coefficients $A_2^{(0)}$ and $B_2^{(0)}$ are small relative to the others because v_A^2/c^2 and q^2/k^2 are small. In this case, our instability analysis reduces to the solution of the equation

$$\Omega^2 - \delta\omega^2 = -A_1^{(0)}. \tag{24}$$

Dispersion relation (24) corresponds to a purely electrostatic convective mode with $\phi_{\mathbf{q}} \gg a_{\mathbf{q}}$. The solution of Eq. (24) shows that the real part of the frequency equals zero and that the growth rate $\gamma \equiv i\Omega$ is

$$\gamma = \left[2q^2|v_E|^2\left(b - 2\frac{v_A^2}{c^2}\right) - \delta\omega^2\right]^{1/2}. \tag{25}$$

Equation (25) shows that a large Alfvén velocity results in a decrease of the instability growth rate and thus plays a stabilizing role. Instability exists for wavenumbers in the range

$$0 < \left(\frac{q}{k}\right)^2 < 8\frac{|B_{\mathbf{k}}|^2}{B_0^2}\frac{k^2}{k_z^2}\frac{\Lambda_{\mathbf{k}}^2}{b^2}\left(b - 2\frac{v_A^2}{c^2}\right). \tag{26}$$

For fixed k, the fastest growth is attained at the wavenumber q given by

$$\left(\frac{q}{k}\right)^2_{\max} = 4\frac{|B_{\mathbf{k}}|^2}{B_0^2}\frac{k^2}{k_z^2}\frac{\Lambda_{\mathbf{k}}^2}{b^2}\left(b - 2\frac{v_A^2}{c^2}\right). \tag{27}$$

The maximum growth rate is thus

$$\gamma_{\text{cell}} = 2^{3/2}\omega_{\mathbf{k}}\frac{|B_{\mathbf{k}}|^2}{B_0^2}\frac{k^2}{k_z^2}\frac{\Lambda_{\mathbf{k}}^2}{b}\left(b - 2\frac{v_A^2}{c^2}\right), \tag{28}$$

Physically, this instability describes the energy transfer from short-scale Alfvénic perturbations to large-scale electrostatic convective motions that is inherent to the inverse cascade.

4. SUMMARY

The IAW parametric instability in a low-density plasma has been investigated under conditions such that the Alfvén velocity is on the order of the speed of light. We have derived nonlinear equations (4) and (5), describing the nonlinear interaction of the IAWs with large-scale convective structures. The latter can be identified in satellite data as wave structures with a great impedance ratio (on the order of or greater than the speed of light).

Using the method developed in [10], we have obtained a nonlinear dispersion relation for convective modes (14) with matrix coefficients (15)–(18). We have derived condition (23) for the onset of the parametric instability of the IAWs, from which it has been concluded that the instability can be suppressed by the effects of a nonzero ratio between the Alfvén velocity and the speed of light.

According to the measurements provided by the *FAST* satellite, the value of the parameter v_A/c in the maximum of the Alfvén velocity (the so-called Dessler's maximum) differs substantially for the day- and nighttime conditions [11, 12]. During the daytime, this ratio is on the order of 0.1–0.2 ($\alpha \ll 1$), whereas during the nighttime, $v_A/c \approx 1$ and the parameter α becomes on the order of unity. Thus, under the nighttime conditions, the parametric instability can be suppressed. It is the case of nighttime ionosphere that is of the most interest for our study. The IAW generation (e.g., as a result of feedback instability) is the most favorable during this time [13, 14].

Observations provided by the *IC-Bulgaria 1300* [15] and *FAST* [16–18] satellites at the auroral zone, below the maximum of the Alfvén velocity, indeed give evidence for the existence in the ionosphere of damped large-amplitude (up to 100 nT) Alfvén waves and convective perturbations with an impedance ratio greater than the speed of light. At higher altitudes, where the Larmor radius is larger than the skin depth, the appearance of convective cells, according to the *Polar* data [19], was not noticed. These facts indirectly confirm the results of our analysis of the parametric instability of kinetic Alfvén waves in a finite-pressure plasma [20].

A more detailed comparison of theoretical results with satellite data requires further development of the model of parametric interaction of Alfvén waves with convective cells in the ionospheric plasma. In particular, it is necessary to take into account the conductive boundaries (E layer), the dipole structure of the magnetic field, etc. Furthermore, the auroral zone is very inhomogeneous along the altitude. The region where the Alfvén velocity is on the order of the speed of light is relatively narrow (on the order of 2000–3000 km). Thus, the wave perturbations in this region are nonlocally linked to those lying in the lower ionospheric layers. All this requires the development of a nonlocal model and quite complex 3D numerical codes. The first results of numerical simulations of nonlinear Alfvén

waves in the ionospheric plasma (using a 2D code) were recently obtained in [21–23]. However, the effects of parametric interactions were not considered because of the low dimensionality of the numerical code.

ACKNOWLEDGMENTS

This study was supported in part by PPARC (grant no. PPA/G/S/2002/00094), ISTC (grant no. 2990), the Russian Foundation for Basic Research (grant no. 04-05-64657), and the Russian Academy of Sciences through the grant "Physics of the Atmosphere: Electrical Processes and Radiophysical Methods." The authors are also grateful to the British Royal Society and to the International Space Science Institute (Bern, Switzerland) for their support.

REFERENCES

1. J. B. Taylor and B. McNamara, Phys. Fluids **14**, 1492 (1971).
2. J. B. Taylor and W. B. Thompson, Phys. Fluids **16**, 111 (1973).
3. H. Okuda and J. M. Dawson, Phys. Fluids **16**, 408 (1973).
4. R. Z. Sagdeev, V. D. Shapiro, and V. I. Shevchenko, Pis'ma Zh. Éksp. Teor. Fiz. **27**, 361 (1978) [JETP Lett. **27**, 340 (1978)].
5. R. Z. Sagdeev, V. D. Shapiro, and V. I. Shevchenko, Fiz. Plazmy **4**, 551 (1978) [Sov. J. Plasma Phys. **4**, 306 (1978)].
6. A. I. Smolyakov, P. H. Diamond, and V. I. Shevchenko, Phys. Plasmas **7**, 1349 (2000).
7. A. I. Smolyakov, P. H. Diamond, and Y. Kishimoto, Phys. Plasmas **9**, 3826 (2002).
8. V. P. Lakhin, Fiz. Plazmy **29**, 157 (2003) [Plasma Phys. Rep. **29**, 137 (2003)].
9. O. G. Onishchenko, O. A. Pokhotelov, R. Z. Sagdeev, *et al.*, Nonlin. Proc. Geophys. **11**, 241 (2004).
10. O. A. Pokhotelov, O. G. Onishchenko, R. Z. Sagdeev, and R. A. Treumann, J. Geophys. Res. **108**, 1291 (2003).
11. C. C. Chaston, J. W. Bonnell, C. W. Carlson, *et al.*, J. Geophys. Res. **108**, 8003 (2003).
12. C. C. Chaston, L. M. Peticolas, J. Bonnell, *et al.*, J. Geophys. Res. **108**, 1091 (2003).
13. V. Y. Trakhtengertz and A. Y. Feldstein, J. Geophys. Res. **96**, 19363 (1991).
14. O. A. Pokhotelov, D. Pokhotelov, A. Streltsov, *et al.*, J. Geophys. Res. **105**, 7737 (2000).
15. V. M. Chmyrev, S. V. Bilichenko, O. A. Pokhotelov, *et al.*, Phys. Scr. **38**, 841 (1988).
16. K. Stasiewicz, P. Bellan, C. Chaston, *et al.*, Space Sci. Rev. **92**, 423 (2000).
17. C. C. Chaston, C. W. Carlson, W. J. Peria, *et al.*, Geophys. Res. Lett. **26**, 647 (1999).
18. C. C. Chaston, J. W. Bonnell, C. W. Carlson, *et al.*, J. Geophys. Res. **109**, A04205 (2004).
19. J. R. Wygant, A. Keiling, C. A. Cattel, *et al.*, J. Geophys. Res. **105**, 18675 (2000).
20. O. A. Pokhotelov, O. G. Onishchenko, R. Z. Sagdeev, *et al.*, J. Geophys. Res. **109**, A03305 (2004).
21. A. V. Streltsov, W. Lotko, J. R. Johnson, and C. Z. Cheng, J. Geophys. Res. **103**, 26 559 (1998).
22. A. V. Streltsov, W. Lotko, A. Keiling, and J. R. Wygant, J. Geophys. Res. **107**, 1173 (2002).
23. A. V. Streltsov and W. Lotko, J. Geophys. Res. **108**, 1289 (2003).

Translated by the authors

Plasma Physics Reports, Vol. 31, No. 10, 2005, pp. 865–870. Translated from Fizika Plazmy, Vol. 31, No. 10, 2005, pp. 933–938.

SPACE PLASMA

Dynamics of a Relativistic Electron Beam in the Vicinity of a Spherical Injecting Body in Space Plasma

E. K. Kolesnikov

Smirnov Research Institute of Mathematics and Mechanics, St. Petersburg State University, St. Petersburg, 198904 Russia

Received November 3, 2004

Abstract—The dynamics of a relativistic electron beam in the vicinity of an injector in the form of a spherical conducting body in a space plasma is considered. An equation describing the radial evolution of a steady electron beam with a self-similar density profile in the electric field of the injector is formulated. A method for calculating the radial evolution of a relativistic electron beam in the vicinity of an injector is developed. The method is based on the numerical integration of a set of ordinary differential equations for the beam radius and field potential in the space charge region under the relevant boundary conditions at the injector surface. Results are presented from numerical simulations of the radial dynamics of an electron beam in the vicinity of a spherical screen system for neutralizing the electric charge carried away by the beam. The numerical results show that the electric field of the injector hastens the beam expansion. © *2005 Pleiades Publishing, Inc.*

1. INTRODUCTION

The problem of the dynamics of charged particle beams in space plasmas has attracted the attention of researchers for over more than 30 years. This problem is of interest primarily in connection with preparing and carrying out experiments on the probing of the Earth's ionosphere and magnetosphere by beams of accelerated charged particles (usually electrons) injected into plasma from high-altitude space vehicles (and, nowadays, from Earth-orbiting satellites) [1, 2]. In recent years, new important applications of this problem have appeared that are associated with research on creating new types of space accelerating systems, such as beam systems for active remote analysis of surface rocks of atmosphere-free celestial bodies [3, 4], space accelerators for investigations in high-energy physics [5, 6], and nonrocket propulsion systems based on accelerated charged particle beams [7]. In this research, the problem of the dynamics of relativistic electron beams (REBs) in space plasmas plays an especially important role because it underlies the concept of most of the space accelerating systems that are currently under development.

In studying the problem of REB dynamics in a low-density space plasma, the evolution of a beam in the vicinity of an injecting body usually requires special consideration because, under the high vacuum conditions of outer space, the strong electric field generated by the beam in the vicinity of the body can substantially influence the beam evolution. In my earlier paper [8], it was shown that a high-altitude space vehicle (SV) injecting a low-current (about 0.1–1 A) electron beam can be charged to a potential of several units of MV or more; in this case, relativistic effects in the motion of the electrons of the neutralizing plasma current become important.

The aim of this paper is to consider the radial dynamics of a steady electron beam in the vicinity of an injector in the form of a spherical conducting body. In practical situations, this corresponds to the injection of a beam from an SV equipped with a spherical screen system for neutralizing the charge carried away by the beam. In contrast to the paper by Fedorov [9], who investigated the effect of the injector's electric field on the dynamics of a nonrelativistic beam, here the problem will be solved under the assumption that relativistic effects can play an important role in the dynamics of both the electrons of the injected beam and the electrons of the plasma current induced during the injection.

2. PROBLEM FORMULATION AND BASIC EQUATIONS

Let us consider an REB with a current J_b that is injected into a space plasma from an injector in the form of a spherical conducting body of a given radius R. We assume that the injector is at rest in the surrounding background plasma and that the plasma itself is collisionless. These assumptions correspond to the conditions

$$L_{ei} \gg R^*, \tag{1}$$

$$V \ll \left(\frac{8kT_{e,i}}{\pi m_{e,i}}\right)^{1/2}, \tag{2}$$

where L_{ei},i are the mean free paths of the plasma electrons and ions, R^* is the characteristic radius of the per-

1063-780X/05/3110-0865$26.00 © 2005 Pleiades Publishing, Inc.

turbed region (see below), T_e and T_i are the electron and ion plasma temperatures, and V is the orbital velocity of the injector. We assume that the beam is injected in exactly the radial direction and that, at the exit from the injector, it is steady and axisymmetric. We also assume that the intensity of the beam is low enough for the electric and magnetic fields of its current and space charge to not seriously affect the distribution of the plasma particles in the main part of the perturbed region (estimates show that this assumption is valid in the cases of most practical interest).

We can readily see that, under the above assumptions, the problem of the beam evolution in the vicinity of the injector splits into two independent problems: one of the radial profile of the electric field in the vicinity of a spherical conducting body from which a negative charge is carried away by the current J_b of the injected beam, and another of the dynamics of a steady electron beam in the electric field of the injector. In the case under consideration here, namely, when the beam is injected in exactly the radial direction, the second problem reduces, in essence, to that of the beam dynamics in a prescribed longitudinal electric field,

$$\mathbf{E}^0 = \frac{\partial \Phi_0(z)}{\partial z}\hat{\mathbf{i}}_z, \quad z \geq R, \tag{3}$$

where the potential $\Phi_0(z)$ of the external electric field is related to the solution $\Phi = \Phi(r)$ to the problem of the radial profile of the field potential in the vicinity of the injector by the relationship

$$\Phi_0(z) = \Phi(r). \tag{4}$$

In [8], it was shown that, under the above assumptions, the problem of determining the potential $\Phi(r)$ reduces to that of solving the following equation for the dimensionless potential $V = e\Phi/m_e c^2$:

$$\frac{d}{d\eta}\left(\eta^2 \frac{dV}{d\eta}\right) = 0.59\left(\frac{kT}{m_e c^2}\right)^{3/2}\left(\frac{R^*}{D}\right)^2 \frac{V+1}{\sqrt{V(V+2)}}. \tag{5}$$

Here, $\eta = r/R^*$ is the dimensionless radial coordinate; D is the Debye radius in the background plasma; and R^* is the radius of the space charge region, at the boundary of which the field potential is specified to have a prescribed value Φ^* satisfying the conditions

$$\frac{e\Phi^*}{kT} \gg 1, \tag{6}$$

$$\frac{e\Phi^*}{m_e c^2} \ll 1. \tag{7}$$

Under condition (6), the value of the radius R^* is close to the value that can be found from the solution to the equation (see [8])

$$J_b/e(8\pi kT/m_e)^{1/2} n_p^9 R^{*2} = 1.47. \tag{8}$$

At the boundary of the space charge region, the dimensionless potential V should satisfy the conditions [8]

$$V(1) = V^* = \frac{e\Phi^*}{m_e c^2}, \tag{9}$$

$$V'(1) = -1.29(V^*)^{1/2}\left(\frac{kT}{m_e c^2}\right)^{3/4}\frac{R^*}{D}. \tag{10}$$

Assuming that the external longitudinal electric field $\mathbf{E}^0$ is known, let us now turn to the problem of the beam dynamics in this field. We restrict ourselves to considering a paraxial beam; i.e., we assume that the transverse and longitudinal velocities of the beam electrons satisfy the condition

$$v_\perp/v_z \equiv \nu \ll 1. \tag{11}$$

Under this condition, the problems of the transverse and the longitudinal motion of the beam electrons can be treated separately (see, e.g., [10]).

The equation of the transverse motion of a beam electron that does not collide with the particles of the background plasma can be written in the form [10]

$$\frac{d\mathbf{p}_\perp}{dt} = -e\nabla_\perp(\varphi - \beta A_z), \tag{12}$$

where $\mathbf{p}_\perp = m_{e0}\gamma\mathbf{v}_\perp$ is the transverse component of the momentum of the beam electron, $\gamma = 1/\sqrt{1 - v^2/c^2}$ is its Lorentz factor, $\beta = v/c$, and φ and A_z are the electric and vector potentials of the self-consistent electromagnetic field.

The equation for the longitudinal motion of a beam electron can be obtained from the energy equation

$$\frac{d\varepsilon}{dt} = e\mathbf{v}\cdot\mathbf{E}, \tag{13}$$

where $\varepsilon = m_{e0}\gamma c^2$ is the relativistic energy. To within terms of first order in the parameter ν, Eq. (13) can be written as [10]

$$\frac{d}{dt} m_{e0}\gamma(v_z)c^2 = e v_z E_z^0, \tag{14}$$

where

$$\gamma(v_z) = [1 - (v_z/c)^2]^{-1/2}.$$

The first integral of Eq. (14) reflects the conservation of the total energy of a beam electron:

$$m_{e0}\gamma c^2 + e\Phi_0 = m_{e0}\gamma_0 c^2 + e\Phi_0^H, \tag{15}$$

where γ_0 and Φ_0^H are the values of γ and Φ_0 at the surface of the injector.

The dependence of the longitudinal velocity v_z on the z coordinate is given by the expression

$$v_z = \frac{dz}{dt} = \frac{c}{\gamma}\sqrt{\gamma^2 - 1} \equiv \Psi(z), \quad (16)$$

where

$$\gamma(z) = \gamma_0 + \frac{e}{m_{e0}c^2}[\Phi_0^H - \Phi_0(z)]. \quad (17)$$

Integrating expression (16) yields the following law for the longitudinal motion of a beam electron injected at the time τ:

$$\int_R^z \frac{dz}{\Psi(z)} = t - \tau. \quad (18)$$

According to conservation law (15), the time dependence of the relativistic energy of a beam electron can be determined from the relationship

$$\varepsilon(t) = \varepsilon_0 + e[\Phi_0^H - \Phi_0(z(t))], \quad (19)$$

where the function $z(t)$ is given by Eq. (18).

Equation (18) and relationship (19) imply that, if the beam at the exit from the injector is monoenergetic, then all the electrons of the beam's arbitrary transverse segment S^τ injected at the time τ move in the same manner along the z coordinate and, at any time, they have the same energy $\varepsilon(t)$ and the same relativistic mass $m_e(t)$.

When there is a statistical spread in the transverse coordinates and momenta of the beam electrons, the distribution function $F^\tau(\mathbf{r}_\perp, \mathbf{p}_\perp, t)$ of the electrons of the segment S^τ in the phase space $(\mathbf{r}_\perp, \mathbf{p}_\perp)$ of the transverse coordinates and momenta evolves according to the equation [10]

$$\frac{\partial F^\tau}{\partial t} + \frac{\mathbf{p}_\perp}{m_e(t)} \cdot \nabla_{\mathbf{r}_\perp} F^\tau - e\nabla_{\mathbf{r}_\perp}(\varphi - \beta A_z) \cdot \nabla_{\mathbf{p}_\perp} F^\tau = 0, \quad (20)$$

where $m_e(t) = \varepsilon(t)/c^2$, the dependence $\varepsilon(t)$ is described by Eq. (18) and relationship (19), and the dependence $\beta(t)$ is given by expressions (16) and (17).

Note that, in the cases of practical interest, the beam density at the surface of the injector is substantially higher than the density of the background plasma. Consequently, the beam evolution in the vicinity of the injector is primarily governed by the influence of the beam's electromagnetic self-field and the electric field of the injector. In this case, the quantity in parentheses in Eq. (20) is equal to $\varphi - \beta A_z = (\gamma^2\beta)^{-1}A_z$ (where A_z is the z component of the vector potential of the beam's magnetic self-field) and Eq. (20) takes the form

$$\frac{\partial F^\tau}{\partial t} + \frac{\mathbf{p}_\perp}{m_e(t)} \cdot \nabla_{\mathbf{r}_\perp} F^\tau - \frac{e}{\gamma^2\beta}\nabla_{\mathbf{r}_\perp} A_z \cdot \nabla_{\mathbf{p}_\perp} F^\tau = 0. \quad (21)$$

By averaging Eq. (21) over the transverse momenta, we obtain the so-called transport equations, i.e., the equations for the first moments of the distribution function F^τ. In [11], it was shown that these equations yield the following equation for the beam envelope, which describes the time evolution of the radius R_b of a beam with a self-similar density profile:

$$\chi(r_\perp, t) = \frac{1}{2\pi R_b^2(t)}\Phi(x), \quad (22)$$

where $\Phi(x)$ is a prescribed function of the dimensionless coordinate $x = r_\perp/R_b$.

In the case under consideration, the beam envelope satisfies the equation

$$\frac{d^2\xi}{dt'^2} + \frac{1}{\gamma}\frac{d\gamma}{dt'}\frac{d\xi}{dt'} - \frac{\gamma_0^3\beta_0}{2\gamma^3\beta}\frac{1}{\xi} = \frac{\gamma_0^2(\varepsilon^2 + \sigma_\theta^2)}{\gamma^2}\frac{1}{\xi^3}, \quad (23)$$

where the dimensionless radius ξ and dimensionless time t' are defined as

$$\xi = R_b/R_{b0}, \quad t' = t/t_0, \quad (24)$$

and the time scale is $t_0 = \gamma_0\eta_\Phi/\omega_{b0}$. The constants ε and σ_θ in Eq. (23) are given by the expressions

$$\sigma_\theta = \frac{2\Phi(x)x^3\dot{\theta}_0(x)\gamma_0}{\omega_{b0}\eta_\Phi}, \quad \varepsilon = \frac{2E_0}{R_{b0}^2\omega_{b0}\eta_\Phi}. \quad (25)$$

Here, the constant in the denominators is defined by the relationship $\omega_{b0}^2 = 4\pi e^2\bar{n}_{b0}/\gamma_0 m_0$ (with $\bar{n}_{b0} = N_b^0/\pi R_{b0}^2$ being the initial electron density in the segment S^τ), $\dot{\theta}_0(x)$ is the radial profile of the angular velocity of the beam electrons, E_0 is the root-mean-square beam emittance in the segment S^τ, and the constant coefficient η_Φ for a given radial profile of the beam density $\Phi(x)$ has the form

$$\eta_\Phi - \left[2\int_0^1 \Phi(x)x^3 dx\right]^{\frac{1}{2}}. \quad (26)$$

In Eq. (23), we switch to a new independent variable z. Using the relationships

$$\frac{d\xi}{dt'} = t_0 v_z \frac{d\xi}{dz}, \quad (27)$$

$$\frac{d^2\xi}{dt'^2} = t_0^2 v_z^2\left(\frac{1}{v_z}\frac{dv_z}{dt}\frac{d\xi}{dz} + \frac{d^2\xi}{dz^2}\right), \quad (28)$$

and taking into account Eq. (14), we then write Eq. (23) in the form

$$\frac{d^2\xi}{dz^2} = \left[\frac{1}{L^E(z)} + \frac{1}{L^{v_z}(z)}\right]\frac{d\xi}{dz} + \frac{\gamma_0^3 u}{2\gamma^3 v_z^3 t_0^2}\frac{1}{\xi} + \frac{\gamma_0^2}{\gamma^2 v_z^2 t_0^2}\frac{(\varepsilon^2 + \sigma_\theta^2)}{\xi^3}. \quad (29)$$

Here, u is the initial longitudinal velocity of the beam electrons in the segment S^τ and

$$L^E(z) = -\frac{\gamma(z) m_0 c^2}{eE_z(z)}, \quad (30)$$

$$L^{v_z}(z) = -\frac{v_z}{dv_z/dz}, \quad (31)$$

are the functions of the z coordinate, which are related to the potential $\Phi_0(z)$ by expressions (16) and (17).

Finally, we reduce Eq. (29) to a dimensionless form by multiplying it by $(ut_0)^2$ and by using expression (16):

$$\frac{d^2\xi}{dz'^2} = \left[\frac{1}{l^E(z')} + \frac{1}{l^{v_z}(z')}\right]\frac{d\xi}{dz'} + \frac{1}{2\xi}\left[\frac{\gamma_0^2 - 1}{\gamma^2 - 1}\right]^{3/2} + \frac{\gamma_0^2 - 1}{\gamma^2 - 1}\frac{\varepsilon^2 + \sigma_\theta^2}{\xi^3}, \quad (32)$$

where $z' = z/ut_0$ is the dimensionless longitudinal coordinate and the dimensionless functions are defined as

$$l^E(z') = L^E/ut_0, \quad l^{v_z} = L^{v_z}/ut_0.$$

Equations (29) and (32) determine the surface described by the boundary of the propagating beam segment S^τ.

Hence, the radial evolution of an electron beam in the vicinity of an injecting body can be determined by numerically solving Eq. (29) or (32). Before solving the equations, however, it is necessary to find analytic approximations for the functions $L^E(z)$, $L^{v_z}(z)$, and $\gamma(z)$ on the right-hand side of Eq. (29) (or for the corresponding functions in Eq. (32)) on the basis of the results of numerically calculating the radial profile of the potential in the vicinity of the injector. This is why, in practice, a more convenient procedure is that of calculating the radial evolution of the beam in the vicinity of the injector by simultaneously solving the equation for the radial beam dynamics and Eq. (5) for the field potential in the space charge region with the corresponding boundary conditions for the beam radius and its derivative, as well as for the potential and its derivative, at the injector surface $z = R$. In this way, the boundary conditions for the potential should be determined in advance by numerically integrating Eq. (5) with conditions (9) and (10) at the outer boundary of the space charge region.

Let us convert Eq. (29) for the radial beam evolution into a form that is suitable for calculations by means of the above procedure. In this equation, we switch from the variable z to the same independent dimensionless variable as in Eq. (5), namely, $\eta = z/R^*$. Using expressions (16), (17), (30), and (31) and performing the corresponding manipulations, we reduce Eq. (29) to the form

$$\frac{d^2\xi}{d\eta^2} = \frac{\gamma}{\gamma^2 - 1}\frac{dV}{d\eta}\frac{d\xi}{d\eta} + \frac{\mu}{2}\left(\frac{\gamma_0^2 - 1}{\gamma^2 - 1}\right)^{\frac{3}{2}}\frac{1}{\xi} + \mu^2\frac{(\varepsilon^2 + \sigma_\theta^2)}{\xi^3}\frac{\gamma_0^2 - 1}{\gamma^2 - 1}, \quad (33)$$

where $\mu = (R^*/ut_0)^2$ is the dimensionless parameter and $\gamma = \gamma_0 + V(\eta) - V_0$, with γ_0 and V_0 being the values of the relativistic factor of the beam electrons and of the dimensionless field potential at the injector surface, respectively.

Particular problems were solved based on a specially devised computer program for numerical integration of the set of Eqs. (5) and (33) (written as a set of four first-order ordinary differential equations) by a fourth-order Runge–Kutta–Merson method with an automatically adjusted integration step [12]. Along with the procedure for numerical integration of the set of Eqs. (5) and (33), the program also contains a procedure that numerically integrates field equation (5) and calculates the corresponding values of the dimensionless potential V and its derivative $dV/d\eta$ at the injector surface for given values of the parameters R, J_b, n_p^0, and T.

3. RESULTS OF NUMERICAL CALCULATIONS

To illustrate how the method developed here can be employed, we consider the dynamics of a steady electron beam in the vicinity of a spherical injecting body in the following particular situation. Let a steady axisymmetric cold electron beam be injected from an SV equipped with a spherical screen system for neutralizing the charge carried away by the beam. The beam parameters are as follows: the electron energy is 5 MeV, the beam current is 20 A, and the initial beam radius is 1 cm. At the exit from the injector, the beam is uniform over its cross section, the initial transverse velocity of the beam electrons being equal to zero, $\mathbf{v}_\perp^0 \equiv 0$. The neutralizing screen system is a spherical conducting shell of radius 30 m, connected electrically to the SV by a set of conductors (the characteristic dimension of the SV is assumed to be much smaller than the screen radius). The parameters of the background plasma are

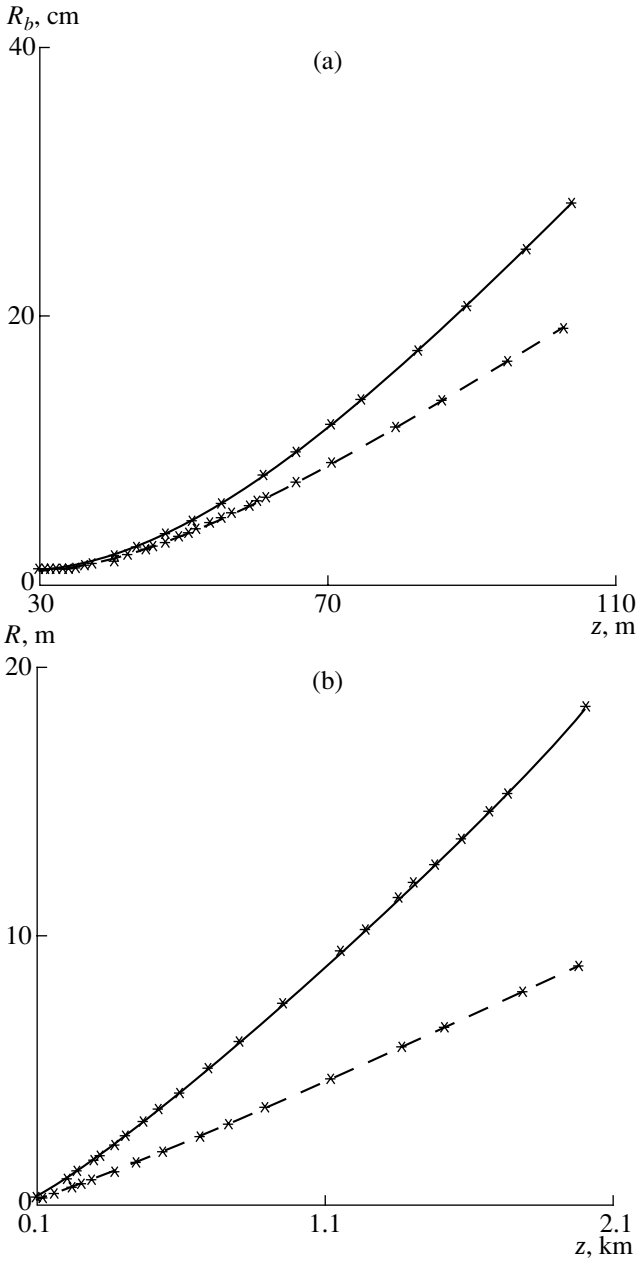

Fig. 1. Calculated beam radius as a function of the distance from the center of the screen at (a) short and (b) long distances from the injector with (solid curves) and without (dashed curves) allowance for the effect of the induced electric field on the beam evolution.

specified to be $n_p^0 = 10$ cm^{-3} and $T = 1$ eV. Let us calculate the transverse beam evolution in the electric field of the charge accumulated in the screen under the assumption that the beam is injected exactly in the radial direction.

According to the analysis carried out in Section 2, the radial profile of the electric potential in the space charge region around the screen is determined by solving Eq. (5) with boundary conditions (9) and (10) at $\eta = r/R^* = 1$. Let the electric potential φ^* at the boundary of the space charge region be equal to 10 V (this corresponds to $e\varphi^*/kT = 10$). For the above values of the beam current J_b^0 and of the unperturbed plasma temperature and density, n_p^0 and T, the radius of the space charge region is equal to $R^* = 2.01$ km. By numerically integrating Eq. (5) with conditions (9) and (10) at the outer boundary of the space charge region, we determine the values of the dimensionless potential V and of its derivative at the screen surface: $V|_{\eta = \eta_0} = 4.20$ and $(dV/d\eta)|_{\eta = \eta_0} = -288$ (in the case at hand, we have $\eta_0 = R/R^* = 0.0149$). The dimensional screen potential and dimensional electric field strength at the screen surface that correspond to these values are equal, respectively, to $\Phi_0 = 2.14$ MV and $E_0 = 71.5$ kV/m.

In accordance with the procedure described in Section 2, the radial beam evolution is determined by the simultaneous numerical integration of Eqs. (5) and (33). The calculated dependence of the beam radius on the axial coordinate z (in the case at hand, it coincides with the radial coordinate r) is illustrated in Fig. 1, which shows the dependence $R_b(z)$ in a zone adjacent to the injector (over a distance of up to 110 m from the injector center) and in a zone distant from the injector (over a distance from 110 m up to the boundary of the space charge region). In order to illustrate the effect of the electric field on the beam expansion, the dashed curve in Fig. 1 shows the radial evolution of a beam with the same parameters that was calculated without allowance for the electric field of the injector. From Fig. 1 it can be seen that, under the action of the injector's electric field, the beam expands far more rapidly.

4. CONCLUSIONS

The main results of the present work can be summarized as follows.

(i) An equation has been obtained that describes the radial evolution of a steady axisymmetric REB with a self-similar density profile in the electric field induced in the vicinity of a spherical injecting body that is at rest in a collisionless background plasma.

(ii) A method for calculating the radial evolution of an REB in the vicinity of the injector has been developed that is based on the simultaneous numerical integration of a set of ordinary differential equations for the beam radius and electric field potential in the space charge region with the relevant initial conditions at the injector surface.

(iii) Results from numerical calculations of the radial evolution of a steady REB in the electric field induced in the vicinity of a spherical screen system for neutralizing the electric charge of a beam-injecting SV have been presented that were obtained for the characteristic background plasma conditions at high-altitude

orbits. The calculated results show that the electric field substantially hastens the beam expansion.

REFERENCES

1. D. R. Winkler, Aerokosm. Tekh. **2** (3), 138 (1984).
2. *Artificial Particle Beams in Space Plasma*, Ed. by B. Grandal (Plenum, New York, 1982; Mir, Moscow, 1985).
3. E. K. Kolesnikov and A. P. Kuryshev, Vestnik LGU (Dep. VINITI), No. 41-82 (1982).
4. E. K. Kolesnikov, A. P. Kuryshev, and A. S. Manuĭlov, *Methods of X-ray Spectral Analysis* (Nauka, Novosibirsk, 1986), p. 85 [in Russian].
5. R. Varley, R. G. Hohlfeld, G. Sandri, *et al.*, Nuovo Cimento B **105**, 23 (1990).
6. V. S. Panasyuk, Kosm. Issled. **33**, 468 (1995).
7. G. Vulpetti, Ann. UMCS. AAA **43**, 373 (1988–1989).
8. E. K. Kolesnikov, Fiz. Plazmy **28**, 360 (2002) [Plasma Phys. Rep. **28**, 327 (2002)].
9. V. A. Fedorov, Kosm. Issled. **26**, 270 (1988).
10. E. K. Kolesnikov and A. S. Manuĭlov, Zh. Tekh. Fiz. **74** (9), 103 (2004) [Tech. Phys. **49**, 1208 (2004)].
11. E. K. Kolesnikov, A. S. Manuĭlov, and B. V. Filippov, *Dynamics of Charged Particle Beams in Gas-Plasma Media* (SPbGU, St. Petersburg, 2002) [in Russian].
12. O. B. Arushanyan and S. F. Zaletkin, *Numerical Solution of Ordinary Differential Equations using FORTRAN* (MGU, Moscow, 1990) [in Russian].

Translated by O.E. Khadin

Plasma Physics Reports, Vol. 31, No. 10, 2005, pp. 871–885. Translated from Fizika Plazmy, Vol. 31, No. 10, 2005, pp. 939–953.

LOW-TEMPERATURE PLASMA

Study of the Dark Phase in the Initial Stage of the Positive Column Formation in an Argon Glow Discharge

N. A. Dyatko[1], Yu. Z. Ionikh[2], A. V. Meshchanov[2], and A. P. Napartovich[1]

[1] *Troitsk Institute for Innovation and Thermonuclear Research, Troitsk, Moscow oblast, 142090 Russia*

[2] *Fock Research Institute of Physics, St. Petersburg State University, Ul'yanovskaya ul. 1, Petrodvorets, St. Petersburg, 198504 Russia*

Received November 18, 2004; in final form, December 27, 2004

Abstract—The initial stage of the positive column formation in an argon glow discharge is investigated both experimentally and theoretically. A decrease in the plasma radiation intensity (the so-called "dark phase") was observed experimentally over a time period of about 1 ms. A similar dip was also observed in the time dependence of the electric field strength. The time evolution of the population of the lowest metastable state of Ar was measured. A relevant theoretical model has been developed and used to perform calculations for the actual experimental conditions. A comparison between the numerical and experimental results shows that the model adequately describes the processes that occur during the formation of the positive column in an argon glow discharge. Experimental and theoretical study shows that the dark-phase effect is related to an excessive amount of metastable Ar atoms at the beginning of a discharge and, consequently, to high rates of stepwise ionization and chemionization. © *2005 Pleiades Publishing, Inc.*

1. INTRODUCTION

The so-called "dark phase" in the initial stage of the positive column formation was first observed in [1, 2], where glow discharges in pure helium and its mixtures with small additives of nitrogen or carbon oxide were investigated under conditions such that the time intervals between the discharge pulses were fairly long. It was found that, when the output voltage of the power supply was high enough, i.e., when the discharge current was mainly determined by the ballast resistance rather than the resistance of the discharge itself, the discharge displayed a number of specific features. In particular, after a short and very intense emission peak at the beginning of the current pulse, the emission intensity from all the spectral lines and bands dropped and remained almost zero over a certain period of time. The dark phase (DP) lasted from a few tens of microseconds to a few milliseconds. The emission intensity then rapidly increased and reached a steady-state level (generally, after a few oscillations). In this case, the discharge current, which was controlled by the ballast resistance, remained almost constant throughout the discharge pulse. A similar effect was observed in a continuous discharge after additional excitation of the plasma by a high-voltage nanosecond pulse [3, 4].

In [2], this effect was explained as follows: In discharges excited in mixtures of helium with a small additive of a molecular gas M, the main ionization process is Penning ionization,

$$\mathrm{He^*} + \mathrm{M} \longrightarrow \mathrm{He} + \mathrm{M^+} + e. \qquad (1)$$

At the beginning of the discharge, when the discharge current is low, the discharge voltage is high and the electric field in the discharge is much higher than its steady-state value. This results in the intense excitation of the gas atoms and molecules and the generation of the initial spike in the emission intensity. At the same time, an excessive amount of metastable atoms are produced. As a consequence, after the current has reached its steady-state level, the density of the electrons produced in reaction (1) is much higher than that in the steady-state phase of the discharge. This leads to a redistribution of the voltage between the discharge and the ballast resistance, the electric field in the discharge decreasing below its steady-state value, and the excitation rate becoming very low. Since the rate of ambipolar diffusion under these conditions is also low, the excess electrons very slowly escape to the wall, so the DP duration can significantly exceed the decay time of the metastable atoms.

In pure helium, reaction (1) does not occur; in this case, however, its role can be played by the two-body collision reaction between metastable He atoms,

$$\mathrm{He^*} + \mathrm{He^*} \longrightarrow \mathrm{He^+} + \mathrm{He} + e. \qquad (2)$$

Processes similar to reaction (2) take place in other noble gases as well. Therefore, it is reasonable to expect that the DP effect will also manifest itself in them. The aim of this study was to observe and study the DP effect in argon.

2. EXPERIMENTAL SETUP

The experimental setup was similar to that described in [2]. The diameter of the U-shaped discharge tube made of molybdenum glass was 2.7 cm, the length of

1063-780X/05/3110-0871$26.00

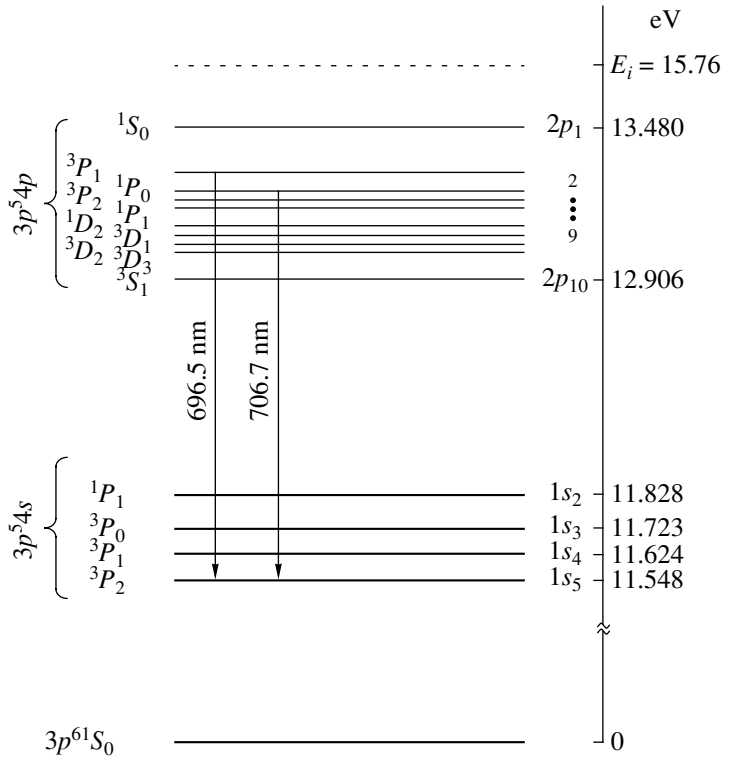

Fig. 1. Schematic diagram of the lower electronic states of Ar.

its horizontal part was 12 cm, and the distance between the cylindrical Ti electrodes was 30 cm. The anode was grounded. Spectrally pure argon (99.999%) was continuously pumped through the discharge tube and a system of liquid-nitrogen traps. A repetitive discharge was produced by means of an electronic switch set in parallel to the discharge tube. The response time of the switch was 0.3 μs.

Optical measurements were performed along the axis of the horizontal part of the tube. The plasma radiation was recorded using a monochromator with a 1200-line/mm diffraction grating, an FEU-106 photomultiplier operating in the photon counting regime, a pulsed amplifier, a 256-channel reverse photon counter with a time resolution of 1 μs (designed by G.V. Zhuvikin and V.A. Ivanov), and a PC. The concentration of metastable Ar atoms was determined from the absorption of the probing radiation produced by a small-size hollow cathode and propagating along the axis of the discharge tube. The ratio between the widths of the emission and absorption lines was found by the method described in [2]. We also measured the integral (over wavelengths) emission intensity from different points of the positive column. These measurements were performed across the tube using a movable photomultiplier tube.

The electric field in the plasma was determined using probes set at the discharge axis, 2.7 cm from one another. The probe signals were fed to a digital oscilloscope through a high-resistance divider and differential amplifier.

3. EXPERIMENTAL RESULTS

Figure 1 shows a schematic diagram of the lower electronic states of Ar. The arrows show the spectral lines whose emission intensities were measured in our experiments.

By analyzing the time evolution of the emission intensity from the positive column, we determined the experimental conditions at which the DP effect was present in an argon discharge. It was found that the pressure should be a few torr and the discharge current should be about 1 mA. Moreover, as was said above, the output voltage of the power supply and the ballast resistance must be high enough. Most of the experiments were carried out at a pressure of $p = 5$ torr, steady-state current of $i = 0.7$ mA, supply voltage of $U = 3.6$ kV, and ballast resistance of $R_b = 4.45$ MΩ. Under these conditions, the reduced electric field was $E/N = 5.5$ Td (when calculating the atomic density N, the gas temperature was assumed to be 300 K, which is the upper estimate found from the heat conduction equation). The corresponding electron density averaged over the discharge cross section was $\sim 1.5 \times 10^9$ cm^{-3}.

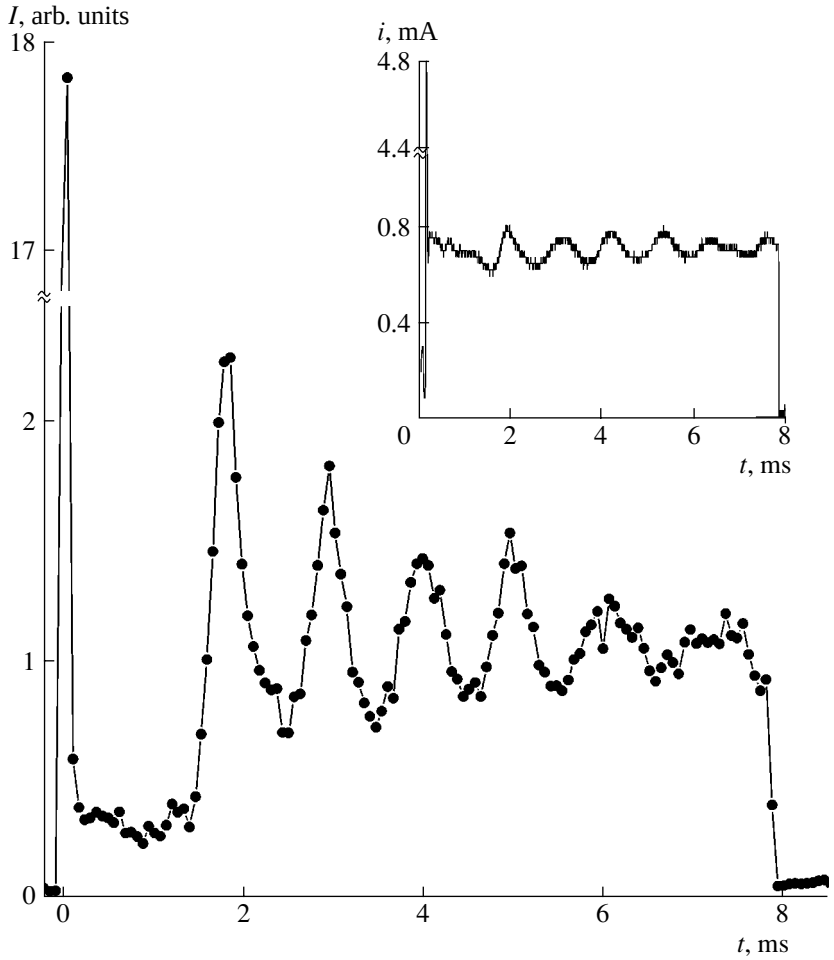

Fig. 2. Measured time evolution of the emission intensity of the 696.5-nm line for $p = 5$ torr, $i = 0.7$ mA, and $T = 80$ ms. The insert shows the waveform of the discharge current.

Figure 2 shows the measured time evolution of the intensity of the Ar 696.5-nm line for a discharge duration of $\tau = 8$ ms and repetition period of $T = 80$ ms. In fact, this is a single-pulse mode because the time interval between pulses is much longer than the plasma decay time (the electron density decreases by two orders of magnitude over a time of $T-\tau = 72$ ms). The line intensity shows a sharp spike at the instant of discharge ignition, and then, over a time interval of about 1.5 ms, it is much lower than that in the steady-state phase. After this, it sharply increases again, performs several oscillations, and reaches a steady-state level. Similar behavior of the plasma radiation intensity was observed in helium [1, 2]; however, the emission intensity of helium plasma during the DP was two orders of magnitude lower than that in the steady-state phase, whereas, in the case of argon, it was only four times lower. The intensities of the other Ar spectral lines behaved in the same manner.

In argon, the range of discharge currents at which the DP was observed was much narrower than that in helium and its mixtures. As the current increased above 1 mA, the effect became less pronounced. This can be seen from Fig. 3, which corresponds to a current of 1.4 mA ($R_b = 2.2$ MΩ). In this case, the emission intensity during the DP was only two times lower than that in the steady state phase. At higher discharge currents, the DP disappeared. This also occurred when the time interval between the discharge pulses was reduced (Fig. 4). In this case, the initial spike in the emission intensity also disappeared. Such behavior is similar to that observed in helium [1, 2].

Figure 5 shows the measured time evolution of the reduced electric field for the conditions corresponding to Figs. 2–4. It can be seen that the time behavior of E/N correlates with that of the line emission intensities. In a single-pulse operating mode (Figs. 5a, 5e; $T = 80$ ms), the reduced field E/N shows a spike at the instant of discharge ignition, a nearly zero value during the DP, and oscillations in the rest of the discharge. Note that the sharp change in the discharge voltage and the low electron density just after breakdown did not allow us to

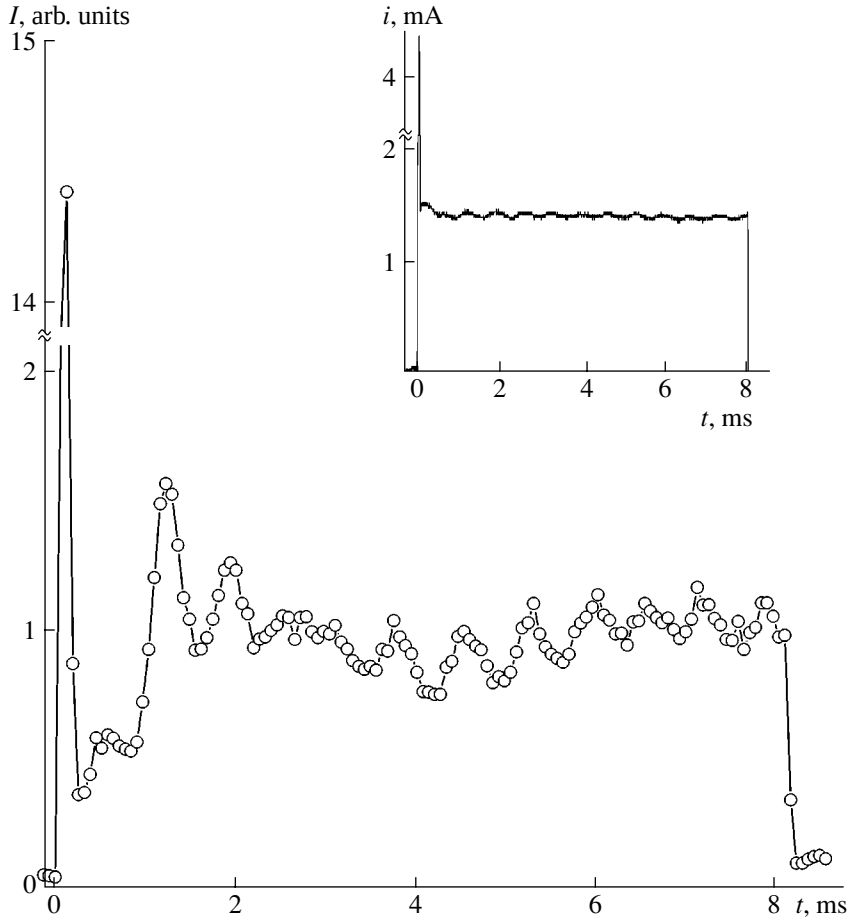

Fig. 3. Measured time evolution of the emission intensity of the 706.7-nm line for $p = 5$ torr, $i = 1.4$ mA, and $T = 80$ ms. The insert shows the waveform of the discharge current.

correctly measure the electric field in the initial stage of the discharge (as well as just after discharge termination). Nevertheless, the electric field during the DP is certainly much lower than the steady-state field. As the time interval between the pulses decreased, the time dependences of the reduced electric field became smoother (see Figs. 5b, 5c) and, then, both the initial spike and the subsequent dip disappeared.

After discharge ignition, the concentration of the $1s_5$ metastable Ar atoms becomes four to ten times higher than that in the steady-state phase (Figs. 6, 7). During the DP, their concentration decreases twofold as compared to that in the steady-state phase. The characteristic decay time of metastable levels during the DP is appreciably shorter than that after the end of the discharge (cf. Figs. 6a, 6b, 7a, and 7b). This can be explained by the large density of the electrons and $Ar(1s_5)$ atoms and, accordingly, the large quenching rate of these levels (see Section 5). A decrease in the time interval between the discharge pulses leads to a substantial decrease in the amplitude of the initial spike in the concentration of metastable atoms.

All the time dependences shown in Figs. 2–7 display oscillations with a period of about 1 ms. Oscillations in the electric field and the local emission intensity (measured across the discharge) were also observed in continuous discharges: at a current of 0.7 mA, the oscillation period was the same as in pulsed discharges, whereas, at a current of 1.4 mA, it was 1.5 times shorter. Optical measurements performed across a continuous discharge showed that the oscillation phase depended monotonically on the photomultiplier position; this means that these oscillations are related to moving striations. Similar measurements performed in a single-pulse mode ($T = 80$ ms) showed a different picture (Fig. 8). In this case, the phases of optical signals from different points along the discharge axis were the same; therefore, the oscillations were caused by in-phase oscillations of the emission intensity from the positive column as a whole. A significant misphasing of oscillations, indicating the origin of moving striations, was observed only at the end of the discharge.

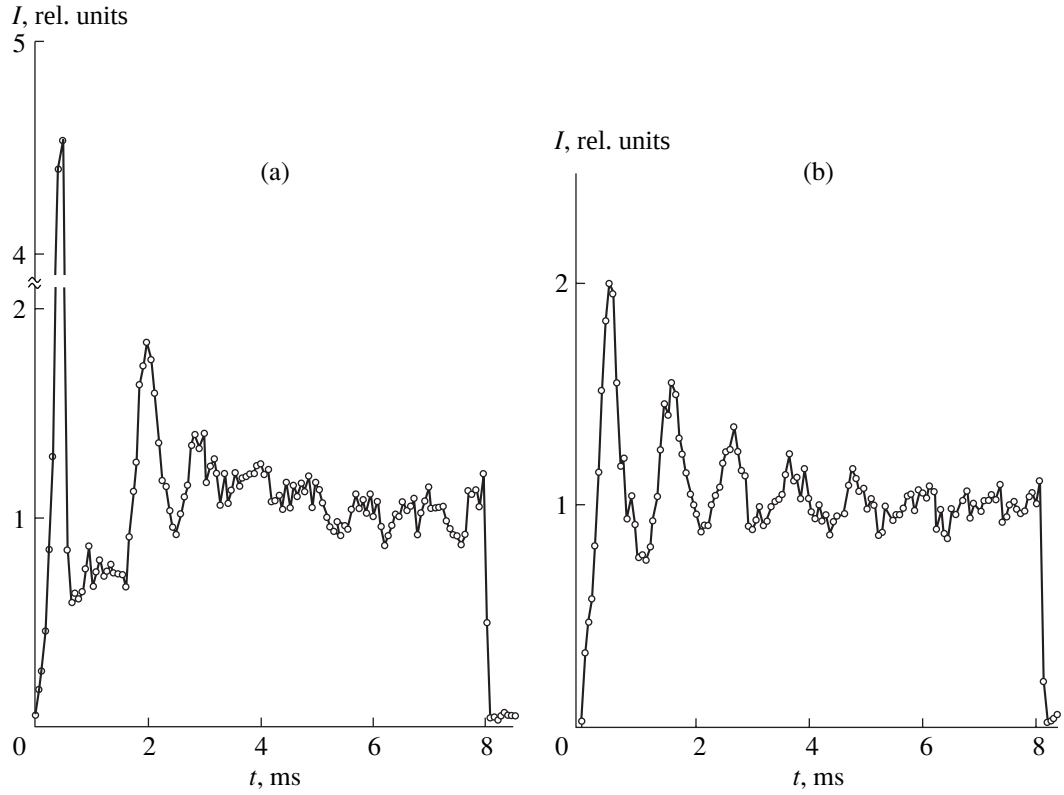

Fig. 4. Measured time evolution of the emission intensity of the 696.5-nm line for $p = 5$ torr, $i = 0.7$ mA, and $T =$ (a) 9 and (b) 8.2 ms.

4. THEORETICAL MODEL

In order to reveal the mechanisms responsible for the DP effect in the positive column of a glow discharge in argon, we have analyzed all the available literature data on the processes governing the population of the excited states and the ionization balance in an argon discharge under actual experimental conditions. Based on these data, a theoretical model has been developed that describes the time evolution of the parameters of the positive column over the time interval from applying the discharge voltage to establishing a steady state. The equations for the electron and ion densities and for the populations of the excited states, the Boltzmann equation for the electron energy distribution function (EEDF), and the equation for the electric circuit are solved self-consistently. The model does not account for the electrode sheaths; i.e., it concerns only the positive column, which is assumed to be uniform along the tube. In other words, the so-called zero-dimensional model is used to describe the kinetics of the electrons, ions, and excited atoms. A schematic of the lower electronic states of Ar is shown in Fig. 1, and the processes included in the model are listed in the table. Let us consider the model in more detail.

The kinetics of the four lower electronic states of Ar is thoroughly taken into account. Two of these levels ($1s_5$ and $1s_3$) are metastable, whereas the other two ($1s_4$ and $1s_2$) are resonant. By analogy to [5], the higher electronic states are combined into two effective levels (F and A), with the level F being the sum of the $3p^5 4p$ levels.

We used the same transport cross section for electron scattering by Ar atoms, cross sections for excitation of electronic levels from the ground state, and cross section for ionization from the ground state as in [5]. In that paper, the rate constants for the excitation of the $1s_5$, $1s_4$, $1s_3$, and $1s_2$ levels were measured and compared to those calculated by solving the Boltzmann equation. The set of cross sections obtained in [5] provides good agreement between the calculated and measured excitation rate constants. Moreover, the calculated values of the drift velocity and the ionization coefficient are also in good agreement with the available experimental data. Therefore, we may consider this set of the cross sections to be self-consistent.

In [5], the transport cross section was chosen according to a recommendation in [6], whereas the ionization cross section was taken from [7]. The values of these cross sections are known with a high accuracy. However, there is a large scatter in both the experimental and theoretical data on the maximum values of the cross sections for the excitation of the $1s_5$, $1s_4$, $1s_3$, and $1s_2$ levels. The maximum of the cross sections for the excitation of the lower $1s_5$ metastable level varies from

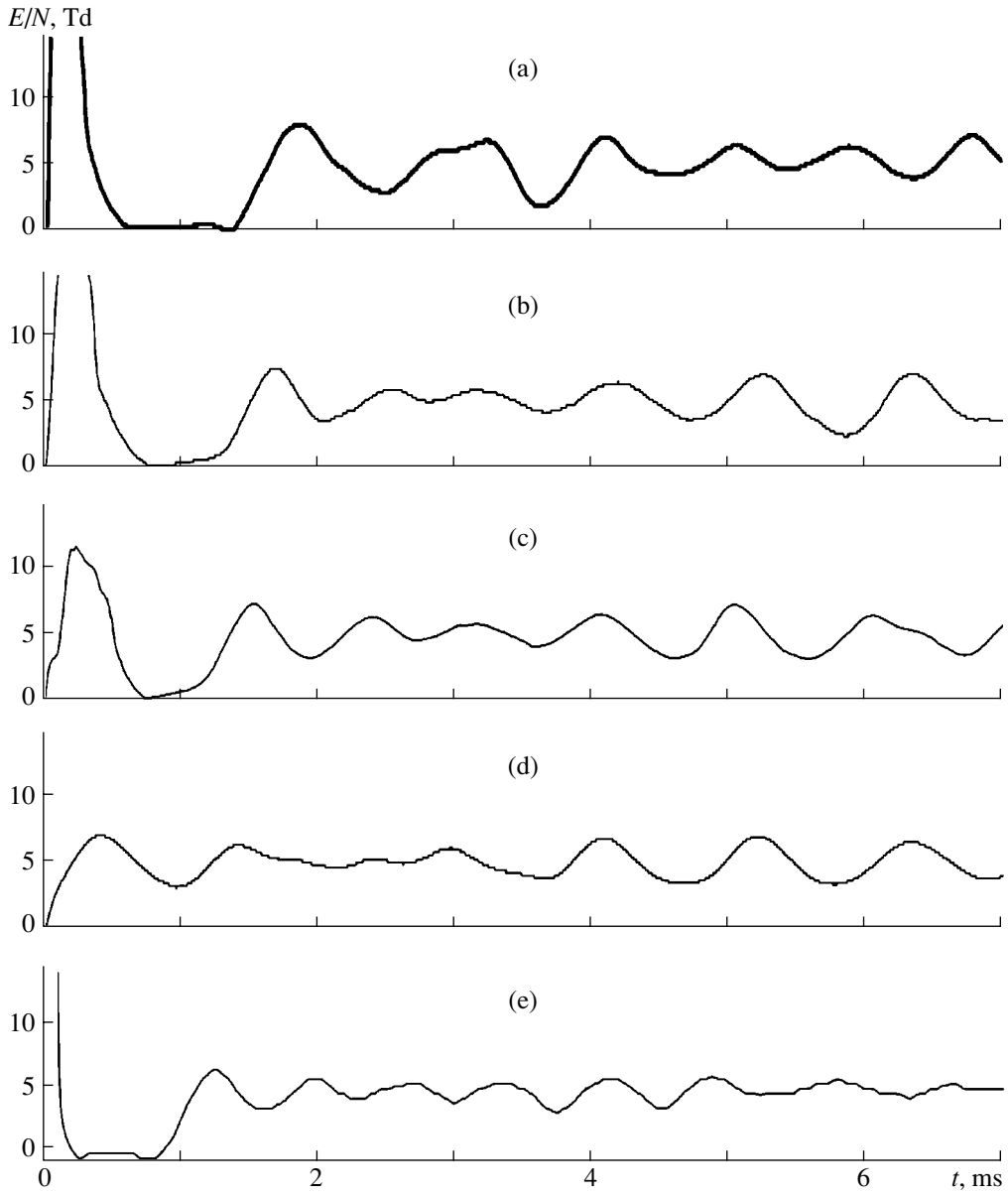

Fig. 5. Measured time evolution of the reduced electric field for p = 5 torr, i = (a–d) 0.7 and (e) 1.4 mA, and T = (a, e) 80, (b) 10, (c) 9, and (d) 8.2 ms.

0.4×10^{-17} cm^2 (experiment [9]) to 10^{-17} cm^2 (experiment [8]) and even to 2.3×10^{-17} cm^2 (computations [8]). There is also scatter in the data on the cross sections for the excitation of the $1s_4$, $1s_3$, and $1s_2$ levels. Note that, in [5], the cross sections for the excitation of the $1s_5$, $1s_4$, $1s_3$, and $1s_2$ levels were taken from [9]; i.e., the minimal known values of these cross sections were used. In this respect, the set of cross sections used in [5] is open to question.

Under our experimental conditions, the main channel for the loss of charged particles is their diffusion to the tube wall. Within the zero-dimensional model of the positive column of a glow discharge, this process is usually characterized by the rate of ambipolar diffusion. When the plasma contains several ion species, the diffusive loss of the charged particles cannot be reduced to conventional ambipolar diffusion only [10]. In our model, we consider two positive ion species: Ar^+ and Ar_2^+. To describe the diffusive loss of the ions and electrons within the zero-dimensional model, we simplified the problem by assuming that the radial profiles of the densities of different ion species are identical and the electron mobility is constant over the tube radius. A general reason for such a simplification is that the mobilities of these ions are close to one another (see

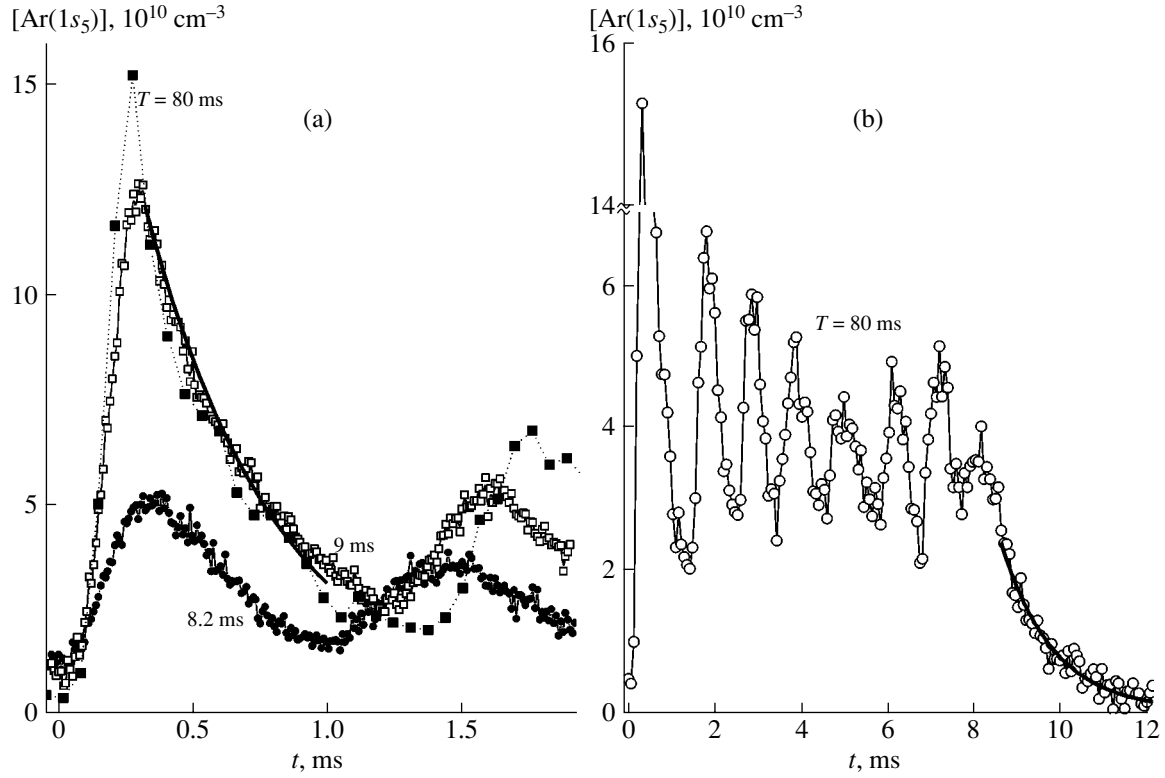

Fig. 6. Measured time evolution of the density of the $1s_5$ metastable Ar atoms (a) in the initial stage of the discharge and (b) throughout the entire discharge for $p = 5$ torr and $i = 0.7$ mA. The heavy solid lines show the exponentials with time constants of (a) 500 μs and (b) 1.2 ms.

below) and the electric field is nearly constant along the tube radius.

In this case, the coefficient of ambipolar diffusion for electron is

$$D_{ea} \approx \frac{D_e}{\mu_e}\left(\frac{n_1}{n_e}\mu_1 + \frac{n_2}{n_e}\mu_2\right), \quad (3)$$

whereas for ions, the coefficients of ambipolar diffusion are

$$D_{1a} \approx \frac{D_e}{\mu_e}\mu_1, \quad D_{2a} \approx \frac{D_e}{\mu_e}\mu_2. \quad (4)$$

In formulas (3) and (4), D_{ea}, D_e, μ_e, and n_e are the coefficient of ambipolar diffusion, the coefficient of free electron diffusion, the electron mobility, and the electron density, respectively; D_{1a}, μ_1, and n_1 are the coefficient of ambipolar diffusion, mobility, and density of Ar^+ ions; and D_{2a}, μ_2, and n_2 are the coefficient of ambipolar diffusion, mobility, and density of Ar_2^+ ions. The plasma is assumed to be quasineutral; i.e., $n_1 + n_2 = n_e$. Formulas (3) and (4) can readily be obtained using a standard procedure for deriving the coefficient of ambipolar diffusion (see, e.g., [11]). The electron mobility and the coefficient of electron diffusion were found by solving the Boltzmann equation for the EEDF. The ion mobilities under normal conditions were taken to be $\mu_1 = 1.6\ cm^2\ V^{-1}\ s^{-1}$ and $\mu_2 = 2.7\ cm^2\ V^{-1}\ s^{-1}$ [12].

For a cylindrical discharge tube, the electron diffusion loss rate is equal to

$$\nu_{ea} = \frac{D_{ea}}{\Lambda^2}, \quad (5)$$

$$\Lambda \approx R/2.4, \quad (6)$$

where Λ is the effective diffusion length. Formulas (5) and (6) were obtained from the solution to the Schottky diffusion equation for the electron density [13], in which the ionization term was assumed to be proportional to n_e. This is the case, e.g., when the atoms and molecules are primarily ionized by electron impact from the ground state. In glow discharges in noble gases, stepwise ionization is dominant; i.e., the ionization rate is proportional to n_e^2. Generally speaking, the use of formulas (5) and (6) in this case is unjustified. Nevertheless, it is possible to use formula (5) for the rate of ambipolar diffusion if one redefines the effective diffusion length, as was done in [14, 15]. In particular, it was shown in [15] that, when the ionization rate

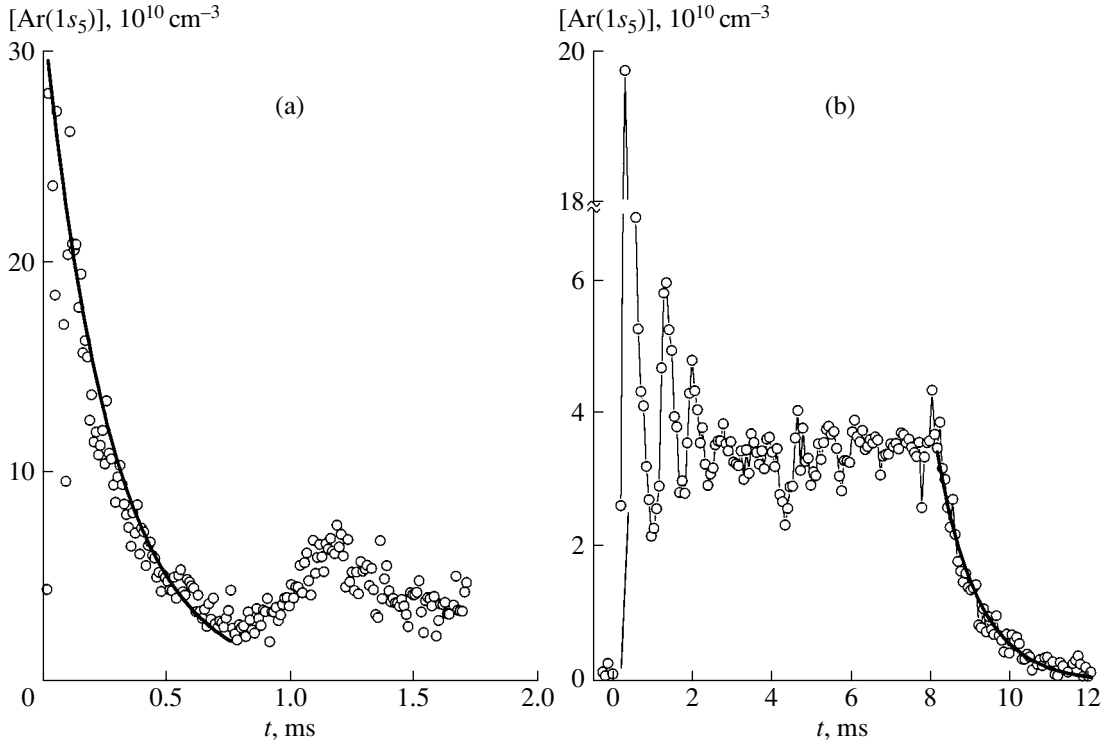

Fig. 7. Measured time evolution of the density of the $1s_5$ metastable Ar atoms (a) in the initial stage of the discharge and (b) throughout the entire discharge for $p = 5$ torr, $i = 1.4$ mA, and $T = 80$ ms. The heavy solid lines show the exponentials with time constants of (a) 270 μs and (b) 1.0 ms.

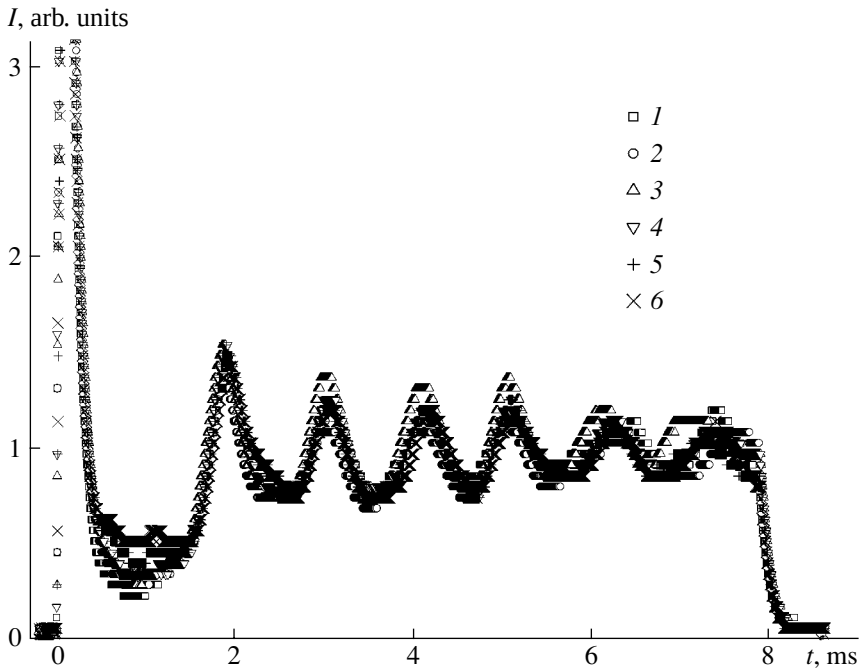

Fig. 8. Integral (over wavelengths) emission intensity measured at different points (*1–6*) spaced a distance of 1 cm from one another along the positive column for $p = 5$ torr, $i = 0.7$ mA, and $T = 80$ ms.

Processes incorporated in the model

No.	Process	k, $cm^6\ s^{-1}$, $cm^3\ s^{-1}$, s^{-1}	References
	Elastic electron scattering		
1	$Ar + e \longrightarrow Ar + e$	Boltzmann equation	[6]
	Excitation from the ground state		
2	$Ar + e \rightleftharpoons Ar(1s_5) + e$	Boltzmann equation	[5]
3	$Ar + e \rightleftharpoons Ar(1s_4) + e$	Boltzmann equation	[5]
4	$Ar + e \rightleftharpoons Ar(1s_3) + e$	Boltzmann equation	[5]
5	$Ar + e \rightleftharpoons Ar(1s_2) + e$	Boltzmann equation	[5]
6	$Ar + e \rightleftharpoons Ar(F) + e$	Boltzmann equation	[5]
7	$Ar + e \rightleftharpoons Ar(A) + e$	Boltzmann equation	[5]
	Ionization from the ground state		
8	$Ar + e \longrightarrow Ar^+ + e + e$	Boltzmann equation	[7]
	Stepwise ionization		
9	$Ar(1s_5) + e \longrightarrow Ar^+ + e + e$	Boltzmann equation	[17]
10	$Ar(1s_3) + e \longrightarrow Ar^+ + e + e$	Boltzmann equation	[17]
	Chemionization		
11	$Ar(1s_5) + Ar(1s_5) \longrightarrow Ar^+ + Ar + e$ $Ar_2^+ + e$	$1.2 \times 10^{-9}\ cm^3\ s^{-1}$	[20, 21]
12	$Ar(1s_3) + Ar(1s_3) \longrightarrow Ar^+ + Ar + e$ $Ar_2^+ + e$	$1.2 \times 10^{-9}\ cm^3\ s^{-1}$	See the text
13	$Ar(1s_5) + Ar(1s_3) \longrightarrow Ar^+ + Ar + e$ $Ar_2^+ + e$	$1.2 \times 10^{-9}\ cm^3\ s^{-1}$	See the text
	Ion conversion		
14	$Ar + Ar^+ + Ar \longrightarrow Ar_2^+ + Ar$	$2.5 \times 10^{-31}\ cm^6\ s^{-1}$	[24]
	Recombination		
15	$Ar_2^+ + e \longrightarrow Ar(A) + Ar$	Boltzmann equation	See the text
	Ambipolar diffusion		
16	$e \longrightarrow$ Tube wall		See the text
17	$Ar_2^+ \longrightarrow$ Tube wall		See the text
18	$Ar^+ \longrightarrow$ Tube wall		See the text
	Electron mixing		
19	$Ar(1s_5) + e \longrightarrow Ar(1s_4) + e$	$2 \times 10^{-7}\ cm^3\ s^{-1}$	See the text
20	$Ar(1s_3) + e \longrightarrow Ar(1s_4) + e$	$2 \times 10^{-7}\ cm^3\ s^{-1}$	See the text
	Emission		
21	$Ar(1s_4) \longrightarrow Ar + h\nu$	$5 \times 10^4\ s^{-1}$	See the text
22	$Ar(1s_2) \longrightarrow Ar + h\nu$	$2.5 \times 10^5\ s^{-1}$	See the text
	Additional electron mixing		
23	$Ar(1s_5,1s_3) + e \longrightarrow Ar(1p_1, \ldots, 1p_{10}) + e$		See the text
24	$Ar(1p_1, \ldots, 1p_{10}) \longrightarrow Ar(1s_2, \ldots, 1s_5) + h\nu$		See the text
	Atomic mixing		
25	$Ar(1s_5) + Ar \longrightarrow Ar(1s_4) + Ar$	$2.3 \times 10^{-15}\ cm^3\ s^{-1}$	[5], See the text
26	$Ar(1s_3) + Ar \longrightarrow Ar(1s_4) + Ar$	$4.3 \times 10^{-15}\ cm^3\ s^{-1}$	[5], See the text
	Formation of dimers		
27	$Ar(1s_5) + Ar + Ar \longrightarrow Ar_2^* + Ar \longrightarrow Ar + Ar + Ar + h\nu$	$1.4 \times 10^{-32}\ cm^6\ s^{-1}$	[5], See the text

Table. (Contd.)

No.	Process	k, $cm^6\ s^{-1}$, $cm^3\ s^{-1}$, s^{-1}	References
28	$Ar(1s_3) + Ar + Ar \longrightarrow Ar_2^* + Ar \longrightarrow Ar + Ar + Ar + h\nu$	$1.5 \times 10^{-32}\ cm^6\ s^{-1}$	[5], See the text
	Diffusion		
29	$Ar(1s_5) \longrightarrow$ Tube wall $\longrightarrow Ar$	$D_0 = 0.09\ cm^2\ s^{-1}$ (under normal conditions)	[5], See the text
30	$Ar(1s_3) \longrightarrow$ Tube wall $\longrightarrow Ar$	$D_0 = 0.09\ cm^2\ s^{-1}$ (under normal conditions)	[5], See the text
	Cascade population		
31	$Ar(A) \longrightarrow Ar(F) + h\nu$		See the text
32	$Ar(F) \longrightarrow Ar(1s_2, \ldots, 1s_5) + h\nu$		See the text

depends quadratically on the electron density, the effective diffusion length can be defined as

$$\Lambda \approx R/1.78. \quad (7)$$

It can easily be seen that the use of expression (7) (instead of (6)) in formula (5) leads to a decrease in the rate of ambipolar diffusion by a factor of 1.8. In our base model, when determining the rate of ambipolar diffusion, the effective diffusion length was calculated by formula (7).

In this context, we should mention paper [16] devoted to the experimental and theoretical study of the steady-state parameters of the positive column of an argon glow discharge. In that paper, in order to fit the simulation results to the measurement data, the rate of ambipolar diffusion was decreased severalfold.

The cross sections for stepwise ionization from the $3p^5 4s$ levels were taken from measurements [17]. Note that the calculated values of these cross sections [18, 19] agree well with the experimental results of [17]. It is assumed in our model that stepwise ionization occurs only from the $1s_5$ and $1s_3$ metastable levels because the populations of the $1s_4$ and $1s_2$ resonant levels (as well as of the higher electronic levels) are small compared to the population of the $1s_5$ state.

The rate constant for chemionization with the participation of Ar atoms in the $1s_5$ metastable state (see table, process no. 11) was taken from [20, 21]. The rate constants for similar reactions with the participation of Ar atoms in the $1s_3$ state (process nos. 12, 13) were assumed to be the same. The yield of molecular ions in these reactions was assumed to be 5% [22]. It should be noted that, in [16, 23], the chemionization rate constant was taken to be approximately one-half that in [20, 21].

The rate constant for the three-body conversion of Ar^+ ions into Ar_2^+ ions was taken from [24]. The energy dependence of the cross section for the dissociative recombination of electrons with Ar_2^+ molecular ions was assumed to depend on the electron energy u as Cu^{-1}. For such an energy dependence of the cross section and a Maxwellian EEDF, the recombination rate constant depends on the electron temperature T_e as $\alpha_r \sim T_e^{-0.5}$, which agrees with theoretical and experimental data [25]. The normalizing factor C was chosen such that $\alpha_r = 7 \times 10^{-7}\ cm^3/s$ at $T_e = 300$ K [25].

An important channel for quenching metastable Ar states is electron-impact excitation from the $1s_5$ and $1s_3$ states to the $1s_4$ and $1s_2$ resonant states (process nos. 19, 20) with a subsequent radiative transition to the ground state (process nos. 21, 22). The cross sections for process nos. 19 and 20 were calculated in [26, 27] and were then used in [28] to determine the rate constants for these processes as a function of the electron temperature. The calculated total rate constant for the quenching of the $1s_5$ level ($k \approx 8 \times 10^{-8}\ cm^3/s$ at $T_e = 1.5$ eV) turned out to be far less than the measured one ($k \approx 2 \times 10^{-7}\ cm^3/s$ at $T_e = 1$–1.7 eV [29]). An additional channel for the electron-impact mixing of metastable and resonant levels is the excitation of the $3p^5 4p$ states with subsequent radiative transition to different $3p^5 4s$ states (process nos. 23, 24). This channel was not considered separately in our model. For process nos. 19 and 20, the mixing rate constant was set at $2 \times 10^{-7}\ cm^3/s$, assuming that this effective value accounts for process nos. 23 and 24. Moreover, using the literature data on the cross sections for stepwise excitation from $3p^5 4s$ to $3p^5 4p$ levels [30–33] (process no. 23), we studied the role of these processes in the EEDF formation under actual experimental conditions. It was found that these processes only slightly affect the EEDF, which is obviously related to the low relative population of metastable states (~10^{-6}).

The radiative decay of the $1s_4$ and $1s_2$ resonance states was considered in the effective lifetime approximation [34]: $\tau_{eff}^{-1} = A\theta$, where A is the probability of spontaneous emission and θ is the probability of a photon escaping from the region under study (the trapping

of radiation was thus taken into account). According to [34], in the case of cylindrical symmetry, we have

$$\theta = \frac{1}{4}\sqrt{\frac{\lambda}{2\pi R}},$$

where λ is the radiation wavelength and R is the tube radius. The calculated values of τ_{eff}^{-1} are listed in the table (process nos. 21, 22). The necessary data on the probabilities of spontaneous emission and the radiation wavelengths were taken from [35].

The decay rate of the lower metastable states of Ar as a function of the gas pressure was studied in [5], where the rates were determined for three types of loss of excited atoms: (i) the loss rate is inversely proportional to the atomic density, (ii) the loss rate is proportional to the atomic density, and (iii) the loss rate is proportional to the atomic density squared. The first type corresponds to the diffusive escape of the excited atoms to the tube wall (process nos. 29, 30), the second type is associated with the mixing of the metastable and resonant atomic levels (process nos. 27, 28), and the third type is related to the formation of dimers and their subsequent rapid radiative decay (process nos. 27, 28). The diffusion coefficients and the rate constants for the relevant processes were taken from [5]. Note that the rate constant for the dimer formation presented in the table agrees well with the data from [36]. It should also be noted that, under our experimental conditions, the diffusive loss of metastable atoms is insignificant.

At the very beginning of a discharge, when the electric field in the plasma is high enough, the higher electronic states are mainly excited. Radiative transitions from these states populate the $3p^5 4s$ levels (see, e.g., [16]). To take into account this cascade population, the model incorporates the processes of spontaneous emission (process nos. 31, 32). The characteristic times of these processes are very short. Hence, it was supposed that the cascade population proceeds instantaneously. It is also necessary to know the fractions of the cascade population from the effective level F (which is a combination of the $3p^5 4p$ levels) to each of the four levels of the $3p^5 4s$ state. According to [5], these fractions are 40%, 24%, 7%, and 29% for the $1s_5$, $1s_4$, $1s_3$, and $1s_2$ levels, respectively.

The equation for the electric circuit was written in the form

$$(U - V_c - EL)/R_b = en_e V_d (S/2.3),$$

where U is the applied voltage, E is the electric field in the plasma, V_c is the cathode fall, L is the interelectrode distance, R_b is the ballast resistance, e is the electron charge, V_d is the electron drift velocity, S is the cross-sectional area of the tube, and n_e is the electron density at the tube axis. The factor 2.3 corresponds to the Bessel radial profile of the electron density. The cathode fall was assumed to be time-independent (V_c = 100 V).

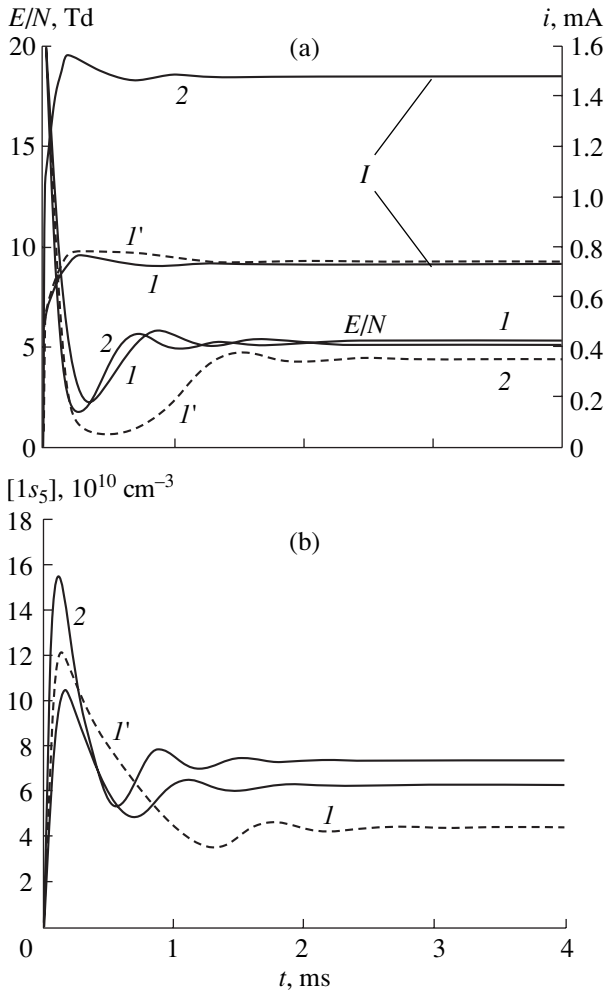

Fig. 9. Calculated time evolution of (a) the discharge current and the reduced electric field in the positive column and (b) the population of the lowest metastable state of Ar for R_b = (*1*) 4.45 and (*2*) 2.2 MΩ. Curves *1*' stand for calculations performed in the test model for R_b = 4.45 MΩ: the cross sections for the excitation of metastable states are increased twofold, the ambipolar diffusion rate is halved, and the rate constant for the mixing of the electronic states by electrons is decreased fourfold.

The Boltzmann equation for the EEDF was solved with allowance for electron–electron collisions and superelastic collisions with excited atoms. The cross sections for superelastic collisions were calculated using the detailed balance principle. The procedure for numerically solving the Boltzmann equation is described in [37]. Note that the EEDF was calculated in the local approximation. The applicability of this approximation under our experimental conditions is disputable. Thus, it was asserted in [38] that the local approximation is inapplicable in argon up to $pR \approx$ 10 cm torr. In our case, $pR \approx 7$ cm torr; therefore, one should expect only qualitative (rather than exact quantitative) agreement between the computation and experimental results.

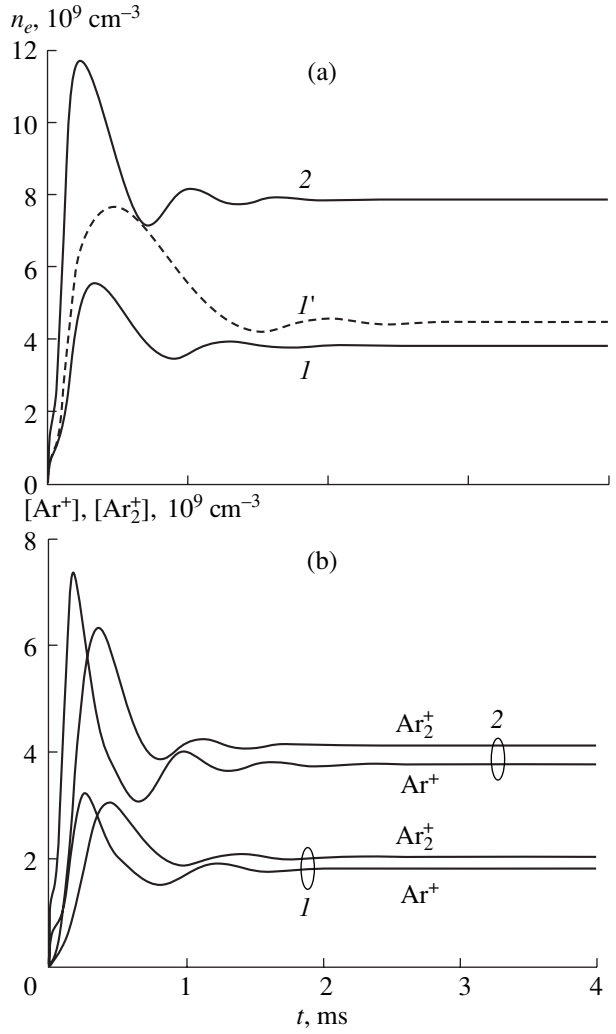

Fig. 10. Calculated time evolution of the (a) electron density and (b) positive ion densities for R_b = (*1*) 4.45 and (*2*) 2.2 MΩ. Curve *1*' stands for calculations performed in the test model for R_b = 4.45 MΩ: the cross sections for the excitation of metastable states are increased twofold, the ambipolar diffusion rate is halved, and the rate constant for the mixing of the electronic states by electrons is decreased fourfold.

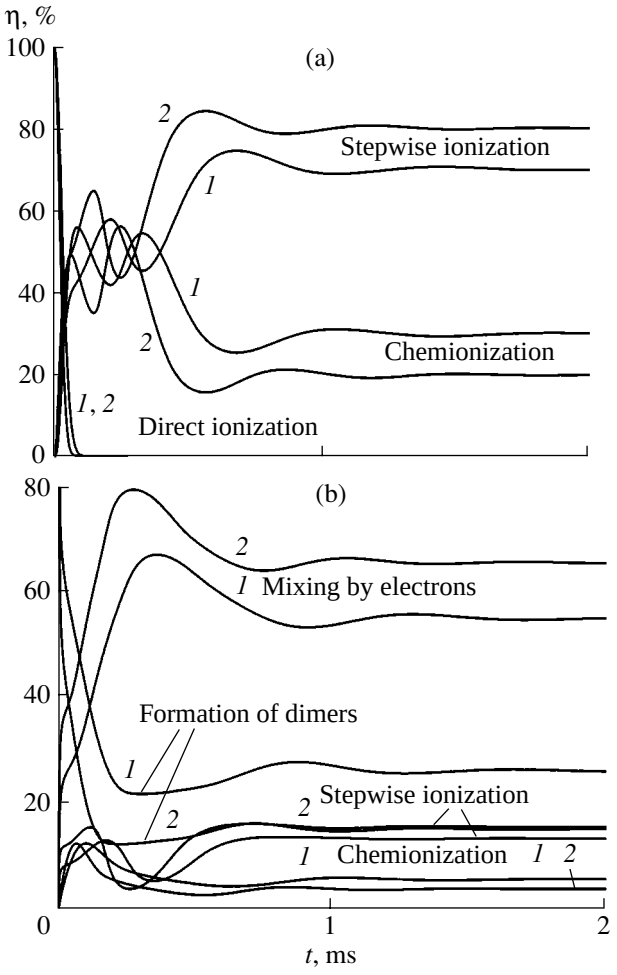

Fig. 11. Calculated time evolution of the relative contributions from different processes to (a) ionization and (b) the decay of the lowest metastable level of Ar for R_b = (*1*) 4.45 and (*2*) 2.2 MΩ.

5. RESULTS OF CALCULATIONS AND COMPARISON TO EXPERIMENT

We performed computations for a pressure of p = 5 torr, supply voltage of U = 3.6 kV, ballast resistance of R_b = 4.45 and 2.225 MΩ, discharge tube length of L = 30 cm, and tube radius of R = 1.35 cm. The two values of the ballast resistance correspond to the two different steady-state discharge currents: ≈0.7 and ≈1.4 mA. In what follows, the two regimes under consideration will be characterized by the corresponding values of the steady-state current. The initial electron density and the population of the metastable levels were assumed to be low, which corresponds to experiments with large time intervals between the discharge pulses. The computation results are presented in Figs. 9–11.

Let us first consider the results obtained with the use of the base model. They are shown by solid curves. Figure 9a shows the time evolution of the discharge current and the reduced electric field in the positive column. It can be seen that, before the steady state is reached, the discharge current passes through a maximum, whose magnitude only slightly exceeds the steady-state current. The nonmonotonic time dependence of the reduced electric field is more pronounced. The reduced field E/N sharply decreases from the initial maximum value to a minimum value, which is almost three times lower than the steady-state reduced field. Thereafter, the reduced field increases and, after a few oscillations, reaches a steady-state level. For both values of the discharge current, the steady-state value of E/N is almost the same, although for $i \approx 1.4$ mA it is a bit lower.

The calculated populations of the lowest metastable level of Ar are shown in Fig. 9b. It can be seen that the

population of the $1s_5$ level increases rapidly from zero to a maximum value and then sharply drops, reaching its steady-state value after a few oscillations. The steady-state populations corresponding to the two values of the discharge currents are close to one another, whereas the maximum population is significantly larger at the higher current. Note also that the populations of the other levels ($1s_4$, $1s_3$, and $1s_2$) are small compared to the population of the $1s_5$ level.

The time evolution of the electron and ion densities is shown in Figs. 10a and 10b, respectively. The electron density behaves similarly to the population of the $1s_5$ level: a rapid increase to the maximum value is followed by a sharp decrease and subsequent damping oscillations. For $i \approx 1.4$ mA, the amplitude of the first maximum in the electron density is much larger than for $i \approx 0.7$ mA (see Fig. 10a). The steady-state values of n_e differ by a factor of 2; i.e., their ratio is equal to the current ratio. The reason for this is that the E/N value is almost the same in both cases. Note that the densities of atomic and molecular ions in both cases are nearly the same (see Fig. 10b).

It follows from Figs. 9 and 10a that the population of the $1s_5$ state reaches its maximum value before the electron density does. The peak in the electron density coincides in time with the dip of the electric field. According to our simulations, the formation of the positive column of an argon glow discharge proceeds as follows: At the initial instant, when the electric field in the plasma is high, the electron density increases sharply due to direct ionization (see Fig. 9a) and the population of the $1s_5$ level grows. As n_e (and, consequently, the discharge current) increases, the electric field in the plasma sharply decreases and direct ionization becomes insignificant as compared to chemionization and stepwise ionization. The rate constant for the excitation of the $1s_5$ level also decreases. Within the framework of our model, the decay rate of this state due to electron mixing and chemionization does not depend on the electric field; therefore, at a certain instant, the production rate of this state becomes equal to the decay rate and the population of the $1s_5$ level reaches its maximum value, which is much larger than the steady-state value. Due to the large concentration of metastable atoms, the rates of both stepwise ionization and chemionization are much higher than the rate of electron loss due to ambipolar diffusion; so, the electron density continuous to grow. Accordingly, the electric field in the plasma decreases. As time elapses, the ionization rate decreases (because of a decrease in the population of the $1s_5$ level) and becomes equal to the rate of ambipolar diffusion. At this instant, the electron density is maximum and the electric field is minimum. Thereafter, the loss of electrons due to ambipolar diffusion dominates over the production of electrons due to ionization and the electron density decreases. This, in turn, leads to an increase in the electric field in the plasma, the maximum electric field being somewhat higher than the steady-state field. Eventually, after a few damping oscillations, the electric field reaches its steady-state value.

The time evolution of the relative contributions from different processes to the rate of electron production and the decay rate of the $1s_5$ level is shown in Fig. 11. It can be seen from Fig. 11a that, when the concentration of metastable atoms is maximum, the contributions from stepwise ionization and chemionization are nearly the same, whereas in the steady-state phase, stepwise ionization prevails. The decay of the $1s_5$ metastable level is mainly caused by electron mixing (see Fig. 11b). Only at the very beginning of the discharge, when the electron density is still relatively low, is the decay of metastable states mainly related to the formation of dimers.

A comparison between the computation and experimental results shows that the model adequately describes the time evolution of the plasma parameters during the formation of the positive column in an argon glow discharge; specifically, it predicts the presence of a peak in the population of the $1s_5$ level and a minimum in the electric field in the initial stage of a discharge. The calculated and measured populations of the $1s_5$ level differ by a factor of less than 2 (cf. Figs. 6, 7, and 9b). Moreover, the calculated steady-state value of E/N agrees well with the measured value (estimated by averaging the data from Figs. 5a and 5e over time). However, in calculations, the period of oscillations of the plasma parameters is shorter and the oscillation amplitude is appreciably smaller than their measured values.

The most drastic difference between the computation and experimental results is that, in calculations, the minimum value of the reduced electric field is much larger than that in the experiment. For example, for $i \approx 0.7$ mA, the calculated minimum value of the reduced field is $(E/N)_{\min} \approx 2.3$ Td, whereas the minimum value of the reduced field estimated from the experimental data is $(E/N)_{\min} \leq 0.5$ Td. Our estimates show that, at $(E/N)_{\min} \approx 2.3$ Td, the emission intensity of the above spectral lines only slightly decreases below its steady-state level. To reduce the calculated value of $(E/N)_{\min}$, it is necessary to increase the maximum electron density. This, in turn, calls for an increase in the population of the $1s_5$ level. In principle, this can be achieved by properly adjusting the cross sections and the rate constants used in our model. For this purpose, test calculations for the case of $i \approx 0.7$ mA were performed in which the cross sections for the excitation of metastable states were increased twofold, the rate constant for electron mixing was decreased fourfold, and the rate of ambipolar diffusion was halved. The relevant computation results are shown in Figs. 9 and 10 by the dashed lines. Let us compare them to the computation results obtained using the base model. It can be seen that the maximum population of the $1s_5$ level increased by ≈15%, the duration of the time interval in which the

population is reduced increased twofold, and the steady-state population decreased by nearly 30%. The maximum electron density increased by ≈28%, whereas the duration of the time interval where n_e is reduced increased twofold. The time evolution of E/N changed most radically. The minimum reduced field $(E/N)_{min}$ decreased by a factor of almost 3.5. The reason for such a significant decrease in $(E/N)_{min}$ is that the electron drift velocity in argon only slightly decreases with decreasing E/N within the range $E/N < 4$ Td. For a fixed current, the 28% increase in the electron density must be balanced by a decrease in the electron drift velocity, which calls for a significant decrease in E/N.

As a whole, the computation results obtained using the test version of the model agree much better with the experiment than those obtained in the base model. The validity of using the test model with modified cross sections and rate constants is questionable, however.

6. CONCLUSIONS

The initial stage of the positive column formation in a low-pressure (p = 5 torr) glow discharge in argon has been studied at discharge currents of ~1 mA (specifically, at 0.7 and 1.4 mA). The time evolution of the emission intensities of the spectral lines, the electric field in the discharge plasma, and the population of the lowest metastable state of Ar were measured. It is found that the initial spike in the emission intensity is followed by a 1- to 1.5-ms-long period during which the emission intensity is lower than that in the steady-state phase of the discharge. The duration of this dark phase decreases with increasing discharge current. The time evolution of the electric field also displays a dip in which the reduced electric field E/N is much lower than its steady-state value. At the same time, the population of the $1s_5$ metastable state in the initial stage of the discharge is much higher than that in the steady-state phase.

A kinetic model has been developed to simulate the positive column plasma of a glow discharge in argon by consistently solving the equations for the electron and ion densities and for the populations of the excited states of Ar, the Boltzmann equation for the EEDF, and the equation for the electric circuit. Using this model, we have calculated the time evolution of the plasma parameters (such as the electron density, the reduced electric field, and the population of the metastable levels). The calculated results agree satisfactorily with the experimental data.

Our experimental and theoretical study has shown that the DP effect is related to the production of an excessive amount of metastable Ar atoms at the beginning of the discharge and, consequently, to high rates of stepwise ionization and chemionization. The high ionization rate leads to an increase in the electron density and, accordingly, to a significant decrease in the electric field in the positive column. This, in turn, results in a sharp decrease in the rate constants for the electron-impact excitation of the electronic states of Ar and a decrease in the emission intensity.

It is also shown that quantitative agreement between numerical and experimental results can be achieved by adjusting the cross sections and rate constants incorporated in the model. The validity of such an adjustment is questionable, however.

ACKNOWLEDGMENTS

This study was supported by the Russian Foundation for Basic Research (project no. 03-02-16917) and the "RF Presidential Program for State Support of Leading Scientific Schools" (grant no. 794.2003.2).

REFERENCES

1. Yu. Z. Ionikh, I. N. Kostyukevich, and N. V. Chernysheva, Opt. Spektrosk. **74**, 455 (1993) [Opt. Spectrosc. **74**, 274 (1993)].
2. Yu. Z. Ionikh, Yu. G. Utkin, N. V. Chernysheva, and A. S. Evdokimenko, Fiz. Plazmy **22**, 289 (1996) [Plasma Phys. Rep. **22**, 267 (1996)].
3. R. Kh. Amirov, É. I. Asinovskiĭ, and V. V. Markovets, Teplofiz. Vys. Temp. **19**, 47 (1981).
4. R. Kh. Amirov, É. I. Asinovskiĭ, and V. V. Markovets, Fiz. Plazmy **27**, 450 (2001) [Plasma Phys. Rep. **27**, 424 (2001)].
5. K. Tachibana, Phys. Rev. A **34**, 1007 (1986).
6. M. Hayashi, Report No. IPPJ-AM-19 (Institute of Plasma Physics, Nagoya University, Nagoya, 1981).
7. D. Rapp and P. Englander-Golden, J. Chem. Phys. **43**, 1464 (1965).
8. M. A. Khakoo, P. Vandeventer, J. G. Childers, *et al.*, J. Phys. B **37**, 247 (2004).
9. A. Chutjian and D. C. Cartwright, Phys. Rev. A **23**, 2178 (1981).
10. V. A. Rozhanskiĭ and L. D. Tsendin, *Collisional Processes in Partially Ionized Plasma* (Énergoatomizdat, Moscow, 1988) [in Russian].
11. Yu. P. Raizer, *Gas Discharge Physics* (Nauka, Moscow, 1987; Springer-Verlag, Berlin, 1991).
12. *Tables of Physical Quantities*, Ed. by I. K. Kikoin (Atomizdat, Moscow, 1976) [in Russian].
13. W. Schottky, Phys. Z. **25**, 635 (1924).
14. F. W. Crawford, J. Appl. Phys. **51**, 1422 (1980).
15. G. L. Rogoff, J. Appl. Phys. **52**, 6601 (1981).
16. C. M. Ferreira and J. Loureiro, J. Appl. Phys. **57**, 82 (1985).
17. A. J. Dixon, M. F. A. Harrison, and A. C. H. Smith, *VIII International Conference on the Physics of Electronic and Atomic Collisions, Belgrade, 1973*, Abstracts of Papers, Vol. 1, p. 405.
18. D. Ton-That and M. R. Flannery, Phys. Rev. A **15**, 517 (1977).
19. H. A. Hyman, Phys. Rev. A **20**, 855 (1979).

20. N. B. Kolokolov, in *Plasma Chemistry*, Ed. by B. M. Smirnov (Énergoatomizdat, Moscow, 1985), Vol. 13 [in Russian].
21. N. B. Kolokolov and A. B. Blagoev, Usp. Fiz. Nauk **163** (3), 55 (1993) [Phys. Usp. **36**, 152 (1993)].
22. V. B. Borisov, V. S. Egorov, and N. A. Ashurbekov, *IV All-Union Conference on Physics of Low-Temperature Plasma, Leningrad, 1983*, Abstracts of Papers, p. 20.
23. Z. Donko, N. Sadeghi, N. Baguer, and A. Bogaerts, in *Proceedings of the 17th European Conference on Atomic and Molecular Physics of Ionized Gases, Constanta, 2004*, p. 161.
24. L. I. Virin, G. V. Dzhagatspanyan, R. V. Karachevtsev, *et al.*, *Ion–Molecule Reactions in Gases* (Nauka, Moscow, 1979) [in Russian].
25. M. A. Biondi, in *Plinciples of Laser Plasmas*, Ed. by G. Bekefi (Wiley, New York, 1976; Énergoizdat, Moscow, 1982).
26. K. Bartschat and V. Zeman, Phys. Rev. A **59**, R2552 (1999).
27. A. Dasgupta, K. Bartschat, D. Vaid, *et al.*, Phys. Rev. A **65**, 042724 (2002).
28. V. M. Donnelly, J. Phys. D **37**, R217 (2004).
29. V. A. Ivanov and I. V. Makasyuk, Opt. Spektrosk. **69**, 514 (1990).
30. A. Dasgupta, M. Blaha, and J. L. Giuliani, Phys. Rev. A **61**, 012703 (2000).
31. A. Dasgupta, M. Blaha, and J. L. Giuliani, Phys. Rev. A **65**, 039905(E) (2002).
32. C. M. Maloney, J. L. Peacher, K. Bartschat, and D. H. Madison, Phys. Rev. A **61**, 022701 (2000).
33. B. J. Boffard, G. A. Piech, M. F. Gehrke, *et al.*, Phys. Rev. A **59**, 2749 (1999).
34. L. M. Biberman, V. S. Vorob'ev, and I. T. Yakubov, *Kinetics of Nonequilibrium Low-Temperature Plasmas* (Nauka, Moscow, 1982; Consultants Bureau, New York, 1987).
35. A. A. Radtsig and B. M. Smirnov, *Reference Data on Atoms, Molecules, and Ions* (Énergoatomizdat, Moscow, 1986; Springer-Verlag, Berlin, 1985).
36. C. Brow, in *Excimer Lasers*, Ed. by C. K. Rhodes (Springer-Verlag, New York, 1979; Mir, Moscow, 1981).
37. N. A. Dyatko, I. V. Kochetov, A. P. Napartovich, and M. D. Taran, Preprint No. 3842/12 (Kurchatov Institute of Atomic Energy, Moscow, 1983).
38. E. A. Bogdanov, A. A. Kudryavtsev, L. D. Tsendin, *et al.*, Zh. Tekh. Fiz. **74** (6), 44 (2004) [Tech. Phys. **49**, 698 (2004)].

Translated by N.N. Ustinovskiĭ

Plasma Physics Reports, Vol. 31, No. 10, 2005, pp. 886–890. Translated from Fizika Plazmy, Vol. 31, No. 10, 2005, pp. 954–958.

LOW-TEMPERATURE PLASMA

Long-Lived Plasmoids Generated by Surface Microwave Discharges in Chemically Active Gases

N. K. Berezhetskaya, S. I. Gritsinin, V. A. Kop'ev, I. A. Kossyĭ, and D. van Wie

Prokhorov Institute of General Physics, Russian Academy of Sciences, ul. Vavilova 38, Moscow, 119991 Russia

Received December 23, 2004

Abstract—The generation of long-lived microplasmoids is observed during the irradiation of a metal–dielectric surface with a high-power microwave beam in a chemically active gas mixture ($H_2 + O_2$; $CH_4 + O_2$). The lifetime of these plasmoids substantially exceeds the characteristic recombination and cooling times of plasmoids arising at the target surface in a chemically inactive medium. *© 2005 Pleiades Publishing, Inc.*

1. INTRODUCTION

Plasmoids with an abnormally long decay time (long-lived plasmoids) have been observed in laser sparks [1, 2], microwave discharges [3, 4], high-current arcs [5, 6], etc. Long-lived plasmoids generated under laboratory conditions have attracted interest primarily in connection with attempts to model such an interesting (but poorly understood) phenomenon as ball lightning [7, 8].

Long-lived plasmoids generated by high-current multispark gliding surface discharges were first observed and described in [9]. It was shown that, regardless of the composition of the ambient gas, a gliding surface discharge excited along a multielectrode metal–dielectric system generates thermally equilibrium plasmoids whose decay time is much longer than the characteristic recombination time. When such plasmoids are injected into a chemically inactive gas (argon, nitrogen, air, etc.), their lifetime is determined by radiative cooling. When plasmoids fall into a chemically active gas (such as a $H_2 : O_2$ or a $CH_4 : O_2$ mixture), their lifetime increases substantially. In [9], this effect was attributed to the influx of chemically active particles that compensate for radiative energy losses. Being sustained by a chemically active medium, the plasmoid in turn affects the medium by activating the gas mixture and promoting its ignition.

In this paper, the possibility is investigated of generating long-lived plasmoids in discharges excited by high-power microwave beams at metal–dielectric surfaces in combustible gas mixtures. This type of discharge was described and studied in [10, 11]. In [12–14], it was shown that, when a dielectric surface interspersed with metal grains was irradiated by a high-power microwave beam, multiple sparks (microplasmoids) were generated at the interfaces between the metal grains and the dielectric. The main goal of the present study is to find out whether the surface microplasmoids produced in a chemically active medium may give rise to long-lived plasmoids similar to those observed in experiments with high-current multielectrode gliding discharges [9].

2. EXPERIMENTAL SETUP

A schematic of the experimental setup is shown in Fig. 1. Pulsed microwave radiation generated by magnetron *1* is fed through attenuator *2* and circulator *3* to horn–lens antenna *4*. The antenna forms converging microwave beam *12*, which is launched into cylindrical metal chamber *5* and then into reactor chamber *9*. The reactor chamber is a preevacuated quartz cell that is filled with a working gas before each particular experiment. The pressure in the metal chamber is atmospheric.

Dielectric target *10* is placed in cell *9* in the focal region of the microwave beam. The target surface exposed to microwave beam *12* contains metal grains ≤1 mm in size (see Fig. 2). The number of grains per unit area of the target surface is chosen such that the target is transparent to low-power microwaves. However,

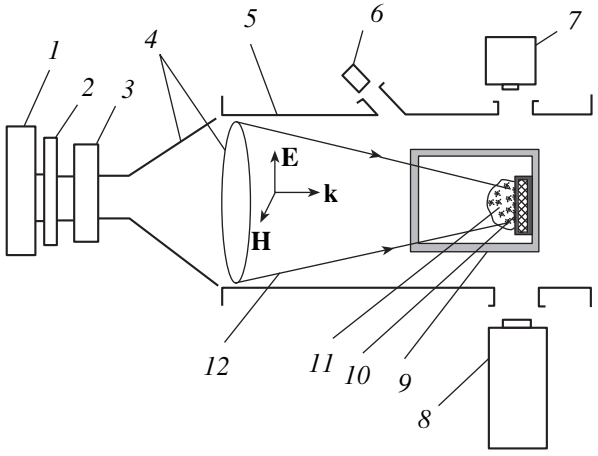

Fig. 1. Scheme of the experiment.

1063-780X/05/3110-0886$26.00 © 2005 Pleiades Publishing, Inc.

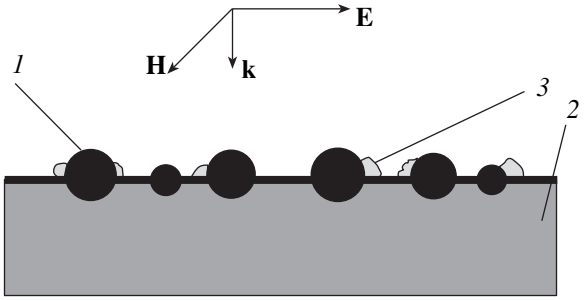

Fig. 2. Sketch of a metal–dielectric target: (*1*) metal grains, (*2*) dielectric substrate, and (*3*) microplasmoids (sparks).

at a microwave intensity of $I \geq 10$–100 W/cm^2, multiple local sparks arise at the interfaces between the metal grains and the dielectric and the transmission coefficient of the target decreases substantially because of microwave absorption by local plasmoids.

The parameters of microwave radiation in our experiments were as follows: the wavelength was $\lambda \cong 2.5$ cm, the pulse duration was $\tau_i \cong 5$–10 μs, and the peak power was $P_i \leq 100$ kW.

The reactor cell was filled with argon or a hydrogen–oxygen ($H_2 : O_2$) or a methane–oxygen ($CH_4 : O_2$) mixture at a pressure of $10 \leq p \leq 200$ torr.

The time evolution of the optical glow from the reactor cell was recorded with the help of FER-7 streak camera *7* (see Fig. 1); KADR-IOFRAN image intensifier *8*, operating in the frame mode (four successive frames with a variable exposure time and variable time delay between them); and collimated photomultiplier *6*.

3. EXPERIMENTAL RESULTS

Figure 3 shows a typical streak image (negative) of the glow from the reactor cell. The slit of the FER-7 streak camera was oriented along the normal to the surface of the metal–dielectric target (along the *z* axis). In this case (see Fig. 4), the radiation was received from the region of width $\Delta x \cong 2.0$ mm and length $\Delta z \cong 4$ cm.

The reactor cell was filled with a $H_2 : O_2$ (180 : 90 torr) mixture. The duration of the microwave pulse was $\tau_i \cong 10$ μs, and the microwave peak power was $P_i \cong 100$ kW.

The target surface is located at $z = 0$, and the microwave pulse is switched on at $t = 0$.

It can be seen from Fig. 3 that local optical bursts arise on the metal–dielectric target irradiated with microwaves. These bursts correspond to microscopic surface discharges developing at the interfaces between the metal grains and the dielectric. The duration of the optical glow from the surface discharges (200–250 μs) substantially exceeds the microwave pulse duration. Periodical pulsations of the glow are observed.

When the cell is filled with a chemically inactive gas (Ar, N_2, O_2, etc.), the glow from surface microscopic discharges (sparks) terminates just after the end of the microwave pulse.

It should be noted that streak images obtained with the help of the FER-7 camera provide information only about a very small region of the metal–dielectric surface. In order to study the formation of microplasmoids beyond the field of view of the FER-7 camera, we carried out experiments with the KADR-IOFRAN image intensifier, operating in the frame mode. This allowed us to obtain a series of four successive photographs of the entire target surface during a microwave pulse. Typical series of photographs taken during a microwave pulse are presented in Fig. 5. The exposure time of each

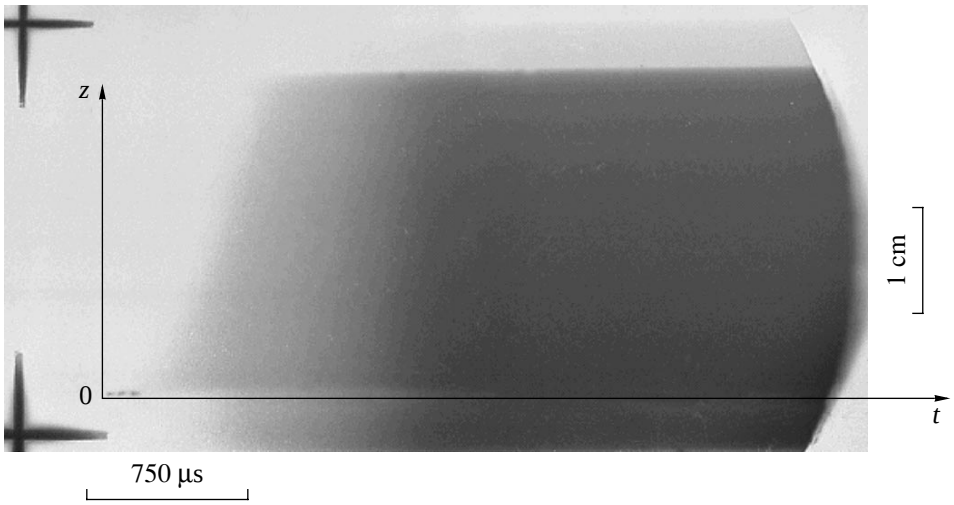

Fig. 3. Typical streak image of the glow from the reactor cell filled with a $H_2 : O_2$ (180 : 90 torr) mixture.

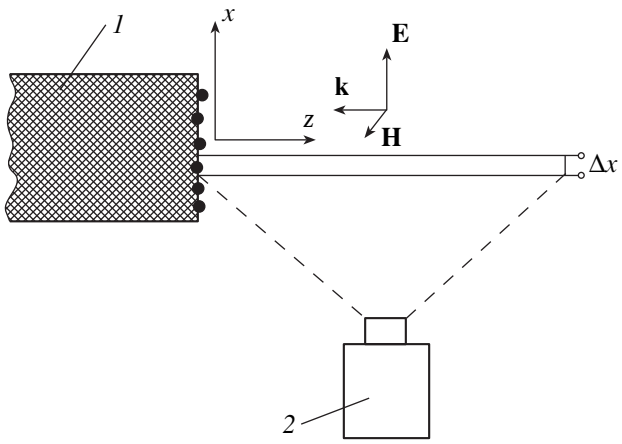

Fig. 4. Scheme of photographing the glow from the reactor cell with the help of an FER-7 streak camera with a slit oriented along the *z* axis.

frame was 30 μs, and the delay time between the frames was 200 μs. The reactor quartz cell was filled with (*1*) a $H_2 : O_2$ (120 : 60 torr) mixture, (*2*) a $CH_4 : O_2$ (45 : 90) mixture, and (*3*) pure oxygen ($p \cong 135$ torr).

It follows from this figure that surface microwave discharges in oxygen decay just after the end of the microwave pulse (Fig. 5a, row *3*). When the reactor cell is filled with a chemically active (combustible) gas mixture (Fig. 5; rows *1*, *2*), the lifetime of microplasmoids increases on average to ~200 μs (Fig. 5b; rows *1*, *2*). However, a few (usually, one or two) microplasmoids continue to glow over a time longer than 600 μs. This effect is most pronounced in a methane–oxygen mixture (Figs. 5c, 5d; row *2*).

Photographs of the glow from a methane–oxygen mixture taken under the same conditions as those in Fig. 5 but at different times with respect to the begin-

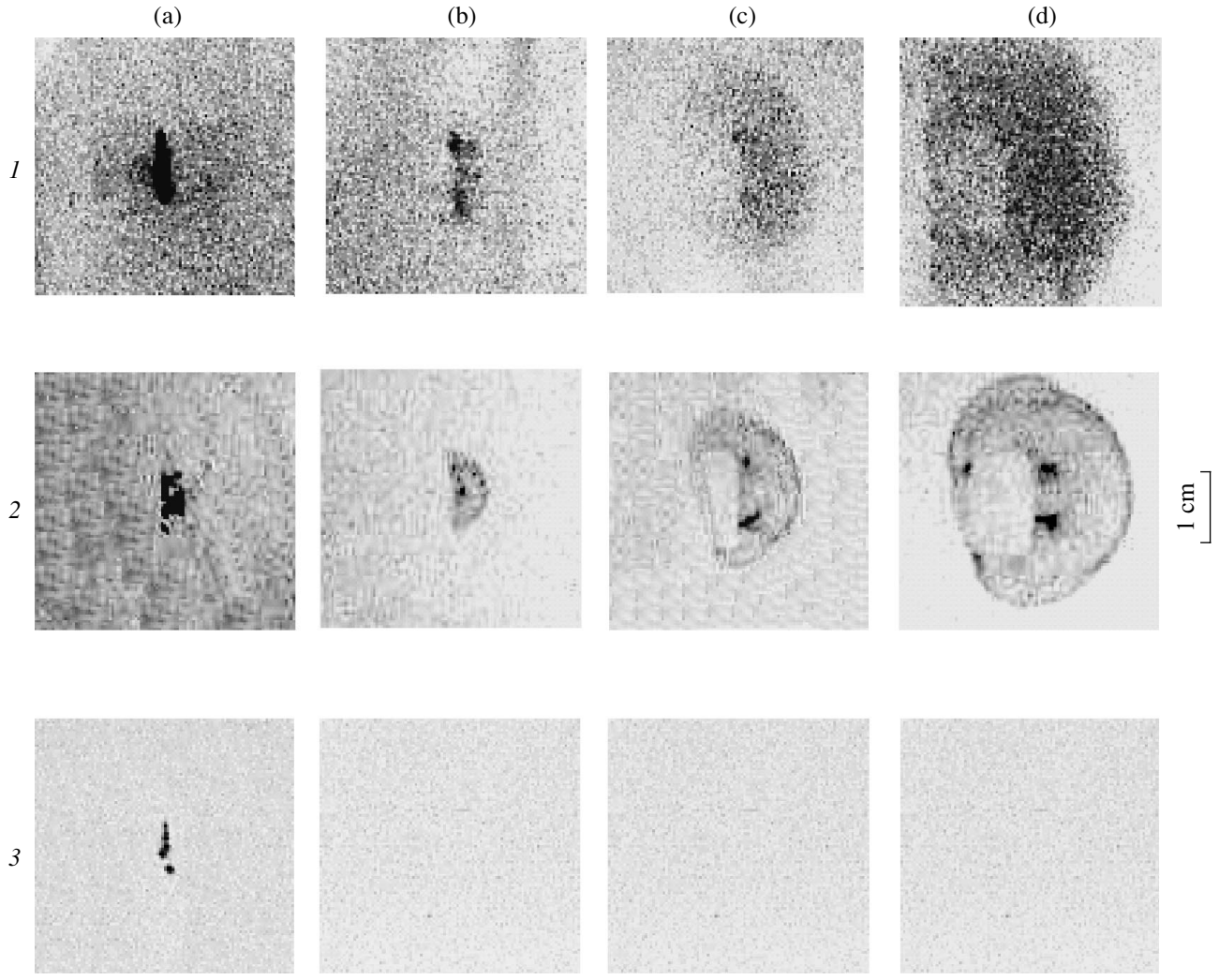

Fig. 5. Typical photographs of the glow from the reactor cell filled with (*1*) a $H_2 : O_2$ (180 : 90 torr) mixture, (*2*) a $CH_4 : O_2$ (45 : 90 torr) mixture, and (*3*) O_2 (135 torr). The exposure time of each frame is 30 μs, and the time delay between the frames is 200 μs.

ning of the microwave pulse showed that long-lived plasmoids existed over 1–1.2 ms, up to the final bright burst occurring over the entire chamber.

In Figs. 3 and 5, one can see quasi-spherical glow waves initiated by surface discharges and identified in [15] as "incomplete-combustion waves."

4. DISCUSSION

Mechanisms for sustaining long-lived plasmoids generated in a chemically active gas mixture by a high-current multispark surface discharge were discussed in [9]. It was suggested that any thermally equilibrium high-temperature plasmoid (regardless of the way in which it was produced) is long-lived if its size is less than a certain critical size: $r_p \le r_{cr}$.

A surface microwave discharge at a metal–dielectric target (see Fig. 2) can also be used to produce plasmoids of this kind. Experiments have shown [10, 11] that the irradiation of a metal–dielectric target under conditions such that

$$\Psi\tau_i \ge 0.1 \text{ J/cm}^2 \quad (1)$$

(where Ψ is the microwave intensity in W/cm^2 and τ_i is the microwave pulse duration in seconds) is accompanied by the generation of multiple plasmoids (sparks) at the interfaces between the metal grains and the dielectric.

An analysis of the possible mechanisms for plasma production allowed the authors of [10, 12] to suggest that the observed phenomenon is related to the injection of electrons from the metal to the conduction band of the dielectric at the metal–dielectric interface. The electron emission at the metal–dielectric interface can be substantially intensified due to the following two effects: (i) a decrease in the work function of the metal and (ii) an increase in the microwave electric field at the metal grains.

The injection of electrons into the dielectric increases the conductivity of a narrow dielectric layer adjacent to the metal up to a value typical of semiconductors (see [16]). Microwave absorption in the dielectric layer with the induced conductivity is accompanied by its heating. As the temperature at the metal–dielectric interface grows, both the dielectric conductivity and the electron flux into the dielectric from the metal increase. The resulting thermal instability [16] leads to explosive energy release at the metal–dielectric interface and a solid–plasma phase transition.

This processes may lead to the generation of long-lived plasmoids observed in our experiment. These plasmoids are sustained by the influx of chemically reacting particles from the ambient medium. The plasmoids in turn can influence the medium [9], thus promoting volume combustion in the reactor cell.

Microplasmoids generated by a surface microwave discharge (in contrast to those generated by high-current gliding discharges [9]) do not undergo axial acceleration under the action of electrodynamic forces. As a result, they stay over several milliseconds near the metal–dielectric interface, where they were produced.

5. CONCLUSIONS

Our experiments have shown that microplasmoids arising at metal–dielectric surfaces irradiated by high-power microwave beams in hydrogen–oxygen and methane–oxygen mixtures can evolve into long-lived plasmoids similar to those observed in experiments with high-current multielectrode gliding discharges.

Our experimental results confirm the assumption that long-lived plasmoids can arise when small-size, thermally equilibrium plasmoids with a sufficiently high temperature are somehow produced in a chemically active gas mixture.

In view of these findings, it is expedient to more thoroughly investigate the parameters of long-lived plasmoids and to search for new methods for their excitation, including laser-spark excitation.

It is also of interest to study the problem of utilizing long-lived plasmoids to initiate the combustion of gas mixtures, in particular, in supersonic flows (see [15, 17]).

ACKNOWLEDGMENTS

This work was supported in part by the Russian Foundation for Basic Research (project no. 02-02-16066) and ISTC/EOARD (project no. 2681p).

REFERENCES

1. G. A. Askar'yan, M. S. Rabinovich, M. M. Savchenko, and A. D. Smirnova, Pis'ma Zh. Éksp. Teor. Fiz. **1** (6), 18 (1965) [JETP Lett. **1**, 162 (1965)].
2. G. A. Askar'yan, M. S. Rabinovich, M. M. Savchenko, and V. K. Stepanov, Pis'ma Zh. Éksp. Teor. Fiz. **3**, 465 (1966) [JETP Lett. **3**, 303 (1966)].
3. P. L. Kapitsa, Zh. Éksp. Teor. Fiz. **57**, 1801 (1969) [Sov. Phys. JETP **30**, 973 (1969)].
4. J. R. Powell and D. Finkelstein, Amer. Scientists **58**, 2318 (1970).
5. A. G. Basiev, F. I. Vysikaĭlo, V. A. Gurashvili, and E. R. Shchekotov, Fiz. Plazmy **9**, 1076 (1983) [Sov. J. Plasma Phys. **9**, 627 (1983)].
6. A. P. Ershov, S. P. Bytskevich, I. B. Timofeev, and S. N. Chuvashev, Teplofiz. Vys. Temp. **28**, 583 (1990).
7. B. M. Smirnov, *The Problem of Ball Lightning* (Nauka, Moscow, 1988) [in Russian].
8. J. D. Barry, *Ball Lightning and Bead Lightning: Extreme Forms of Atmospheric Electricity* (Plenum, New York, 1980; Mir, Moscow, 1983).
9. I. A. Kossyĭ, V. P. Silakov, N. M. Tarasova, *et al.*, Fiz. Plazmy **30**, 375 (2004) [Plasma Phys. Rep. **30**, 343 (2004)].
10. G. M. Batanov, E. F. Bol'shakov, A. A. Dorofeyuk, *et al.*, J. Phys. D **29**, 1641 (1996).

11. G. M. Batanov, S. I. Gritsinin, and I. A. Kossyi, J. Phys. D **35**, 2687 (2002).
12. G. M. Batanov, N. K. Berezhetskaya, V. A. Kop'ev, *et al.*, Fiz. Plazmy **28**, 945 (2002) [Plasma Phys. Rep. **28**, 871 (2002)].
13. G. M. Batanov, N. K. Berezhetskaya, I. A. Kossyi, *et al.*, in *Proceedings of the International Workshop on Strong Microwaves in Plasmas, Nizhni Novgorod, 2002*, Ed. by A. G. Litvak (IPFAN, Nizhni Novgorod, 2003), Vol. 2, p. 631.
14. G. M. Batanov, N. K. Berezhetskaya, I. A. Kossyi, *et al.*, Eur. Phys. J. Appl. Phys. **26**, 11 (2004).
15. N. K. Berezhetskaya, S. I. Gritsinin, V. A. Kop'ev, *et al.*, in *Proceedings of the 43rd AIAA Aerospace Sciences Meeting, Reno, NV, 2005*, Report No. AIAA-2005-0991.
16. Yu. N. Vershinin, *Electric Discharges in Solid Dielectrics* (Nauka, Novosibirsk, 1968) [in Russian].
17. I. A. Kossyi, N. K. Berezhetskaya, S. I. Gritsinin, *et al.*, in *Proceedings of the 42nd AIAA Aerospace Sciences Meeting, Reno, NV, 2004*, Report No. AIAA-2004-836.

Translated by N.F. Larionova

Plasma Physics Reports, Vol. 31, No. 10, 2005, pp. 891–892. Translated from Fizika Plazmy, Vol. 31, No. 10, 2005, pp. 959–960.

OBITUARY

In Memory of Yakov Borisovich Faĭnberg (September 7, 1918–March 7, 2005)

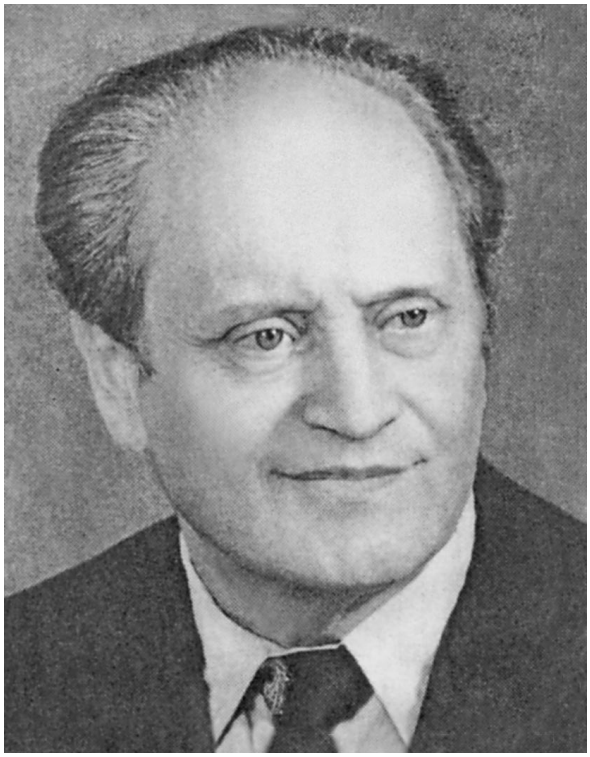

Yakov Borisovich Faĭnberg, an academician of the National Academy of Sciences of Ukraine and an eminent physicist who contributed greatly to plasma physics and the physics of accelerators, passed away March 7, 2005.

Faĭnberg was born September 7, 1918, in the small Ukrainian town of Zolotonosha, into the family of a pharmacist and school teacher. In 1935, he enrolled at the Physics and Mathematics Department of Kharkov State University, where he was lucky enough to listen to lectures by L.D. Landau and K.D. Sinel'nikov. In 1940, Faĭnberg became a postgraduate student. World War II tore him away from the university over long six years. During the war, he worked on defense applications. In 1944–1945, he served a senior engineer in one of the technical units of the Soviet Central Intelligence Agency.

After 1946, the scientific activity of Faĭnberg was indissolubly linked to the Kharkov Institute of Physics and Technology (KIPT). In 1947, he carried out his first theoretical studies on the dynamics of particles accelerated by a travelling wave field. He developed the theory of phase and radial stability of particles accelerated in slow-wave structures. Based on his theoretical investigations, the first linear electron accelerators in the Soviet Union were built at the KIPT. Faĭnberg participated in developing the theory of high-energy accelerators. In particular, calculations were performed for the largest in Europe, a 2-GeV linear accelerator. Together with A.I. Akhiezer, he supervised these works. Faĭnberg performed a series of studies on the dynamics of particles in proton accelerators and the electrodynamics of accelerating systems of such accelerators. He took part in designing all of the proton accelerators ever built at the KIPT. He was one of the first to investigate charged particle acceleration in anisotropic media and helical waveguides. In 1953, he proposed a fundamentally new method of simultaneous radial and longitudinal stabilization of particles in a linear accelerator—the so-called method of alternative phase focusing, in which two-dimensional dynamic stabilization of the accelerated particles is achieved with the help of an accelerating RF field whose phase varies periodically along the accelerator. In recent years, this method has been implemented in a number of new accelerators.

In 1956, at the Geneva Conference on High-Energy Physics, works by V.I. Veksler, A.M. Budker, and Faĭnberg were reported in which the basic ideas of a fundamentally new direction in the physics of accelerators—methods of collective acceleration—were formulated. The method proposed by Faĭnberg for accelerating charged particles by space charge waves in plasma waveguides and uncompensated electron and ion beams has been further developed and is currently considered a very promising method, allowing one to create new-generation accelerators.

In their pioneering paper published in 1948, Faĭnberg and A.I. Akhiezer predicted beam–plasma instability. This instability is a manifold physical phenomenon, having a lot of practical applications. A thorough theoretical and experimental analysis of the beam–plasma instability became the basic line of the long-term activity of Faĭnberg and his collaborators and students. In 1957–1958, beam–plasma instability was observed experimentally in both magnetized and unmagnetized plasmas, a new type of discharge—a beam–plasma discharge—was discovered, and a new method of collisionless plasma heating—beam heating—was developed.

Faĭnberg (together with E.K. Zavoĭskiĭ, V.A. Suprunenko, and others) is a coordinator of the discovery

1063-780X/05/3110-0891$26.00

"Turbulent Heating and Anomalous Plasma Resistivity."

In 1961, Faĭnberg formulated the problem of control over plasma microinstabilities; in particular, he proposed a method for controlling beam–plasma instability, which was implemented experimentally in 1961–1965. Faĭnberg was one of the first to understand and evaluate the great potentialities of using relativistic electron beams (REBs). In 1969, he (together with V.D. Shapiro and V.I. Shevchenko) carried out the first studies on the nonlinear theory of the interaction of REBs with plasmas. Later (together with V.I. Kurilko), he developed the nonlinear theory of the interaction of REBs with plasma-filled cavities. Experimental studies of the interaction of high-current REBs with plasmas demonstrated its high efficiency. These investigations made it possible to substantially increase microwave power (1974–1975) and to create a powerful UV laser based on collective interactions (1969–1971). In 1974–1987, a series of experimental studies were performed on the interaction of low-divergent monoenergetic REBs with a dense plasma (10^{15}–10^{17} cm^{-3}). In those experiments, an anomalously fast relaxation of the beam was observed for the first time. In 1984, it was proved that, in high-current REBs propagating in plasma waveguides, the Cherenkov mechanism of emission is replaced with the anomalous Doppler mechanism. As a result, the emission efficiency does not decrease as the beam energy and the degree to which the system is nonequilibrium increase.

In 1955–1960, Faĭnberg predicted the phenomenon of the frequency multiplication related to the double Doppler effect during the reflection from a plasma propagating in a slow-wave system. This effect was observed experimentally and, in recent years, has received renewed attention. In 1986, a plasma-filled free-electron laser was proposed and investigated.

In all of his studies, Faĭnberg's exhibited a characteristic feature of his scientific activity—an aspiration for carrying his ideas to experiments, which were performed, as a rule, under his guidance and with his immediate participation.

Over more than 20 years (starting in 1949), Faĭnberg gave lectures on the physics of accelerators and special issues of electrodynamics at Kharkov State University. His basic pedagogical principles were (i) to learn to study and (ii) that to understand is more important than to know.

Faĭnberg believed that a professional duty of each scientist was to train pupils. More than 25 doctors and 30 candidates of sciences regard themselves as pupils of Faĭnberg's scientific school. Ideas proposed by Faĭnberg continue to be developed at the Institute of Plasma Electronics and New Methods of Acceleration.

For his major contributions to science, Faĭnberg was elected in 1964 a corresponding member and, in 1979, an academician of the Academy of Sciences of the Ukrainian Soviet Socialist Republic. In 1982, he was awarded the title of an Honored Scientist of the Ukrainian Soviet Socialist Republic and, in 1996, the State Prize of Ukraine in Science and Technology. Since 1991, he was the chairman of the Scientific Council on Plasma Electronics and New Methods of Charged Particle Acceleration of the National Academy of Sciences of Ukraine. Faĭnberg was awarded a number of orders and medals of the Soviet Union and Ukraine.

In spite of his high position in the scientific community, Faĭnberg was exclusively democratic man, but, at the same time, he was intolerant of idlers and those who restricted their scientific activity to their working time. "In science, one is to be engaged in what is pleasant for him. As a rule, nothing can be gained without inspiration," he said in a moment of frankness. Being a tactful and kind man in private talks, he could turn into a bright, passionate, and expressive speaker at seminars and meetings of scientific councils, combining his wittiness and nimble mind with deep anger and sizzling sarcasm when somebody equivocated with scientific results or violated scientific ethics. Having unique teaching abilities, he could make his audience (either students or the members of a scientific council) listen with keen interest to the most complicated physical issues.

Faĭnberg gained world-wide recognition as a brilliant and original scientist who succeeded in coupling the physics of accelerators and electronics to modern plasma physics. The death of Yakov Borisovich Faĭnberg is an irreplaceable loss for science.